HEMP NANOCELLULOSE: FABRICATION, CHARACTERISATION AND APPLICATION

A thesis submitted for the degree of Doctor of Philosophy

By

Dasong Dai

School of Engineering and Design

Brunel University

United Kingdom

August 2012

Contents

Abstract

Nanocellulose has gained lots of attentions in recent years due to the development of nanotechnology. Thousands of publications have been reported about the fabrication, characterization and application of nanocellulose, among which most of the nanocelluloses were fabricated from the microcrystalline cellulose (MCC) or pulp, and only two methods about the nanocellulose fabrication have been reported, i.e. sulphuric acid hydrolysis and mechanical treatment. The sulphuric acid method can only obtain low yield of nanocellulose and the mechanical treatment can not fabricate nanocellulose with high crystallinity index (CI) and well separation. These problems limit the scale up of nanocellulose to industrial area. Moreover, none of works has reported the application of nanocellulose for the modification of natural fibres and only a few works reported the reinforcement of epoxy with nanocellulose.

In this this research, we fabricated nanocellulose directly from hemp fibres by employing oxidation/sonication method with the aim to solve the main problems of nanocellulose fabrication with sulphuric acid hydrolysis or mechanical. By using this method the yield of nanocellulose could up to 54.11 % and the crystallinity of nanocellulose was 86.59 %.

In order to expand the application of nanocellulose, we investigated the modification of natural fibres (hemp) with nanocellulose and the fabrication of nanocomposite. Two-step modification, i.e. dodecyltrimethylammonium bromide (DTAB) pretreatment and nanocellulose modification, was used to modify hemp fibres. In this process, we systematically investigated the deformation of hemp fibres, revealed the mechanism of deformation on the mechanical property of single fibre by using Fourier transform infrared spectroscopy (FTIR) and investigated the effect of deformation on the hemp fibre modification with nanocellulose by using energy dispersive X-ray (EDX). The two-step modification increased the mechanical properties of hemp fibres significantly. Compared with raw hemp fibres, the modulus, tensile stress and tensile strain of the two-step nanocellulose modified hemp fibres increase by 36.13 %, 72.80 % and 67.89 %, respectively. Moreover, two-step modification facilitated the improvement of interfacial property of fibres. This novel natural fibre modification provides new clue to exploit nanocellulose as a green chemical agent for natural fibres modification.

We modified nanocellulose by using curing agent of epoxy---diethylenetriamine (DETA). This modification could increase the dispersity of nanocellulose in epoxy and reinforce epoxy. Compared with epoxy, the modulus, tensile stress and tensile strain of the modified nanocellulose/epoxy nanocomposite increased 1.42 %, 15.44 % and 27.47 %, respectively.

Acknowledgements

I gratefully acknowledge the guidance from my supervisors Professor Mizi Fan and Dr. Philip Collins. Firstly, it is a great opportunity for me to work with him and his research group. Secondly, Prof. Fan has tirelessly assisted me with every step of my research and never been short of good advice and direction when it was needed most in the past four years. I would also like to give thanks to my previous supervisor in China, Professor Biao Huang, for his kindly encouragement, assistance and guidance.

My sincere thanks to my family for their enormous support and affection they have always given me during my PhD study.

I would like to thank the technicians at the Department of Civil Engineering who have provided the technical assistance for my research. I would also like to thank the people who have kindly given help for instrument analysis in Department of ETC in Brunel University. I also would like to thank Dr. Shuxia Wang who gave me encouragement during the writing of my thesis.

Finally, my thanks go to all the research students and administrative personnel in the Department of Civil Engineering who in one way or another helped me during my research.

Abbreviations

AFM	Atomic force microscopy
ATR-FTIR	Attenuated total refraction Fourier transform infrared spectroscopy
AVOVA	Analysis of variance
BC	Bacterial cellulose
CAB	Cellulose acetate butyrate
CCD	Central composite design
CF	Carbon fibre
CI	Crystallinity index
CMC	Carboxymethyl cellulose
CTAB	Cetyltrimethylammonium bromide
DETA	Diethylenetriamine
DLS	Dynamic light scattering
DSC	Differential scanning calorimetry
DTAB	Dodecyltrimethylammonium bromide
EDTA	Ethylene diamine tetraacetic acid
EDX	Energy dispersive X-ray
FE	Finite element
FEG-SEM	Field emission scanning electron microscopy
FTIR	Fourier transform infrared spectroscopy
G	Guaiacyl
GMA	Glycidyl methacrylate
H	P-hydroxyphenyl
HPO	Hydroperoxide
KAS	Kissinger-Akahira-Sunose
LbL	Layer-by-layer
LCC	Lignin-carbohydrate complex
LCs	Liquid crystals
MCC	Microcrystalline cellulose
MDI	Diphenylmethane-4,4-diisocyanate
MFA	Microfibril angle
MFC	Microfibrillated cellulose
ML	Middle lamellae
NFC	Nanofibrillated cellulose
NMR	Nuclear magnetic resonance
NT	Nanotechnology
NTA	Nanoparticle tracking analysis
OM	Optical microscopy
PEO	Poly(ethylene oxide)
PF	Phenol-formaldehyde
phr	parts per one hundred

PLLA	Poly-L-lactic acid
PRESS	Predicted residual error sum of squares
PVA	Polyvinyl alcohol
PXRD	Powder X-ray diffraction method analysis
RSM	Response surface methodology
S	Syringyl
SANS	Small-angle neutron scattering
SAXS	Small-angle X-ray scattering
SB	Šesták-Berggren
SEM	Scanning electron microscopy
SLS	Static light scattering
TEM	Transmission electron microscopy
THC	Tetrahydrocannabinol
USAXS	Ultra-small-angle X-ray scattering
WAXS	Wide-angle X-ray scattering
XPS	X-ray photoelectron spectroscopy
XRD	X-ray diffraction

List of Figures

List of Tables

Chapter 1 Introduction

1.1 Non-wood lignocellulosic fibres

The utilization of natural fibres was superseded in last century by a wide-range of synthetic polymers which was developed based on raw materials from the new low cost petroleum. However, since the 1990s, increasing attention has been re-paid on the utilization of natural fibres, especially the lignocellulosic fibres. The most abundant lignocellulosic fibres are wood fibres; however, due to the depletion of timber resources, non-wood lignocellulosic fibres (e.g. hemp fibres) are becoming important in use. The growing importance of the non-wood lignocellulosic fibres can be evident from the increasing number of publication in the last 40 years (see Fig.1.1). It should be noted that we searched these publications from the ISI Web knowledge database by entering the words fibres as topic and the name of fibre (including, bamboo, flax, hemp, jute, kenaf, ramie, banana, pineapple, sisal, coir and oil palm) as title only with journal type. We found that, 2547 publications from journal publications about the application of non-wood lignocellulosic fibres have been produced in the last 40 years (i.e., from 1970 to 2010); among which from 1990s, the number of publications increased rapidly, especially from 2005 to 2010.
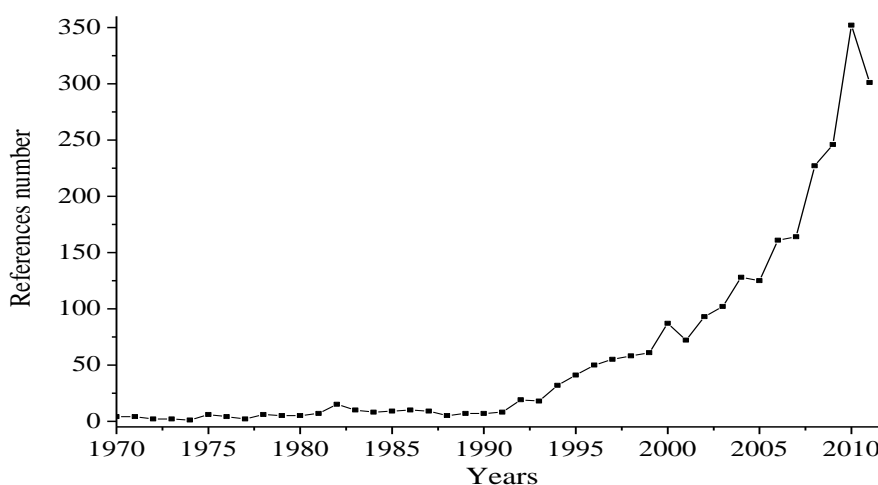
Fig. 1.1 Number of references by publication year.

Among these publications, most of them focus on the application of non-wood lignocellulosic fibres in fibre-based composites; up to 67.14 % (see Fig. 1.2) of these publications demonstrate the fabrication of fibre-based composites. The applications of non-wood lignocellulosic fibres in traditional industries, e.g. textile industry and pulp and papermaking industry, still play an important role; in our statistics, as shown in Fig. 1.2, 15.86 % of the reports refer to the applications in textile industry and 8.21 % of the reports refer to the applications in paper industry. Moreover, the extraction of nano-scale cellulose from non-wood lignocellulosic fibres shows a

strong growing tendency in the last ten years (see Fig. 1.3), but only 3.77 % (see Fig. 1.2) of the publications refer to this topic.
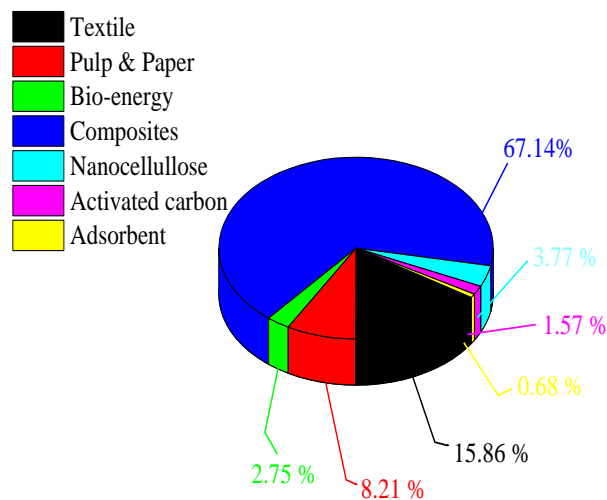
Fig. 1.2 Application of lignocellulosic fibres.
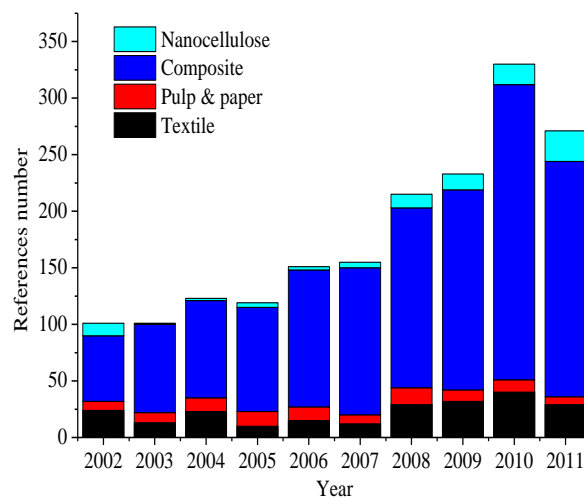
Fig. 1.3 Number of references in nanocellulose, composite, pulp & paper and textile in last 10 years.

1.1.1 Mechanical and surface properties of non-wood lignocellulosic fibres

1.1.1.1 Mechanical property

Non-wood lignocellulosic fibres are in general suitable for reinforcing inorganic polymers, synthetic polymers and natural polymers due to their relative high strength, stiffness and low density [1] (see Table 1.1). The characteristic values for flax could reach to levels close to those for E-glass fibres [2]. However, the range between minimum and maximum characteristic values, as one of the drawbacks for all natural products, is remarkably wider than that of synthetic fibres (Table 1.1), which can be

explained by the differences in fibre structure due to the overall environmental conditions during growth. It is apparent from Table 1.1 that comparing with wood fibres, non-wood fibres show similar mechanical properties. The fibre properties and fibre structure are influenced by several conditions and varies by area of growth, climate and the age of the plant [3, 4]. Further, the technical digestion of the fibre is another important factor which determines the structure as well as the characteristic values of the fibres.

Table 1. 1 Mechanical properties of non-wood lignocellulosic fibres as compared to conventional reinforcing fibres

Types of fibres	Fibres	Density (g/cm^3)	Elongation (%)	Tensile strength (MPa)	Young modulus (GPa)	References
Stem fibres	Bamboo	0.6-0.91	1.4	193-600	20.6-46.0	[5-7]
	Flax	1.5	1.2-3.2	345-2000	15-80	[8-10]
	Hemp	1.48	1.6	550-900	26-80	[3, 11, 12]
	Jute	1.3	1.16-1.5	393-800	13-55	[9, 13]
	Kenaf	1.45	1.6	157-930	22.1-60	[14-18]
	Ramie	1.5	1.2-3.8	400-938	61.4-128	[19]
Leaf fibres	Banana	0.72-0.88	2.0-3.34	161.8-789.3	7.6-9.4	[20]
	Pineapple	1.07	2.2	126.6	4.4	[21]
	Sisal	1.5	3.0-7.0	468-700	9.4-22	[19]
Fruit fibres	Coir	1.2	17-47	175	4.0-6.0	[2, 22]
	Oil palm	0.7-1.55	4-18	50-400	0.57-9.0	[23, 24]
Wood fibres	Softwood Kraft (spruce)	1.5	-	1000	18-40	[25]
	Hardwood Kraft (birch)	1.2	-	-	37.9	[26]
Synthetic fibres	E-glass	2.5	2.5	2000-3500	70	[2]
	S-glass	2.5	2.8	4570	86	[2]
	Aramide	1.4	3.3-3.7	3000-3150	63.0-67.0	[2]

For example, Fig. 1.4 illustrates tensile strength of natural fibres, showing the influence of the deformation of the fibres [27]. By employing the finite element (FE) method, Nilsson et al [27] investigated the effect of deformation on the tensile performance of natural fibres and found that the elastic stiffness of fibre was greatly affected by deformations and that the S-shaped stress vs. strain curve can be explained by non-linear geometric effects and yielding of the hemicellulose in the deformation areas. Their FE analysis agrees well with previous work by Baley [28]. Fig. 1.5 [28] shows the initiative of cracks in the flax fibre which in general appears around the deformation of fibres during a tensile loading. Tensile strength of the fibres is also influenced by the fineness of the fibre [29]. A decrease in fibre fineness gives rise to higher fibre strength. The tensile strength of natural fibres also depends on the test length of the specimens which is of vital importance in terms of its reinforcing efficiency.
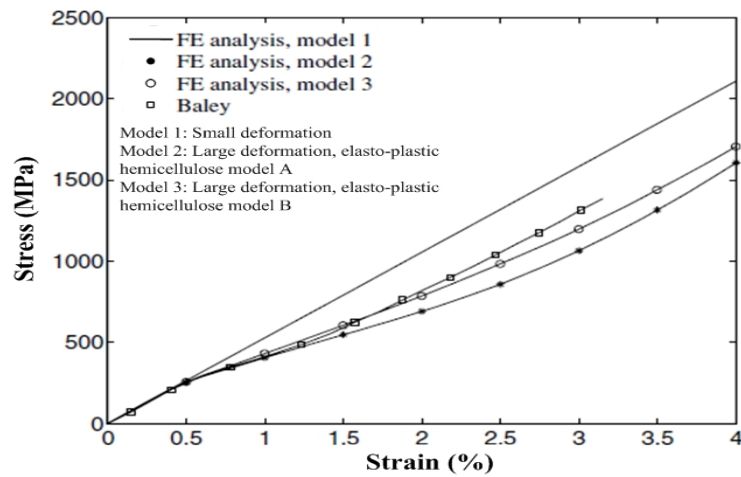
Fig. 1.4 Effect of dislocation on the tensile strength of natural fibres.
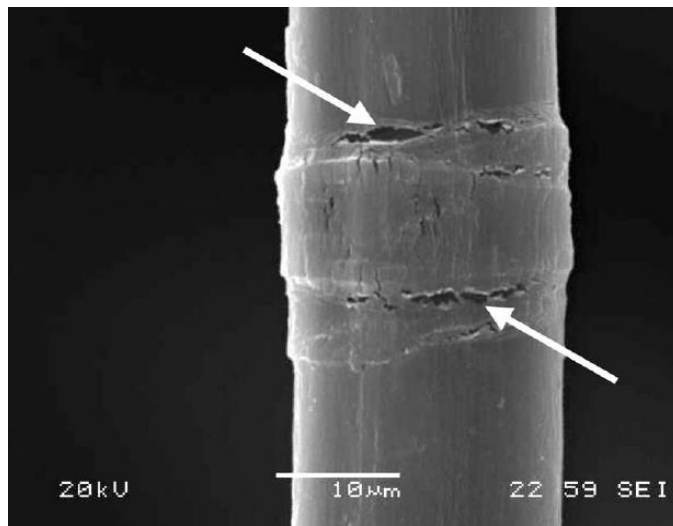
Fig. 1.5 Start of cracks in a flax fibre in the area of deformation.

1.1.1.2 Surface property

Fig. 1.6 shows morphologies of bamboo ((a) [30], (b) [31], (c) [30]), banana ((d) [32], (e) [20], (f) [32]) and coir ((g) [33], (h) [34], (i) [35]) fibres from cross section to fractographs. The fracture of fibre ((c), (f), (i)) shows splintering (Fig. 1.6(c) and 1.6(i)) and cross fracture (Fig. 1.6(f)) modes. The splintering fracture indicates that fibres have low cellulose content, high microfibril angle and low aspect ratio, while fibres such as banana having high cellulose content, smaller microfibril angle and high aspect ratio exhibit a cross fracture mode indicated by no pull-out microfibrils. The surface morphologies of fibres are shown in Fig. 1.6(b), 1.6(e) and 1.6(h) which also indicates considerable hemicelluloses, lignin, waxes, oils and surface impurities on the fibre surface. The surface property is influenced by fibre morphology, extractive chemicals and processing conditions, which in fact is the key property of natural fibres (surface properties of parts of non-wood lignocellulosic fibres are

summarized in Table 1.2), as it can affect the interfacial adhesion of resins on the surface of fibres and the mechanical properties of natural fibre-based composite. Due to the high polar feature on the surface, the fibres are also less compatible with non-polar resins. Therefore, the combination of the inherent polar and hydrophilic features of natural fibres and the non-polar characteristics of resins give rise to difficulties in compounding these materials, resulting in poor stress transfer efficiencies. The use of different kinds of physical (i.e. corona discharge) and chemical surface treatment methods (i.e. coupling agents such as silanes) leads to changes in the surface structure of the fibres as well as to changes of surface properties (extensive illustration will be described in 2.*1.3 Modification of hemp fibres*).
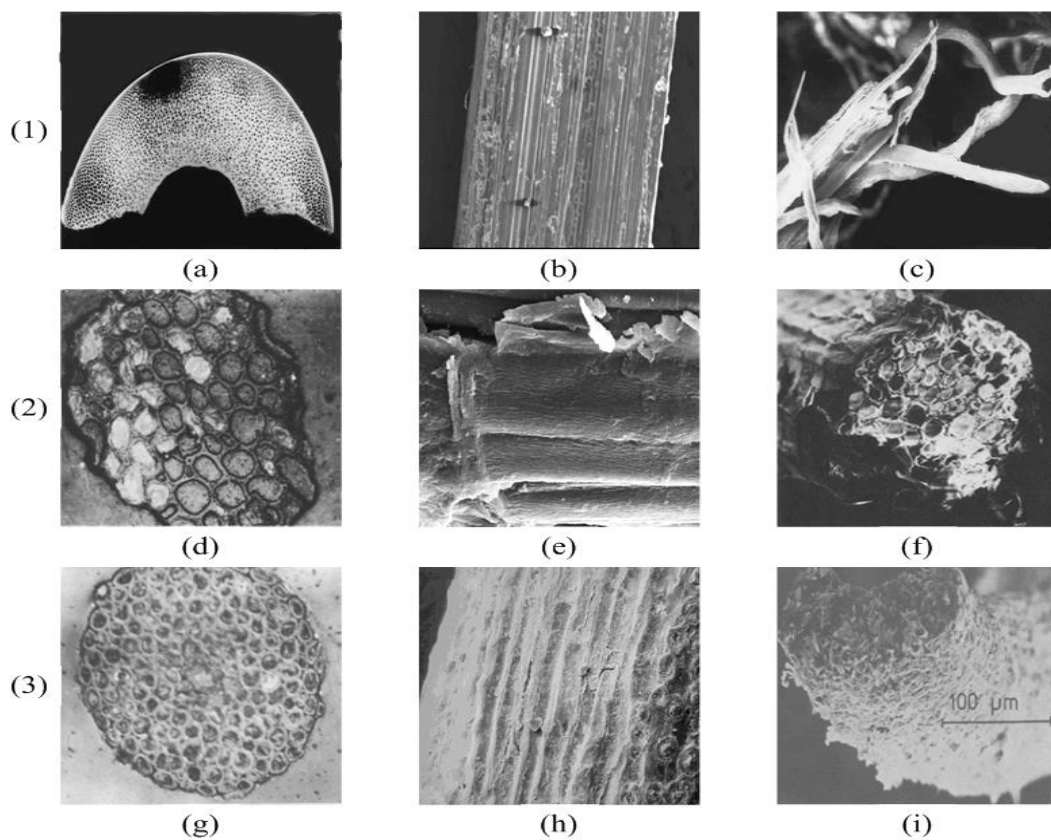
Fig. 1.6 Morphologies of natural fibres: cross section (a), surface (b) and fractural surface (c) of bamboo fibres (1); cross section (d), surface (e) and fractural surface (f) of banana fibres (2); (g) cross section, surface (h) and fractural surface (i) of coir fibres (3).

Table 1. 2 Surface properties of natural fibres

Fibres	Surface area (m^2/g)	γ^d dispersive surface energy (mJ/m^2)	$(\zeta_0-\zeta_\infty)/\zeta_0$ (mV)	$\zeta_{plateau}$ (mV)	References
Flax	0.31~0.79	23.85	0.88~0.95	-1.1~ -0.21	[36-39]
Hemp	0.75	31.6	0.91	-0.1	[37, 39, 40]
Sisal	1.63	32.9-33.3 48.35	0.76~0.88	-1.7~ -0.4	[37-39, 41]
Coir	0.48	45.05	0.22	-4.6~ -3.8	[38, 41, 42]

1.1.2 Physical structure of non-wood lignocellulosic fibres

The cell wall of natural fibres is formed out of crystalline microfibrils based on cellulose, which are connected to a complete layer by lignin and hemicellulose. Till date, many authors [43-48] tried to illustrate the correlation between physical structure and mechanical properties for natural fibres (parts of physical structure for natural fibres are summarized in Table 1.3). In 1980, McLaughlin et al [35] firstly carried out a detailed statistical analysis of physical structure-property relations. They found that a positive correlation between mechanical properties (tensile strength and Young's modulus) and the physical structure (cellulose content and microfibril angle (MFA)), see Fig. 1.7(a) and 1.7(b) [49]).

Table 1. 3 Structural parameters of natural fibres

Fibres	Microfibril angle (°)	Crystallinity index (%)	References
Bamboo	2-10	66.3	[6, 50]
Flax	5-10	42.9	[18, 50, 51]
Hemp	2.2-6	55-66.3	[18, 52-54]
Jute	8-8.1	50-58.9	[6, 18, 55, 56]
Kenaf	-	54.6	[57]
Ramie	7.5	69.4	[18, 50]
Banana	11	45-68	[6, 58, 59]
Pineapple	8-14	44-60	[59, 60]
Sisal	10-22	57	[18, 61]
Coir	39-49	27-33	[6, 59]
Oil palm	-	40	[53]

(a)   (b)
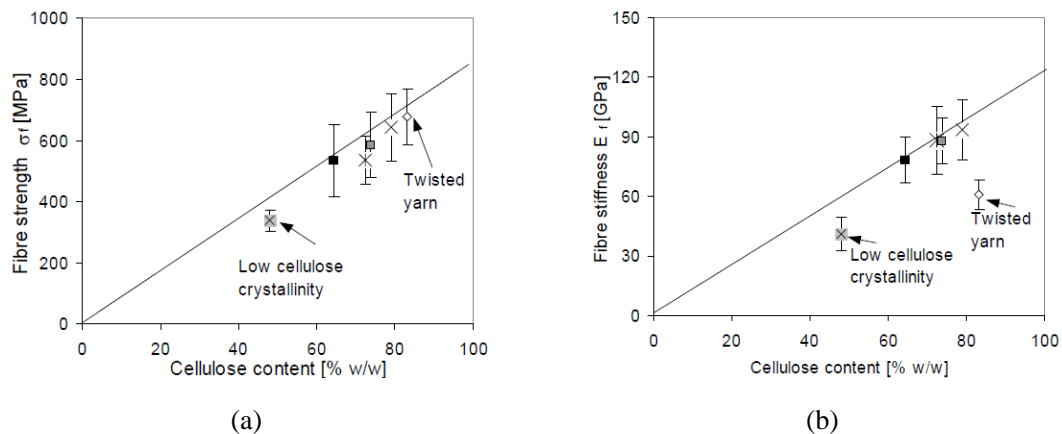
Fig. 1.7 Effect of cellulose structure on fibre mechanical properties: (a) tensile strength; (b) stiffness.

The correlation between tensile strength and physical structure (i.e. cellulose content, MFA, fibres length and fibre diameter) were developed by Mukherjee et al [62] as shown in Eq. 1.1:

$$Y = KX_cCos\theta(\frac{L}{D})^a + C \quad \text{(Eq. 1.1)}$$

where Y is the tensile strength, K and C are constants for equation; X_c is the cellulose content; θ is MFA; L is the length of fibres and D is the diameter of fibre. Three different equations were developed to calculate fibre stiffness with respect to the fibre axis:

(1) Without deformation (MFA <45°)

$E_| = [X_{1C}E_{\|,C}+(1-X_{1C})E_{NC}]\cos^2 X_2 = E^*\cos^2 X_2$ (Eq. 1.2)

where $E_{\|,C}$ is the Young's modulus of fibre in the parallel direction, E_{NC} is the Young's modulus of non-crystalline parts, X_{1C} is the content of the crystalline part in the fibre and X_2 is microfibril angle.

(2) Deformation (MFA>45°)

$E_| = K_{NC}^*(1-2\cot^2 X_2)^2/(1-X_{1C}) = K(1-2\cot^2 X_2)^2$ (Eq. 1.3)

where K_{NC} is the bulk modulus of non-crystalline parts, X_{1C} is the content of the crystalline part in the fibre and X_2 is microfibril angle.

(3) General formulation

$$E_| = \frac{E \times \cos^2 X_2 \times [K \times (1-\cot^2 X_2)^2]}{E \times \cos^2 X_2 + K(1-2\cot^2 X_2)^2} \quad \text{(Eq. 1.4)}$$

where X_2 is microfibril angle and K is the constant for equation.

1.1.3 Chemical compositions of non-wood lignocellulosic fibres

The composition of non-wood lignocellulosic fibres are cellulose, hemicellulose, lignin, pectin, waxes and water soluble substances (chemical compositions values are shown in Table 1.4), with cellulose, hemicellulose and lignin as the basic compositions with regard to the physical properties of the fibres.

Table 1. 4 Chemical composition of natural fibres [2, 63, 64]

Fibres	Cellulose (%)	Hemicellulose (%)	Lignin (%)	Pectin (%)	Water soluble substances (%)	Wax (%)
Bamboo	24-43	30	21-31	-	-	-
Flax	62.8-69.0	17.1-18.6	2.2-2.8	2.0-4.2	4.3-11.6	1.5-1.7
Hemp	57.66-74.4	16.7-17.9	3.7-6.55	0.9-7.04	2.3-8.99	0.8-3.06
Jute	71.5-71.6	13.3-13.4	13.1	0.2	1.2	0.6
Kenaf	65.7	8.1	15.7	0.4	9.3	0.8
Ramie	76.2	14.6	0.7	2.1	6.1	0.3
Banana	63-64	19	5	-	-	-
Pineapple	81	-	12.7	-	-	-
Sisal	73.1	13.3	11	0.9	1.4	0.3
Coir	32-43	0.15-0.25	40-50	-	-	-
Oil palm	65	-	29	-	-	-

1.1.3.1 Cellulose

In 1838, the French chemist Anselme Payen extracted same substance from various plants, to which he gave the name of *cellulose* [65]. Cellulose is the most abundant polymer with the molecular formula $(C_6H_{10}O_5)_n$ (Fig. 1.8) in the world. This polymer consists of a linear chain of several hundred to over ten thousand $\beta(1\rightarrow4)$ linked D-glucose units [66]. It is the structural component of the primary cell wall of green plants (Fig. 1.9), many forms of algae and the oomycetes. For industrial use, cellulose is mainly obtained from wood pulp and cotton. Although the chemical structure of cellulose is understood in detail, its supermolecular state, including its crystalline and fibrillar structure, is still open to debate [67]. It is mainly used to produce paperboard and paper; to a smaller extent it is converted into a wide variety of derivative products such as cellophane and rayon. Converting cellulose from energy crops into biofuels such as cellulosic ethanol is under investigation as an alternative fuel source. Recently fabricating the nano-scale fibril from cellulose is new tendency which attracts significant investment from government all over the world.

The basic structural element of cellulose fibres is the so-called elementary fibril [68]. Several elementary fibrils associate to form larger aggregations of so-called microfibrils and macrofibrils. Due to the versatile properties (e.g. specific surface area [69] and high elastic modulus [70-72]), cellulose microfibrils have gained increasing attention around the world. Much more details about the microfibril will be discussed in *2.2 Nanocellulose*.
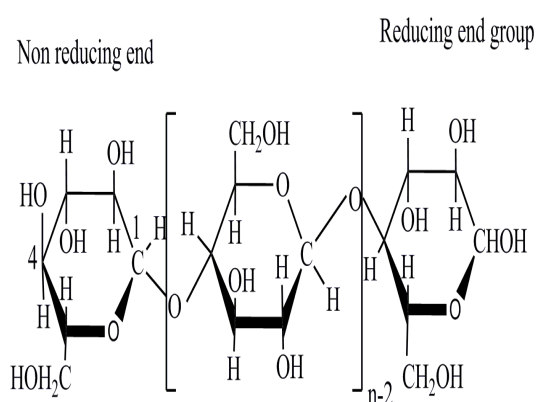
Fig. 1.8 Hawthorne projection formula of cellulose.
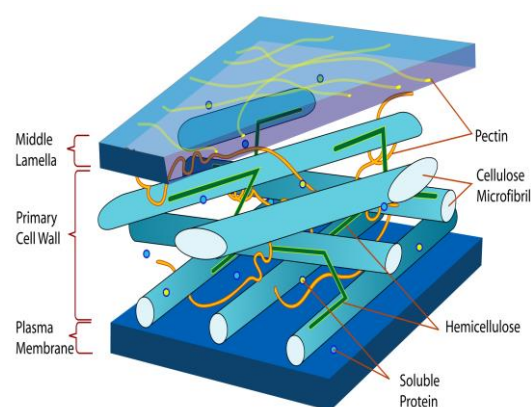
Fig. 1.9 Location and arrangement of cellulose microfibrils in the plant cell wall.

1.1.3.2 Hemicellulose

Hemicellulose is the second most common polysaccharides in nature, representing about 20-35% of lignocellulosic biomass [73]. It is a low molecular weight polysaccharide with a degree of polymerization ranging from 70 to 200. Hemicellulose acts as a compatibilizer between cellulose and lignin, which can form lignin-carbohydrate complex (LCC) by ester and ether bonding. Isolated hemicellulose is found to be amorphous and either water soluble. Hemicelluloses are

heterogeneous polymers of pentoses (xylose, arabinose), hexoses (mannose, glucose, galactose), and sugar acids. Unlike cellulose, hemicelluloses are not chemically homogeneous. In contrast to the strictly linear structure of cellulose, hemicellulose is mainly branched molecules. In hardwood, hemicellulose is predominantly partially acetylated acidic xylan, with a small percentage of mannan. In softwood, hemicelluloses are predominantly partially acetylated galactogluco-mannans, with a low amount of xylan similar to the hardwood xylan. Hemicelluloses are flexible polysaccharides that characteristically bind to the surface of cellulose. They may form tethers that bind cellulose microfibrils together into a cohesive network (Fig. 1.10). In addition, they act as a slippery coating to prevent direct microfibril–microfibril contact.

1.1.3.3 Lignin

In 1838, Anselme Payen [65] treated wood with nitric acid and alkaline solutions and yielded an insoluble fraction, designated cellulose and a soluble fraction, which he called *incrustant*. This soluble materials was named *lignin* in 1857 by Schulze [74]. Lignin is the second most abundant plant substance in vascular plants. Although precise structure of lignin is not known because it is difficult to extract lignin from plants, it is now generally accepted that lignins are the complex three-dimensional network aromatic polymers composed by the phenol-propane basic units with C-C bonds or C-O-C bonds. In the cell wall of plant, lignins are deposited mainly in the thickened secondary wall but can also occur in the primary wall and middle lamella, they serve as a matrix for the embedded cellulose fibres (Fig. 1.10) [75] and strengthen stems and vascular tissue, allowing upward growth and permitting water and minerals to be conducted through the xylem under negative pressure without collapse of the tissue. Its physical toughness deters feeding by animals, and its chemical durability makes it relatively indigestible to herbivores. Finally, lignin is also permanent glue, bonding cells together in the woody stems and thus giving the stems their well known rigidity and impact resistance.
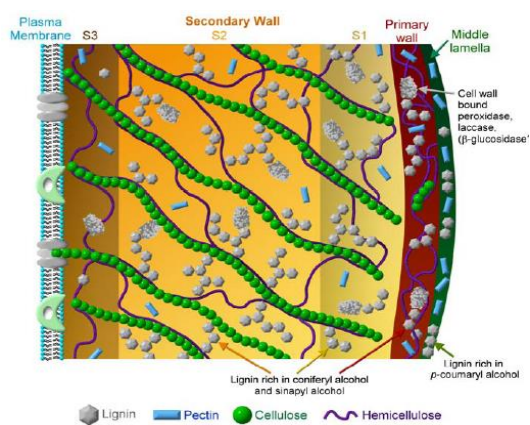
Fig. 1.10 Illustration of a plant cell wall.
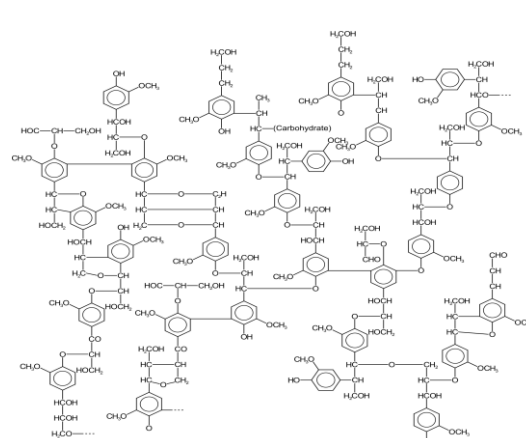
Fig. 1.11 Schematic diagram of a representative

section of the molecular structure of lignin.

Lignin is cell-wall polymers made of phenylpropane units (Fig. 1.11) [76], three basic units in lignins are p-hydroxyphenyl (H), guaiacyl (G) and syringyl (S) [77, 78]. They can be divided into three major classes: guaiacyl, guaiacyl-syringyl lignin and guaiacyl-syringly-p-hydroxyphenyl lignin. The types of lignin vary from plant to plant. Gymnosperm mainly contains guaiacyl lignin; dicotyledonous angiosperm mainly contains guaiacyl-syringyl lignin and monocotyledon mainly contains guaiacyl- syringly-p-hydroxyphenyl lignin.

1.2 Aims and objectives of research

The aims of this research were (i) to fabricate nano-scale cellulose directly from non-wood lignocellulosic fibres (hemp fibres) with oxidation/sonication method; by using the developed nanocellulose for (ii) the modification of hemp fibres and (iii) the reinforcement of epoxy. It is expected this project will (i) better understanding of various parameters that contribute to the high yield production of nanocellulose without further damage on the crystalline region of cellulose and (ii) revealing the mechanisms of strengthening natural fibres with nanocellulose reinforcement on the interface characteristics of the reinforced fibrous materials.

The specific objectives of the projects are:
- to develop a novel process for fabricating nanocellulose;
- to produce nanocellulose materials;
- to characterize the developed materials;
- to examine the deformation of hemp fibres in order to establish their correlation with the strength of hemp fibres;
- to modify single fibre by means of nanocellulose in order to improve the mechanical properties of fibre;
- to understand and enhance the interfacial adhesion between fibre and matrix by nanocellulose modification;
- to develop the improved composite by means of adding nanocellulose.

1.3 Schematic of research

The plan of the research is described in Fig. 1.12. In summary, this research includes: (1) nanocellulose fabrication and the application of nanocellulose, namely, (2) the modification of hemp fibres with nanocellulose and (3) fabrication of nanocellulose/ epoxy nanocomposite.

In the first part about the nanocellulose fabrication, response surface methodology (RSM) will be used to design the experiment of nanocellulose fabrication. The fabrication of nanocellulose will be developed by oxidation/sonication method, and the processing will be optimized by using Design-expert software. Seven analytical instruments will be used to analyze nanocellulose and investigate (i) the size distribution and morphologies of nanocellulose; (ii) the chemical structure and

crystalline of nanocellulose and (iii) the thermal property of nanocellulose.

The second part of the research focus on the modification of hemp fibres with nanocellulose. Deformation in hemp fibres is the first focus point in this part. Microscopy and spectroscopy technology will be used to reveal the effect of deformation on the mechanical properties of hemp fibres. This novel modification will be carried out by repairing the deformations of hemp fibres. By employing energy dispersive X-ray (EDX), field emission scanning electron microscopy (FEG-SEM) and X-ray diffraction (XRD) to reveal mechanism of repair on the deformation is the second focus point in this part. The third focus point is about the interfacial property of nanocellulose modified hemp fibres. X-ray photoelectron spectroscopy (XPS) and Fourier transform infrared spectroscopy (FTIR) will be used to reveal the interfacial adhesion of modified fibres with resin (unsaturated polyester).

A novel method of nanocellulose modification is developed in the third part. With the treatment of diethylenetriamine (DETA), the modified nanocellulose will be used to reinforce epoxy. The effect of nanocellulose on the mechanical properties of nanocomposite and the cure kinetics of epoxy are investigated in this part.
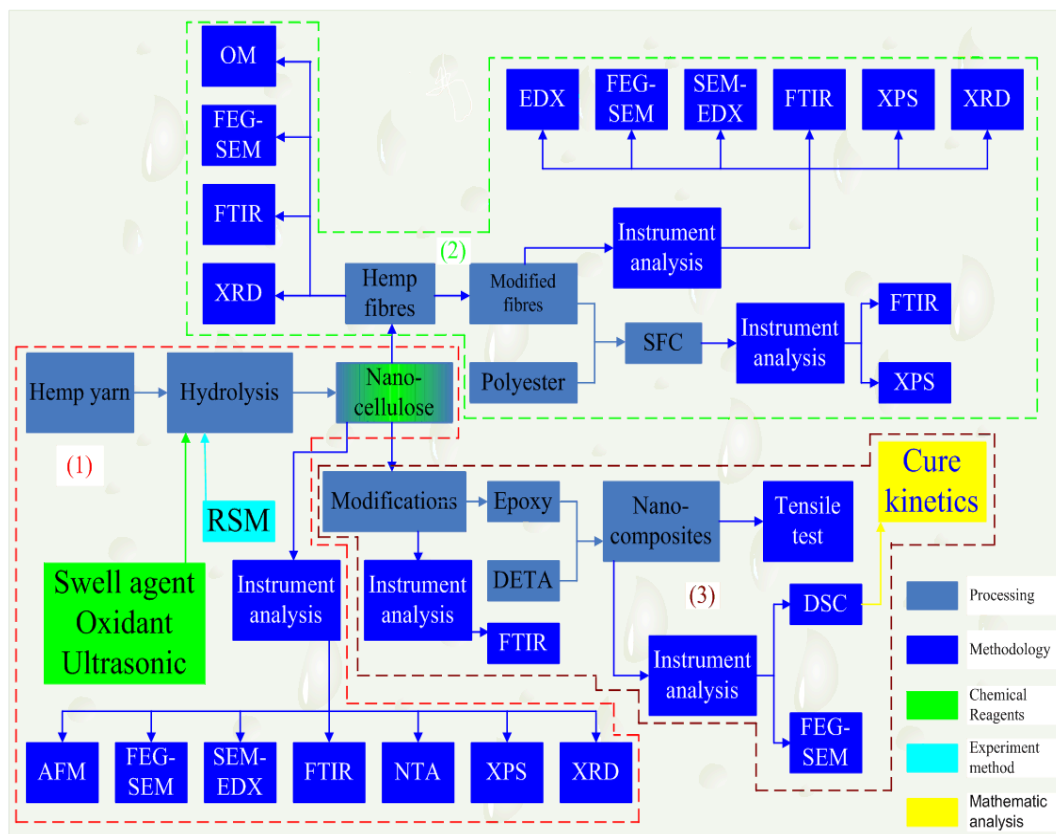
Fig. 1.12 Schematic of research.

Chapter 2 Literature Review

2.1 Hemp fibres

2.1.1 Morphology of hemp fibres

The stem of hemp (see Fig. 2.1 [49]), which consists of various layers, is the main supporting structure of hemp and serves to transport and to store water and food. Diameter of hemp stem ranges from 0.6 to 4.5 cm, the value is determined by the various factors, such as sowing date, plant density, species and soil [79-81]. Hemp fibres are presented in bundles as long as the stems, which can easily be peeled off the xylem, surface by hand or machine. The outer layer of stem, the epidermis, is covered by a 2-5 μm surface layer [82]---cuticle, which protects the plant from drying, and it consists of waxy matter [83]. Epidermis layer (20-100 μm), consisting of colour-binding media and stomata (pores), through which the plant ventilates and regulates evaporation, is the thin outside protective layer of plant cells [84]. Cortex layer is a thin layer of walled cells that has no fibre, but does contain chlorophyll.
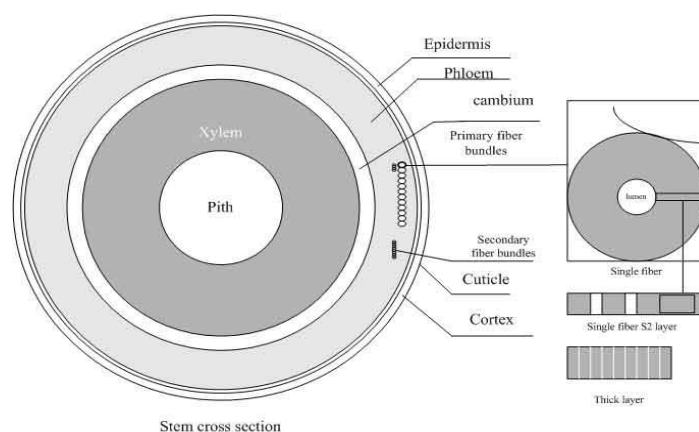
Fig. 2.1 Model of transverse hemp stem section zooming to single fibre, secondary cell wall and finally the cell wall lamella.

Phloem layer contains short cells that have chlorophyll and long cells that are bast fibres. Phloem layer consists bundles of 100-300 polygonal-shaped primary and secondary fibres cells (see Fig. 2.2(a) and 2.2(b) [85]) with 4 to 6 sides (see Fig. 2.2(c) [86]). Both are thick-walled, with a high content of cellulose and a low content of hemicellulose and lignin [87]. About 92-95% [81, 88] hemp fibres are from the primary fibres cells. The thickness of cell wall in primary and secondary fibres cells are about 7-13 μm and 3-6 μm, respectively [88], while the average length of fibres in primary and secondary fibres cells are about 20 mm and 2 mm, respectively. The secondary fibres are more brittle than the primary fibres [89]. Cambium layer (10-50 μm) is the growth area which produces hards on the inside and bast and bark on the outside. Although this is the differentiation layer, it is also an abscission layer where fibres and hards separate during the retting/breaking process. Hollow cylinder of 1-5

mm thick xylem is the center of the plant and exists throughout the stem except at the joints. Xylem is a continuous system of tubes running from the roots to the leaves. It consists of empty and dead cells with thickened sidewalls [90]. Pith layer which is empty space in dry stems is composed of thick and woody tissue used to support the plant. The product from this area is called hards which comprises 60-75 % of the total mass.
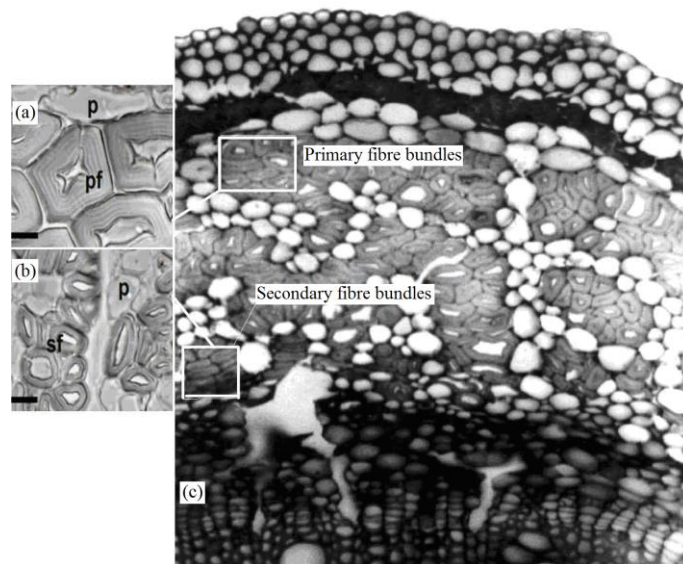
Fig. 2.2 Structure of hemp fibre bundles in phloem layer: (a), primary fibre bundles; (b), Secondary fibre bundles and (c) cross section of hemp stem.
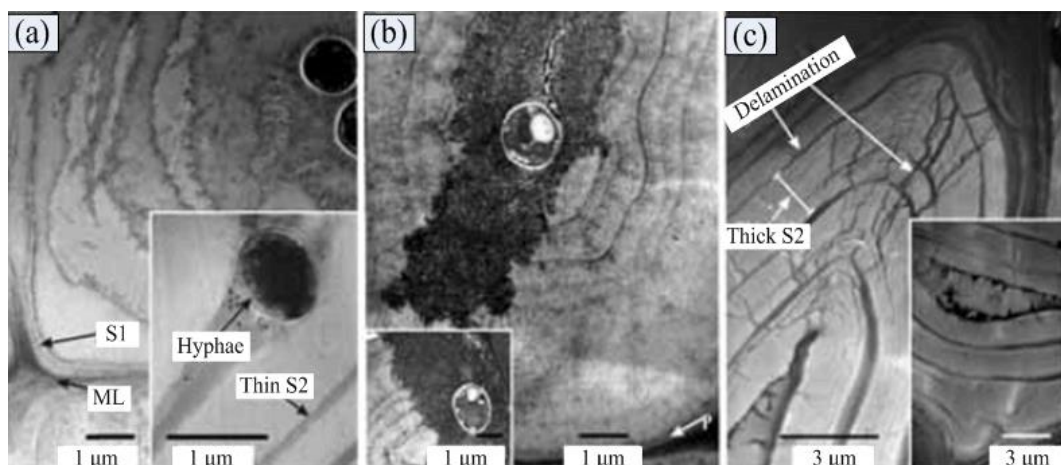
Fig. 2.3 TEM micrograph of single hemp fibres partially decayed by fungus: (a), P.mutabilis decay; (b), P.radiata L 12-41decay and (c), P.radiata Cel 26 decay.

The microstructure of the fibre wall in the hemp fibres including middle lamellae (ML, 30-50 nm), primary wall (70-100 nm) and the secondary cell wall which was composed of a 100-130 nm thin S1 layer (the first layer in the secondary cell wall) and a 3-13 μm thick S2 layer (the secondary layer in the secondary cell wall). Transmission electron microscopy (TEM) observations [49] (Fig. 2.3) showed that the

S2 layer had a laminate structure of 1 to 4 concentric layers of 1-5μm in thickness. These layers were constructed of 100 nm thick lamellae. Thin layers of 200-240 nm in thickness were located in between the concentric layers. These thin layers seem to lack cellulose [49]. The microfibril angle can strongly influence mechanical properties of fibres like tensile strength and modulus [91-94].
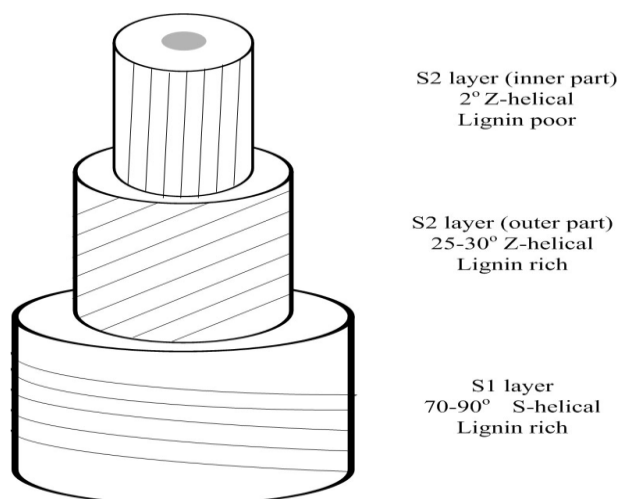
Fig.2.4 Model of the microfibril orientation throughout the secondary cell wall (the S3 layer was not found in hemp fibres).

As shown in Fig. 2.4 [49], the microfibril angle in S1 layer of hemp is in the range of 79-90° compared with 25-30° in the outer part of S2 layer, and 0-5° in the inner part of S2 layer. The distribution of lignin, pectin and waxes in the cell wall of hemp fibre varies between different cell walls and layers. The inner part of secondary wall contained less lignin, while outer part contained the same amount of lignin with middle lamellae. Both the parenchyma cells and the single fibre compound middle lamellae contained pectin, while the secondary wall lacked pectin. Wax could be found in the epidermis cells with highest content in the cuticle layer. According to the histochemical investigation, pectin degradation can provide separation of the fibre bundles from the xylem surface, while separation of the fibre bundles into single fibres requires both lignin and pectin degradation. Wax can inhibit binding between fibres and resin.

The single hemp fibre cells are bonded together with pectins and small amounts of lignin framing the next level of microstructure, the technical fibres, with diameters of 50–100 mm. These filaments are fixed together with a pectin-lignin matrix that forms the fibre bundles in the cortex of the plant stems. Thus, bast fibres are bundles of individual strands of fibres held together by a pectin-lignin interface [95].

2.1.2 Chemical composition of hemp fibres

Fibres from different plant species can appear quite differently. However the chemical composition is fairly similar. Plant fibres consist mainly of cellulose, hemicellulose

and lignin in different proportions. These components comprise 80-90 % of the dry material (Table 1.4). Variation in the chemical composition can occur within the hemp species depending on variety, area of production, maturation [96], processing, research methods [97], environmental conditions and within the hemp plant between woody cores, bast fibres and leaves [49]. The main component of most plant fibres is cellulose, lignin and hemicellulose, which have been described in *1.1.3 Chemical compositions of non-wood lignocellulosic fibres*.

2.1.3 Modification of hemp fibres

Compared with other natural fibres (wool and cotton), bast fibres need to be degummed and separated into fine fibres. Various such methods have been reported, e.g. chemical degumming [98-100], physical degumming [82, 101, 102] and biological degumming [103]. After degumming, due to the increase of the crystallinity index (CI), degree of orientation, the accessibility of hemp fibres decrease which may effects the posttreatment of hemp fibres for the end products. Therefore, modification of hemp fibres is getting more and more interesting. The modification of hemp fibres can be classed in four methods: chemical modification, physical modification, biological modification and nanotechnology modification.

2.1.3.1 Physical modification

Physical modification has always been done by using some instruments to change the structural and surface properties of the fibres with the aims of increase the strength of fibres. The hydrophobicity of the fibres thereby influences the mechanical bonding with the matrix. The traditional methods involve thermotreatment [104, 105], calendaring [106, 107], and stretching [108]. Thermotreatment is the useful way to modify the natural fibres in the traditional method. When fibres are subjected to heat treatment much above the glass transition temperature of lignin, it is postulated that lignin will be softened and migrate to the fibre surface. According to the report by Cunha et al [105], kraft lignin is having a glass transition temperature at 142 °C. Lignin begins to degrade at around 214 °C, hence heating the fibres to 200 °C would be expected to cause some softening [109]. During heating of flax fibres above 150 °C for approximately 2 h, the hemicellulose and lignin are depolymerised into lower molecular aldehyde and phenolic functionalities [110], which are combined by further curing reaction forming into water resistant resins. These resins keep the microfibrils together. Prasad et al [92] thermally treated hemp fibres in an enclosed vessel in air as well as inert environment, and found that there were openings of fibres upon heating, both along the length as well as along the diameter or the width directions. Inert environment treated fibres had a lesser moisture uptake rate compared to untreated fibres. For the same weight of the fibre, the total count of fibres increased during heat treatment, with increment up to 32 % for inert environment and 39 % for air environment.

Surface modification by discharge treatment [111, 112], such as low-temperature plasma, sputtering, and corona discharge, is of great interest in relation to the improvement in functional properties of natural fibres. Since the 1960s scientists in some industrialized countries, such as France, Japan and the United States have carried out the surface treatment of different fibres with various plasma techniques. To date scientists in most countries have studied this topic to develop their own industrial projects. Plasma technology has been widely used as an effective method for surface modifications of natural fibres such as flax [113, 114], sisal [115], keratin [116]. Plasma treatment (see Fig. 2.5, Fig. 2.5(a) from [117], Fig. 2.5(b) from [118], Fig.2.5(c) from [119]) causes mainly chemical implantation, etching, polymerization, free radical formation and crystallization, whereas the sputter etching brings about mainly physical changes, such as surface roughness, and this leads to increase in adhesion [113]. Jovančić et al [119, 120] reported that the wettability and dyeability of hemp fibres are significantly enhanced after plasma treatment. Longer treatment time, leading to rougher surface, results in better surface wettability and dyeability. Titova et al [121] separated the lignin of bast fibres (hemp, flax and jute) by plasma–solution treatment. They found that the plasma-solution treatment, which together with improved traditional technologies, is an effective delignification method of bast fibres. The results showed that the delignification degree can be increased under this treatment, in this case, the delignification degree for hemp, flax and jute is 64 %, 68 % and 39 %, respectively. These results indicated that the main admixtures in bast fibres, in particular, lignin, underwent destructive process under plasmochemical treatment. However, it has been found that the plasma treatment can reduce the strength of fibres. Baltazar-y-Jimenez et al [122] found that the strength of fibres (hemp, flax and sisal) decreases significantly with the increase in the time of plasma treatment. Ragoubia et al [118] used corona discharge to modify hemp fibres and found that the corona discharge modification of hemp cellulosic reinforcements rather than polypropylene allowed the greater improvement of the composites properties with an enhancement of 30 % of Young modulus, 32 % of tensile strength.

2.1.3.2 Chemical modification
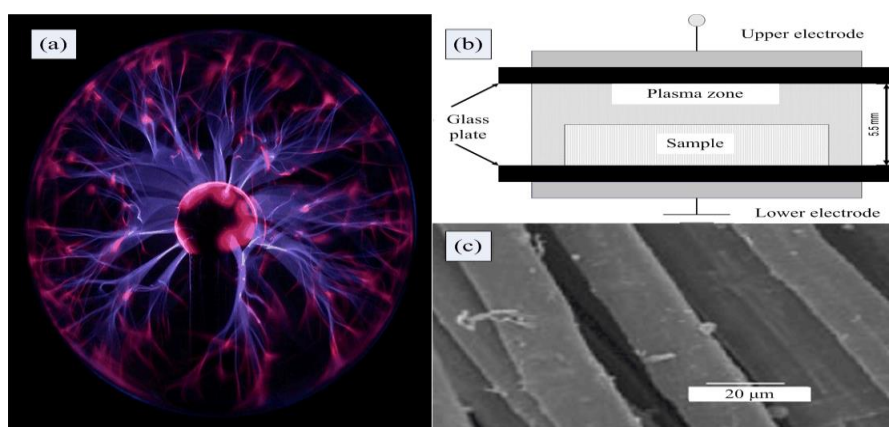
Fig. 2.5 Schematic of plasma treatment: (a), plasma lamp; (b), plasma system and (c), hemp fibre after plasma treatment.

Chemical modification utilizes chemical agents to modify the surface of fibres or the whole fibres throughout. The modification can be classed in five methods: mercerization, oxidation, crosslink, grafting and coupling agent treatment (Fig. 2.6).
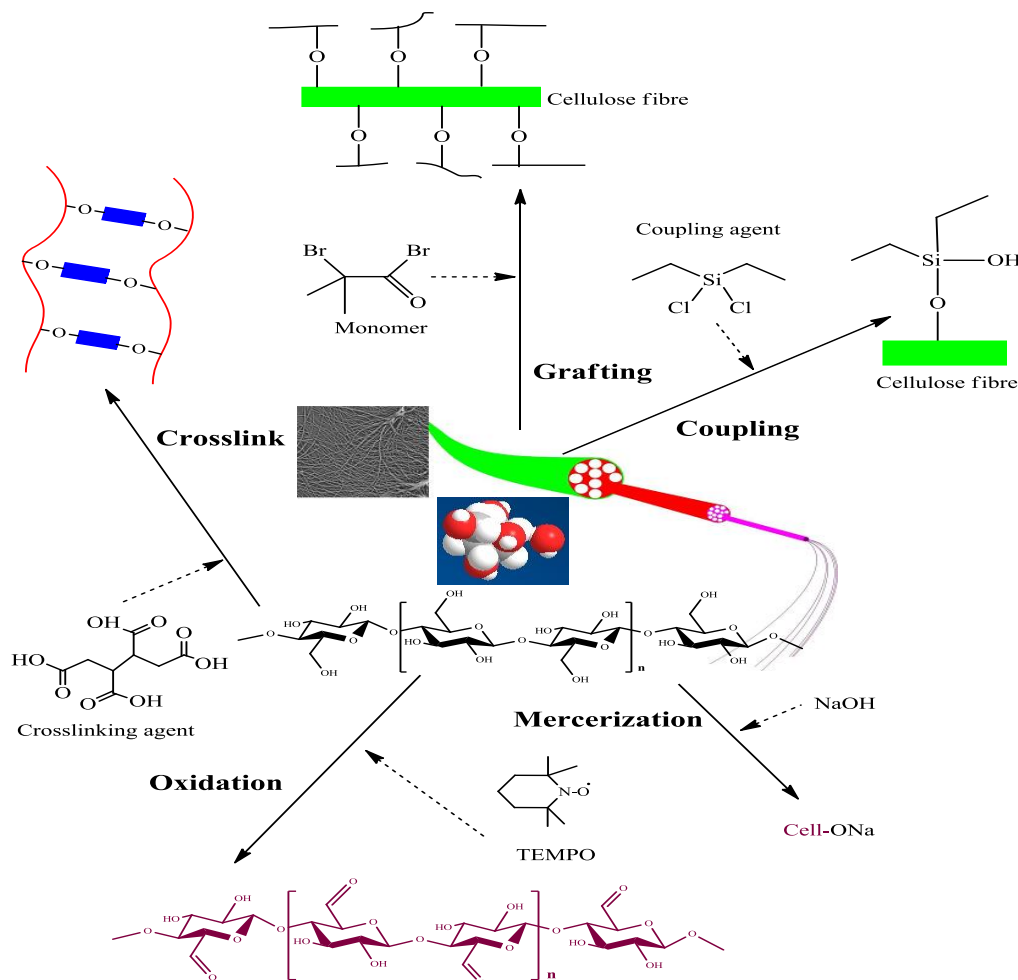
Fig. 2.6 Main chemical treatments and modify mechanism of natural fibres.

2.1.3.2.1 Mercerization

Mercerization is an old method of cellulose fibre modification which is an alkaline treatment method for cellulose fibres. The process was devised in 1844 by John Mercer of Great Harwood, Lancashire, England, who treated cotton fibres with sodium hydroxide [123]. This treatment caused the fibres to swell; about 25 % of hydrogen bonds are broken during the swelling process, in the posttreatment (drying) [124]. These bonds will re-bond and the following effects of the re-bond have been reported in the literature: (i) decreasing the spiral angle of the microfibrils and increasing the molecular direction [2]; (ii) producing fibre fibrillation, i.e., axial splitting of the elementary fibres (or microfibres) that constitute the elementary fibre [125-127]. This process leads to a decrease in fibre diameter, increasing the aspect ratio and the effective surface area available for wetting by a matrix in a composite. There is also an increase in fibre density as a consequence of the collapse of its

cellular structure; (iii) changing the fine structure of the native cellulose I to cellulose II [128-131]. These changes may result in improvement in fibre strength and hence stronger composite materials [56, 126, 132].

It was reported that after immersion in alkali for 48 h, the globular pultrusion present in the untreated fibre disappeared, leading to the formation of a larger number of voids. Systematic investigations [124] have already revealed three important phenomena of cellulose swelling in aqueous alkali, i.e. (i) the passing of the swelling value through a maximum in dependence on lye concentration; (ii) a qualitatively similar but quantitatively different behavior of all the alkali hydroxides in aqueous solution from LiOH to CsOH on interaction with cellulose in an aqueous medium; and (iii) a phase transition within the regions of crystalline order above a lye concentration of 12-15 % due to a so-called intracrystalline swelling caused by inclusion of NaOH and H_2O into the crystallites.

In textile industry, the mercerization process have always been conducted under the condition: temperature 15-18 °C, concentration of sodium hydroxide 31-35 %, treating time 55 s [133]. Mwaikambo et al [134] investigated the effect of mercerization on the mechanical properties of hemp fibres and found that the tensile strength of hemp fibres reached maximum (1050 MPa) when the concentration of sodium hydroxide was 6 %, and the Young modulus of hemp fibres reached maximum (65 GPa) when the concentration of sodium hydroxide was 4 %. Compared with the hemp fibre composite without pretreatment, this modification can increase tensile strength, modulus and strain of composite 47.75 %, 22.54 % and 66.67 %, respectively. Investigation from Gulati et al [135] showed that hemp fibres treated with mercerization can get the biggest surface energy and the lowest free energy of absorption and enthalpy of absorption.

2.1.3.2.2 Oxidation

Oxidation modification can be done under mild condition. In this case carboxyl groups, aldehyde group and kenote group can be introduced in the cellulose chains by the selective oxidation of primary or secondary hydroxyl group in the cellulose chains. In 1938, Yackel et al [136] firstly employed NO_2 as oxidant to oxidate cellulose selectively. After that, various primary [137-144] and secondary [145-149] oxidative systems have been reported. Recently, due to the excellent selective oxidation, TEMPO-NaBr-NaClO and TEMPO-NaClO-NaClO$_2$ oxidative systems [144, 150-160] have received more attention around the world. Potthast et al [161] investigated the new functional groups on the surface of hemp fibres which were introduced by the TEMPO oxidation system. Results showed that the content of hydroxyl groups was influenced by the concentration of oxidant and the treat time. Matsui et al [162, 163] investigated the influence of ozone oxidation pretreatment on the graft copolymerization of mechyl methacrylate on the surface of hemp fibres. They found that, as the increase of oxidation time, hydroperoxide (HPO) increased from 0

mol/cell. molecule to 160 mol/ cell. molecule, and CI of fibres decreased from 69.7 % to 68.3 %, but the degree of grafting increased significantly from 14 % to 129 %.

2.1.3.2.3 Crosslink

Multi-functional compounds which have more than two functional groups always be used as crosslink agent to crosslink the interchains of cellulose by react with the hydroxyl groups. Crosslink modification of cellulosic fibres always been done by etherification [164] and esterification [165]. The crosslinking of cellulose has been found its important commercial application in textile finishing of cellulose-based fabrics with end-use properties, e.g. wrinkle resistance, permanent press and easy care properties. Lee et al [166] utilized diphenylmethane-4, 4-diisocyanate (MDI) to crosslink hemp fibres for making castor oil/polycaprolactone-based polyure-thane/hemp composite, and found that urethane bonding can form between the hydroxyl groups of the fibre surface and the isocyanate groups of MDI.

2.1.3.2.4 Grafting

Chemical modification through graft copolymerization is an effective method of modifying the properties of natural fibres. The technique involves the grafting of various monomers onto the surface of cellulosic fibres [167, 168].The reaction is usually initiated by free radicals of cellulose molecules. The cellulose is exposed to high-energy ionizing radiation. After treatment with selected ions, transition metal ions, oxidative reagents, as initiating agents, initiate free radicals on cellulose [169]. The radical sites initiate grafting of alkyl acrylates (such as methyl, ethyl, butyl, and propyl), vinyl monomer (such as methyl methacrylate and acrylonitrile) to cellulosic surface. Pracella et al [170] modified hemp fibres by means of melt grafting reactions with glycidyl methacrylate (GMA) in order to improve the fibres-matrix interactions. Due to the improvement of fibre-matrix interfacial adhesion which caused by the grafting modification, the tensile strength, modulus and stiffness of modified hemp fibres based composite increased significantly compared with the composites without any treatment.

2.1.3.2.5 Coupling

Coupling agents can be defined as the substances that are used in small quantities to treat a surface so that bonding occurs between it and other surfaces between filter and matrix. Coupling agents can be subdivided into two broad categories: bonding agents and surfactants (also known as surface active agents). At present, over forty coupling agents have been used in the production and research of natural fibre composites [171]. The most popular treatments include the use of silanes and isocyanates. However, the reinforcement effect of this coupling agent seems weaker than that by the mercerization [172].

2.1.3.3 Biological modification

Biological treatments involve the use of naturally occurring microorganisms, namely bacteria and fungi. These treatments occur in aqueous environments and are relatively cheap to perform, but tend to be time consuming and water polluting. One commonly used biological fibre treatment is retting treatment. Retting is the controlled degradation of plant stems to free the bast fibres from their fibre bundles, as well as to separate them from the woody core and epidermis. During the retting process, bacteria (predominantly Clostridia species) and fungi, release enzymes to degrade pectic and hemicellulosic compounds in the middle lamella between the individual fibre cells [92]. Generally, the retting process produces high quality fibre, but is very much dependent on weather conditions [173] and the skill and judgement of the farmer. Compared with the conventional sodium hydroxide treatment, the enzymatic treatment can remove much more noncellulosic materials without destroying the cellulose crystalline structure by enzymatic treatment [174, 175].

2.1.3.4 Nanotechnology (NT) modification

NT is by the National Nanotechnology Initiative of USA defined as the understanding, manipulation, and control of matter at the dimensions around 1 to 100 nm. Currently, most major governments around the world are investing heavily in NT (Fig. 2.7 [176]) and many see it as the fuel for the next Industrial Revolution. With the large amount of fundamental research under the government funding today, NT has applications across nearly all economic sectors and allows the development of new critical enabling science with broad commercial potential, such as nano-structured materials, nanoscale-based manufacturing processes, and nano-electronics. It was demonstrated in recent years that NT can be used to modify natural fibres to introduce new function onto the surface of fibres and enhance the performance of final fibres-based products.
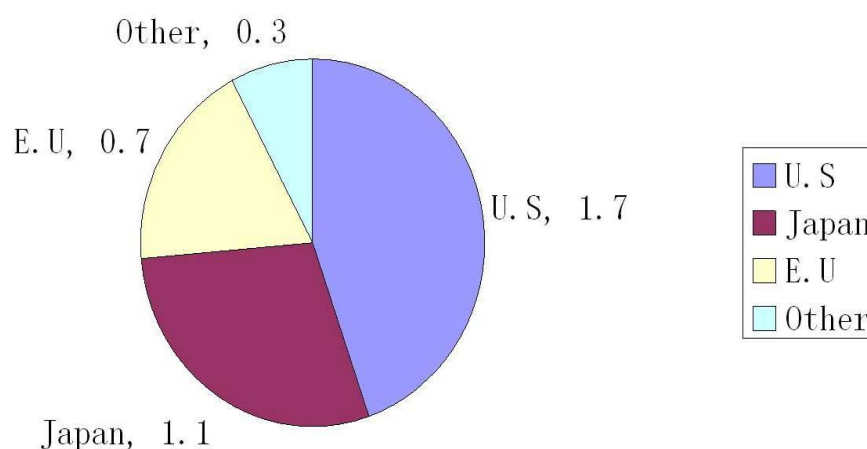
Fig. 2.7 Corporate nanotechnology funding by country in 2004 ($US billions).

This modification has been used in textiles [177, 178], paper industry [179] successfully. It is believed that the application of NT to modify natural fibres offers high economic potential for the development of natural fibre-based industry.

Various approaches were developed to immobilize nanoparticles on the surface of natural fibres, among which, layer-by-layer (LbL) deposition [180-183] and sol-gel process [184-187] are the main approaches which have commonly been employed by the researchers. Different kinds of nanoparticles (e.g. AgNPs [180, 188-191], TiO_2 [191, 192], SiO_2 [193-195], ZnO [196, 197]) were developed to impart multifunctional properties (e.g. anti-bacteria, UV resistant, antiwrinkle finishing, water repellent) to natural fibres.

A novel way of combining biological technology with NT was firstly reported by Juntaro et al [198] in 2007. This green technique firstly employed bacteria *Gluconacetobacter xylinus* strain BPR 2001 to treat natural fibres (hemp and sisal), then fabricated bacterial cellulose on the surface of natural fibres. These modified natural fibres were then incorporated into the renewable polymers cellulose acetate butyrate (CAB) and poly- L-lactic acid (PLLA). They found that the modified sisal PLLA composites, the parallel strength increased by 44 % the off-axis composite strength by 68 %.

2.1.4 Application of hemp fibres

As a result of a growing awareness of the interconnectivity of global environmental factors, the principles of sustainability, industrial ecology, ecoefficiency, and green chemistry and engineering are being integrated into the development of the next generation of materials, products, and processes [199]. In 2003, the UK government established highly ambitious long-term goals relating to climate change, with the objective of moving towards a 'low carbon economy' and a target to cut CO_2 emissions by 60 % by mid 21st Century in the White Paper. The White Paper states that this should be achieved without detriment to UK competitiveness or security. After that, to effectively reduce CO_2 emissions while keep economic growth, different countries have begun to search for new development paths among which low-carbon development has become a widely advocated one [200]. To date, approximately 30 countries in Europe, Asia, and North and South America currently permit farmers to grow hemp [201]. In 2009, the product of hemp fibres around the world reached up to 69735 tonnes [202]. Some estimate that the global market for hemp consists of more than 25,000 products in nine submarkets: agriculture; textiles; recycling; automotive; furniture; food/nutrition/beverages; paper; construction materials; and personal care [203]. The application of hemp fibres can be classed in three different ways (the flowchart for hemp fibre applications is shown in Fig. 2.8): (i) direct utilization (e.g. textile, paper, animal bedding, and fabric); (ii) degradation (e.g. bio-fuel) and (iii) composite. Hemp based composites are the main application and thereby get much more attention by the researchers.
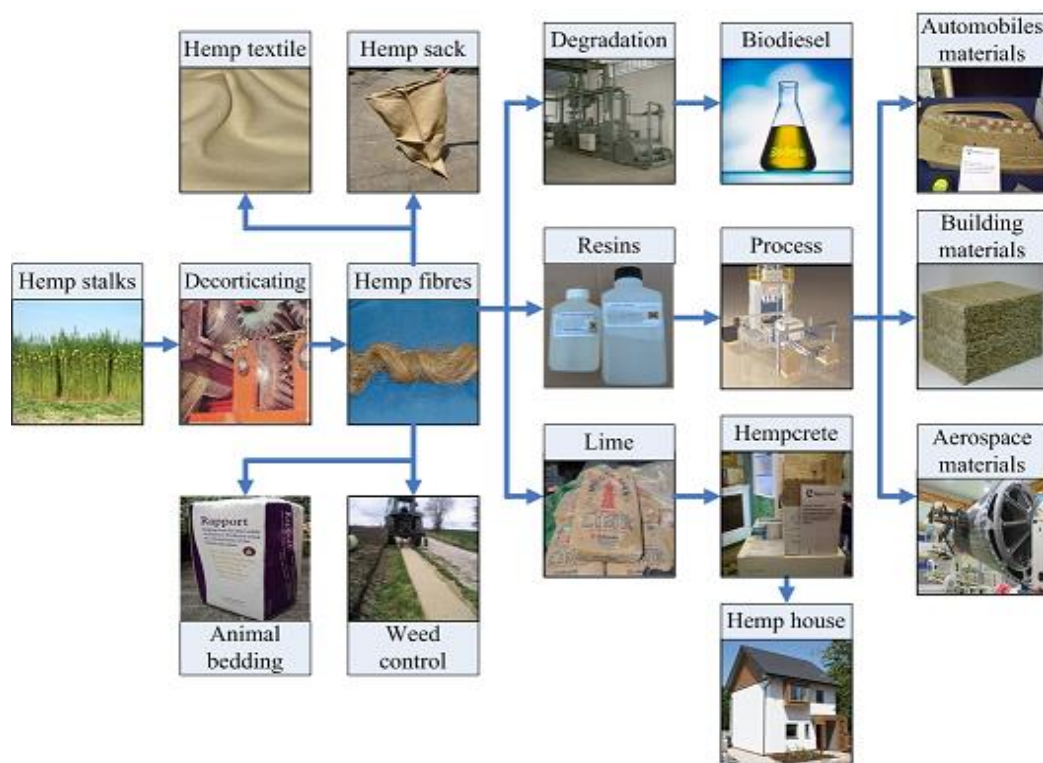
Fig. 2.8 Flowchart for hemp fibre applications.

2.1.4.1 Hemp fibres/inorganic compound composite

The mixture of hemp and lime also been called hempcrete [204]. Hemp chips were first introduced in buildings in France in the early 1990s. At that time, restoration of historic half- timbered buildings required a substitute for wattle and daub, and it was found that the hemp mixed with a lime-based binder provided a natural solution. It was also dimensionally stable and long-lasting.

Over the past few years hemp lime products have been used to construct a number of non-housing projects. This innovative insulation material has already been analyzed in different countries e.g. Belgium [205, 206], France [207], Canada [208], and England [209]. In 2009, BRE and Lime-Technology worked together and developed a new house based on hempcrete (Fig. 2.9 [210]). The house is based around using renewable materials to deliver a low cost, affordable house that meets Level 4 of the Code for Sustainable Homes [211] through materials alone, with a build cost of £75,000. Compared with other inorganic composite, hempcrete shows some advantages: (i) hempcrete provides a form of construction that can be built onsite quickly and efficiently or prefabricated offsite; (ii) hempcrete allows conventional mainstream builders to incorporate the materials into their normal practices with little adjustment; and (iii) hempcrete can capture carbon dioxide and lock it up into buildings.

Busbrid et al [212] found that hempcrete made from hemp fibres and clay has lowest embodied energy (49 MJ m^{-3}) and negative embodied carbon -196 KgCO$_2$ m^{-3} , which far below those for concrete (Fig. 2.10). Elfordy et al [213] currently developed a novel process to make hempcrete. A dry premix of lime and shive is conducted by air through a hose, and pulverised water is added before the hose outlet. They investigated the influence of the projection distance on the homogeneity and density of lime and hemp concrete blocks. This new interesting process accelerated setting kinetics and reduced drying times to less than one month, induced a better compaction of the particles. Peyratout and his research team [214, 215] investigated the influence of chemical treatment on the adhesion between hemp and the lime, and found that the modifications induced by specific chemical treatments (EDTA, NaOH) on fibres play a major role in the strengthening of the lime/fibres interface. As for the porous [216], water vapour absorption [216] and the transient hygrothermal [217] of hempcrete have been reported in the recent years.

Fig. 2.9 Hempcrete house in BRE.
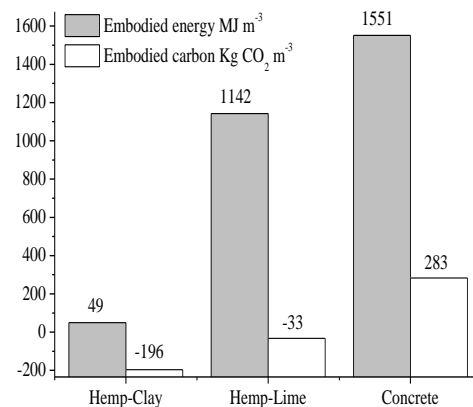
Fig. 2.10 Comparison of the embodied energy and carbon of hemp-clay, hemp-lime and concrete.

2.1.4.2 Hemp fibres/natural polymer composite

Natural polymers used to mix with hemp for making composite include rubber, starch and soy protein. Results shows that composite from the hemp fibres/starch and hemp fibres/ soy protein displays higher mechanical properties, and the order of reinforcement is soy protein > starch > rubber. This may be due to the interfacial issue between hemp fibres and the matrix.

Mohanty et al [218] used twin-screw extrusion and injection moulding process to make biocomposites from soy based bioplastic and chopped industrial hemp fibre and found that the tensile modulus and strength of 30 % fibre reinforcement increased by 1.5 and 9 times respectively compare to those of soy based bioplastic. The reinforced effect has also been observed in the hemp reinforced starch composite, Ochi [219] found that the tensile and flexural strengths of the composites increased with increasing fibre content up to 70 %. The composites possessed extremely high tensile

and flexural strengths of 365 MPa and 223 MPa, respectively. Nättinen et al [220] compared the hemp fibres/starch composite with flax fibres/starch composite and found that when the content of fibres was 10 %, the tensile strength, modulus and impact strength for hemp reinforced composite was 7.9 MPa, 0.68 GPa and 6.8 KJ m^{-2} , respectively. The relevant value for the flax fibres reinforced composite was 7.6 MPa, 0.60 GPa and 12 8 KJ m^{-2}, respectively. Osabohie et al [221] utilized the hemp fibres power as filler for rubber. Compared with carbon black, the hemp fibres/rubber had lower tensile strength (only 2/3 of that of carbon black/rubber), but the hemp fibre/rubber showed superior hardness (1.26 times of that of carbon black/rubber).

2.1.4.3 Hemp fibres/synthetic polymer composite

A high performance composite can be made from the blending of hemp fibres and synthetic polymers by various processes (e.g. bag molding [222], compression molding [134, 223], pultrusion [224], filament winding [225, 226]). Recently some of the composite have been used in our life, such as automobiles materials, building materials and aerospace materials.

Table 2. 1 Summary of mechanical properties of hemp fibres/resin composite

Matrix	Tensile (MPa)		Young's modulus (GPa)		References
	Pure resin	Composite	Pure resin	Composite	
Polypropylene	22.8-35.46	28.1-45.33 (40% hemp fibres)	1.07-1.1	3.5-3.72 (40% hemp fibres)	[227-229]
Polylactic acid	47.5-51	75-85 (30% hemp fibres)	3.5-5	8-11 (30% hemp fibres)	[230, 231]
Polystyrene	34.1±0.68	40.4±0.55 (22.5% hemp fibres)	-	-	[232]
Epoxy	25	60±5 (30% hemp fibres)	0.7	3.6±0.4 (30% hemp fibres)	[233]
Polyester	12.5±2.5	60±5 (35% hemp fibres)	1.1±0.2	1.75±1.5 (35% hemp fibres)	[234]
Unsaturated polyester	25±5	65±2.5 (30% hemp fibres)	1.5±1	8.75±1.25 (30% hemp fibres)	[235]

The data from ISI website from 2000 to now show that 59 articles about hemp fibres/ synthetic polymer composite are published, with 35 articles about reinforced thermoplastic polymers and 24 articles about reinforced thermosetting polymers. Table 2.1 summarizes the mechanical properties of hemp fibres reinforced synthetic polymers. It shows clearly that the addition of hemp fibres resulted in a great improvement in the mechanical properties of composite. Due to chemical reaction between the thermoplastic and the hydroxyl groups on the surface of fibres, hemp

fibres reinforced thermoplastic polymers demonstrate much better effect. Meanwhile, these reports also discussed the influence of hemp length, content of hemp fibres and modification on the mechanical properties of composites.

2.2 Nanocellulose

After Anselme Payen firstly extracted cellulose from plants in 1838, the cellulose science developed rapidly with the effort of thousands of scientists. In 1870, the first kind of cellulose derivatives (celluloid) was successfully produced in industrial scale by Hyatt Manufacturing Company. Since that, cellulose extracted from wood became an important raw material for modern industry. From 1920s with the development of analytical chemistry and instrument, especially the development of XRD analysis technique, scientists have got much more information from cellulose, e.g. morphologies of cellulose with much smaller scale, structure of cellulose. During 1940s-1960s, with the observation of scanning electron microscopy (SEM) and determination of XRD on the hydrolysis cellulose, researchers consequently investigated the crystalline structure of cellulose from various resources [236-249].
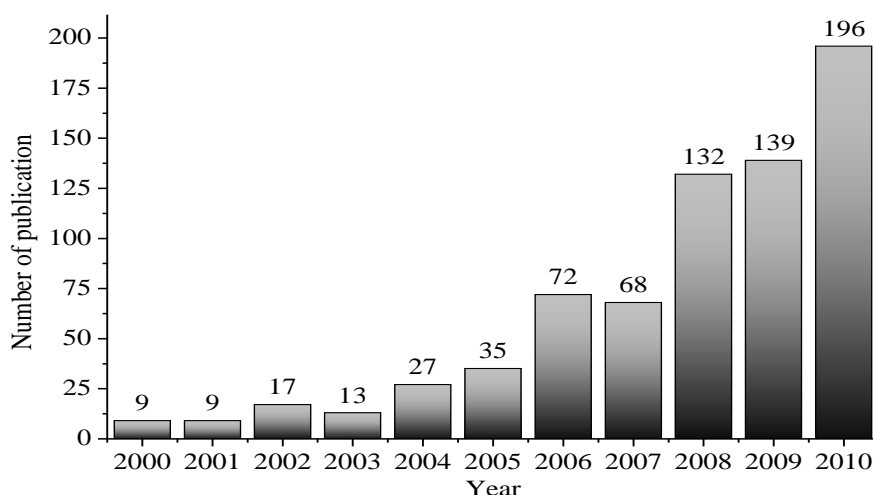
Fig. 2.11 Number of references about nanocellulose by publication year (from 2000 to 2010).

In 1947, Nickerson et al [239] firstly employed hydrochloric and sulfuric acid hydrolysis to produce cellulose crystallites from cellulose materials. Their excellent research on the nanocellulose gave rise to attention by the other researchers [238, 240, 245, 247]. In the early 1980s, nanocellulose which was called microfibrillated cellulose (MFC) at that time was developed by Turbak et al [250-253], which was a new form of expanded high-volume cellulose, moderately degraded and greatly expanded in surface area, obtained through a homogenization process. This new material was intended to be used in such products as foods, cosmetics, and medical products. Up to middle 1990s, there have been no attempts to employ MFC into new application despite its attractive structure. Nanocellulose has attracted more concerns since Favier et al [254, 255] firstly reported the fabrication of nanocellulose-based nanocomposite in 1995. After 2000, due to much more funding from government and

corporation on the exploit of cellulose with nano-scale, the research about nanocellulose develops rapidly, close to 200 articles were published in 2010 (see Fig. 2.11).

2.2.1 Fabrication of nanocellulose

Nanocellulose can be obtained with various treatments from different kinds of natural sources which are summarized as follows (see Fig. 2.12, while the microstructure of microfibrils from various sources is summarized in Table 2.2):

(a)   (b)   (c)
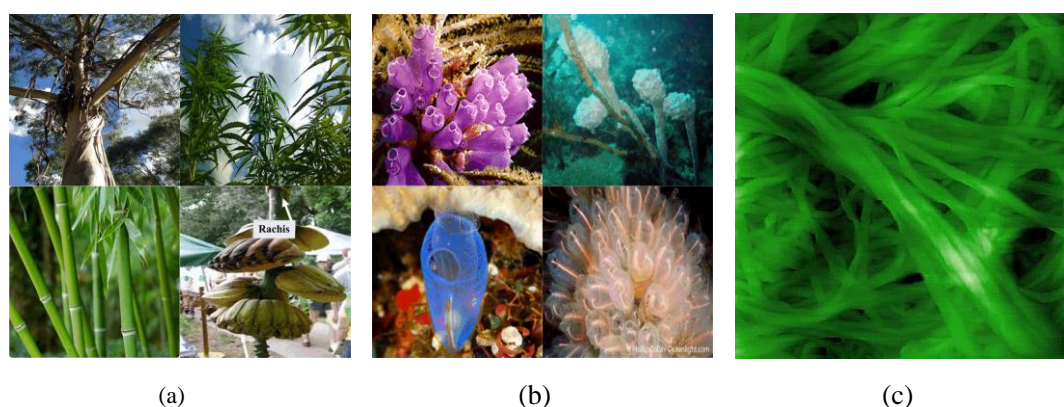
Fig. 2.12 Sources of nanocellulose: (a), plant cellulose; (b), animal cellulose, and (c) bacterial cellulose.

(1) Plant cellulose

Right now, plant cellulose is the most widely used raw material for nanocellulose fabrication. This kind of cellulose mainly comes from wood, bast fibres (e.g. flax, hemp, and so on), herbaceous plant (e.g. bamboo, cotton), and agricultural waste (e.g. wheat straw, rice straw, banana rachis).

(2) Animal cellulose (tunicate)

Tunicates, also known as urochordates, are members of the *subphylum Tunicata*. It has long been known that the tunic of ascidians contain a polysaccharide that is similar to cellulose and is named tunicin.

(3) Bacterial cellulose

Bacterial cellulose (BC) is an extracellular product of Acetobacter xylinum, a gram-negative strain of acetic-acid-producing bacteria [256]. It is chemically identical to plant cellulose, β-1,4-glucans [257], but is secreted as a ribbon-shaped fibril, less than 100 nm wide, itself a bundle of much finer 2–4 nm nanofibrils [258]. These fibrils have excellent intrinsic properties due to their high crystallinity (up to 84–89 %), including a relatively high elasticmodulus of 78 GPa. BC is one of the most promising biological based materials with broad prospective applications. BC has been widely used in foods, in acoustic diaphragms for audio speakers or headphones, for making unusually strong paper, and has medical applications as

wound dressings and artificial skins, artificial blood vessels, and tissue engineering scaffolds.

Table 2. 2 Microstructure properties of cellulose microfibril from various sources [259, 260]

Source	Length (nm)	Width (nm)	Aspect ratio
Wood	100-200	1-5	70
Cotton	100	1-5	20
Wheat straw	150-200	20	7.5-10
Tunicate	1000-2000	10-20	100
Bacterial cellulose	300	10	30

Table 2. 3 Summary of nanocellulose preparation procedures

Raw materials	Method	Procedure	Nanocellulose dimension	References
Soft-wood	Chemo-Mechanical method	TEMPO oxidation firstly, then fibrillated with ultrasonication	2.5-4 nm width	[155]
	Chemical hydrolysis	Acid hydrolysis (3M HCl boiled 3 h), then oxidized by TEMPO for 3 days at pH 4.8 with 60 ^{o}C	3-5 nm width, 200-400 nm length	[261]
		Mercerized, then acid hydrolysis, finally oxidized by TEMPO	4-7 nm width, 50-150 nm length	[261]
Hard-wood	Mechanical	The cellulose fibres at 1 % consistency were first passed through a refiner by various passes, further fibrillation was done using a high-pressure homogenizer.	10-25 nm width	[262]
	Chemo-Mechanical method	The bleached pulp was firstly oxidized with TEMPO, then disintegrated using a domestic food mixer for 5 min.	3-4 nm width	[263]
		After dewax treatment, the samples were further treated with an acidified sodium chlorite solution at 75 ^{o}C for 1 h, and then treated with 5 % potassium hydroxide at 90 ^{o}C for 2 h. Finally, the cellulose suspensions obtained were then sonicated for 30 min using an ultrasonic processor	10-20 nm width	[264]
Flax	Chemo-mechanical method	Flax pulps were pretreated with three different agents, then the pulps were homogenized using two microfludizer	2-50 nm width, 21-350 nm length	[265]

Table 2.3 Continued

27

		Flax fibres were milled firstly by ball milling, and then hydrolyzed by sulphuric acid solution (60-64 %) at various temperatures.	2-18 nm width, 21-340 nm length	[265]
Hemp	Chemo-Mechanical method	Acid Hydrolysis (1M HCl, 80°C, 1.5h), then alkaline Treatment (2 % NaOH, 2h, 80°C), and then cryo-crushing in Liquid Nitrogen, finally using high pressure defibrillation	30-100 nm width	[266]
	Chemical hydrolysis	Chopped hemp fibres were mixed in 400 mL of 3.2 mol/L H_2SO_4 for 5 days at 40°C with mechanical stirring.	60 nm width, 340 nm length	[267]
		Chopped hemp fibres were mixed with a sulfuric acid aqueous solution (250 mL, 64 %) and stirred vigorously at 45 °C for 4 h.	20-40 width	[268]
Sisal	Chemical hydrolysis	Curaua fibres were hydrolyzed with sulphuric acid solution (60 %) at 45 °C for 20 min.	30.9 ± 12.5 nm width	[269]
Bamboo	Chemical hydrolysis	Bamboo pulp was treated with a set of acidified sodium chlorite ($NaClO_2$) treatments at 70 °C for 3 h and an alkaline treatment with 5 % potassium hydroxide (KOH) at 80 °C for 2 h.	15-20 nm width	[270]
Cotton	Chemical hydrolysis	Dewaxed firstly, then treated with 6.5 M sulphuric acid at 45 °C and stirred vigorously for 75 min.	6-18 nm width, 85-225 nm length	[271]
		Hydrolyzed with 30 % sulfuric acid at 60 °C for 6 h.	90 nm width, 1200 nm length	[272]
Banana rachis	Chemo-Mechanical method	Degum, then treated with 80 % acetic acid and 70 % nitric acid at 120 °C for 15 min, finally ultrasonication	5 nm width, 500-1000 nm length	[273]
		Degum, then pre-treated with KOH at various concentrations for 14 h with room temperature, finally homogenized with homogenizer for 10 min	5 nm width, few micrometer length	[274]
Bagasse	Mechanical method	Bagasse pulp was disintegrated by high-shear mixer; finally the refined fibres were homogenized using a two-chamber high-pressure homogenizer.	7-24 nm width	[275]
	Chemo-Mechanical method	Bagasse pulp was firstly treated with 5 % NaOH for 45 min at 50 °C, and then disintegrated by high-shear mixer; finally the refined fibres were homogenized using a two-chamber high-pressure homogenizer.	11-30 nm width	[275]

Table 2.3 Continued

28

	Enzyme-assisted	Bleached bagasse pulp were treated with crude xylanase enzymes in citrate buffer, then disintegrated by high-shear mixer, finally the refined fibres were homogenized using a two-chamber high-pressure homogenizer.	9-25 nm width	[275]
Curaua	Chemical hydrolysis	Curaua fibres were hydrolyzed with sulphuric acid solution (60 %), hydrochloric acid solution (37.5 %), mixture of sulphuric and hydrochloric acid solutions (2:1 v/v) respectively at 45 ^{o}C for 75 min.	6–10 nm width, 80–170 nm length	[276]
Wheat straw	Chemo-Mechanical method	The pre-treated pulp was hydrolyzed by 1 M of hydrochloric acid (HCl) at 80 ± 5 ^{o}C for 2 h and then washed with distilled water repeatedly, then The pulp was treated once more with the 2 % NaOH solution at 80 ± 5 ^{o}C for 2 h, finally treated with mechanical treatment this procedure includes cryocrushing, disintegration and defibrillation steps.	10–80 nm width, several micrometers length	[277, 278]
	Chemical hydrolysis	The wheat straw pulp was hydrolyzed with sulphuric acid (65 %).	5 nm width, 150-300 nm length	[279]
Tunicate	Chemical hydrolysis	Curaua fibres were hydrolyzed with sulphuric acid solution (55 %) at 60 ^{o}C for 20 min.	10-20 nm width, 100 nm to several micrometers length	[255]

Toward exploiting the attractive properties of nanocellulose, various processes were developed. These methods lead to different types of nanofibrillar materials, depending on the cellulose raw material and its pretreatment, and the disintegration process itself. The preparation procedures of nanocellulose which are reported in recent years are summarized in Table 2.3. As Table 2.3 shows, the process of nanocellulose fabrication can be classified into two methods, namely, mechanical fabrication and chemical fabrication. It has been proved that the sources [264] and the conditions of fabrication [265] process affect the final dimension of microfibrils significantly. Meanwhile, these preparation methods of nanocellulose allow the control over the final properties, which may open novel applications in materials science, for example, as reinforcement in composites and as templates for surface modification.

2.2.1.1 Mechanical fabrication

The fabrication of nanocellulose can be obtained through mechanical treatments. These methods include: high pressure homogenization [258], ultrasonication [155, 280-282], cryocrushing [277, 283], grinding [284-286] and so on, among which these methods, the homogenization seems to be the popular one (see Fig. 2.13 [287]). The

refining process is carried out prior to homogenization due to the fact that refining produces external fibrillation of fibres by gradually peeling off the external cell wall layers (P and $S1$ layers) and exposing the $S2$ layer. It also causes internal fibrillation that loosens the fibre wall, preparing the fibres for subsequent homogenization treatment.

The passes through the homogenizer is considered as influencing parameters for the resulting fibril dimensions and the physical properties of fibril. For the influence of passes through, it has been found that (i) additional passes contribute to the increase of surface area on the cellulose fibrils with a decrease in diameter of fibrils; (ii) the value of aspect ratio of fibre bundles firstly increase with the increase of the pass number through at less number, but after a certain number this value decreased [288]; (iii) higher passes gives rise to the a reduction of diameter distribution [265].
Mechanical treatment may result in longer and entangled nanoscale cellulose elements
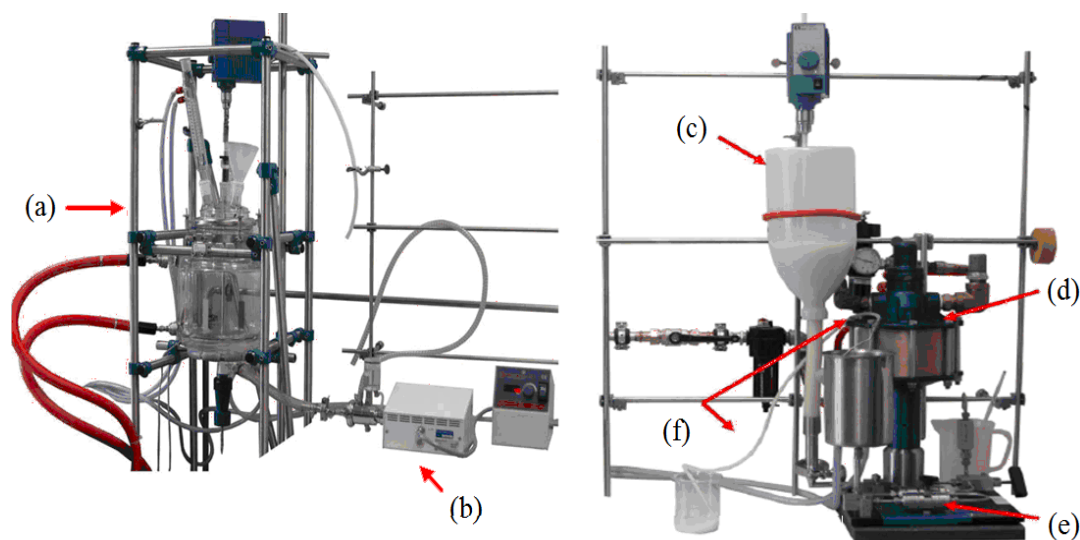
Fig. 2.13 Lab-scale equipment for the mechanical pre-treatment of cellulosic raw materials: (a) ten liter reactor for suspending cellulose raw material in water; (b) inline dispersing system for the extraction of cellulose fibril bundles; (c) container for the CFB suspension equipped with Stirrer; (d) air pump for the generation of high processing pressure (up to 1500 bar); (e) patented interaction chambers (Y- and Z-type); (f) cooling loop and product outlet.

leading to stronger networks and gels, but this treatment tends to damage the microfibril structure by reducing molar mass and degree of crystallinity. In addition, a higher number of passes through a mechanical homogenizer increases the energy consumption for disintegration. Therefore, researchers use various pretreatments in order to overcome the above disadvantages. It has been found that, combined with other pretreatments; it leads to a controlled fibrillation down to nanoscale and a network of long and highly entangled cellulose elements. Among these combination, enzyme-assisted [275, 289-291] and chemo-mechanical technique [261, 264, 278, 292] are the main ways for pretreatment among these methods.

Enzymatic pretreatment can increase the reactivity and swelling of cellulosic fibres, due to the degradation of enzyme on cellulose chain. The enzymatic processes are carried out generally by three types of enzymes (Fig. 2.14 [290]): (i) endocellulase breaks internal bonds to disrupt the crystalline structure of cellulose and expose individual cellulose polysaccharide chains; (2) exocellulase cleaves 2-4 units such as cellobiose from the ends of the exposed chains produced by endocellulase; and (3) cellobiase or β-glucosidase hydrolyzes the exocellulase product into individual monosaccharides. This degradation contributes to the cellulosic fibre disintegration during homogenization and reduces energy consumption. Enzymatic pretreatment was found to give higher average molar mass and larger aspect ratio than nanocellulose resulting from acidic pretreatment [289].
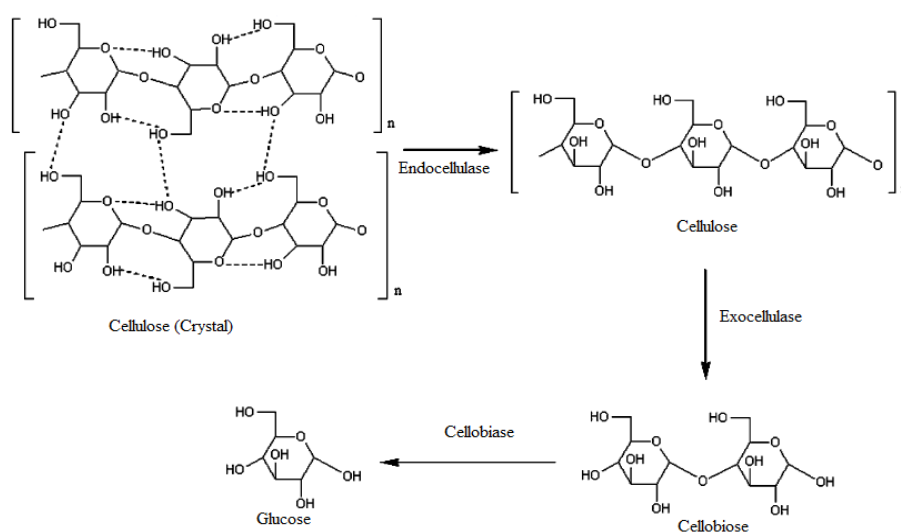
Fig. 2.14 Enzymatic processes by three types of cellulases.
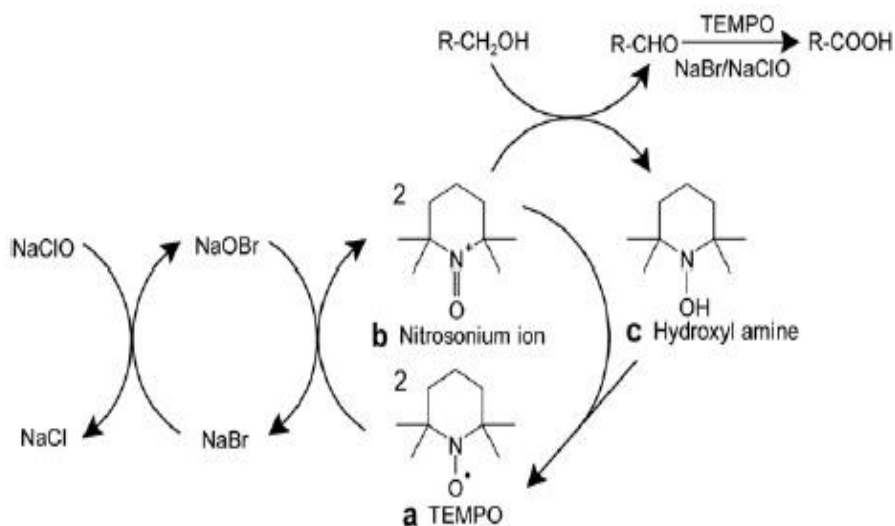
Fig. 2.15 Reaction scheme of TEMPO-mediated oxidation of primary hydroxyls.

Chemical pretreatments typically promote fine production and fibre swelling, making defibrillation easier. The combined chemical pretreatment with sonication is a common way for chemo-mechanical technique. In 2004, Saito [293] firstly

reported the fabrication of nanocellulose with TEMPO-mediated oxidation. TEMPO mediated oxidation of fibres produces easily fibrillated products, regulating exposure time to a homogenizer can be used to control the nanofibril fraction within a fixed volume of oxidized fibres. In addition, researcher found that films of TEMPO-oxidized nanocellulose had high optical transparency, flexibility, high dimensional thermal stability and high oxygen barrier properties [294]. The mechanism of TEMPO pretreatment was showed in Fig. 2.15 [263]. This pretreatment introduces carboxylic acid groups in the C6 position of the glucose unit, which also may be utilized for surface modification. Small amounts of aldehyde groups are also introduced by the TEMPO pretreatment.
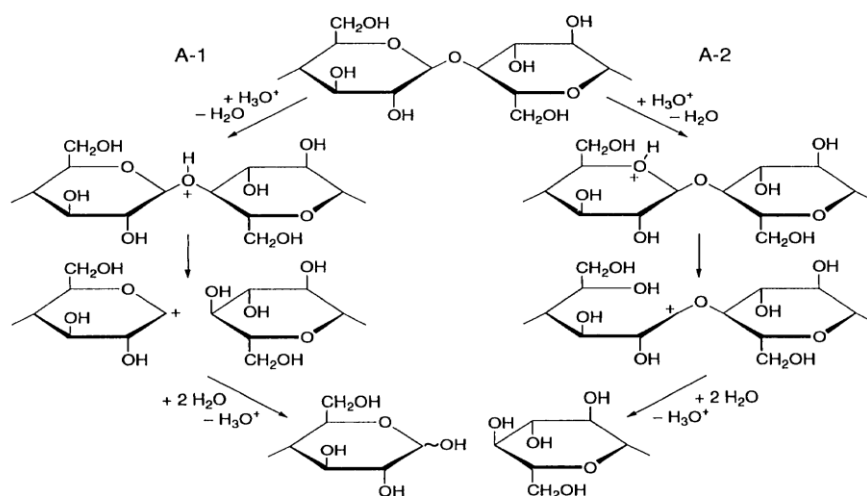
Fig. 2.16 Mechanism for acid hydrolysis of cellulose.

2.2.1.2 Chemical fabrication

Nickerson et al [239] firstly employed hydrochloric and sulfuric acid hydrolysis to produce cellulose crystallites from cellulose materials. However, this extraction method has not been successfully used to prepare a stable suspension of colloidal-sized cellulose nanocrystals until 1950s by the contribution of Rånby [242, 243]. Sulfuric acids are commonly used to produce nanocellulose since 1950s. Sulfuric acid treatment of cellulose results in scission of glycosidic bonds, and thus, causes a reduction in DP. The glycosidic bond scission occurs in three steps (see Fig. 2.17 [295]): (1) protonation of glycosidic oxygen, (2) fission of the glycosidic bond with transfer of the positive change to C-1, and (3) attack on the carbonium ion by water and re-formation of the hydronium ion. It has been found that the hydrolysis conditions, including reaction time, acid-to-pulp ratio and acid type, have a great influence on the dimensions and surface charge of the cellulose nanofibres [265]. Sulphuric acid provides a highly stable suspension with high negative charge (e.g. -69.7 mV for nano-scale cotton fibril [296]) due to the introduction of sulphate ester groups on the surface of crystallites [297]. Hydrochloric acid also has been used for obtaining nanocellulose [298], hydrochloric hydrolysis increases the thermal stability

of cellulose nanostructures, but chloride ions are easily removed by repeated washings with water and minimal surface charge on the cellulose nanofibres. One of the major challenges when using acid hydrolysis to fabricate nanocellulose is to increase the final yield after processing, typically around 30% (of initial weight), which potentially limits scale-up by this method [299].

2.2.2 Characterization and properties of nanocellulose

With the development of analytical techniques and the nanotechnology, researchers have revealed more details about nanocellulose. The main analytical techniques for the characterization include: microscopy, spectroscopy and scattering techniques. These characterizations are serviced for three purposes: (i) determination of the nanocellulose geometrical dimensions; (ii) properties investigation of nanocellulose (e.g. mechanical properties, optical properties, liquid crystallinity); and (iii) evaluation of nanocellulose modification.

2.2.2.1 Morphology and size of nanocellulose

As described in Table 2.2 the geometrical dimensions of nanocellulose from different sources vary. The precise shape size of nanocellulose can be evidenced by microscopy (e.g. atomic force microscopy (AFM) (Fig. 2.17(a) [300]), SEM (Fig. 2.17(b) [301]), TEM(Fig. 2.17(c) [273])), spectroscopy (e.g. FTIR [302], nuclear magnetic resonance (NMR) [303], XRD [304],) and scattering techniques (e.g. DLS [305], small-angle neutron scattering (SANS) [306, 307], small-angle X-ray scattering (SAXS) [259, 308], wide-angle X-ray scattering (WAXS) [309]).

SEM, AFM and TEM are the common analytical instruments for the morphological analysis (Fig. 2.18), although a slight difference among them. AFM as well as SEM can be used for structure and morphologies determination of cellulose whiskers and their nanocomposites. Field emission scanning electron microscopy (FEG-SEM) allows a quick examination, giving an overview of the sample. However, the resolution was considered insufficient for detailed information. Conventional

<div align="center">(a)   (b)   (c)</div>
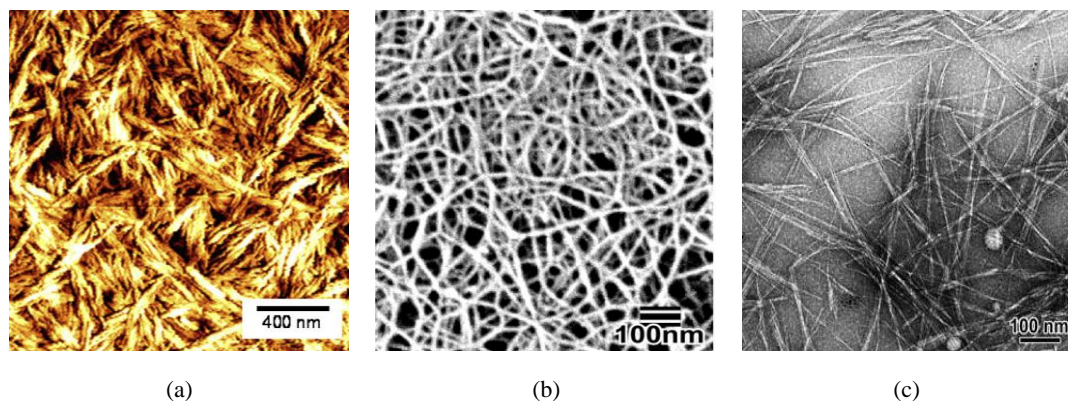
Fig. 2.17 AFM (a), SEM (b) and TEM (c) image of nanocellulose.

bright-field transmission electron microscopy (TEM) is possible to identify individual nanocellulose, which enables determination of their sizes and shape. AFM can be used to overestimate the width of the nanocellulose due to the tip-broadening effect. It has be found that cross-section of the microfibrils observed by TEM is square, whereas the AFM topography of these microfibril surfaces shows a rounded profile due to convolution with the shape of the AFM tip [310].

| (a) | (b) |
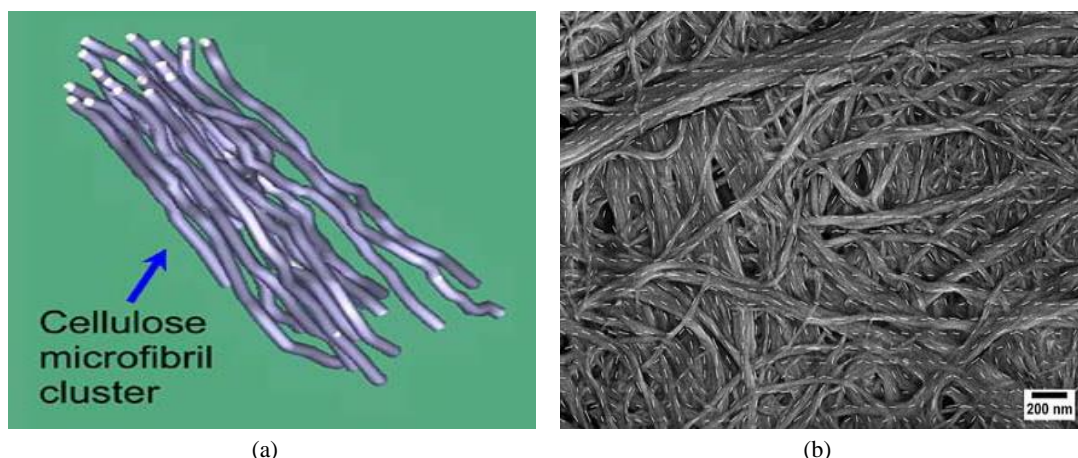
Fig. 2.18 Computer assisted of cellulose microfibrils cluster (a) and nanocellulose film (b).

Recently, combined analytical instrument and computer-assisted techniques have been developed. Xu et al [311] firstly investigated 3D organization of cellulose microfibrils in plastic resin-embedded, delignified cell walls of radiata pine early wood. By using IMOD software, they determined the diameter of microfibril (around 3.2 nm). Meanwhile, they estimated the length of individual cellulose microfibrils. They tracked 90 slices out of the 144 reconstructed slice images in the 150 nm thick specimen (Fig. 2.18(a)). Within the 90 tracked slices, the length of the cellulose microfibrils is about 95 nm. With the Image program, Chinga-Carrasco et al [312] assessed the multiscale structure of NFC-films (Fig. 2.18(b)) in detail and found that (i) the films made on the dynamic sheet former are exposed to shear forces during the fibril deposition on the forming wire; (2) the quantified local fibril orientations of the surface layers did not seem to reflect such differences; (3) the orientation anisotropy values were between 0.1 and 0.2 for all the samples; and (4) the surface structures have thus random orientations.

2.2.2.2 Mechanical properties of nanocellulose

By employing AFM [70, 71, 313-316] and spectroscopic techniques [317-320] researchers have revealed the mechanical properties of nanocellulose. The elastic modulus of nanocellulose has been measured in the axial direction (E_A) and in the transverse direction (E_T). The instruments for mechanical measurement and the results are summarized in Table 2.4.

As shown in Table 2.4, axial elastic properties are typically measured by using AFM atomic three-point bending of individual nanocellulose, XRD and in situ combination

of tensile tests experiments with Raman spectroscopy of thin mats of nanocellulose impregnated with epoxy. The axial elastic modulus is around 57–180 GPa, which is in agreement to model calculations of E_A = 124–155 GPa [321]. The transverse elastic properties have been measured using a combination of high-resolution AFM indentation and modelling, in which individual nanocellulose from wood E_T = 18–50 GPa, and tunicate E_T = 9 ± 3 GPa, respectively. These results are similar to the theoretical model calculations of E_T = 10–57 GPa [322, 323]. Note that there is a high probability of errors with such measurements that are associated with testing at AFM sensitivity limits, and model assumptions used to extract the mechanical properties.

Table 2. 4 Mechanical properties of nanocellulose

Techniques	Source	E_A (GPa)	E_T (GPa)	References
AFM	BC	78 ± 17	-	[70]
	Lyocell	92-104	-	[71, 313]
	Tunicate	TEMPO-oxidation 145.2 ± 31.3	-	[314]
		Acid hydrolysis 150.7 ± 28.8	-	
	Wood	-	18-50	[315]
	Tunicate	-	9 ± 3	[316]
XRD	Ramie	137	-	[317]
Raman Spectroscopy	Tunicate	143	-	[318]
	Cotton	57-105	-	[319]
	BC	114	-	[320]

E_A: elastic modulus in axial direction, E_T: elastic modulus in transverse direction.

2.2.2.3 Optical properties and liquid crystallinity of nanocellulose

In plant cell walls, cellulose microfibrils are arranged in a helicoidal pattern which has been considered as an analog to a cholesteric order [324]. Stiff rod-like particles are known to show liquid crystallinity [325]. Due to high stiffness and aspect ratio, nanocellulose has a strong tendency to align along a vector director under certain conditions, yet the crystals are readily dispersible, lyotropic (in solution) behavior is observed. This behaviour influences the other properties of nanocellulose significantly, such as polyelectrolytic nature and rheological behaviour.

When the nanocelluloses are isolated from plant cell walls and put into a dilute regime, the initial ordered domains are similar to the tactoids. As nanocellulose concentration is increased, the system becomes semi-diluted where rotation becomes inhibited. At still higher concentration, an isotropic concentrated phase should be reached where rod motion is confined to small volumes. When a critical rod concentration is reached, the system becomes biphasic and some of the rods form an anisotropic phase in equilibrium with the isotopic phase. With increasing concentration in the biphasic region, the proportion of the anisotropic phase increases while the proportion of the

isotropic phase decreases until the system becomes completely nematic liquid crystalline at a second critical concentration (Fig. 2.19 [326]), and the chiral nematic orders can be retained after evaporation of the solvent. Marchessault et al [248] firstly observed the birefringment character of nanocellulose suspension. The birefringment feature of nanocellulose suspension can be observed directly (Fig. 2.20 [327]). After drying, the nematic liquid crystal phase can be observed clearly with polarized microscopy (Fig. 2.21 [328]) due to that nanocelluloses have high optical rotatory power reflecting a circularly polarized light in a limited wavelength band.
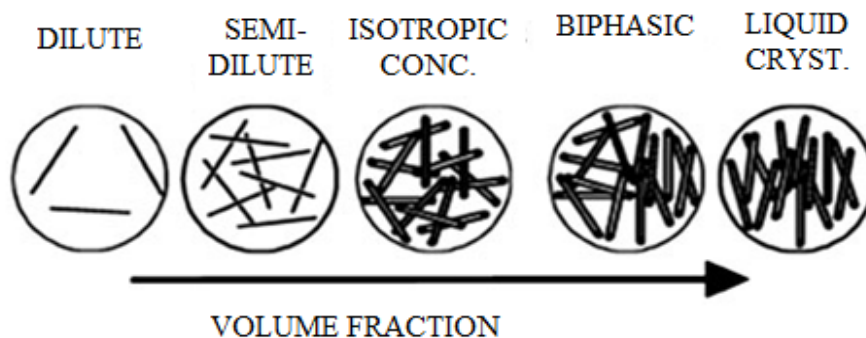
Fig. 2.19 Phase behavior of fluid dispersed rod.

Fig. 2.20 Photograph of an aqueous suspension of nanocellulose (0.50 %) observed between cross nicols showing the formation of birefringent domains.
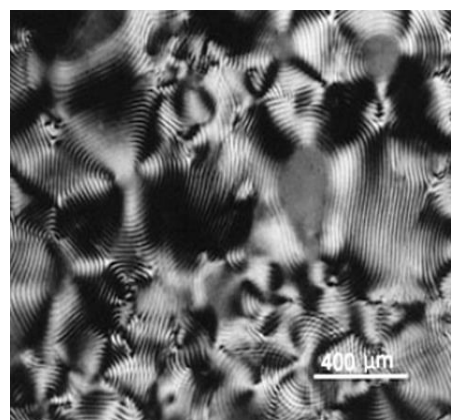
Fig. 2.21 Cholesteric fingerprint texture liquid crystalline cellulose dispersion.

Various factors such as size [329, 330], electrolyte [328, 331-333], dispersity, charge, and external stimuli can affect the liquid crystallinity behavior. Liquid crystallinity behaviour also can be influenced by the different process for preparing nanocellulose (Fig. 2.22 [334]). Due to the less single nanocellulose separated, the birefringence was somewhat weaker for sonicated suspension compared to the homogenized and hydrolysed suspensions [334]. The different acid hydrolysis also can result in different liquid crystallinity behavior, e.g. sulphuric acid and phosphoric acid derived crystals give chiral nematic structure whereas hydrochloric acid derived crystals with posttreatment sulfonation giving a birefringent glassy phase [335, 336] that shows a crosshatch pattern.
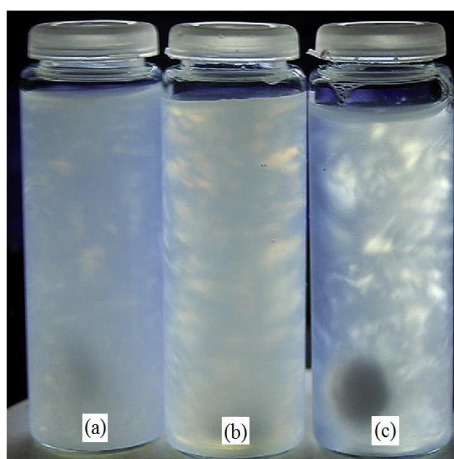
Fig. 2.22 Birefringence of isolated nanocellulose (a) sonified (b) homogenized and (c) hydrolysed treatment.

(a)   (b)   (c)
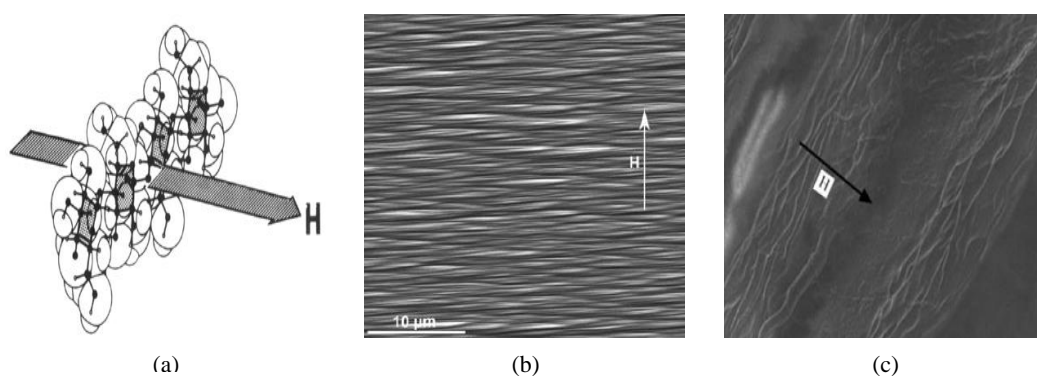
Fig. 2.23 Schematic diagram showing the orientation of cellulose fragment with respect to the field H (a);

FEG-SEM pictures of an etched surface of the nanocellulose/PVA nanocomposite (b) and (c) all-cellulose

nano-composite fabricated in high magnetic field (H represents the direction of the field).

Because cellulose crystallities have a helical twist down the long axis, similar to a screw [336], when nanocellulose submitted to a magnetic field, the long axes of nanocellulose becomes perpendicular to the magnetic field direction [337] (Fig. 2.24(a)) and the distance between nematic planes along the cholesteric axis is shorter than that between the rods in a nematic plane [329]. Employed this feature, aligned nanofibres [338] and nanocellulose base composites (e.g. nanocellulose/PVA nanocomposite [193] (Fig. 2.24(b)), nanocellulose/wood pulp composite [260, 339] (Fig. 2.24(c)) have been developed. The results showed that the mechanical properties along the direction perpendicular to the magnetic field were much stronger than that parallel to the magnetic field.

2.2.2.4 Polyelectrolytic nature of nanocellulose

The scattering technique was used to investigate cellulose microfibrils in 1961 and was pioneered by Marchessault et al [249]. Scattering techniques was also used to investigate the polyelectrolytic behaviour of nanocellulose. These techniques include

ultra-small-angle X-ray scattering (USAXS) [340], small-angle X-ray scattering (SAXS) [308], static light scattering (SLS) [341, 342] and dynamic light scattering (DLS) [341-343].

For the charged rods, the electrostatic interactions play a main role in the phase stability. It has been proved that the effect of the electrostatic interactions on the liquid crystal phase transition in solutions of rodlike polyelectrolytes can be characterized by two parameters, namely, the effective diameter and the twisting action. Additionally, the excess of added monovalent electrolyte induced a decrease in the strength of the chiral interactions between the rods [328].

Furuta et al [340] firstly investigated the ordering structure of nanocellulose with USAXS. The results showed the presence of a single broad scattering peak. The peak is shifted towards lower q values with the addition of simple electrolytes, and disappeared at higher salt concentrations because of the disruption of the ordered arrangement. By using SLS and DLS, de Souza Lima et al [342] revealed that the tunicate nanocellulose suspension is the strong electrostatic interaction and the long-range odder in this system.

2.2.2.5 Rheological properties of nanocellulose suspension
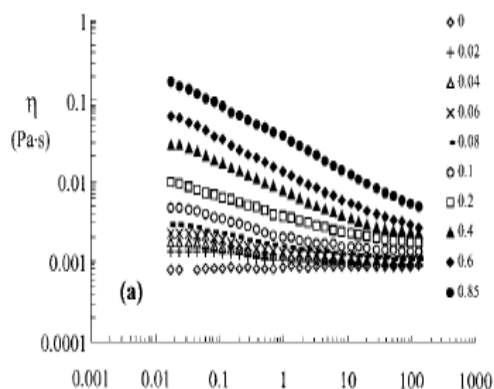
Fig. 2.24 Viscosity vs shear rate for nanocellulose suspensions from tunicate at low concentration.
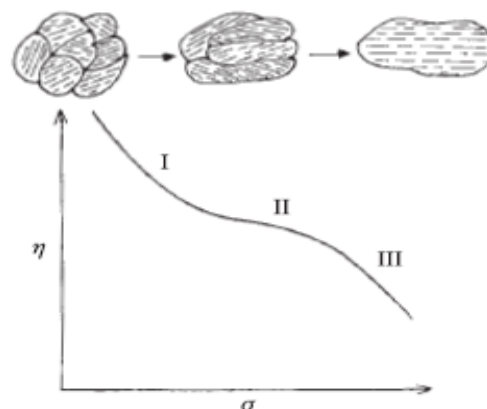
Fig. 2.25 Schematic showing the viscosity vs shear rate for lyotropic LCs.

Marchessault et al [249] firstly investigated the rheological properties of nanocellulose suspension and found that the hydrodynamic properties of nanocellulose are related to the size and length distribution of the particles in suspensions. Liquid crystals (LCs) may be divided into two subgroups: (1) lyotropic LCs, formed by mixing rigid rodlike molecules with a solvent, and (2) thermotropic LCs, formed by heating. Typically, the molecular weight, concentration, and shear rate are main factors that can affect the rheological behaviour of lyotropic LCs suspension. Due to the effect of liquid crystallinity and polyelectrolytic nature, the rheological behaviour of nanocellulose suspension is complicated. At low concentration, nanocellulose suspensions in the dilute regime were shear thinning and

this behavior increased as concentration was raised and showed concentration dependence at low rates and very little concentration dependence at high rates (see Fig. 2.24 [344]). However, at higher concentrations where the suspensions were lyotropic, the shear rate vs viscosity plot obeys lyotropic LCs (see Fig. 2.25 [345]). The effect of processing on the rheological behaviour has been demonstrated by the previous work [298], which found that the H_2SO_4-treated suspension showed no time dependence in viscosity, while the HCl-treated suspension was thixotropic at concentrations >0.5 % (w/v) and anti-thixotropic <0.3 %. Additionally, the effect of additives [346, 347], modification of nanocellulose [348-351] and post-treatment [352] on the rheological properties have been studied in recent years.

2.2.3 Application of nanocellulose

From middle 1990s, with the development of nanocellulose based composite [254, 255], the application of nanocellulose was opened into a new stage. In the last 26 years there has been extensive research in the application of nanocellulose. There have been more than 30 review articles and books describing preparation [353], morphology and structure [354, 355], properties [353, 355], modification [69], application of nanocellulose [353, 356, 357] and the patent about nanocellulose [358, 359]. Especially, nanocellulose nanocomposites [358, 360-365] have attracted lots of attention, these outstanding review demonstrated the development of nanocellulose nanocomposite in recent year. Although most of the investigations about the application of nanocellulose still in laboratory stage, we can believe in optimism, with the development of new technology, especially nanotechnology, nanocellulose will be used industrially and open into much more new fields. Due to the high purity, nanocelluloses from bacterial celluloses have been exploited into commercial products. Bacterial celluloses can be applied in areas where plant cellulose can hardly be used. Most of them are realities in the health-care sector, e.g. skin transplants for sides, donor and receptor. For nanocellulose from plant and tunicate cellulose, their application (in laboratory-scale) can be done by two methods: (i) without any modification; (ii) with some modifications.

2.2.3.1 Application of nanocellulose without modification

Nanocellulose without modification can be utilized as the follows:

(1) Nanopaper

The application of nanocellulose in paper industry can be used as raw material for prepare nanopaper [366-371] or paper additives [372-374]. Using nanocellulose from wood cellulose, researchers have prepared high performance paper, which almost matches steel for strength. The foldable, low thermal expansion, and optically transparent nanocellulose paper (see Fig. 2.26 [375]) is the perfect candidate for substrates for continuous roll-to-roll processing in the future production of electronic

devices, such as flexible displays, solar cells, e-papers, and a myriad of new flexible circuit technologies, and could replace the costly conventional batch processes based on glass substrates currently used. Nakagaito et al [258] firstly fabricated high content nanocellulose nanocomposite by mixing nanocellulose with phenol- formaldehyde (PF) resin. Henriksson et al [366] firstly described the fabrication of nanopaper by using solvent exchange techniques. This nanopaper sample shows very high toughness (W_A=15 MJ m^{-3}), high strain-to-failure (10 %), high porosity (28 %) and Young's modulus (13.2 GPa) and tensile strength (214 MPa) are remarkably high. Olsson et al [367] demonstrated an interesting stiff magnetic nanopaper by compacting bacterial cellulose nanofibril aerogels. Recently, Berglund and his co-researchers [368, 370] (see Fig. 2.27) developed a novel nanopaper with addition of clay. This clay nanopaper has high strength (232 MPa) and modulus (13.4 GPa) and is characterized by substantial optical transparency (T$_{600}$ of 42 %), 200 mm diameter, flatness, and surface smoothness (surface roughness of 21.9 nm). Meanwhile, clay nanopaper extends the property range of cellulose nanopaper, e.g. self-extinguishing characteristics, gas barrier properties.

Fig. 2.26 Optically transparent nanofibre paper (left) and conventional paper (right).

Fig. 2.27 Bacterial cellulose aerogel.

(2) Aerogel

Aerogels are highly porous and very lightweight materials that feature a multitude of interesting properties, such as large specific surface area, extremely low thermal conductivity and sound propagation or excellent shock adsorption [376]. Aerogels can be prepared by replacing the liquid solvent in a gel by air without substantially altering the network structure or the volume of the gel body. The first aerogels were reported by Kistler in 1931 [377]. Aerogels based on nanofibrillated cellulose (NFC) may offer advantages due to its renewable. In 2001, Tan and co-workers [378] firstly prepared cellulose aerogel. In 2004, Jin et al [379] firstly fabricated nanofibrillar cellulose aerogels with dissolution/regeneration of cellulose in aq. calcium thiocyanate. Various drying methods (regular freeze drying, rapid freeze drying, and solvent exchange drying) were investigated. It was found that solvent exchange drying gave highly porous aerogel composed of approx. 50 nm wide cellulose microfibrils and highest specific surface area (160–190 m^2 g^{-1}). Later, a new

method-supercritical drying developed by Hoepfner et al [380] for making nanocellulose aerogel was demonstrated. Compared with freeze drying, SCD is the most effective method for the synthesis of homogeneous aerogels. This method can get much higher specific surface areas (250 m^2 g^{-1}) and bending strength (2 MPa). Recently, some novel nanocellulose based aerogel have be described, e.g. nanocellulose/clay aerogel [381], nanocellulose/ titanium dioxide aerogel [382]; and bacterial cellulose have been used as raw material to make nanocellulose aerogel [367, 376, 383, 384] (see Fig. 2.27). Sehaqui et al [385] introduced Tert-butanol freeze-drying to make aerogel, due to the nature of tertbutanol, a lower extent of surface tension effects (capillary action) are displayed during the drying process. This resulted in aerogels with higher specific surface area (max. of 284 m^2 g^{-1} for nanocellulose) compared to those prepared by conventional freeze-drying.

(3) Template
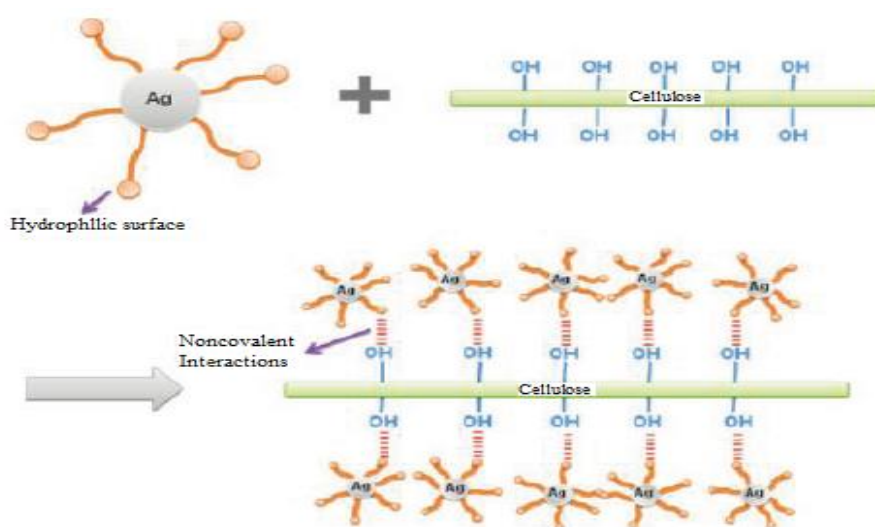
Fig. 2.28 Synthesis mechanism for the formation of Ag nanoparticles on the surfaces of nanocelluloses.

Due to the nano scale, nanocellulose was exploited as template to make nano-metal (e.g. nickel nanoparticle [386], porous titania [387], silver nanoparticle [388, 389], gold nanoparticle [390]), nano-nonmetal [391], nano-metal oxide [392, 393]. Nanocellulose releases electrons during the carbonization process [394] and displays reducibility. Utilizing this mechanism, Yongsoon et al [386] fabricated nickel nanoparticle by thermal reduction process and prepared well-dispersed Ni nanocrystals on the carbonized nanocellulose with about 5–12 nm in size. They also successfully synthesized selenium nanoparticles [391] by thermal reduction process with nanocellulose. In 2010, Padalkar et al [395] firstly synthesized metallic nanoparticle chains by using a modified reductive deposition procedure involving the cationic surfactant cetyltrimethylammonium bromide (CTAB, which acts as a nanoparticle stabilizer) and tunicate nanocellulose suspension. As Fig. 2.28 [395] shows, Ag nanoparticles are formed via the conventional reduction of $AgNO_3$, which is quite different from the thermal reduction. This method resulted in the successful

decoration of nanocellulose surfaces with Ag, Cu, Au, and Pt nanoparticles. Later in 2011, this research group successfully employed the same way to synthesized semiconductor [393].

(4) Nanocomposites (matrices are hydrophilic polymers which include natural polymers and water soluble polymers)

Table 2. 5 Mechanical properties of nanocellulose (without modification) reinforced nanocomposites

Type of matrix	Matrix	Strain (%)		Tensile strength (MPa)		Modulus (MPa)		References
		Pure matrix	Nano-composite	Pure matrix	Nano-composite	Pure matrix	Nano-composite	
Natural polymer	Starch	68.2±3.1	57.3±2.4 (5 %)	3.9±0.3	4.5±0.2 (5 %)	31.9±5.1	34.5±4.3 (5 %)	[268]
	Amylo-pectin	3.8±0.7	2.4±0.8 (10 %)	16.4±6.6	15.3±4.2 (10 %)	683±294	822±279 (10 %)	[396]
	Rubber	576±36	849±11 (6 %)	0.56±0.13	2.3±0.4 (6 %)	0.5±0.14	1.0±0.1 (6 %)	[397]
	Chitosan	8.9	5.5-6.5	40	80-140	1.4	1.5-7.5	[275]
	Soy protein	29	2.5-11	16	32	0.5	1.19	[272]
Water soluble polymer	Polyvinyl alcohol	141.8	149.71 (5 %)	32.38	33.07 (5 %)	254.92	536.69 (5 %)	[398]
	Poly (ethylene oxide)	176.4±44.3	588±102.5 (0.4 %)	1.01±0.15	1.74±0.09 (0.4 %)	32.7±5.9	96.1±10.7 (0.4 %)	[399]

Nanocomposites in general are two-phase materials in which one of the phases has at least one dimension in the nanometer range (1−100 nm). The advantages of nanocomposite materials when compared with conventional composites are their superior mechanical, barrier and thermal properties at low reinforcement levels, as well as their better recyclability, transparency and low weight [400, 401]. Due to the high density of hydroxyl groups, nanocelluloses exhibit strong hydrophilic surface. Nanocellulose without modification always mixed with hydrophilic polymers for making nanocomposite. Solution casting is the main processing technique for nanocellulose (without modification) reinforced polymer matrix composites. Electrospinning also has been reported for making nanofibres [399, 402].

Nanocellulose has been used as reinforcing agent for nanocomposites. As Table 2.5 shows, the addition of nanocellulose significantly reinforces the tensile and modulus of matrix, especially polyvinyl alcohol (PVA) and poly (ethylene oxide) (PEO). As for the strain, it shows an interesting difference between natural polymers and water soluble polymers. The addition of nanocellulose seems to be able to facilitate the increase of strain for water soluble polymers. Due to the homogeneous and the strong

hydrogen bonding interaction between the nanocellulose and matrix, nanocellulose content has profound effects on the nanocomposite mechanical properties. Additionally, the addition amount of nanocellulose [268], source of nanocellulose [93, 398] and the fabrication of nanocellulose [403] are thought as the factors which affect the mechanical properties of nanocomposite.

The effect of nanocellulose on water uptake of composite depends on the matrix. For the matrix which have lower water sensitivity (e.g. rubber), the addition of nanocellulose results in the increase of water uptake [404]. In contrast, for the matrixes which have stronger hydrophilicity (e.g. starch, soy protein) the formation of microfibril network in the matrix prevents the swelling of matrix and decrease of water uptake. It has been proved that water sensitivity linearly decreases with the nanocellulose content [405-407]. Favier et al. [254, 255] firstly reported the demonstration of the reinforcing effect of cellulose whiskers on a thermoplastic matrix. The addition of tunicin whiskers displayed a spectacular improvement in the storage modulus of matrix. These outstanding properties were ascribed to a mechanical percolation phenomenon, yielded by cellulosic nanoparticles interactions through hydrogen bond forces with matrix.
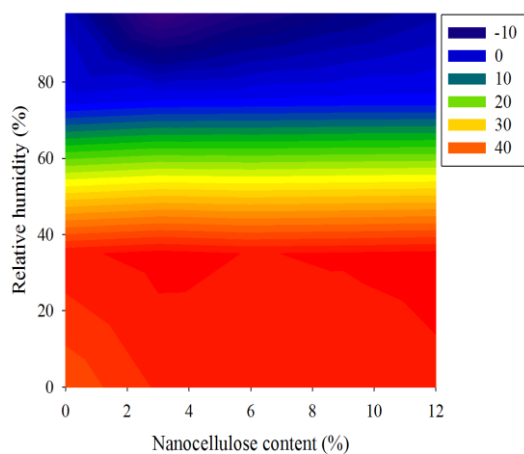
Fig. 2.29 Effect of relative humidity and
nanocellulose content on the glass transition
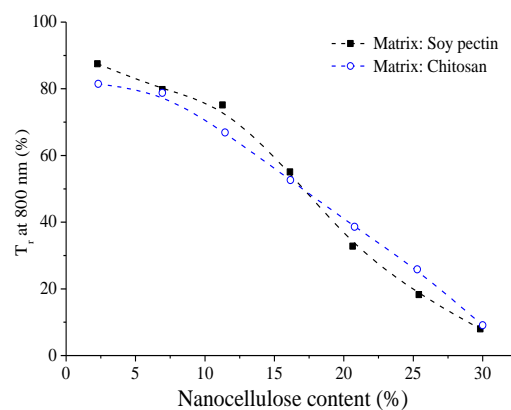
Fig. 2.30 Dependence of the nanocellulose content
on the optical transmittance (T_r) for soy pectin and
chitosan matrix at 800 nm.

The hydrogen bonding also gives rise to increase of thermal stability [272, 403, 404, 408-410] (see Fig. 2.29 [409]). Besides, nanocellulose/matrix interactions decrease with the increase of relative humidity (RH). The addition of nanocellulose affects the optical properly of nanocellulose nanocomposite. For instance, Fig. 2.30 (chitosan/ nanocellulose film is cited from [411], and soy protein is cited from [272]) shows optical transmittance of the films decreasing with increasing of the cellulose whisker content due to the occurrence of microphase separation which caused by the aggregation of fillers within the matrix.

2.2.3.2 Application of nanocellulose with modification

As described above, nanocellulose possesses an abundance of hydroxyl groups on the surface, where chemical reactions take place. Among the three kinds of hydroxyl groups, the OH group on the sixth position acts as a primary alcohol, where most of the modification predominantly occurs [412]. Various chemical modifications of nanocellulose, such as acetylation [413-415], esterification [416-419], silylation [420, 421], oxidation [422-424] and grafting [425-427] have been reported. Most of these focused on the improvement of its dispersity and compatibility in different solvents or matrices that are suitable in the production of nanocomposites. These modifications open a wide field for the application of nanocellulose. To date there is increasing research focus on modification of nanocellulose because of the increasing potential applications of modified nanocellulose in various industrial sectors, such as stabilizer, nanocomposites, and so on.

(1) Stabilizer
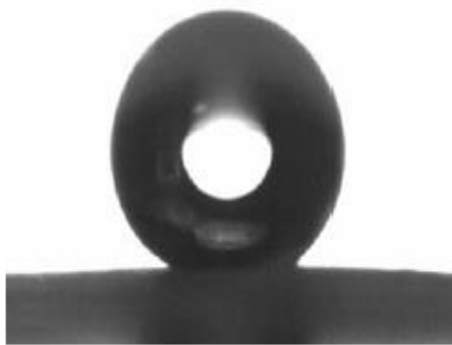
Fig. 2.31. Shape of water droplet on hydrophobized nanocellulose surface.
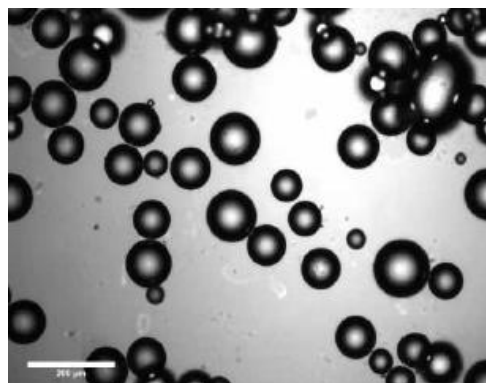
Fig. 2.32 Optical micrographs of emulsions prepared with silylated nanocellulose.

Since the beginning of the twentieth century, it has been known that colloidal particles that are partially wetted by both the aqueous and the oil phases are capable of stabilizing emulsions [428, 429]. The effectiveness of these solids as stabilizers depends on factors such as particle size, interparticle interactions and the wettability of the particles. In general, the formation of an oil-in-water (o/w) emulsion is favored when the three-phase contact angle between the oil, solid and water is < 90°. When the angle is > 90°, the water-in-oil (w/o) emulsion will be stabilized. At the interface, the particles form rigid structures that can sterically inhibit the coalescence of emulsion droplets. Highly crystalline cellulosic materials also show this ability. In 1986, Oza and Frank [430] firstly demonstrated the microcrystalline cellulose (MCC) stabilized emulsion. The authors proposed that, in addition to the "active" role at the interface, the MCC particles form a three-dimensional network structure in the continuous phase, which provides further retardation of coalescence through entrapment of emulsion droplets. In 1997, Ougiya et al. [431] presented a study comparing o/w emulsions stabilized by bacterial cellulose (BC) to those stabilized by MCC and nanocellulose. These previous reports describing the use of fibrillated cellulose materials as emulsion stabilizers dealt with o/w emulsions. Due to the

hydrophilic nature of cellulose, the fibrils and microfibrils are better wet by water than oil, and thus tend to stabilize water-continuous emulsions. In 2006 and 2007, Andresen et al [432, 433] firstly investigated the application of nanocellulose as w/o emulsion stabilizer. They utilized chlorodimethyl isopropylsilane to modify the surface of nanocellulose. The resulting material has a contact angle >90° (Fig. 2.31 [432, 433]), and should consequently stabilize w/o emulsions (Fig. 2.32 [432, 433]). Recently, some investigations [434-437] about the fabrication of hydrophobized nanocellulose as the w/o or o/w stabilizer with novel methods have been reported consequently.

(2) Nanocomposites (Matrix is hydrophobic polymer)

It has been found that the addition of nanocellulose led to higher mechanical properties for matrix (see Table 2.6). Compounding extrusion, film stacking and casting-evaporation have been used for preparing nanocomposite. There have been some studies about the homogeneous dispersion of nanocellulose in the matrix. With the aim to overcome this difficult, roll-mill dispersion [438], various chemical pretreatments (see Table 2.7) have been reported. Oksman and his co-worker [439] employed PVA, maleic anhydride, acetic anhydride to modify nanocellulose for reinforcing PLA matrix. As shown in Fig. 2.33, acetylation modification demonstrates significant effect on the mechanical properties of nanocomposite. For instance, after maleic anhydride modification, the tensile strength and modulus increase 90.46 % and 34.48 %, respectively.
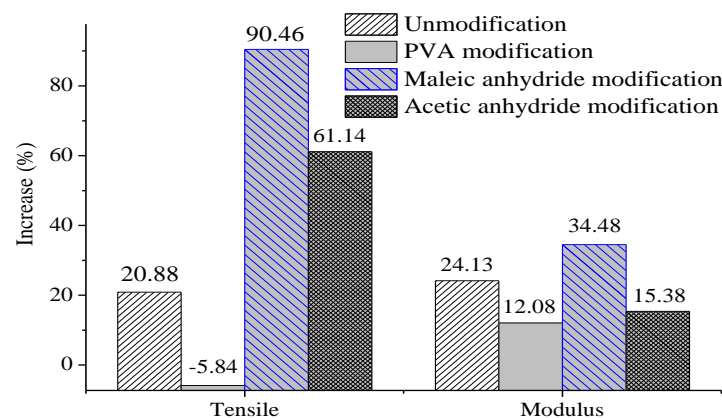
Fig. 2.33 Comparison of tensile strength and modulus for unmodified and modified nanocellulose reinforced polylactic acid nanocomposite.

Nanocellulose is an environmentally-friendly material that could serve as a valuable renewable resource. New and emerging industrial extraction processes need to be optimised to achieve more efficient operations and this will require active research participations from the academic and industrial sectors. Due to the availability of materials based on nanocellulose is still limited, the application of nanotechnology in developing nanocellulose to more valuable products is required. Increasing attention is devoted to produce nanocellulose in larger quantities, and to explore various

modification processes that enhance the properties, making it attractive for use in a wide range of industrial sectors. So far, most of the studies focus on the mechanical and chiral nematic liquid properties of nanocellulose nanocomposites while other research directions are also being explored. In nanocomposite systems, the homogeneous dispersion of nanocellulose in a polymer matrix is still a challenging point, as aggregation or agglomeration of nanocellulose is commonly encountered.

The appropriate modification of nanocellulose to impart functional characteristics to these nanomaterials is highly needed if nanocellulose is to be successfully incorporated into a specific product system. It is anticipated that nanotechnology innovations in renewable resources, such as nanocellulose, will create a larger market for future products based on nanocellulose.

Table 2. 6 Mechanical properties of nanocellulose reinforced hydrophobic polymer

Matrix	Amount of nanocellulose (%)	Strain (%)	Tensile strength (MPa)	Modulus (GPa)	References
Polylactic acid	0	3.4±0.4	58.9±0.5	2.9±0.6	[440]
	5	2.7±0.1	71.2±0.6	3.6±0.7	
Polyurethane	0	751.4±31.4	7.5±1.0	8.2±0.9	[441]
	0.5	1087±61.9	26.9±1.5	40.9±3.3	
	1	994.2±75.3	61.5±4.8	42.4±3.0	
	5	1110.3±101.1	49.8±6.6	44.9±2.4	
Polyester	0	1.75	16.40	1.38	[442]
	1	1.86	16.97	1.58	
	2	1.89	17.81	1.74	
	3	1.53	18.02	1.90	
	4	1.80	21.69	2.51	
	5	2.50	22.64	2.59	

Table 2. 7 Comparison of mechanical properties for unmodified and modified nanocellulose reinforced polylactic acid nanocomposite

Modification	Amount of nanocellulose (%)	Strain (%)	Tensile strength (MPa)	Modulus (GPa)	References
Unmodification	0	3.4±0.4	58.9±0.5	2.9±0.6	[440]
	5	2.7±0.1	71.2±0.6	3.6±0.7	
PVA modification	0	3.4±0.2	71.9±2.0	3.31±0.12	[439]
	5	2.4±0.2	67.7±0.8	3.71±0.07	
Maleic anhydride modification	0	1.9±0.2	40.9±3.2	2.9±0.1	[400]
	5	2.7±0.5	77.9±6.7	3.9±0.3	
Acetic anhydride modification	0	2.06638	44.4431	0.91	[414]
	6	0.98534	71.615	1.05	

Chapter 3 Fabrication of Nanocellulose and Statistical Analysis

3.1 Introduction

Nanocellulose is a material composed of nanosized cellulose fibrils. The typical dimensions of nanocellulose are 5–20 nanometers in width and up to 2000 nanometers in length [443]. This feature endows nanocellulose with a high aspect ratio (length to width ratio). Moreover, comparing with natural fibres, nanocellulose displays unique advantages, e.g. high specific surface and mechanical properties [444]. These advantages are leading nanocellulose as a versatile nanomaterial for a wide range of potential applications.

Many researches has been reported on the fabrication [261-263], characterization [70, 259, 319] and application [375, 379, 395] of nanocellulose among which most of the isolation methods are sulphuric acid hydrolysis and mechanical treatment while there is less report about the fabrication process by using oxidation/sonication. Sulfuric acids are commonly used to produce nanocellulose since Rånby [242, 243] firstly used this method in 1950s. The sulphuric acid hydrolysis can provide a highly stable suspension with high negative charge due to the introduction of sulphate ester groups on the surface of crystallites [297]. However, the low yield of nanocellulose (around 30 % [299]) limits nanocellulose to be scaled up to industrial areas [299].

Nanocellulose also can be obtained through mechanical treatments, e.g. high pressure homogenization [258], ultrasonication [155, 280-282], cryocrushing [277, 283] and grinding [284-286], among which the homogenization has become the most popular type of nanocellulose fabrication [288]. Mechanical treatment can result in longer and entangled nanoscale cellulose elements leading to stronger networks [291], but this treatment tends to damage the microfibril structure of nanocellulose by reducing molar mass and degree of crystallinity [445]. Additionally, the raw materials among these reports are refined wood fibres or microcrystalline cellulose (MCC). But there is less report about the fabrication of nanocellulose from natural fibres without refined pretreatment.

In order to solve the main problems (low yield, crystallinity damage) as described above, in this work, we develop a novel method (oxidation/sonication) to fabricate nanocellulose directly from natural fibres (in this case hemp). In this chapter we will focus on the optimization of nanocellulose fabrication. Response surface methodology (RSM) based on a five-level-four-variable (hydrolysis time, hydrolysis temperature, dosage of swelling agent and dosage of oxidant) central composite design (CCD) is applied to design the experiment. Effect of process variables on the yield of nanocellulose will be discussed and the fabrication will be optimized with the assist of Design-Expert software.

3.2 Materials and methods

3.2.1 Materials

The chemical reagents, the raw material, chemical reagents and instrument used for research including the providers are summarized in Table 3.1.

Table 3. 1 Summary of chemical reagents and instruments for analysis

Chemical reagent, raw material, instrument	Provider
Hemp Yarns	Shanxi Greenland Textile Ltd
Oxidant	Sigma-Aldrich Company Ltd
Swelling agent	Sigma-Aldrich Company Ltd
EDTA	Sigma-Aldrich Company Ltd
Na_2S	Sigma-Aldrich Company Ltd
BioDesign™Dialysis tubing	Fisher Scientific UK Ltd
Membrane filter (0.2μm)	Fisher Scientific UK Ltd
Fisherbrand®Centrifuge	Fisher Scientific UK Ltd
L&W Pulp Disintegrator	Lorentzen & Wettre Ltd
Freeze dryer	MMM Medcenter
Fisherbrand®PH meter	Fisher Scientific UK Ltd
Oil free pump	Fisher Scientific UK Ltd
IKA®Overhead stirrer	Fisher Scientific UK Ltd
Fisherbrand®Ultrasonic bath	Fisher Scientific UK Ltd
MMM Vacucell 22 litre Vacuum Oven	MMM Medcenter

3.2.2 Fabrication of nanocellulose

Fig. 3.1 shows the process of nanocellulose fabrication. The chopped hemp yarns (the length is around 1 mm which in favor of the disintegration of disintegrater) were firstly soaked in water in the disintegrator for 30 minutes and the materials were then removed to three-neck flask (500 ml). In these experiments, 14.2365 g of dried chopped hemp fibres were used for each time, and the final concentration of hemp fibres pulp was controlled at 5 %. Sodium hydroxide and sodium hypochlorite were added as swelling agent and oxidant, respectively. The mixture was then continuously stirred at normal speed (900 rpm) combined with continuous sonication under various hydrolysis temperatures and times (the levels of hydrolysis temperature and hydrolysis time are shown in Table 3.2).

Then heating was stopped. When the suspension was cooled down to room temperature (i.e. 25 ℃), the obtained suspension was neutralized with glacial acetic acid. Then the suspension was centrifuged (into order to separate as much salts from nanocellulose suspension as possible the centrifugal speed was set to the maximum value of this instrument, namely, 8500 rpm) by the centrifuger to separate salts from nanocellulose suspension. The separation of salts by centrifuger was repeated couple

times until none of deposit appear on the bottom of centrifugal tube.

After centrifuging, in order to obtain good dispersion of suspension, nanocellulose suspension was sonicated for 0.5h. For further separate the salt from the nanocellulose suspension, in this study, the separation of salt was carried out by dialysis method. The suspension was stored in the pretreated dialysis tubing (305 mm length, 49.5 mm diameter). The tubing was pretreated with the following procedure as described : soaked the tubing in hot solution (80 °C) containing 1 % EDTA and 0.3 % sodium sulfide for one minute; then the tubing was washed with 60 °C distilled water for two minutes and finally washed with distilled water at room temperature (25 ºC) for three hours. The tubing was subjected to dialysis in a 4×L container filled with distilled water, the distilled water was changed one for per 24 hours, in order to separate salt and pure nanocellulose, the dialysis process was continued for seven days. Nanocellulose powder was obtained by freezing dryer as described by Habib et al [446]. The response of yield of nanocellulose was calculated as follow:

$$Yield \ /\% = \frac{W_t}{W_0} \times 100 \quad \text{(Eq. 3.1)}$$

where W_0 is the weight of raw hemp yarn, W_t is the weight of nanocellulose.
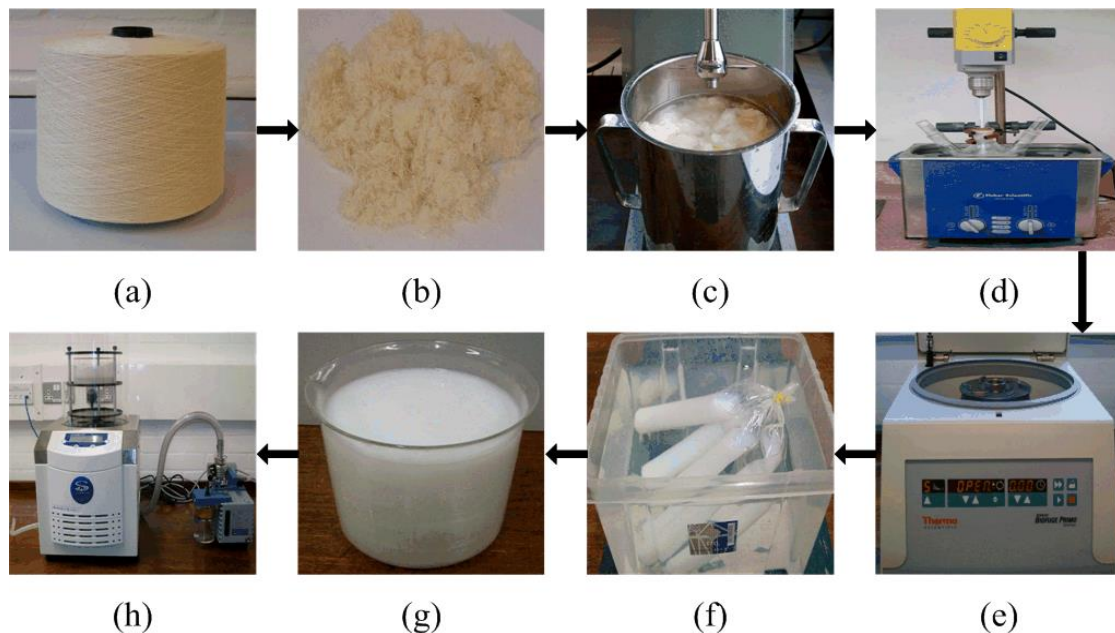
Fig. 3.1 The process of nanocellulose fabrication: (a) hemp yarn; (b) short hemp fibres (chopped from hemp yarn); (c) disintegration; (d) chemical degradation and ultrasonication; (e) centrifugation; (f) dialysis; (g) nanocellulose suspension and (h) freezing dried.

3.2.3 Response surface methodology (RSM) design

RSM explores the relationships between independent variables and dependent response variables. The main idea of RSM is to use a sequence of designed

experiments to obtain an optimal response [447]. The most popular RSM is the CCD. CCD was firstly described by Box and Wilson in 1951 [448] and improved upon by Box and Hunter in 1957 [449]. The main advantage of CCD is to reduce the number of experimental works [450]. In this present work, the CCD was applied through the use of Design-Expert software 8.0.6 (Stat-Ease, Inc., USA). The range and the levels of the test variables are given in Table 3.2. It should be mentioned that the dosage of swelling agent and oxidant are presented on the weight of dried fibres.

Table 3. 2 Experimental range and levels of the independent variables

Variables	Range and levels				
	-2	-1	0	1	2
A-Time (h)	2	3	4	5	6
B-Temperature (°C)	55	60	65	70	75
C-Dosage of swelling agent (NaOH) (%)	8	10	12	14	16
D-Dosage of oxidant (NaClO) (%)	20	40	60	80	100

3.2.4 Statistical analysis

This software was released by Stat-Ease and can provide the tools for RSM analysis for process optimization. The analytical process in this software includes 6 steps [451-453]:

(i). Transformation

By default, the transformation option is set to "none". A ratio of the maximum to the minimum greater than 10 usually indicates a transformation is required [453]. This software provides 8 kinds of response transformation, namely, square root, natural log, base 10 log, inverse square root, inverse, power, logit and arcsin square root. Various types of data can be carried out with relevant transformation, e.g. the yield data can be transformed by the square root transformation.

(ii). Fit summary

The fit summary option collects the important statistics used to select the correct starting point for the final model. The software provides suggested model. And the suggested model can be edited by the Model option.

(iii). Model

On the Model screen, the model selected initially contains all of the terms. But the model can be edited by removing the negligible terms (has) or adding new terms. The model reduction can be done manually or automatically. There are three basic types of automatic model regression, namely, backward, forward, stepwise. After selecting or editing model, click on the ANOVA button. The edited model can be evaluated by analysis of variance (ANOVA).

(iv). Perform the ANOVA

In the ANOVA option, the software provides the ANOVA results with annotations and the final equations. A significant model and not significant lack of fit is desired. If the lack of fit shows significant or any term displays high value of p-value (greater than 0.1) go back to the model option and edit the model again

(v). Diagnostics

Graphical summaries for case statistics can be seen by selecting the Diagnostics button. Most of the plots display residuals, which show how well the model satisfies the assumptions of the analysis of variance.

(vi). Model graphs

This software provides various graphs to interpret the model selected. These are generated by clicking on the Model Graph button. For RSM designs, the primary graphs will be the contour and 3D surface. Both of them show how any two factors affect the response.

The analysis of experimental data shown in Table 3.3 was performed by the Design-Expert Version 8.0.6 software. The maximum and the minimum response value (yield) shown in Table 3.3 are 42.02 % (Std 21) and 2.52 % (Std 23), respectively. Therefore, the ratio of maximum response value to minimum response value is 16.67. This means that a transformation is required. In this experiment, the square root transformation was used to transform the response. This equation is:

$$y` = \sqrt{y + k} \quad \text{(Eq. 3.2)}$$

where y` is the transformed response, y is the response and k is a constant. We selected randomly a positive value as a constant. In Fit Summary, the model what the software provided was quadratic model. Then the model and k were adjusted by steps (iii) to (v) as described above. The final value of k was 32967. Backward method was used as the model regression, because it was the most robust choice for algorithmic model reduction [451]. The removal term in this model was term AB.

SigmaPlot software can provide high-quality graph. Therefore, in this experiment, the model graphs drawing were performed by using SigmaPlot Version 12.0 (Systat Software Inc., USA). Such three dimensional surfaces could yield accurate geometrical representation and provide useful information about the behavior of the system within the experimental design.

Table 3. 3 Central composite design experimental data and predicted values for RSM

Std	A	B	C	D	Time (h)	Temperature (°C)	Dosage of Swelling agent (%)	Dosage of Oxidant (%)	Yield (%)	Predicted Yield (%)
1	-1	-1	-1	-1	3	60	10	40	9.03	10.89
2	1	-1	-1	-1	5	60	10	40	20.55	17.44
3	-1	1	-1	-1	3	70	10	40	17.54	18.99
4	1	1	-1	-1	5	70	10	40	23.38	25.55
5	-1	-1	1	-1	3	60	14	40	10.72	10.94
6	1	-1	1	-1	5	60	14	40	8.22	12.41
7	-1	1	1	-1	3	70	14	40	14.03	14.00
8	1	1	1	-1	5	70	14	40	15.97	15.47
9	-1	-1	-1	1	3	60	10	80	27.90	29.42
10	1	-1	-1	1	5	60	10	80	31.54	32.07
11	-1	1	-1	1	3	70	10	80	34.31	30.61
12	1	1	-1	1	5	70	10	80	32.46	33.26
13	-1	-1	1	1	3	60	14	80	21.07	21.49
14	1	-1	1	1	5	60	14	80	21.58	19.06
15	-1	1	1	1	3	70	14	80	15.61	17.63
16	1	1	1	1	5	70	14	80	14.46	15.19
17	-2	0	0	0	2	65	12	60	23.63	22.51
18	2	0	0	0	6	65	12	60	27.03	26.63
19	0	-2	0	0	4	55	12	60	12.95	12.14
20	0	2	0	0	4	75	12	60	17.09	16.38
21	0	0	-2	0	4	65	8	60	42.02	42.00
22	0	0	2	0	4	65	16	60	25.50	23.99
23	0	0	0	-2	4	65	12	20	2.52	0.15
24	0	0	0	2	4	65	12	100	17.55	18.41
25	0	0	0	0	4	65	12	60	27.73	27.66
26	0	0	0	0	4	65	12	60	27.88	27.66
27	0	0	0	0	4	65	12	60	27.10	27.66
28	0	0	0	0	4	65	12	60	27.66	27.66
29	0	0	0	0	4	65	12	60	27.77	27.66
30	0	0	0	0	4	65	12	60	27.79	27.66

3.3 Results and discussion

3.3.1 ANOVA analysis and fitting of quartic model

Table 3.4 presents a summary of relevant statistics for the model from Fit Summary step. Predicted R^2 is a measure of variation in new data given by the model and predicts how well the model can predict the response; adjusted R^2 is a measure of the amount of variation around the mean explained by the model, adjusted for the number

of terms in the model [454]. Adjusted R^2 and Predicted R^2 should be as high as possible and within approximately 0.20 of each other to be in reasonable agreement [454]. As shown in Table 3.4, quadratic model has higher R^2, Adjusted R^2 value and the highest Predicted R^2 value. Moreover, in quadratic model, Adjusted R^2 and Predicted R^2 is within approximately 0.20. Therefore,we selecte quadratic model.

Table 3. 4 Model summary statistics

Source	Standard deviation	R^2	Adjusted R^2	Predicted R^2	PRESS
Linear	0.1080	0.4656	0.3801	0.2113	0.4307
2FI	0.1141	0.5475	0.3093	0.1356	0.4721
Quadratic	0.0345	0.9673	0.9367	0.8122	0.1026
Cubic	0.0184	0.9957	0.9820	0.3997	0.3279

An ANOVA table is commonly used to summarize the tests performed. Table 3.5 shows the ANOVA results of the reduced quadratic model for nanocellulose yield. The significant factors can be ranked based on the F-value or p-value (also named "Prob. > F" value). The larger the magnitude of F-value and correspondingly the smaller the "Prob. > F" value, the more significant is the corresponding coefficient [455]. It can be seen from Table 3.5 that the F-value of the model is 34.1906 and the corresponding p-value (Prob. > F) is very low (less than 0.0001), implying that the model is significant. The p-values are used as a tool to check the significance of each of the coefficients [456]. Values of "Prob. > F" less than 0.05 indicates the model terms are significant [457]. In this work, the main effect of hydrolysis time (A), hydrolysis temperature (B), dosage of swelling agent (C), dosage of oxidant (D), inter-effect of hydrolysis time with hydrolysis temperature (AB), hydrolysis time with dosage of swelling agent (AC), hydrolysis time with dosage of oxidant (AD), hydrolysis temperature with dosage of swelling agent (BC), hydrolysis temperature with dosage of oxidant(BD), dosage of swelling agent with dosage of oxidant (CD), the quadratic effect of hydrolysis time (A^2), hydrolysis temperature (B^2), dosage of swelling agent (C^2) and dosage of oxidant (D^2) are significant model terms. The mean square value of lack of fit is 0.00005. This implies the lack of fit is not significant relative to the pure error [458].

Post-ANOVA statistics in Table 3.5 shows the R^2 value for the yield of nanocellulose is calculated as 0.9653, which is close to 1 and implies that the sample variation of 96.53 % for yield of nanocellulose is attributed to the independent variables, and only about 3.47 % of the total variation cannot be explained by the model. R^2 is a measure of the amount of variation around the mean explained by the model [459]. Therefore the high R^2 value indicates that the accuracy and general ability of the modified quadratic model is good. The predicted R^2 of 0.8421 is in reasonable agreement with the adjusted R^2 (which is more suitable for comparing models with various numbers of independent variables) of 0.9370, which has advocated a high correlation between the observed values and the predicted values. This means that the regression model

provides an excellent explanation of the relationship between the independent variables (factors) and the response (selectivity). Adequate precision is comparable with the range of the predicted values at the design points to the average prediction error. In terms of the signal to noise ratio, a ratio greater than 4 is desirable [451]. In this case, the ratio of 27.8347 indicates an adequate signal and suggests that the model can be used to navigate the design space.

Table 3. 5 ANOVA for response surface quartic model

Source	Sum of squares	df	Mean square	F-value	p-value Prob>F
Model	0.0163	13	0.00126	34.1906	< 0.0001
A-Time	0.0002	1	0.00019	5.2586	0.0357
B-Temperature	0.0002	1	0.00021	5.5727	0.0313
C-Swelling agent	0.0037	1	0.00369	100.4036	< 0.0001
D-Oxidant	0.0037	1	0.00379	103.2154	< 0.0001
AC	0.0002	1	0.00020	5.3419	0.0345
AD	0.0001	1	0.00012	3.1521	0.0948
BC	0.0002	1	0.00019	5.2621	0.0357
BD	0.0004	1	0.00036	9.8775	0.0063
CD	0.0005	1	0.00048	13.1463	0.0023
A^2	0.0001	1	0.00012	3.3700	0.0850
B^2	0.0023	1	0.00233	63.4942	< 0.0001
C^2	0.0004	1	0.00037	10.0981	0.0058
D^2	0.0044	1	0.00439	119.5071	< 0.0001
Residual	0.0006	16	0.00004		
Lack of Fit	0.0006	11	0.00005		
Pure Error	0	5	0		
Cor Total	0.0169	29			
Std. Dev.	0.0061	R^2	0.9653		
Mean	181.6281	Adjusted R^2	0.9370		
C.V. %	0.0033	Predicted R^2	0.8421		
PRESS	0.0027	Adequate precision	27.8347		

The prediction equation is provided in both coded factors and actual factors. The coded equations are determined first by the software, and the actual equations are derived from the coded [451]. The final equation is:

$$y` = \sqrt{y + 32967} = 179.38604 + 0.04891 * Time + 0.05555 * Temperature$$
$$+ 0.00957 * NaOH + 0.0097 * NaClO - 0.00175 * Time * NaOH$$
$$- 0.00013 * Time * NaClO - 0.00035 * Temperature * NaOH - 0.00014$$
$$* NaOH * NaClO - 0.00212 * Time^2 - 0.00037 * Temperature^2 +$$
$$0.00092 * NaOH^2 - 0.00003 * NaClO^2$$

(Eq. 3.3)
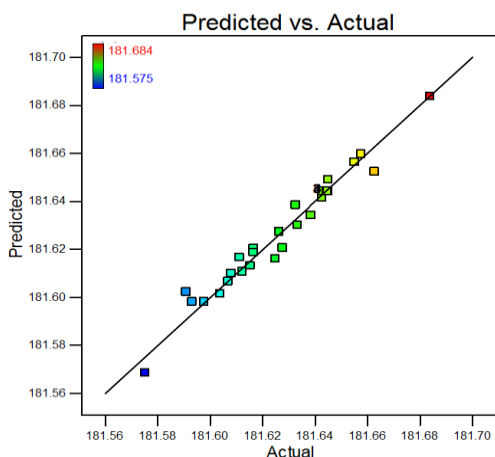
Fig. 3.2 Plot of predicted vs. actual for nanocellulose yield.
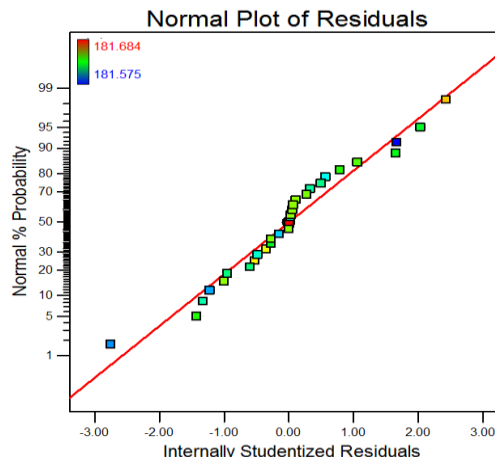
Fig. 3.3 Normal plot of residuals for nanocellulose yield.
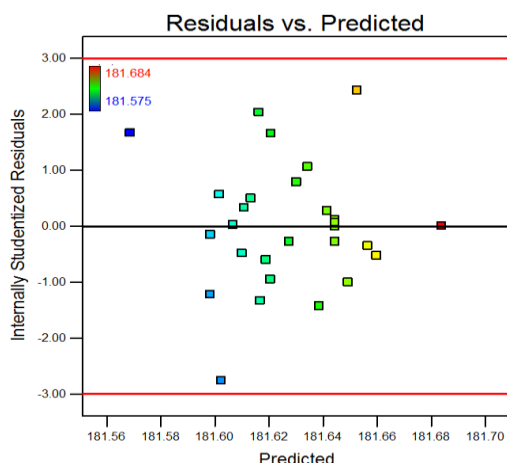
Fig. 3.4 Plot of residuals vs. predicted response for nanocellulose yield.
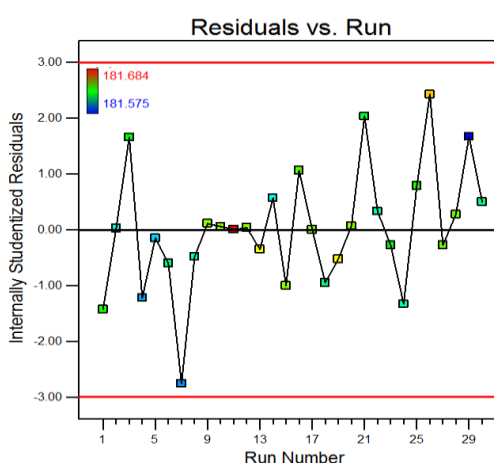
Fig. 3.5 Plot of residuals vs. run for nanocellulose yield.

By employing the diagnostic option, the adequacy of quartic model was further checked. The diagnostic plots are shown in Figs. 3.2-3.5. A check on the plots in Figs. 3.2 and 3.3 reveal that the residuals generally fall on a straight line implying that the errors are distributed normally. Fig. 3.2 compares experimental yields to the predicted values obtained from the model described in Eq. 3.3. The agreement between the predicted and experimental values implies the high accuracy of the model. Therefore, this model could be used to predict the yield of nanocellulose.

Three plots related to residuals diagnostic are presented: the normal probability plot against internally studentized residuals, the plot of internally studentized residuals vs. predicted values of yields and internally studentized residuals vs. run number (Fig. 3.3, Fig. 3.4 and Fig. 3.5, respectively). In Fig. 3.3, points fall closely around the straight line. Such observation indicates that there are no serious violations in the quartic assumptions (i) that errors are normally distributed and are independent of each other; (ii) that the error variances are homogeneous and (iii) that residuals are independent. Test for the modified quartic model of constant variance is given by plot presented in

Fig. 3.4. It can be seen that the points are randomly scattered and all values lie within the range of −2.754 and 2.429 (values between −3 and +3 are considered as the top and bottom outlier detection limits). Fig. 3.5 shows that the minimum appears in run number 7 and the maximum appears in run number 26. Based on the plots presented from Figs. 3.2 to 3.5, it can be concluded that response transformation used was appropriate, that there was no apparent problem with normality, and that developed quartic model is successful in capturing the correlation between studied key operating process parameters of nanocellulose fabrication system.

3.3.2 Effects of process variables on the yield of nanocellulose

To investigate the interactive effects of two factors on the response values, three dimensional surface and contour plots were drawn by considering two variables at a time while keeping the other two variables at the central (0) level, based on the final equation (Eq. 3.3).

By keeping hydrolysis temperature (B) at the central level (65 °C) and dosage of oxidant at the central level (60 %), the combined effect of hydrolysis time and dosage of swelling agent was investigated. The results are illustrated in Fig. 3.6 in the form of 3D surface (Fig. 3.6(a)) and contour plots (Fig. 3.6(b)). It should be noted that, comparing with the other inter-effect terms the F-value of AB term is the lowest. Therefore, in this section we will not discus their combined effect on the yield of nanocellulose. As can be seen, the yield of nanocellulose decreases almost linearly when the dosage of swelling agent changes from 8 % to 16 %. This is may be due to the peeling reaction which can result in the hydrolysis of hemp fibres. The best hydrolysis time ranges from 3.98h to 4.91h.

The combined effect of hydrolysis time and dosage of oxidant was shown with 3D surface and contour plots in Fig. 3.7(a) and 3.7(b) respectively (the level of hydrolysis temperature and dosage of swelling agent was 65 °C and 12 %, respectively). It can be seen that the yield of nanocellulose would increase as hydrolysis time and dosage of swelling agent increase from 2 to 4.03h and from 20 to 68.75 %, respectively. The yield of nanocellulose would decrease when the hydrolysis time is longer than 4.77h or the dosage of oxidant is larger than 72.89 %.

The surface plot showing the effect of hydrolysis temperature and dosage of swelling agent at 4h hydrolysis time and 60 % oxidant (Fig. 3.8(a) and 3.8(b)), shows a saddle-shaped surface, exhibiting an optimum temperature 65.63-69.79 °C and dosage of swelling agent 8 %. At 8 % swelling agent, the highest nanocellulose yield (>42 %) is observed. The yield of nanocellulose increases when the temperature increases from 55 °C to 65.63 °C at 8 % swelling agent, and then starting to decrease from 69.79 °C.

Fig. 3.9 shows the combined effect of hydrolysis temperature and dosage of oxidant on the yield of nanocellulose. It seems that when the dosage of oxidant less than 30 %,

hydrolysis temperature has insignificant effect on the yield of nanocellulose. Above 30 % oxidant, the yield of nanocellulose increases with the increasing of hydrolysis temperature at first then decreases with the temperature increasing. As Fig. 3.9 shows, the best conditions for the yield of nanocellulose are: temperature 63.38-67.11 °C and dosage of oxidant 66.23-71.89 %. The saddle-shaped surface can be observed in Fig. 3.10, which shows the mutual effect of swelling agent and oxidant on the yield of nanocellulose. The yield of nanocellulose can reach maximum when the dosage of swelling agent is 8 % and the addition of oxidant around 70-87.43 %.
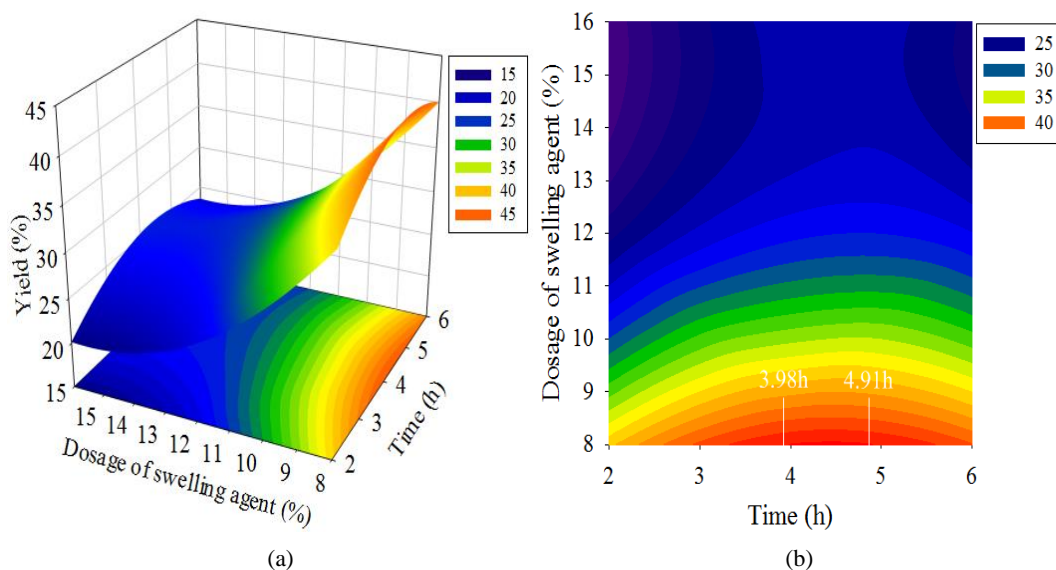
Fig. 3.6 Response surface plots (a):3D graph; and (b) contour graph showing the effect of time, swelling agent and their mutual effect on the yield of nanocellulose. Other variables are constant: temperature, 65 ℃ and dosage of oxidant, 60 %.
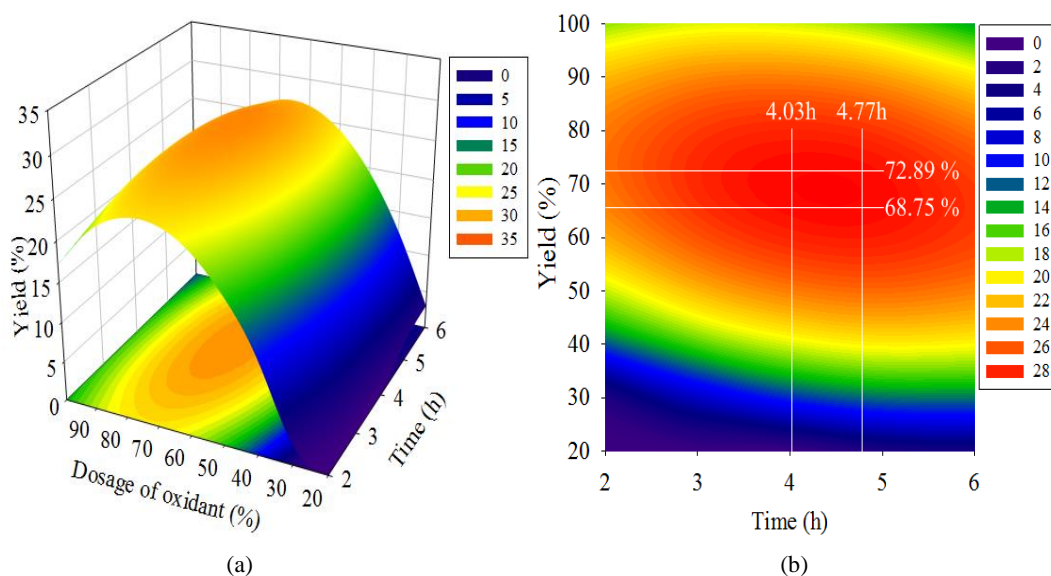
Fig. 3.7 Response surface plots (a):3D graph; and (b) contour graph showing the effect of time, oxidant and their mutual effect on the yield of nanocellulose. Other variables are constant: temperature, 65 ℃ and dosage of swelling agent, 12 %.
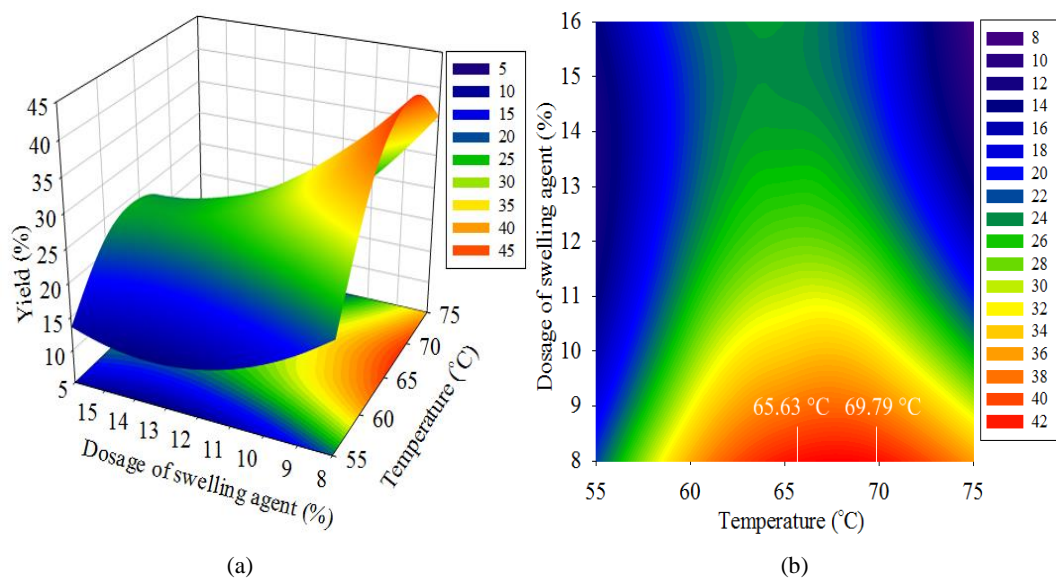
Fig. 3.8 Response surface plots (a):3D graph; and (b) contour graph showing the effect of temperature, swelling agent and their mutual effect on the yield of nanocellulose. Other variables are constant: time, 4 h and dosage of oxidant, 60 %.
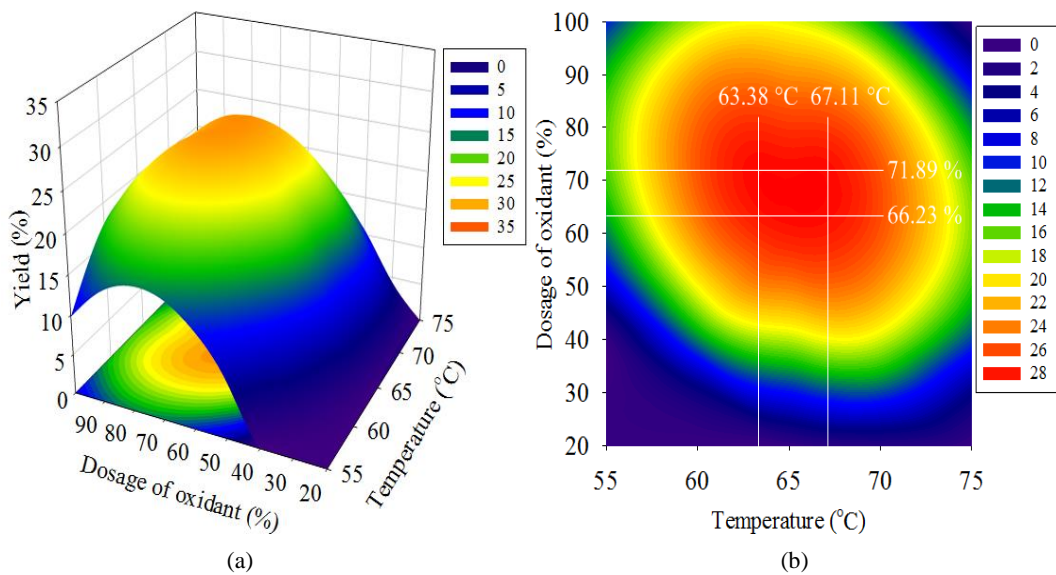
Fig. 3.9 Response surface plots (a):3D graph; and (b) contour graph showing the effect of temperature, oxidant and their mutual effect on the yield of nanocellulose. Other variables are constant: time, 4 h and dosage of swelling agent, 12 %.
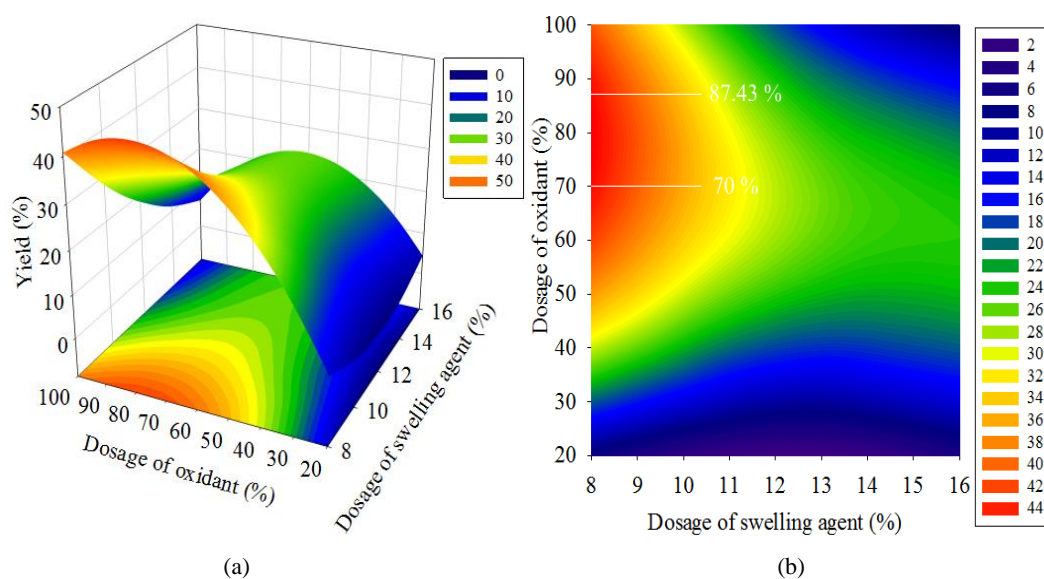
Fig. 3.10 Response surface plots (a):3D graph; and (b) contour graph showing the effect of swelling agent, oxidant and their mutual effect on the yield of nanocellulose. Other variables are constant: time, 4 h and temperature, 65 ℃.

3.3.3 Optimization of the fabrication process

Table 3. 6 Optimization criteria for nanocellulose fabrication

Criteria	Goal	Lower limit	Upper limit
Yield (%)	Maximize	2.52	50
Time (h)	In range	4	5
Temperature (℃)	In range	60	70
Dosage of swelling agent (NaOH) (%)	Equal to	8	8
D-Dosage of oxidant (NaClO) (%)	In range	70	87

In this work, numerical optimization method was carried out by Design-Expert software to optimize the fabrication process. Because numerical optimization presents a comprehensive and up-to-date description of the most effective methods in continuous optimization [460]. In the numerical optimization, yield of nanocellulose was set to a maximum range whereas hydrolysis time, hydrolysis temperature and dosage of swelling agent were set in a range between low and high level and dosage of oxidant was set to an exact value (8%). The desired criteria are summarized in Table 3.6. Table 3.7 shows software generated three optimum conditions of independent variables with the predicted values of responses. Solution number 1 has the maximum desirability value was selected as the optimum conditions of nanocellulose fabrication. To validate the model adequately, the fabrication at this condition was done and the yield of nanocellulose was 47.79 %. The experimental value obtained was in good agreement with the value predicted from the models. In order to optimize the addition of swelling agent, we investigated the effect of the

dosage of swelling agent on the yield of nanocellulose at the same condition. It can be seen from the Fig. 3.11 that when the addition of swelling agent is 0, 2, 4, 6 and 8 %, respectively, the yield of nanocellulose is 38.23 %, 44.43 %, 54.11 %, 49.51 % and 47.79 %, respectively. It is apparent that the best addition of swelling is 4 %.

Table 3. 7 Solutions for optimum conditions

Number	Time (h)	Temperature (°C)	NaOH (%)	NaClO (%)	Yield (%)	Desirability
1	5	67	8	70	48.0049	0.958
2	4.97	66.99	8	70	47.95	0.957
3	4.92	66.82	8	70	47.8628	0.955
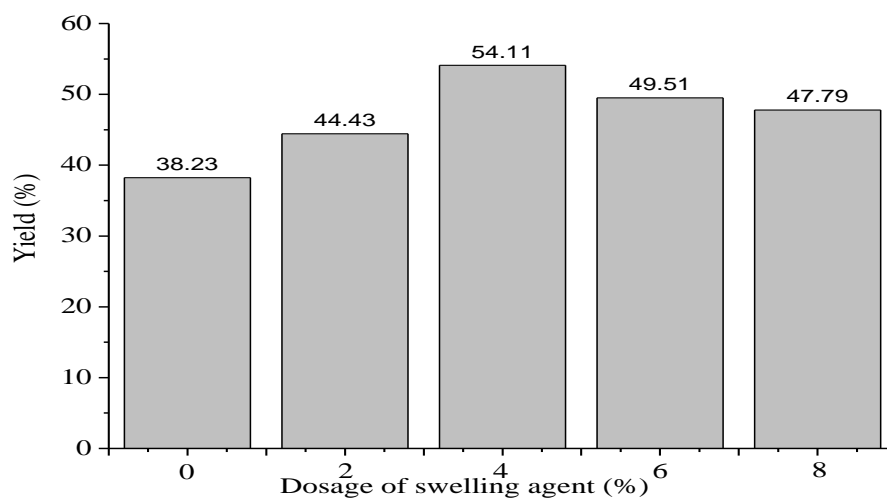
Fig. 3.11 Effect of dosage of swelling agent on yield of nanocellulose.

3.4 Interim conclusions

In this chapter, oxidation/sonication method was used to fabricate nanocellulose successfully. RSM based on a five-level-four-variable CCD was employed to optimize the preparation conditions of nanocellulose. The four variables considered were hydrolysis time, hydrolysis temperature, dosage of swelling agent and dosage of oxidant.

Reduced quartic model has been used to describe the correlation between the response and other variables. The main effects, quadratic effects and interactions of the four variables on the yield of nanocellulose were investigated by the analysis of variance (ANOVA). In this work, the main effect of hydrolysis time (A), hydrolysis temperature (B), dosage of swelling agent (C), dosage of oxidant (D), inter-effect of hydrolysis time with dosage of swelling agent (AC), hydrolysis temperature with dosage of swelling agent (BC), hydrolysis temperature with dosage of oxidant(BD), dosage of swelling agent with dosage of oxidant (CD), the quadratic effect of hydrolysis temperature (B^2), dosage of swelling agent (C^2) and dosage of oxidant (D^2) were significant model parameters.

Predicted values from the reduced quartic model were found to be in good agreement with observed values, indicating that the regression equations could be used to predict and optimize the yield of nanocellulose. The optimal values of variables were obtained at hydrolysis time 5h, hydrolysis temperature 67 °C, dosage of swelling agent 4.00 % and dosage of oxidant 70 %. Under this optimal condition the yield of nanocellulose could be up to 54.11 %.

Chapter 4 Characterization of Nanocellulose

4.1 Introduction

With the development in analytical techniques and the nanotechnology, researchers are now able to reveal more details about nanocellulose. The precise shape size of nanocellulose can be observed by microscopy (e.g. AFM [259, 310, 461], SEM [255], TEM [279, 310, 462]), spectroscopy (e.g. FTIR [302], NMR [303], XRD [304]) and scattering techniques (e.g. dynamic light scattering (DLS) [305], small-angle neutron scattering (SANS) [306, 307], small-angle X-ray scattering (SAXS) [259, 308], wide-angle X-ray scattering (WAXS) [309]). Combined with analytical instruments, computer-assisted techniques have been developed to investigate the size of nanocellulose. By employing AFM [70, 71, 313-316] and spectroscopic techniques [317-320], researchers are able to examine the mechanical properties of nanocellulose. Scattering techniques are used to investigate the polyelectrolytic behaviour of nanocellulose. These techniques include ultra-small-angle X-ray scattering (USAXS) [340], (SAXS) [308], static light scattering (SLS) [341, 342] and DLS [341-343].

In the present work, we will characterize nanocellulose fabricated from hemp yarns with various analytical instruments, aiming to reveal the features of nanocellulose fabricated using our novel method. Nanoparticle tracking analysis (NTA), FEG-SEM and AFM are employed to study the size and the morphologies of nanocellulose; Attenuated total refraction Fourier transform infrared spectroscopy (ATR-FTIR), XRD and XPS are utilized to determine chemical and crystal structure of nanocellulose. Finally, the thermal properties of nanocellulose are investigated by differential scanning calorimetry (DSC).

4.2 Materials and methods

4.2.1 Materials

Table 4. 1 Summary of chemical reagents and instruments for analysis

Raw materials, Instrument	Provider
Hemp Yarns	Shanxi Greenland Textile Ltd
Dimension 3100 AFM	Digital Instruments (USA)
Spectrum Two™ ATR-FTIR	PerkinElmer UK Ltd
DSC 6000	PerkinElmer UK Ltd
Zeiss Supra 35 VP FEG-SEM	Oxford Instruments GmbH
Freeze dryer	MMM Medcenter
LM100 NTA	NanoSight UK Ltd
Thermo Scientific™ ESCALAB 210	Fisher Scientific UK Ltd
MMM Vacucell 22 litre Vacuum Oven	MMM Medcenter
D8 FOCUS X-ray powder diffraction	Bruker UK Ltd

The nanocellulose which was fabricated by the optimized conditions was used in this chapter. The other raw material and instrument includes the provider are summarized in Table 4.1.

4.2.2 Characterization of nanocellulose

Table 4. 2 Summary of the aim of characterization of nanocellulose with various instruments

Characterization	Instrument	Aim
Size distribution of nanocellulose	NTA	Determine the size of nanocellulose and find out if the oxidation/sonication could fabricate the nano-scale cellulose.
Morphologies of nanocellulose	AFM FEG-SEG	To characterize the surface morphologies of the nanocellulose.
Chemical structure of nanocellulose	XPS	Compared the elemental composition of nanocellulose with raw material (hemp yarn) and find out the differences to reveal the effect of oxidation/sonication on the elemental composition of nanocellulose.
	ATR-FTIR	Compared the chemical groups of nanocellulose with raw material and find out the changes of nanocellulose under the oxidation/sonication fabrication process.
Crystalline of nanocellulose	XRD	Compared the crystalline of nanocellulose with raw material and find out if the oxidation/sonication could damage the crystalline structure of cellulose.
Thermal property of nanocellulose	DSC	Compared the thermal property of nanocellulose with raw material.

In the characterization of nanocellulose, we employed seven analytical instruments to analyze nanocellulose and investigate (i) the size distribution and morphologies of nanocellulose; (ii) the chemical structure and crystalline of nanocellulose and (iii) the thermal property of nanocellulose. The aims for these characterizations with various instruments are summarized in Table. 4.2. The procedures of these analytical instruments are described as follows.

4.2.2.1 NTA

Nanoparticle tracking analysis (NTA) was performed using a digital microscope LM10 System (NanoSight, Salisbury, UK). 1 ml of the diluted sample (concentration 0.001%) was introduced into the chamber by a syringe. The particles of nanocellulose in the sample were observed using the digital microscope. The video images of the movement of particles under Brownian motion were analyzed by the NTA version 1.3 (B196) image analysis software (NanoSight Ltd, UK). Each video clip was captured for total 22 s. The detection threshold was fixed at 100, whereas the maximum particle jump and minimum track length were both set at 10 in the NTA software.

4.2.2.2 AFM

The AFM was used to examine the surface of feature nanocellulose. A drop of the suspension was deposited onto freshly cleaved mica and left to dry in a desiccating capsule with silica gel for a period of 12 h. A Nanoscope IIIa microscope (Digital Instruments, Santabarbara CA, USA) with a multimode head was used for the measurements. Sample was imaged in tapping mode. Height images were recorded. High resolution images were obtained under the following conditions: a resonance frequency value of 155 kHz, 1 Hz scan rate and a spring constant of 12–103 N m^{-1}. UTHSCSA ImageTool software (which is software for image processing and analysis) was then used to measure the size of nanocellulose.

4.2.2.3 FEG-SEM

About 50 ml nanocellulose suspension was dropped into petri dish (diameter 55 mm). Then, the suspension was dried in vacuum oven at 60 ℃. A thin nanocellulose film was obtained after drying. A small piece of the nanocellulose film was examined with a Zeiss Supra 35 VP field emission scanning electron microscopy (FEG-SEM). The test pieces were coated with a thin layer of platinum on the surface in an Edwards S150B sputter coater to provide electrical conductivity. Following coating, in order to obtain high resolution image, nanocellulose observations were performed under the following conditions: an acceleration voltage of 10 kV and the secondary electron mode with images collected digitally. UTHSCSA ImageTool software was then used to measure the size of nanocellulose.

4.2.2.4 XPS

XPS was performed using a VG Escalab 210 system with an aluminum anode (AlKα= 1486.6 eV) operating at 150 W with a background pressure of 5×10^{-9} mbar. The low-resolution survey scans were taken with a 1 eV step and 50 eV analyzer pass energy; and high-resolution spectra were taken with a 0.1 eV step and 50 eV analyzer pass energy. The angle between X-ray beam and the surface normal was kept at 0 ° and the depth of analysis was practically 10 nm. The atomic ratio of oxygen-to-carbon (O/C) was calculated from their normalized peak areas as:

$$\frac{O}{C} = \frac{I_O}{I_C} \times \frac{S_C}{S_O} \quad \text{(Eq. 4.1)}$$

where I_O and I_C are the normalized integrated area of the peaks for oxygen and carbon, respectively S_C/S_O is the corrected term for the sensitivity factor.

4.2.2.5 ATR-FTIR

About 50 ml nanocellulose suspension was dropped into petri dish (with the diameter of 55 mm). Then, the suspension was dried in vacuum oven at 60 ℃. A thin

nanocellulose film was obtained after drying. Test samples were taken randomly from the film and placed flat on the crystal surface. ATR-FTIR spectroscopy was performed on a PerkinElmer ATR-FTIR spectrometer equipped with 3× bounce diamond crystal and an incident angle of 45 ° (to make sure that the wave can penetrate into the nanocellulose). A total of 16 scans (which can reduce the testing time without affect the accuracy of spectra) were accumulated for each spectrum. Spectra were recorded at a nominal resolution of 4 cm^{-1}, and in order to reveal much more details the spectra were recorded in a full range (i.e. from 4000 to 650 cm^{-1}).

4.2.2.6 XRD

Hemp yarn and nanocellulose were subjected to a powder X-ray diffraction method analysis (PXRD) respectively. For this analysis, a D8 advanced Bruker AXS diffractometer, Cu point focus source, graphite monochromator and 2D-area detector GADDS system were used. The diffracted intensity of CuKα radiation (wavelength of 0.1542 nm) was recorded between 5° and 40° (2θ angle range, this is the normal range for natural fibre crystallinity analysis with XRD) at 40 kV and 40 mA. Samples were analyzed in transmission mode. The CI was evaluated by using Segal et al. empirical method [463] as follows:

$$CI\% = \frac{(I_{002} - I_{am})}{I_{002}} \times 100 \quad \text{(Eq. 4.2)}$$

where I_{002} is the maximum intensity of diffraction of the (002) lattice peak at a 2θ angle of between 21° and 23°, which represents both crystalline and amorphous materials. I_{am} is the intensity of diffraction of the amorphous material, which is taken at a 2θ angle between 18° and 20° where the intensity is at a minimum. It should be noted that the crystallinity index is useful only on a comparison basis as it is used to indicate the order of crystallinity rather than the crystallinity of crystalline regions. 10 replicates were used.

4.2.2.7 DSC

Differential scanning calorimetry (DSC) measurements were performed using a DSC 6000 modulated differential scanning calorimeter from Pekin-Elmer. Samples (around 6 mg, for this instrument the weight of sample between 5-10 mg was preferred [464]) was heated from 30 to 400 °C (in this chapter we focused on investigating the dehydration process of nanocellulose and the raw fibres, and the maximum temperature for this process was 400 °C) at a normal heating rate of 10 °C min^{-1} under nitrogen atmosphere (the purity is 99.9999%, and the gas input rate was 30 ml min^{-1} (which is the default value)).

4.3 Results and discussion

4.3.1 Size distribution and morphologies of nanocellulose
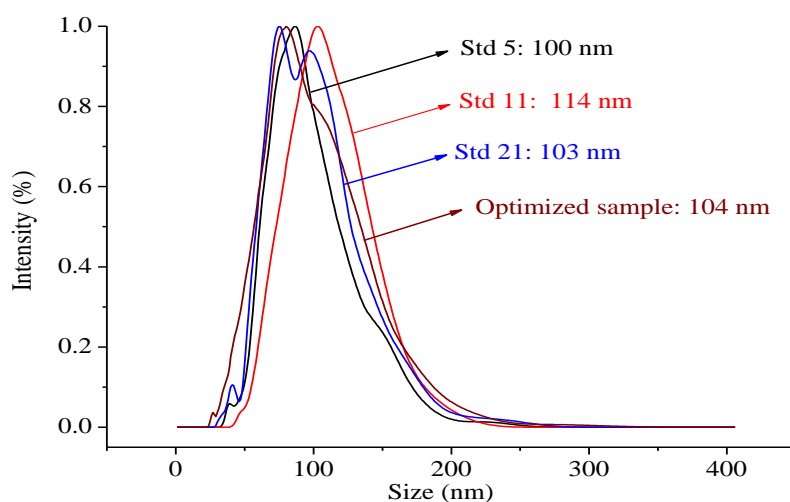
Fig.4.1 Number size distribution from NTA video of nanocellulose (std5, std11, std21 and optimized sample).

(a)   (b)
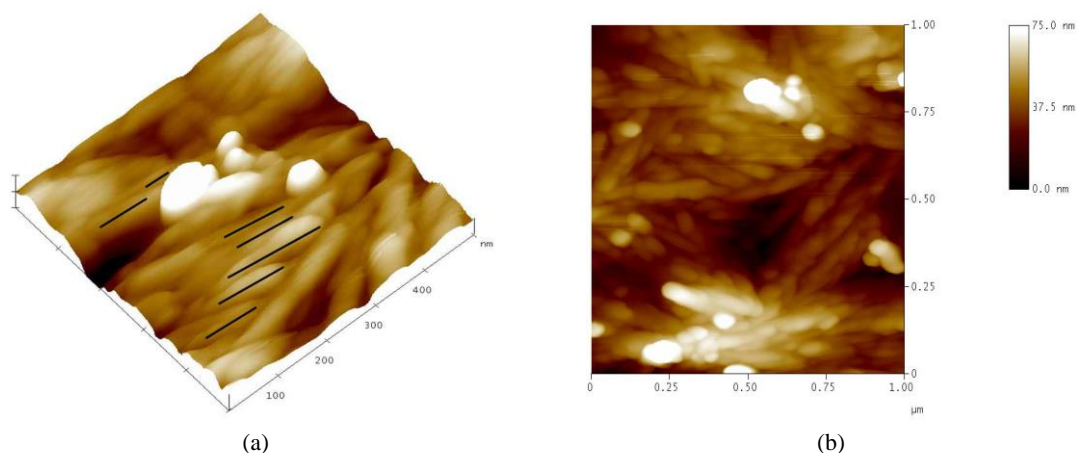
Fig. 4.2 AFM morphology of nanocellulose: (a) 3D image and (b) height image.

We selected three samples randomly for the NTA from the RSM experiment which have been described in chapter 3 to compare with the sample which was fabricated under the optimized conditions. The results of NTA are shown in Fig. 4.1. According to the NTA, the size range of nanocellulose for std5, std11, std21 and the optimized sample, respectively, is 31-281 nm, 38-278 nm, 29-321 nm and 23-405 nm respectively, and the average size of nanocellulose for std5, std11, std21 and optimized samples is 100 nm, 112 nm, 103 nm, and 104 nm respectively. Compared with the acid hydrolysis [269], nanocellulose fabricated by oxidation- sonication shows wider size range and higher average size. Nevertheless, the NTA results demonstrated that oxidation-sonication can also fabricate nano-scale cellulose. The yields of nanocellulose for std5, std11 and std21 as shown in Table 3.3 are 10.72%, 34.31% and 42.02% respectively. Nanocellulose from optimized sample was further characterized by AFM (Fig. 4.2) and FEG-SEM (Fig. 4.3). AFM images of nanocellulose show a slight difference from FEG-SEM, as illustrated in Fig. 4.2, where not only particles can be observed in these images but also rod like of fibril can

be found. This may be due to the difference of preparation of samples. Moreover, by using ImageTool software measure, we found that the average aspect ratio of nanocellulose was 4 which far less than that of acid method or mechanical method. According to FEG-SEM characterization (Fig. 4.3), the size of nanocellulose ranges from 45.45 to 168 nm.

(a)   (b)

(c)   (d)
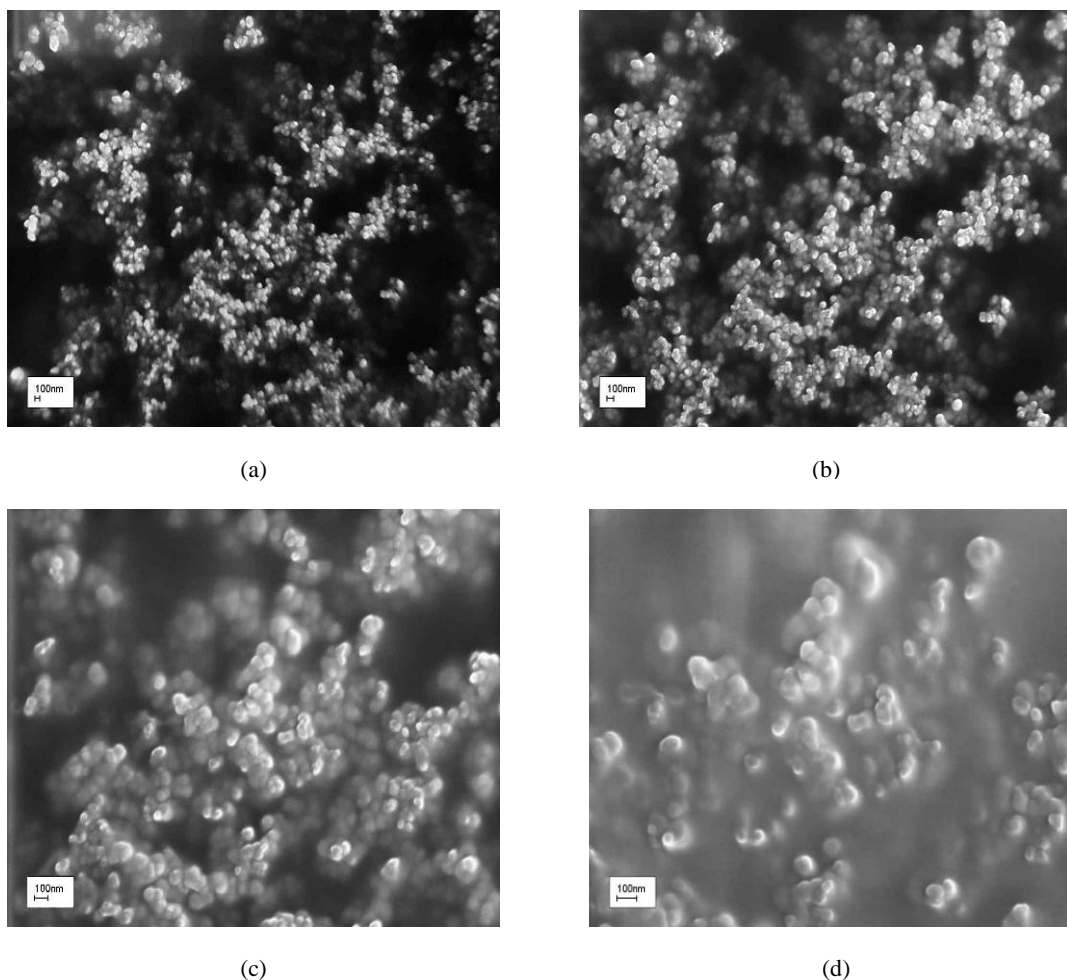
Fig. 4.3 FEG-SEM morphology of nanocellulose particles at different magnification: (a), ×40 000; (b), ×50 000; (c), ×100 000; (d), ×150 000.

4.3.2 Chemical structure and crystalline of nanocellulose

4.3.2.1 XPS analysis of nanocellulose

X-ray photoelectron spectroscopy (XPS) is a quantitative spectroscopic technique that measures the elemental composition. It is a useful surface chemical analysis technique that can be used to analyze the surface chemistry of a material in its "as received" state. This powerful tool has been widely used to investigate natural fibres, cellulose and nanocellulose, which focuses on the chemical changes resulting from the surface modification [465-469]. A detailed analysis of the oxygen (O ls) peak is generally less useful. Thus, quantitative data on the surface chemical composition are mainly

obtained from the O/C atomic ratio and the relative amount of each type of carbon (C 1s).

Name	Pos.	At %
O1s	531.855	50.41
C1s	284.855	49.59
O1s	531.987	45.24
C1s	284.987	54.76
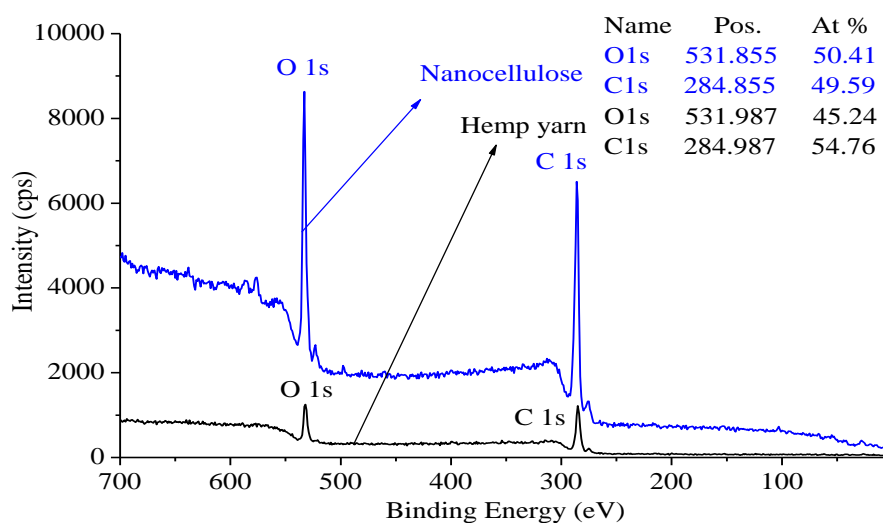
Fig. 4.4 XPS wide scans from hemp yarns and nanocellulose.
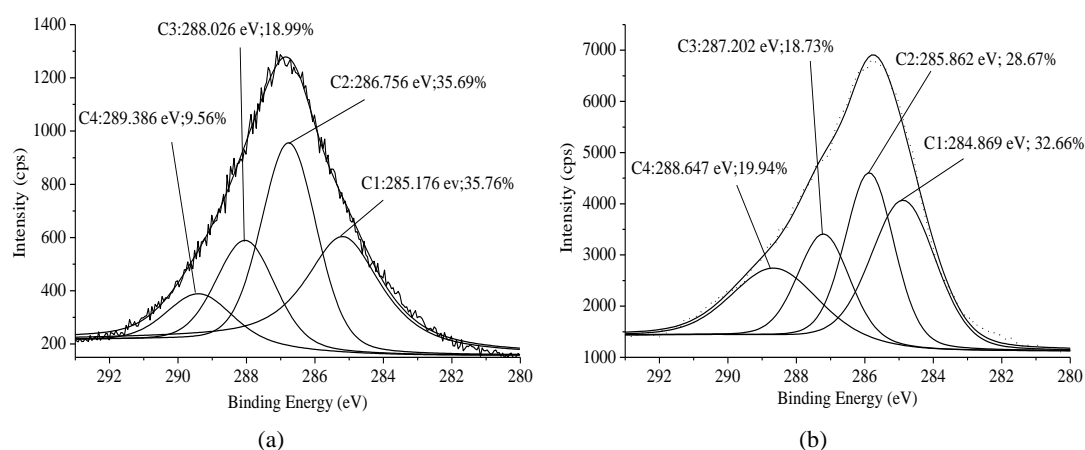
Fig. 4.5 C1s XPS spectra for hemp yarns (a) and for nanocellulose (b).

The wide scan XPS spectra of hemp yarn and nanocellulose are presented in Fig. 4.4. As expected, the main elements detected are carbon and oxygen. Using area sensitivity factors, the oxygen-to-carbon (O/C) atomic ratio was calculated as an initial indication of surface oxidation. As shown in the Fig. 4.4, the O/C atomic ratio of hemp yarn measured by XPS is 0.826, which is very close to the theoretical O/C value of 0.83 based on the formula of cellulose. It is interesting to note that oxidation/ sonication treatment leads to a significant increase in the O/C atomic ratio (1.017) which is due to the oxidation of cellulose during the process of hydrolysis. Additionally, chemical shifts for C 1s and O 1s can be observed in the XPS spectra. The binding energy for hemp yarn in C 1s and O 1s are 284.987 eV and 531.987 eV, respectively. Nevertheless, the binding energy of C 1s and O 1s shift to lower value, which are 284.855 eV and 531.855 eV respectively. This may be due to the increase of hydrogen bonding in the nanocellulose.

To obtain more detailed information, a high-resolution scan is conducted on the C 1s. The C1s XPS spectra shown in Fig. 4.4 for hemp yarn and nanocellulose are deconvoluted into four peaks in Fig. 4.5(a) and 4.5(b), respectively. In cellulosic materials, four categories of carbon bonds can be identified by XPS: C1 carbons bonded to other carbons or hydrogen (C–C, C–H); C2 carbons bonded to one oxygen atom (C–O); C3 carbons attached to two oxygen atoms or a carbonyl group (C=O, O–C–O) and C4 carbons from carboxyl groups (O-C=O) [470]. Fig. 4.5 shows two main differences between hemp yarn and nanocellulose. These differences can be described as follows:

i. The binding energy is different, the binding energy of hemp yarn for C1, C2, C3 and C4 are 285.176 eV, 286.756 eV, 288.026 eV and 289.386 eV, respectively; while for nanocellulose, these bonds binding energy have a slight decrease with the value being 284.869 eV, 285.862 eV, 287.202 eV and 288.647 eV respectively. This can be ascribed to the oxidation of hydroxyl in the cellulose chain, which results in the formation of carboxyl groups in the cellulose chain. The carboxyl groups can form hydrogen bonds which can reduce the binding energy of carbon bonds with the hydroxyl groups [471].

ii. Contribution of each carbon bond is different: the contribution of C1, C2, C3 and C4 in hemp yarn are 35.76 %, 35.69 %, 18.99 %, 9.56 %, respectively; while for the nanocellulose, the contribution of C1, C2, C3 and C4 are 32.66 %, 28.67 %, 18.73 %, 19.94 %. For nanocellulose, the significant decrease of C2 (C-O) and significant increase of C4 (O-C=O) indicates that parts of the hydroxyl groups in cellulose chains are oxidized into carboxyl groups during the oxidation/sonication process.

4.3.2.2 ATR-FTIR analysis nanocellulose
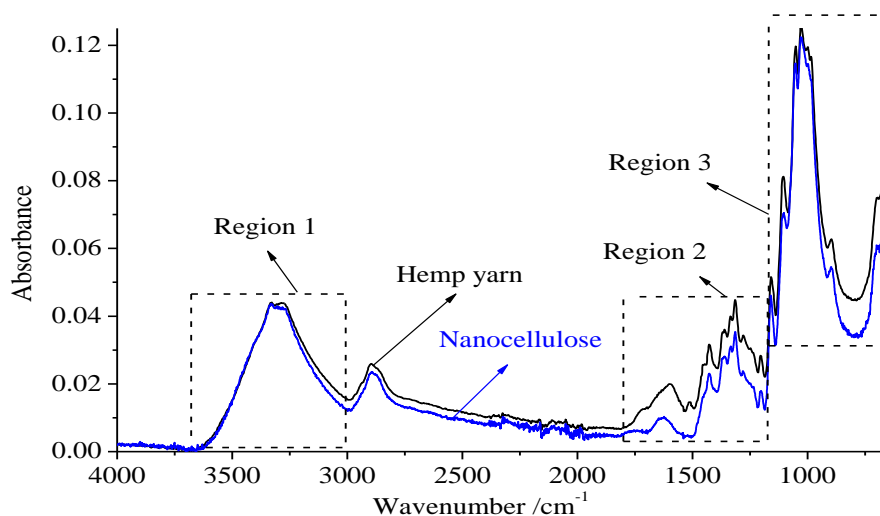
Fig. 4.6 ATR-FTIR spectra of hemp yarns and nanocellulose.

Fig. 4.6 shows the ATR-FTIR spectra of hemp yarns and nanocellulose fabricated with oxidation/sonication from 4000 to 650 cm^{-1}. The peak positions of the major ATR-FIIR bands for both of them are summarized and compared in Table 4.3. The decreasing absorbance can be observed from the ATR-FTIR spectrum of nanocellulose. In order to investigate the position of oxidation in cellulose and confirm the removal of impurity, hemicellulose and lignin, three regions (region1, region 2 and region 3) in the spectra were discussed.

Table 4. 3 Band characteristics of ATR-FTIR spectra related to hemp yarns and nanocellulose

Wavenumber (cm^{-1}) range of peak		$\Delta \upsilon$ (cm^{-1})	Assignment	Sources
Hemp yarn	Nanocellulose			
3336	3330	-6	OH stretching	Cellulose, Hemicellulose [472, 473]
2896	2892	-4	C–H symmetrical stretching	Cellulose, Hemicellulose [473, 474]
1722	Disappear	-	C=O stretching vibration	Pectin, Waxes, Hemicellulose [475-478]
1645	1651	6	C=O stretching vibration	Lignin [479]; Oxycellulose [480]
1613	1623	10	OH bending of absorbed water	Water [481]
1587	1598	-	Aromatic skeletal vibrations (from hemp yarn); C=O stretching (from nanocellulose)	Lignin [482, 483]; Oxycellulose [480]
1508	Disappear	-	C=C aromatic symmetrical stretching	Lignin [482, 483]
1455	1449	-6	OH plane deformation vibration	Cellulose [484]
1427	1428	1	HCH and OCH in-plane bending vibration	Cellulose [472, 473, 485-488]
1368, 1361	1371, 1362	3, 1	In-the-plane CH bending	Cellulose, Hemicellulose [473, 483, 489]
1335	1334	-	S ring stretching (for hemp yarn); OH plane deformation vibration (from nanocellulose)	Lignin [483, 490], Cellulose [484]
1315	1315	0	CH$_2$ rocking vibration at C6	Cellulose [131, 481, 486]
1279	1281	2	CH$_2$ deformation	Cellulose, Hemicellulose [484]
1248	1248	-	C-C plus C-O plus C=O stretch; G condensed > Getherfied	Lignin-carbohydrate Complex [479], Cellulose [484]

Table 4.3 Continued

1236	1235	-1	COH bending at C6	Cellulose [482, 486]
1204	1202	-2	C-O-C symmetric stretching, OH plane deformation	Cellulose, Hemicellulose [481, 491]
1159	1160	-1	C-O-C asymmetrical stretching	Cellulose, Hemicellulose [472, 481, 490]
1105	1103	-2	Ring asymmetric valence vibration	Cellulose [484]
1051	1053	2	C-C, C-OH, C-H ring and side group vibrations	Cellulose, Hemicellulose [481, 482, 492]
1028	1029	1	C-C, C-OH, C-H ring and side group vibrations	C-C, C-OH, C-H ring and side group vibrations [131, 481, 490, 492]
999,984	998, disappear	-1, -	C-C, C-OH, C-H ring and side group vibrations	Cellulose, Hemicellulose [131, 481]
896	898	2	COC,CCO and CCH deformation and stretching	Cellulose [472, 481, 486, 488]
696	696	0	Rocking vibration CH_2	Cellulose [490]
660	663	3	C-OH out-of-plane bending	Cellulose [473, 490]
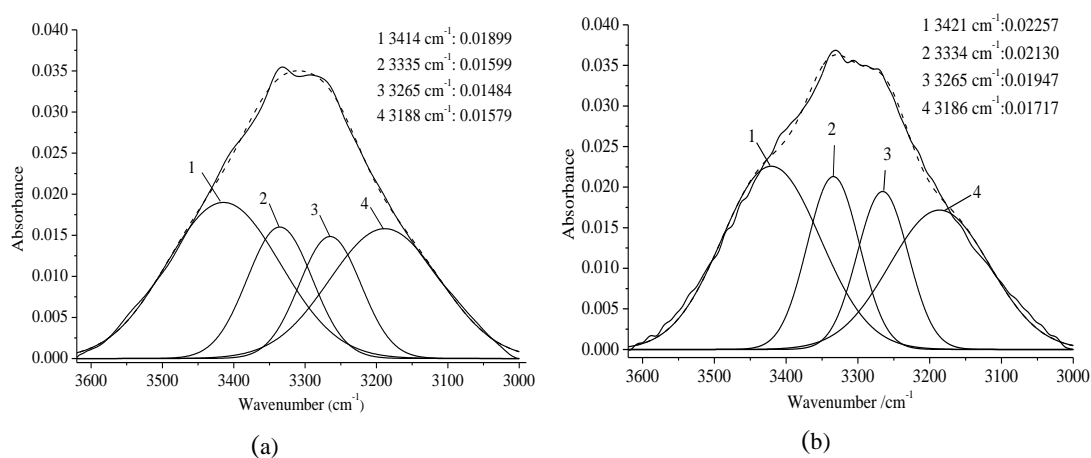
Fig. 4.7 Deconvolved ATR-FTIR spectra from 3620 to 2990 cm^{-1} for hemp yarns (a) nanocellulose (b). (Solid curves= experimental data; dashed curves=calculated data).

A hydrogen bond is the attractive interaction of a hydrogen atom with an electronegative atom, such as nitrogen, oxygen or fluorine, that comes from another molecule or chemical group [493]. It is well known that cellulose is a liner polymer of 1-4 linked β-D-glucose. Hydroxyl groups in the C2, C3 and C6 of cellulose contribute to the formation of various kinds of inter- and intra-molecular hydrogen bonds. For cellulose, the intra-molecular hydrogen bonds include O(2)H---O(6) [494] O(3)H---O(5) [494, 495] and intermolecular hydrogen bond includes O(6)H---O(3`) [494-496] (see Fig. 4.7(a) and 4.7(b)). The IR spectra for the hydrogen bonds in

cellulose appears from 3500 cm^{-1} to 2990 cm^{-1} [495-497]. The IR absorption bands in region 1 in Fig. 4.6 for hemp yarn and nanocellulose were deconvolved into four bands for a curve fitting as shown in Fig. 4.7(a) and 4.7(b). We can conclude from Fig. 4.7 that: (i) the peak position for the hydrogen bonds in nanocellulose shifted to lower wavenumber, excluded peak 1; and (ii) the peak intensity for each hydrogen bond in nanocellulose was higher than that in hemp yarn. Compared with hemp yarn, the value of absorbance increased 18.85 %, 33.21 %, 31.20% and 8.74%, respectively. It indicates the increase of hydrogen bonding in nanocellulose for both of inter- and intra-hydrogen bonds. This may be ascribed to the oxidation of hydroxyl in C2, C3 and C6 on the chains of nanocellulose. Much more details in 1800 and 660 cm^{-1} for hemp yarn and nanocellulose are shown in Fig. 4.8(a) and 4.8(b).

(a)   (b)
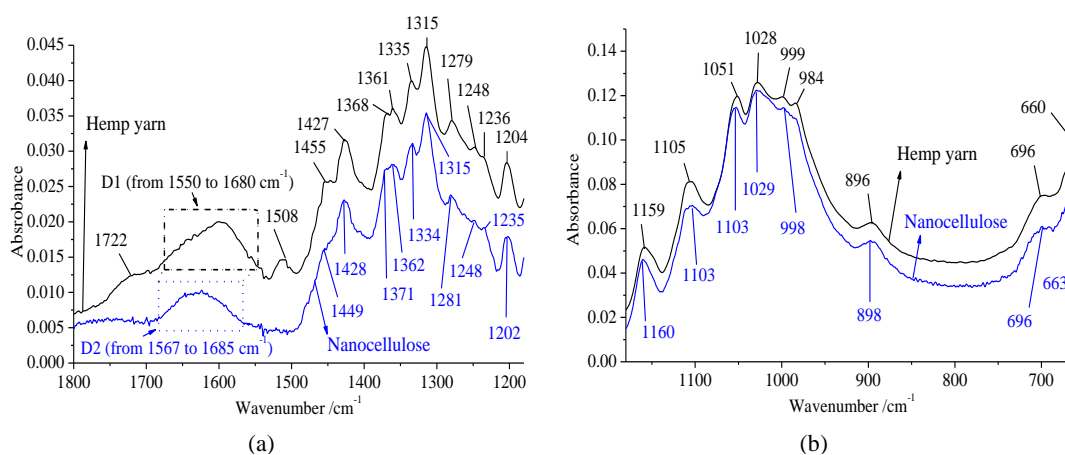
Fig. 4.8 ATR-FTIR spectra of hemp yarns and nanocellulose from 1800 to 1180 cm^{-1} (a); and (b) to from 1180 to 660 cm^{-1}.

(a)   (b)
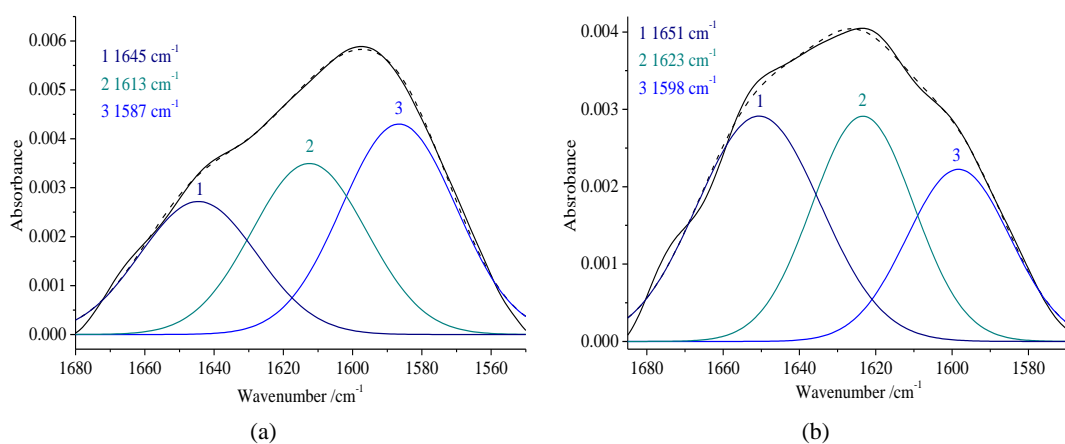
Fig. 4.9 Deconvolved ATR-FTIR spectra from 1680 to 1550 cm^{-1} for hemp yarns (a) and 1685 to 1567 cm^{-1} for nanocellulose (b). (Solid curves= experimental data; dashed curves=calculated data).

The disappearance of peak at 1722 cm^{-1} and 1508 cm^{-1} was observed in the spectrum of nanocellulose. This indicates that most of the hemicelluloses and lignin have been extracted during the hydrolysis process. The band at 1722 cm^{-1} assigned as the C=O stretching vibration which may be contributed from pectin, waxes, hemicellulose; and

72

the band at 1508 cm^{-1} is assigned as C=C aromatic symmetrical stretching which is contributed from lignin. Therefore, the disappearance of both bands indicates that most of the pectin, waxes, hemicelluloses and lignin are extracted during the hydrolysis process. The lower absorbance at 1315 cm^{-1} in nanocellulose has been observed in Fig. 4.8(a), which indicates that hydroxyl at C6 may be oxidized during the process of hydrolysis. This oxidation gave rise to an improvement of hydrophilicity of nanocellulose. It was observed in Fig. 4.8(b) that the peak band at 984 cm^{-1} disappeared with the nanocellulose which may be ascribed to the loss of C-OH vibration. In order to better understand the difference between nanocellulose and its raw material, the region D1 and region D2 in Fig. 4.8 were deconvolved into three bands for a curve fitting as shown in Fig. 4.9(a) and 4.9(b), respectively. The deconvolution reveals that the three peaks for hemp yarns appear at 1645 cm^{-1}, 1613 cm^{-1} and 1587 cm^{-1}. For nanocellulose, they appeared at 1651 cm^{-1}, 1623 cm^{-1} and 1598 cm^{-1}. Generally, band at 1645 cm^{-1} is assigned as C=O stretching vibration, band at 1587 cm^{-1} is assigned as aromatic skeletal vibrations. For hemp yarn, both of them may be contributed from lignin, but for nanocellulose both of them may be contributed from C=O stretching. It should be noted that, similar phenomenon appears at 1335 cm^{-1}. For hemp yarn, this band can be assigned as S ring stretching, but for nanocellulose it is assigned as OH plane deformation vibration.

4.3.2.3 XRD analysis of nanocellulose

In order to analyze the crystallinity of hemp yarns and nanocellulose, in this chapter, X-ray powder diffraction was carried out. The XRD spectra of hemp yarns and nanocellulose are given in Fig. 4.10. It can be seen from Fig. 4.10 that the major crystalline peak of the hemp yarn and nanocellulose occurred at 2θ=22.977° and 2θ=22.846° respectively, which represents the cellulose crystallographic plane (002, Bragg reflection). The minimum intensity between 002 and 110 peaks (I_{am}) for hemp yarn and nanocellulose is at 2θ=18.8588° and 2θ=19.4458° respectively. The CI of
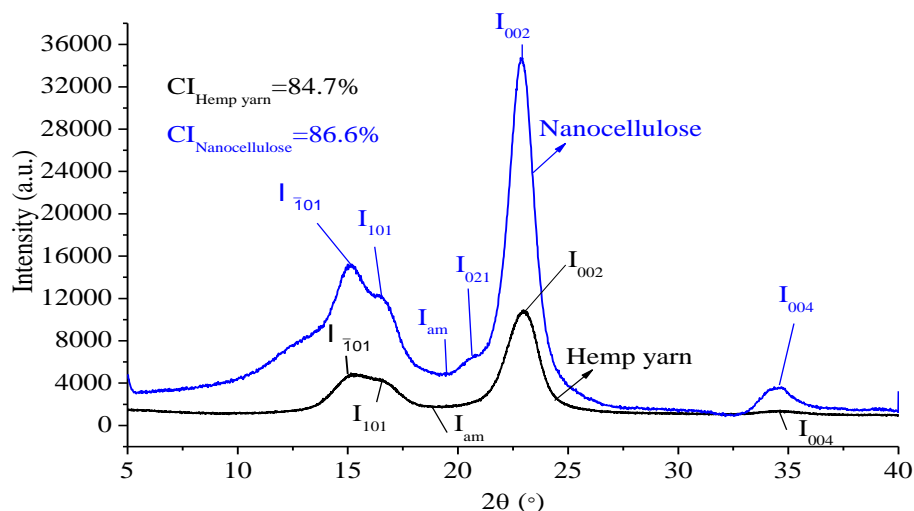
Fig. 4.10 X-ray diffractogram of hemp yarns and nanocellulose.

hemp yarn is 84.7 %. Other well-defined peaks present on the X-ray diffractogram of hemp yarn are at 2θ=15.2267°, 2θ=16.6667° and 2θ=34.6163°, while those of nanocellulose are at 2θ= 15.1809°, 2θ=16.4387°, and 2θ=34.5599, respectively. These reflections correspond with the ($\bar{1}$01), (101) and (004) crystallographic planes, respectively. The results of CI determined for hemp yarn and nanocellulose are given in Table 4.4 which shows the CI of hemp yarns and nanocellulose are 84.66 % and 86.59 % respectively. For nanocellulose, the higher CI may be due to the removal of hemicellulose and lignin. Compared with the previous reports [266, 271], the increase of the CI for nanocellulose seems insignificant, but this result confirms that oxidation/sonication could be used to fabricate nano-scale cellulose without damage the crystalline structure of cellulose.

Table 4. 4 Results of CI of hemp yarns and nanocellulose determined by XRD

Samples	2θ (°)		Intensity (a.u)		CI (%)
	I_{am}	I_{002}	I_{am}	I_{002}	
Hemp yarn	18.8588	22.977	1673	10909	84.66
Nanocellulose	19.4458	22.846	4658	34748	86.59

4.3.3 Thermal property of nanocellulose

Cellulose can be classified as a polymer of moderate thermal stability. Thermal degradation of cellulose in a dry, inert atmosphere is considered to proceed mainly by two chemical processes: (i) splitting off of water along the cellulose chain forming dehydrocellulose and leading to occasional chain scission, but maintaining in principle the β-1,4-polysaccharide skeleton (25-400 °C); and (ii) pyrolytic fragmentation leading to aromatized entities and finally most probably to a highly crosslinked carbon skeleton (400-700 °C) [124]. During the dehydration process, cellulose undergoes three main processes: (i) evaporation of bound water (from room temperature to 150 °C); (ii) elimination of water on the chain of cellulose (from 150 to 240 °C); and (3) the break of glucosidic bond (from 240 °C to 400 °C) [124].

The present work employs DSC to investigate the thermal behaviour of nanocellulose by comparing with hemp yarn. The DSC results are recorded in Fig. 4.11. Hemp yarn, as shown in Fig. 4.11, shows two sharp endothermic peaks at 119.3 °C (which corresponding to the water evaporation), and 361.4 °C (which corresponding to the fusion of its crystalline part), respectively. However, compared with hemp yarn, the nanocellulose shows very different ways: the first peak is endothermic peak and appears at 124.9 °C, while the second peak is exothermic peak and appears at 367.5 °C. It indicates that nanocellulose has lower carbonization temperature. This result is in agreement with the previous works [498, 499]. It has been reported that the activation energies of the degradation of nanocelluloses which were fabricated via sulphuric acid hydrolysis were significantly lower than raw material due to the introduction of sulfate groups via sulfuric acid hydrolysis [500]. Furthermore, the high surface area of nanocellulose might play an important role in diminishing their

thermostability due to the increased exposure surface area to heat [498] or the increase of active groups [501]. Moreover, the nanocellulose has been reported to function as efficient pathways for phonons, leading to their higher thermal conductivity [501]. The better thermal conductivity of nanocellulose might be ascribed to smaller phonon scattering in the bundle of crystallized cellulose chains in the nanocellulose than the amorphous random chains in cellulose powder

.
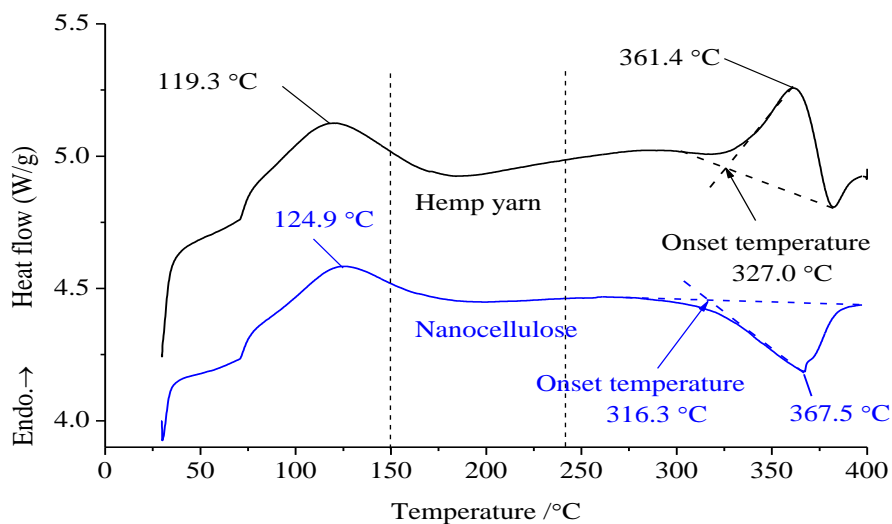
Fig. 4.11 DSC curves of hemp yarn and nanocellulose.

4.4 Interim Conclusions

This chapter systematically investigated the characterization of nanocellulose which was fabricated from hemp yarn with a novel fabrication method---oxidation/ sonication developed in this study. Three main characteristics of the oxidation/sonication fabricated nanocellulose, namely, size distribution and morphologies, chemical structure and crystalline, and thermal properties, were characterized with various analytical instruments. Outcomes of the study can be concluded as follows:

(1) NTA results disclosed that oxidation/sonication method was able to fabricate nano-scale cellulose which was evidenced by the morphologies characterization with AFM and FEG-SEM. Morphologies analysis revealed that nanocellulose fabricated by oxidation/sonication had a low aspect ratio value (only 4) far less than that of acid method or mechanical method,

(2) XPS results showed the main elements for both hemp yarns and cellulose were carbon and oxygen. The oxygen-to-carbon (O/C) atomic ratio which calculated from the XPS wide scan spectra of hemp yarns and nanocellulose were 0.826 and 1.017, respectively. This may be due to the oxidation of cellulose during the process of hydrolysis. Further analysis with deconvolution method in C1s identified the same four categories of carbon bonds for both of hemp yarns and nanocellulose. The binding energy and the contribution of these four bonds of nanocellulose displayed differences. These differences confirmed uniformly that hydroxyl groups in cellulose are oxidized into carboxyl groups during the oxidation/sonication process. The chemical structure of nanocellulose was further characterized by ATR-FTIR. ATR-FTIR results showed that parts of hydroxyl group in C2, C3 and C6 were during the process. XRD showed that the CI for hemp yarn and nanocellulose was 84.66 % and 86.59 %, respectively. The slight increase may be due to the removal of hemicellulose and lignin, but in the other hand, it indicated that oxidation/sonication was able to produce the nanocellulose without the damage of crystalline.

(3) DSC results showed that nanocellulose had lower carbonization temperature and thermostability.

Chapter 5 Modification of Hemp Fibres with Nanocellulose

5.1 Introduction

Cellulose is one of the most abundant materials in the world. With an increase in environmental awareness in the past few decades, exploiting cellulose has arose much interest and become of importance. Natural fibres which are rich in cellulose have been attracting great attentions. Compared with glass fibre-based composites, natural fibre-based bio-composites display several excellent advantages, e.g. low density, renewability and low cost. Bio-composites made from natural fibres have been widely used for automotive materials [502] and building materials [503, 504], and many corresponding manufacturing technologies have been reported, such as for the production of composites [134, 222-224, 505] and for fibres extraction from bamboo [506], banana [507], coir [508], flax [509], hemp [510], jute [511], kenaf [512], ramie [513], sisal [514] and wood [515]. However, these natural fibres display their drawbacks (e.g. high polarity and hydrophilicity) which make the natural fibres poorly compatible with polymer and result in loss of mechanical properties of natural fibre based materials upon their atmospheric moisture adsorption [516]. Various treatments (e.g. physical treatments, chemical treatments, biological treatments) on the natural fibres have been investigated widely by researcher.

New technologies (e.g. nanotechnology, biological technology) have also recently been employed by researchers to modify natural fibres and the treatment technique can be grouped into three approaches, namely, (1) soaking; (2) layer-by-layer deposition and (3) sonochemical deposition. These approaches were mainly developed to immobilize nanoparticles on the surface of natural fibres which were used for textile in the finishing process. The nanotechnology-based finish techniques give rise to new properties, e.g. anti-bacteria [517-519], self-cleaning [520-522], water repellent [523-525] and UV light blocking [197, 526, 527] to the natural fibres and enhance the performance of final clothing product. In 2006, Gulati et al [528] for the first time employed the biological technology to modify natural fibres. The hemp fibres treated with fungus *Ophiostoma ulmi* showed the improved acid–base characteristics and resistance to moisture. Furthermore, the flexural strength and flexural modulus of the modified hemp fibres-polyester composites were improved by 21 % and 12 %, respectively. Bismarch et al [529, 530] used the bacteria Gluconacetobacter xylinus strain BPR 2001 to modify natural fibres (hemp fibres and sisal fibres). By using biological technology, the nanosized bacterial cellulose has been deposited around natural fibres, and such the adhesion of fibres to renewable polymers improved.

In this chapter, we firstly aim to characterize of natural fibres (hemp) with systematic method. Secondly, we will employ FTIR to study the deformations in the fibres. Thirdly, we will employ the nanotechnology to modify natural hemp fibres. The

nanocellulose fabricated by oxidation/sonication will be used as "coupling agent" to treat the natural fibres. Much attention will be paid to the mechanical properties and interfacial properties of the modified natural fibres. Energy dispersive X-ray (EDX), FEG-SEM and XRD are used to study the mechanism of tensile strength increase of the fibres with nanocellulose modification. XPS and ATR-FTIR will be used to investigate the surface properties of natural fibres coated with unsaturated polyester with the aim to study the mechanism of interface structure and improvement upon nanocellulose modification.

5.2 Materials and Methods

5.2.1 Materials

Hemp yarns were obtained from Shanxi Greenland Textile Ltd. Hemp fibres were supplied by a Hemp Farm & Fibre Company Ltd, UK. Dodecyltrimethylammonium bromide (DTAB), ethylene diamine tetraacetic acid (EDTA), copper nitrate (II), cobalt chloride (II), sodium hydroxide, sodium hypochlorite and sodium sulfide were supplied by Sigma-Aldrich. Unsaturated polyester was obtained from CFS Ltd. The cement was provided by HMG Plaints Ltd.

5.2.2 Microfibril angle (MFA) measurement

Hemp fibres (0.1 g) were placed into two beakers which contained 100 ml copper nitrate (II) and cobalt chloride (II) solution (5%, wt/vol), respectively. These beaker containers were placed into ultrasonic bath and treated at 80 °C for 2h without ultrasonic treatment at first. They were then treated with ultrasonic treatment at the some temperature for 2h. The treated hemp fibres were then finally washed with distilled water. Photomicrographs were obtained by using BX51 Reflected Light Microscope equipped with a CAM-XC50-5MP cooled CCD camera, then used UTHSCSA ImageTool software to measure the microfibril angle of S1 and S2 layers. 50 test pieces were used. The MFA on the fracture part of hemp fibres was firstly objected with optical microscopy (OM); UTHSCSA ImageTool software was then used to measure the MFA.

5.2.3 DTAB-Nanocellulose modification

As one kind of cationic surfactant, dodecyltrimethylammonium bromide (DTAB) is always used as in dyeing baths as solubilizer for anionic dye [531, 532], because this surfactant can be adsorbed by cellulose due to the hydration [533] and form ion pair with anionic dye by coulomb attraction [534]. Recently, Blomstedt et al [535] employed DTAB and carboxymethyl cellulose (CMC) to modify softwood pulp and found that this treatment markedly increased the internal and tensile strengths of the handsheets. Cellulose like CMC is a polysaccharide made of monomeric glucose residues connected by β(1-4)glycosidic linkages [536]. Moreover, the surface of

nanocellulose exhibits high density of hydroxyl groups [69], when nanocellulose dispersed in the water which result in the much more negative charge on the nanocellulose surface than CMC. Therefore, in this chapter, we employed DTAB to pretreat hemp fibres. This pretreatment introduced the cation into the surface of hemp fibres. Then we used nanocellulose to modify the pretreated hemp fibres. This modification was carried out in two steps:

(i) DTAB pretreatment

The cationization of fibres process always carried out under alkaline condition with a little amount cationic reagent [537]. In order to investigate the effect of pH value of solution and the dosage of DTAB, the DTAB pretreatments were designed as Table 5.1.

Table 5. 1 Experimental levels of the independent variables

Experiments	pH	Dosage of DTAB (%)
D1	10	0.05
D2	10	0.1
D3	10	0.15
D4	11	0.05
D5	11	0.1
D6	11	0.15
D7	12	0.05
D8	12	0.1
D9	12	0.15

Hemp fibres (1 g) were soaked in beaker (50 ml) which contained 30 ml DTAB solution with various dosages of DTAB (0.05 %, 0.1 % and 0.15 % (on the weight of dried fibres)) under various pH values (10, 11 and 12). The beaker was then loosely covered with a glass and supported in an ultrasonic bath at 60 ℃ for 1 hour (this condition suitable for the natural fibre treatment under alkaline condition [535]). Then the hemp fibres were wished with distilled water.

(ii) Nanocellulose modification

After DTAB pretreatments, the modified hemp fibres (P1) were soaked in beaker (30 ml) which contained 2 % nanocellulose suspension at 25 ℃ for 10 min. Then, the nanocellulose modified hemp fibres were dried with vacuum oven at 70 ℃ for 24h. Then, the dried fibres were conditioned at 20±2 °C and 65±2 % relative humidity before testing.

5.2.4 Tensile test

Each conditioned individual fibre (from M2) was temporarily fixed on the mounting

card (Fig. 5.1(a)) by adhesive tape. Then a droplet of cement (HMG Plaint Ltd) was applied on the edge of both sides of the hole along the length of card. The whole set-up was then fixed on Instron 5566 for tensile strength testing. The mounting card was cut along the line as shown in Fig. 5.1(b). Finally, run Intron (the crosshead speed was of 3 mm min^{-1}). About 20 samples from untreatment, DTAB pretreatment and two-step modification were tested respectively.
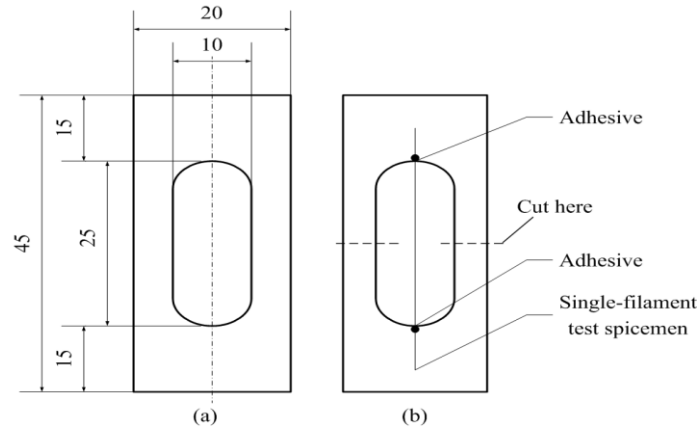
Fig. 5.1 Set-up of single fibre test: (a) specimen mounting card (dimensions in mm); (b) test specimen mounted on the mounting card.

5.2.5 EDX analysis

In order to investigate the effect of deformation on the two-step modification, we design an experiment base on the EDX technique. EDX is a useful analytical technique to analyze the material surface by element analysis [538]. In the two-step modification, we use DTAB to pretreat hemp fibres. Obviously, the absorption of cationic reagent on the fibres will in favour of the absorption of anionic nanocellulose on the fibre. Nanocellulose has high mechanical properties [444] and high density of hydroxyl groups [69], therefore, the more nanocellulose absorbed on the hemp fibres, the stronger hemp fibres will be obtained. The same element between the hemp fibres and DTAB is carbon, but the carbon ratios in both of them are different. As we know, the linear formula of DTAB is $CH_3(CH_2)_{11}N(CH_3)_3Br$ [539]; the molecular weight of DTAB is 308.34 [539]; and the atomic weight of carbon is 12.011 [540]. Therefore in the DTAB, the carbon ratio (by weight) is 58.43 %. The average carbon ratios which are determined by EDX in the deformations and without deformation region in R2 are 49.43 % and 48.88 %, respectively. The absorption ratios of DTAB on the region without deformations and with deformation were evaluated by Eqs. 5.1 and 5.2, respectively:

$$A_{ud} = \frac{C_{ud} - 48.88}{58.43 - 48.88} \qquad \text{(Eq. 5.1)}$$

$$A_d = \frac{C_d - 49.43}{58.43 - 49.43} \qquad \text{(Eq. 5.2)}$$

where A_{ud} is the absorption ratio of DTAB in the region without deformations, C_{ud} is the carbon ratio in the region without deformations; A_d is the absorption ratio of DTAB in the region with deformations, and C_d is the carbon ratio in the region with deformations.

The EDX were performed with Zeiss Supra 35 VP FEG-SEM which was coupled to an EDX INCA 400 system (Oxford Instruments GmbH, UK). The fibre was firstly observed with FEG-SEM. Then the surfaces of sample in the region of deformation or without deformation were selected for element measure respectively. The acceleration voltages for EDX measurement was 7 KV which was in the recommended range of 5 to 10 kV for analysis. For quantitative element analyses, the recorded EDX results were analyzed by using Oxford INCA Version 4.02.

5.2.6 Resin adsorption measurements

Unsaturated polyester which was ordered from CFS Ltd was diluted with styrene until the volatile content was 95%. Then, hemp fibres (0.5 mg) with various treatments (without modification; DTAB pretreatment; two-step modification) were respectively immersed in 20 ml of diluted unsaturated polyester in a glass bottle. 2 % (on the weight of polyester) of catalyst was then added to the bottle. After degassing with ultrasonic bath for 5 min, the temperature was raised from 25 ℃ to 80 ℃. These compounds were treated for 15 min at 80 ℃. After cooling, the fibres were washed with distilled water. Finally, the fibres were dried with vacuum oven at 60 ℃ for 24h.

In addition, the ATR-FTIR, FEG-SEM, XPS and XRD analysis were carried out as described in *4.2.2 Characterization of nanocellulose*. Application of these analyses and the OM characterization in this chapter are summarized in Table 5.2.

Table 5. 2 Summary of analytical instruments and the corresponding characterization

Analytical instrument	Characterization
ATR-FTIR	(i) Crystallinity determination, chemical compositions determination of deformation of hemp fibres; (ii) Interfacial property analysis of hemp fibres without and with modification.
FEG-SEM	Surface morphologies characterization of hemp fibres without and with modification.
OM	(i) Characterization of deformation of hemp fibres; (ii) Characterization of fracture of hemp fibres.
XPS	Interfacial property analysis of hemp fibres without and with modification.
XRD	Crystallinity determination of hemp fibres without and with modification.

5.3 Results and Discussion

5.3.1 Characteristic and performance of hemp fibres

5.3.1.1 Microfibril angle (MFA) of hemp fibres

It has been reported that the MFA of wood fibres can be determined by optical microscope, e.g. Wang et al [541] used both copper (II) nitrate and cobalt (II) chloride solutions combining ulstrasonication to treat wood fibres, then they employed optical microscope to measure the MFA of wood fibres. In our experimentals, we found that the orientations of MFA in the samples treated with the copper (II) nitrate chloride solution were much more distinctive than those with the cobalt (II) chloride solution treatment. An example of microfibril orientations in S1 and S2 layers observed under light microscope at 1000× magnification is given in Fig. 5.2(a) and 5.2(b). It was found that, microfibrils in S1 layer have S-helical orientation (Fig. 5.2(a)); while in S2 layer have Z-helical orientation (Fig. 5.2(b)). These results agree well with the previous work which had been conducted by Thygesen [49]. The results of MFA measurement are summarized in Table 5.3. As shown in Table 5.3, the average MFA in S1 layer is 80.35°, which is in good agreement with the results of previous workers [542] who found the average angle in S1 layer was 70-90º. The average MFA in S2 inner layer is 2.65°, which is smaller than 4° measured previously by Fink [543] which may be due partly to the different hemp fibres from different geographical sources.

(a)   (b)
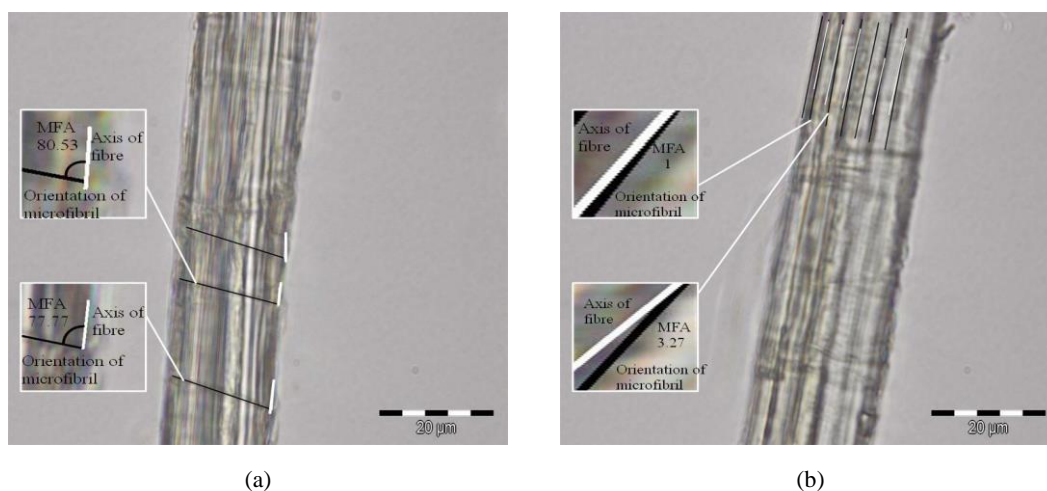
Fig. 5.2 Microfibril angle of hemp fibre: MFA in S1 layer (a); MFA in S2 layer (b).

Table 5. 3 MFA of S1 layer and inner part of S2 layer

Layer	MFA (°)	C.V. of MFA (%)
S1	80.35	3.05
S2 inner	2.65	16.49

5.3.1.2 Forms of deformation of hemp fibres

There exist a great number of definitions on fibre deformations. In natural lignocellulosic fibres, deformations have been called kink, nodes, dislocations, slip planes etc. [544]. But in other papers, these forms of deformation were also defined as defects [545, 546]. In this study, we defined these forms as deformation. Deformations appear when there is a change in microfibril direction and a distorsion

of the fibrils [544]. These occur during plant growth [547] or the post treatment of fibres [544]. Deformations not only result in a decrease in the tensile strength of single fibre [27], but also affect the strength of paper [548] and fibre-based composites [547]. The results of numerous examinations (1000 test pieces) of hemp fibres can be cataloged into four forms of deformation from hemp fibres (Fig. 5.3). The characteristic of each form deformation are as follows: (a) kink bands, formed in the fibres as a result of axial curing stresses; (b) nodes, formed in the regions of localized delamination and compressive strain; (c) dislocations, appeared in untreated natural fibre; and (d) slip planes, crinkled in the cell wall resulting from a slight linear displacement of the wall lamellae.

5.3.1.3 Breaking process

(a)

(b)

(c)

(d)
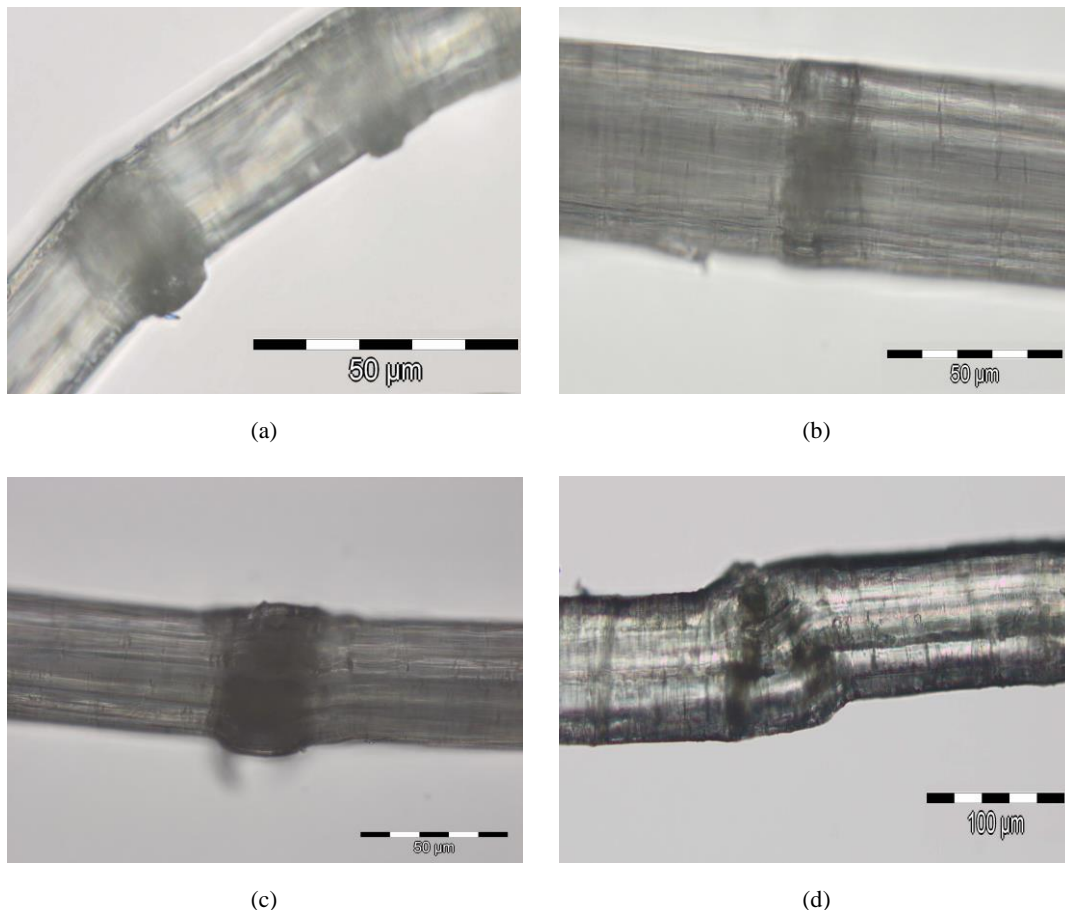
Fig. 5.3 Deformation of hemp fibre: (a) kink band (x 500 magnification), (b) node (x 500 magnification), (c) dislocation (x 500 magnification), (d) slip plane (x200 magnification).

Fig. 5.4(a) and 5.4(b) illustrate the initial and final fracture of an elementary hemp fibre. It can be found from Fig. 5.4(a) that the initial crack of hemp fibres starts from the primary cell wall. This may be due to the fact that the primary cell wall contains a large fraction of amorphous pectin, hemicelluloses and lignin, and these materials could result in the decrease of mechanical properties of fibres [2, 549, 550]. Generally, cell wall of hemp contains primary and secondary cell wall [3], and the secondary cell

wall consists of highly crystalline (CI 70 %) [49]. The crack would proceed into the secondary cell wall which forms the major part of hemp fibre. The secondary cell wall of hemp is composed of a thin S1 layer and a thick S2 layer, and the S2 layer contains outer and inner part [49]. As described above, the MFA in S1 layer is 80.35°, the MFA in the inner part of S2 layer is 2.65°. The MFA in the outer part of S2 layer ranges from 23° to 30° [49]. The microfibril angle can strongly influence mechanical properties of fibres, such as tensile strength and modulus [35], which decrease with MFA increases. Therefore, the breaking process in secondary wall of hemp fibres is from S1 layer to outer part of S2 layer to inner part of S2 layer.

(a)   (b)
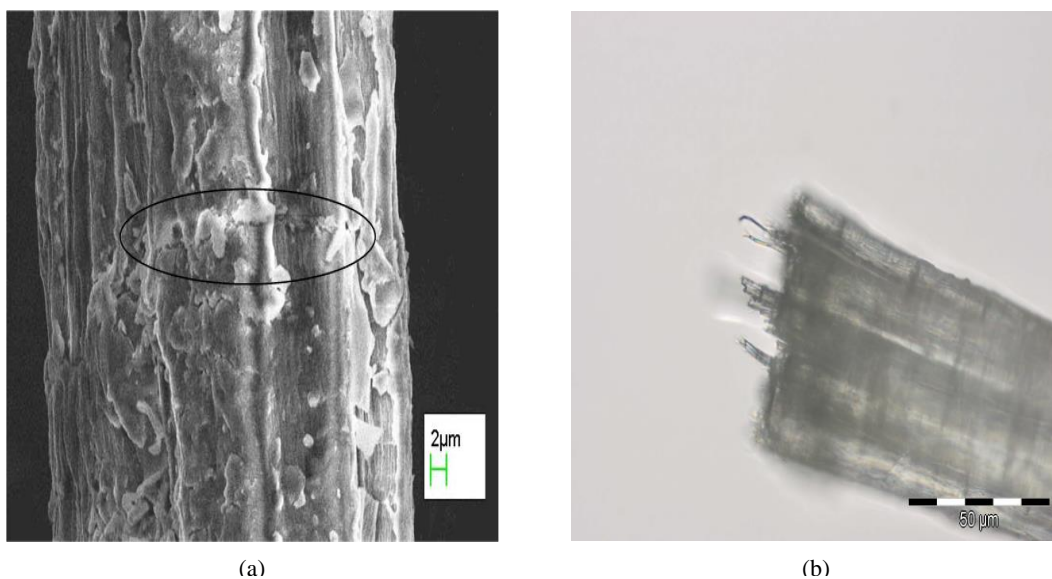
Fig. 5.4 Breaking process under tension: initial crack (a) and fracture (b) of hemp fibre.

Fig. 5.4(b) shows the fractography of hemp fibre. The microfibril can be observed clearly in the fracture surface of hemp fibres. The MFA in the S2 layer at fracture point was measured and their mean value was 6.16° with respect to the fibre axis. Compared with the MFA in the S2 layer without fracture, the higher MFA indicates that the fractures of hemp fibres under tensile loading tend to appear in the deformation points of fibres. This confirms that deformation is the weak link point of fibres.

5.3.2 Deformations of hemp fibres

5.3.2.1 Morphologies of deformation

The morphologies of deformations observed by OM and FEG-SEM are given in Fig. 5.5(a) and 5.5(b). The fracture within deformation regions and that without deformations are also showed in Fig. 5.5(c) and 5.5(d) respectively. It is evident that OM could not provide the detailed features of the deformation except the black color around the surface of the fibres (Fig. 5.5(a)). However, the method is able to identify the deformation easily and quickly.

The results from FEG-SEM shows that overall the surface of deformations of hemp

fibres looks more amorphous than that of hemp fibres without deformations (Fig. 5.5(b)). This may be due to the loss of hemicelluloses or lignin, which could combine fibrils together, after beating, mechanical treatment or other effects (e.g. acidic exposures). It is also evident that the fibrils distort in the deformation regions, which could affect the stiffness and stress of fibres with the stiffness and stress decreasing with the increase of deformation angle. Fig. 5.5(c) and 5.5(d) compare different fractures within deformation regions and that without deformation, showing different fracture behavior with a form of fibrillar break in deformation regions and a form of granular break in the other regions.
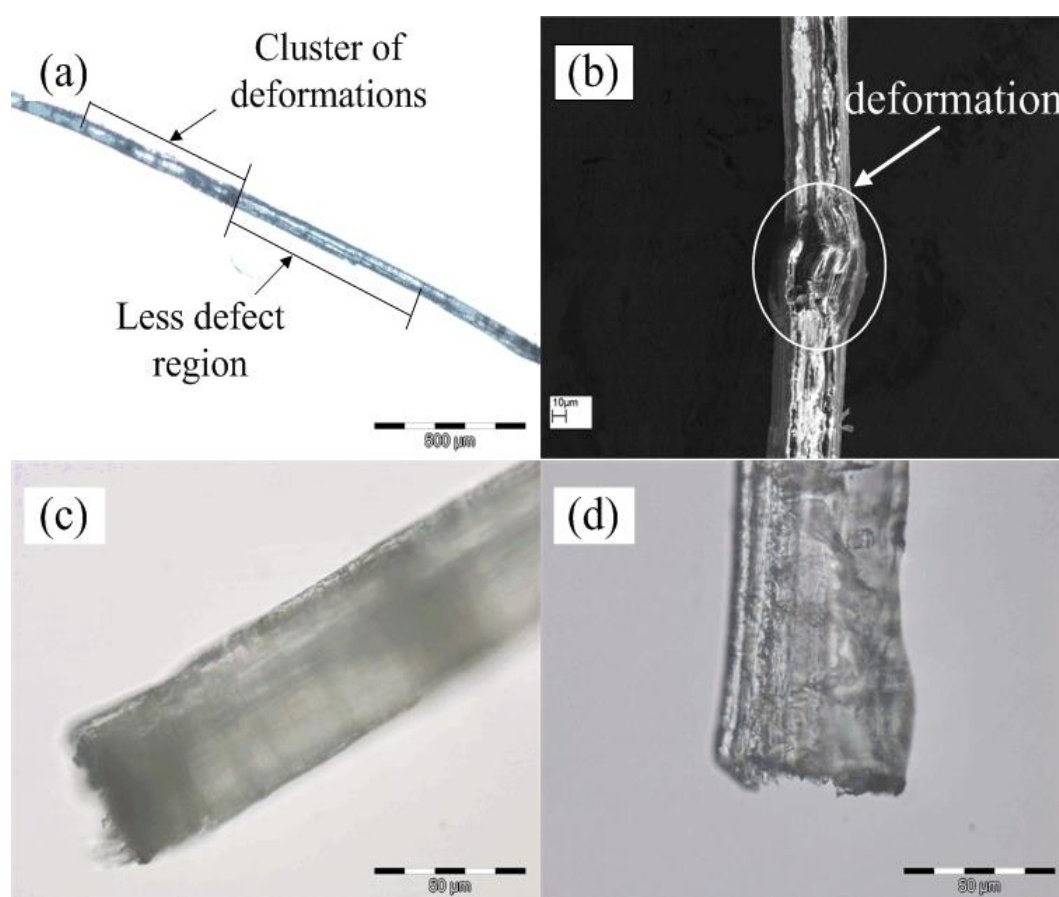
Fig. 5.5 Deformation of hemp fibres (a) by OM (x 50 magnification), (b) by FEG-SEM (x 1500 magnification), (c) the fracture within deformation regions (x 500 magnification) and (d) without deformation (x 500 magnification)

5.3.2.2 Crystallinity index of deformation

Because the XRD measurement needs a lot of samples, it is very difficult to collect the samples from the deformation regions in hemp fibres to meet the requirement of XRD measurement. Therefore, in this chapter, we employed FTIR to determine the CI of hemp fibres in deformations. For the FTIR evaluation, three ratios of absorbance at 1423 cm^{-1} and 895 cm^{-1}, 1368 cm^{-1} and 2883 cm^{-1} or 1368 cm^{-1} and 662 cm^{-1} are always used to measure CI [52, 551-553]. In order to select the best ratio of

absorbance to evaluate hemp fibres, we employed XRD and FTIR to determine CI of hemp fibres without deformation at first. Then, by comparing the CI values calculated from these three ratios of absorbance with that of XRD calculation, the closest one was selected. XRD spectrum for hemp fibres without deformation is given in Fig. 5.6. The results of CI determined for hemp fibres both with and without deformations are given in Table 5.4. In this study, the ratio of absorption band A_{1368}/A_{2883} is above 1 which seems to be unsuitable for evaluation, while the ratios of absorption band A_{1423}/A_{895} and A_{1368}/A_{662} are 72.6 % and 48.4 % respectively. The value calculated by using Segal empirical method is 56.0 %, indicating that the ratio of absorption band A_{1368}/A_{662} is more suitable for CI evaluation. Table 5.4 shows that the CI which was calculated by FTIR method in deformation regions is only 41.3 %, which is lower than that of without deformation region of hemp fibres. According to the two-phase model theory [554], there exist two regions in cellulose chain, namely amorphous and crystalline regions. The higher CI in the hemp fibres without deformation indicates that there exist a higher content of crystalline regions in the hemp without deformation than in deformation regions.
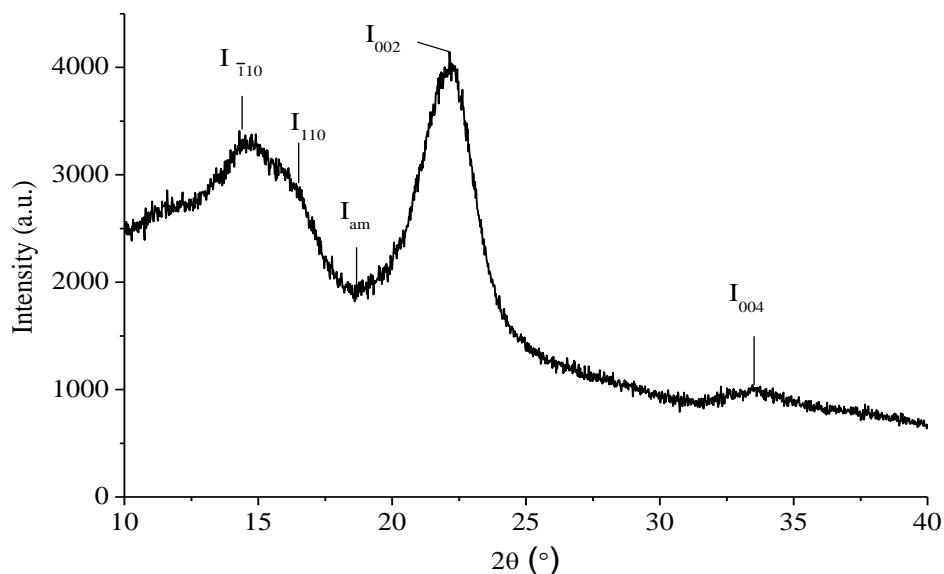
Fig. 5.6 X-ray diffractogram of hemp fibres without deformation.

Table 5. 4 Results of CI of hemp fibres determined by XRD and FTIR

2θ (°)	Without deformation (XRD testing)	Without deformation (FTIR testing)		Deformation regions (FTIR testing)	
	Intensity (a.u)	Wavenumber (cm^{-1})	Absorbance	Wavenumber (cm^{-1})	Absorbance
19.11 (I_{am})	1822	662	0.1286	663	0.1131
22.63 (I_{002})	4144	1368	0.0621	1367	0.0467
CI (%)	56.0	48.4 (c.v. 2.6%)		41.3 (c.v. 9.1%)	

5.3.2.3 Hydrogen bonds of cellulose in deformations

Fig. 5.7 shows the FTIR spectra of hemp fibres with and without deformation regions. The peak positions of the major IR bands for both situations are summarized and compared in Table 5.5. It can be seen in Fig. 5.7 that the absorbance of hemp fibres without deformations in the X-H (O-H and C-H) stretching region is much higher than that with deformations (Fig. 5.7).
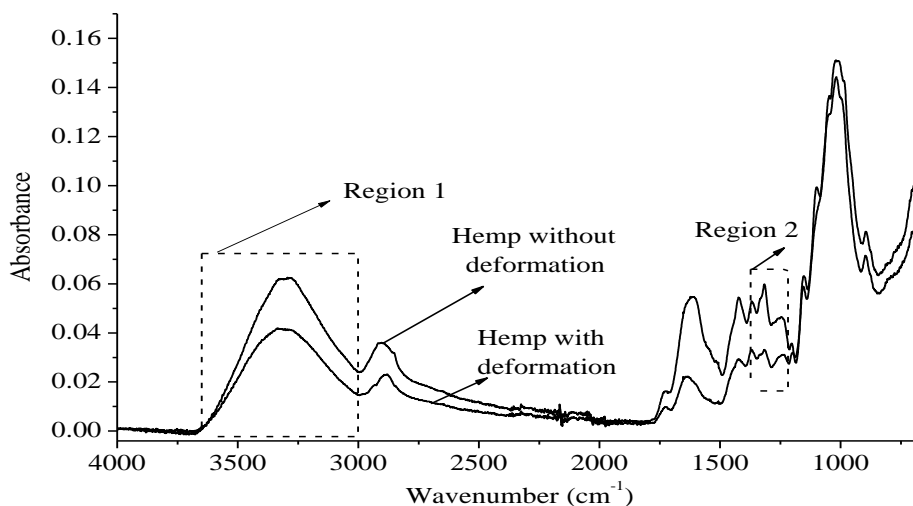
Fig. 5.7 FTIR spectra of hemp fibres without deformation and deformatiton regions.

Fig. 5.8 Deconvolved FTIR spectra of the υ_{OH} region of hemp without deformation (a) and with deformation regions (b). (Solid curves= experimental data; dashed curves= calculated data).

The IR absorption bands for OH stretching region (Region 1 in Fig. 5.7) in without deformation and deformation regions were deconvolved into four bands for a curve fitting as shown in Fig. 5.8(a) and 5.8(b). The peak positions of the four bands for hemp fibres with and without deformations are summarized in Table 5.3. The bands are 3450 cm^{-1} (1), 3346 cm^{-1} (2), 3262 cm^{-1} (3) and 3161 cm^{-1} (4) for the hemp without deformations, and 3451 cm^{-1} (1), 3350 cm^{-1} (2), 3264 cm^{-1} (3) and 3167 cm^{-1}

(4) for the deformation regions. These bands are related to the valence vibration of hydrogen bonded OH groups [555], i.e. band 1 relating the intramolecular hydrogen bond of O(2)H---O(6), band 2 to the intramolecular hydrogen bond of O(3)H---O(5), band 3 relating the intermolecular hydrogen bond of O(6)H---O(3`) and band 4 relating the O-H stretching respectively. It can be seen that the wave-numbers of peak position of deformations are higher than those of hemp fibre without deformation. This indicates that the degree of hydrogen bonding in deformation regions is lesser than that in without deformation regions.

Furthermore, it can be seen from Fig. 5.8(a) and 5.8(b) that the absorbance of these bands in the deformation regions is much lower than that in the regions without deformations. The absorbance of the deformation regions is only about 79.3 % for band 1, 64.4 % for band 2, 64.9 % for band 3 and 75.7 % for band 4 respectively against that of hemp without deformations. These mean that the number of hydrogen bonds in deformations is lower than in parts without deformations according to Beer-Lambert law. For example, the big decrease of absorbance in band 2 which is assigned to the intramolecular hydrogen bond of O(3)H---O(5) indicates that in deformation regions the cellulose molecular chains are more flexible than that in the hemp without deformation. The formation of inter- and intra-molecular hydrogen bonds in cellulose not only has a strong influence on the physical properties of cellulose (including solubility [556, 557], hydroxyl reactivity [558, 559], and crystallinity [560, 561], but also plays an important role in the mechanical properties of cellulose [444]. The strain energy, calculated by Tashiro et al [323], was found mainly being distributed to the deformation of the glucose rings (about 30.0 %), the bending of the ether linkages connecting the adjacent rings (about 20.0 %) and the O(3)H---O(5) hydrogen bond (about 20.0 %). This comes to a conclusion that the weaker inter- and intra-molecular hydrogen bonding in the deformations may be the main cause that induces the decrease of tensile strength in the hemp fibres, especially the intra-molecular hydrogen bond of O(3)H---O(5).

Table 5. 5 Band characteristics of FTIR spectra related to regions without and with deformation

Wavenumber (cm^{-1}) range of peak		$\Delta\upsilon$(cm^{-1})	Assignment	Sources
Without deformation	Deformation regions			
3327	3332	5	OH stretching	Cellulose, Hemicellulose [472, 473]
2883	2882	-1	C–H symmetrical stretching	Cellulose, Hemicellulose [473, 474]
1724	1724	0	C=O stretching vibration	Pectin, Waxes, Hemicellulose [475-478]
1623	1624	1	OH bending of absorbed water	Water [481]
1506	disappear	-	C=C aromatic symmetrical stretching	Lignin [482, 483]

Table 5.5 Continued

1423	1423	0	HCH and OCH in-plane bending vibration	Cellulose [472, 473, 485-488]
1368, 1363	1367,1363	-1,0	In-the-plane CH bending	Cellulose, Hemicellulose [473, 483, 489]
1325	1325	0	S ring stretching	Lignin [483, 562]
1314	1313	-1	CH_2 rocking vibration at C6	Cellulose [131, 481, 486]
1259	1261	1	G ring stretching	Lignin [483, 562]
1245	1244	-1	C-C plus C-O plus C=O stretch; G condensed > G etherified	Lignin-carbohydrate Complex [479]
1232	1231	-1	COH bending at C6	Cellulose [482, 486]
1204	1199	-5	C-O-C symmetric stretching, OH plane deformation	Cellulose, Hemicellulose [481, 482]
1152	1156	4	C-O-C asymmetrical stretching	Cellulose, Hemicellulose [472, 481, 490]
1046	1043	-3	C-C, C-OH, C-H ring and side group vibrations	Cellulose, Hemicellulose [481, 482, 492]
1020	1018	-2	C-C, C-OH, C-H ring and side group vibrations	Cellulose, Hemicellulose [131, 481, 490, 492]
994	996	2	C-C, C-OH, C-H ring and side group vibrations	Cellulose, Hemicellulose [131, 481]
895	894	-1	COC,CCO and CCH deformation and stretching	Cellulose [472, 481, 486, 488, 490]
662	663	1	C-OH out-of-plane bending	Cellulose [473, 491]

Table 5. 6 Hydrogen bonds characteristics of FTIR spectra related to without and with deformation

Wavenumber (cm^{-1}) range of peak		$\Delta\upsilon(cm^{-1})$	Assignment
Without deformation	Deformation regions		
3450	3451	1	O(2)H---O(6) intramolecular in cellulose [497]
3346	3350	4	O(3)H---O(5) intramolecular in cellulose [495, 497]
3262	3264	2	O(6)H---O(3`) intermolecular in cellulose [495-497]
3161	3167	6	O-H stretching [563]

5.3.2.4 Hemicellulose and lignin in deformations

A scrutiny of the IR spectra from 1370 cm^{-1} to 1330 cm^{-1} shows that the band at 1368 cm^{-1} and 1363 cm^{-1} almost disappear in deformation regions (Fig. 5.9a). The bands at 1368 cm^{-1} and 1363 cm^{-1} assigned as the in-plane CH bending may be from hemicellulose or cellulose. The near disappearance of bands of 1368 cm^{-1} and 1363 cm^{-1} may be probably due to the removal of the hemicelluloses in deformation regions.

Hemicelluloses can form a linkage between cellulose and lignin, permitting the effective transfer of shear stress between cellulose microfibrils and the lignin [71]. Hemicellulose also can form lignin-carbohydrate complex with lignin by ether bonds [72]. The removal of hemicelluloses in deformation regions may cause the decrease of transfer of shear stress under tensile loading and loss of lignin as well. Fig. 5.9(b) shows the FTIR spectra of hemp fibres with and without deformations from 1330 cm^{-1} to 1215 cm^{-1}. It must be noted that the S ring stretching, CH$_2$ rocking at C6 in cellulose, G ring stretching, C-C plus C-O plus C=O stretch and COH bending at C6 in cellulose could normally be seen in bands at 1325, 1314, 1259, 1245 and 1232 cm^{-1} respectively for the hemp fibres without deformation. Due to overlapping of the bands, only two peaks can be seen in Fig. 5.9(b).
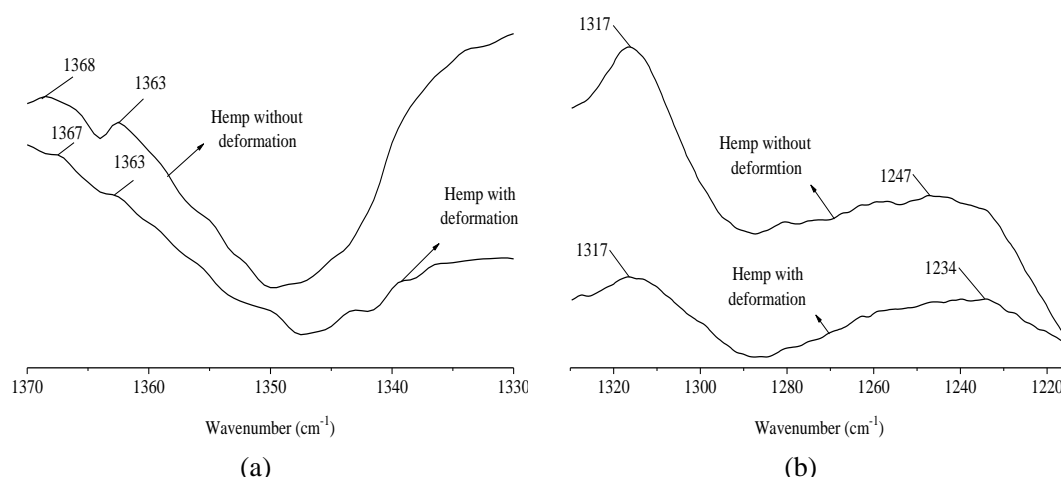
Fig. 5.9 FTIR spectra of hemp fibres from 1370 cm^{-1} to 1330 cm^{-1}(a); from 1330 cm^{-1} to 1215 cm^{-1} (b) with and without deformation.

The deconvolved FTIR spectra in Fig. 5.9(b) are shown in Fig. 5.10(a) (without deformation) and 5.10b (deformation regions). Lignins are composed of three basic units, namely *p*-hydroxyphenyl (H), guaiacyl (G) and syringyl (S) [50]. Guaiacyl (G) and syringyl (S) are the main units of lignin, but the ratio of S/G varies from one to another plant. It was reported recently by del Río et al. [52] that S/G values calculated upon FTIR were in agreement with those calculated upon Py-GC/MS at the bands of 1271 cm^{-1} and 1327 cm^{-1} respectively. However, in this study, the bands at 1271 cm^{-1} and 1327 cm^{-1} assigned as G ring stretching and S ring stretching respectively were found shifted to lower wavenumbers. For the hemp fibres without deformations (Fig. 5.10(a)), the G ring and S ring stretching appear at the bands of 1259 cm^{-1} and 1325 cm^{-1}, for the deformation regions, they appear in the wavenumbers of 1261 cm^{-1} and 1325 cm^{-1} (Fig. 5.10(b)). The ratio of S/G in hemp plant was reported as about 0.8 (molar contents of G-lignin is 51.0 %, molar contents of S-lignin is 40.0 %) [52], but in this study, the ratio of S/G is 1.1 for the hemp fibre without deformations and 0.9 for the deformation regions. According to the investigation carried out by Love et al. [73], syringyl-rich areas of the lignin network were more rigid than guaiacyl-rich areas. It could therefore be concluded that the lignin network in the parts without

deformations would be more rigid than that in deformation regions. The lower absorbance in deformations means that part of the lignin was removed from deformation regions. It can such be concluded from this study that the cellulose content in deformations would be higher than that in hemp fibres without deformations.
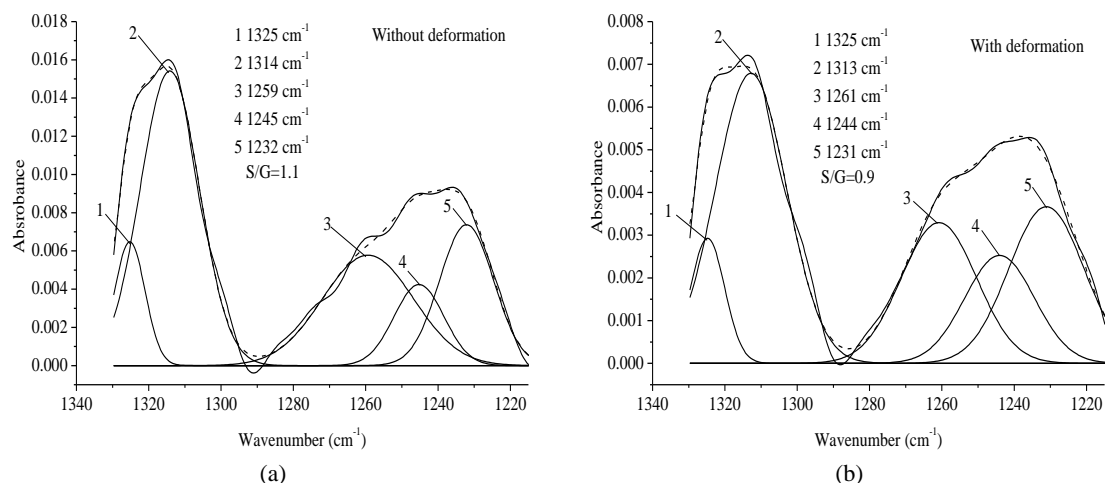
Fig.5.10 Deconvolved FTIR spectra from 1330 to 1215 cm^{-1} of without deformation (a) and with deformation regions (b). (Solid curves= experimental data; dashed curves= calculated data).

5.3.3 DTAB-Nanocellulose modification

5.3.3.1 Mechanical properties of DTAB-nanocellulose modified natural fibres

Table 5. 7 Mechanical properties of unmodified, DTAB pretreatment and two-step modified hemp fibres

Experiments	Diameter (μm)	C.V of diameter (%)	Modulus (GPa)	Tensile stress (MPa)	Tensile strain (%)
Unmodified	46.76	17.43	28.29	696.68	2.29
DTAB (pH11, 0.1%)	45.10	10.66	29.83	735.29	2.47
D1 (pH10, DTAB 0.05%)	57.28	12.12	39.98	917.76	3.09
D2 (pH10, DTAB 0.1 %)	53.27	15.65	39.10	1060.39	3.33
D3 (pH10, DTAB 0.15 %)	55.05	16.50	36.34	994.93	3.39
D4 (pH11, DTAB 0.05 %)	54.50	14.48	38.88	1087.94	3.54
D5 (pH11, DTAB 0.1 %)	51.39	14.70	38.51	1203.85	3.84
D6 (pH11, DTAB 0.15 %)	53.97	13.00	44.99	1124.20	3.06
D7 (pH12, DTAB 0.05 %)	52.78	17.00	32.21	934.22	3.27
D8 (pH12, DTAB 0.1 %)	50.13	18.99	37.79	1190.39	3.62
D9(pH12, DTAB 0.15 %)	50.17	16.74	33.01	1006.93	3.43

Mechanical properties of hemp fibres with various treatments were summarized in Table 5.7. As shown in Table 5.7, the two-step (DTAB-nanocellulose) modification increases the mechanical properties of hemp fibres significantly. By comparing with un-modification, DTAB pretreatment increases the modulus, tensile stress and tensile

strain of hemp fibres by 5.44 %, 5.54 % and 7.86 % respectively; and the two-step treatment, under the condition pH 11 and dosage of DTAB 0.1 %, can increase the modulus, tensile stress and tensile strain of hemp fibres are increased by 36.13 %, 72.80 % and 67.69 % respectively. This indicates that the two-step modification can increase the mechanical properties of hemp fibres significantly. Compared with the previous works which used alkalization [564] or grafting [565] modification, this two-step modification still displays more significant reinforcement on the mechanical properties of natural fibres. As deformation is the weakest link in natural fibres [565-567], the increase of mechanical properties may be due to the "repair" of deformation in the fibres. In order to reveal the reinforcement mechanism, we employed three analytical instruments: (i) EDX; (ii) FEG-SEM and (iii) XRD. These results will be discussed in sections *5.3.3.1.1, 5.3.3.1.2 and 5.3.3.1.3* respectively.

Moreover, it can be found from Table 5.7 that pH of the solution and the dosage of DTAB also play main roles on the improvement of the mechanical properties of hemp fibres. The modulus of fibres does not display any correlation with the pH value of solution and the dosage of DTAB, but the tensile stress and tensile strain of fibres display strong correlation with the pH value of solution and the dosage of DTAB. As shown in Table 5.7, under the same pH, the 0.1 % dosage of DTAB displays the highest improvement on the tensile stress and tensile strain of hemp fibres; under the same dosage of DTAB, pH 11 displays highest improvement. These can be explained by as follows:

(i) Maximal absorption of nanocellulose. In water solution, surfactant can form micelle due to the association of surfactant molecules [568], above a certain concentration in the solution (which is defined as critical micelle concentration) micellisation or aggregation takes place [569]. In the critical micelle concentration, the interface of micelle is at (near) maximum coverage and to minimise further free energy [569], which will results in the maximal absorption of surfactant on the surface of cellulose [570]. The critical micelle concentration of DTAB is 0.03 % [571]. In our experiments, when the dosage of DTAB is 0.1 %, the concentration of DTAB is 0.033 %. This concentration is very close to the critical micelle concentration of DTAB. Therefore under the 0.1 % addition, the absorption of DTAB in the hemp fibres will be the highest. Obviously, this will result in much more absorption of anionic nanocelluloses on the fibre.

(ii) The swelling of hemp fibres by alkali (sodium hydroxide). Under the alkaline condition, due to the swelling of cellulose by the interaction with sodium hydroxide, the accessibility of cellulose will increase [572]. The increase of the accessibility of cellulose induces much more chemical reagent penetrate into the cellulose [573], but with the increase dosage of alkali, the increasing swelling will damage the crystalline structure of cellulose and reduce the strength of cellulose chains [124]. Therefore the best pH 11 can be ascribed to the swelling of hemp fibre.

5.3.3.1.1 Effect of deformation on the absorption of nanocellulose
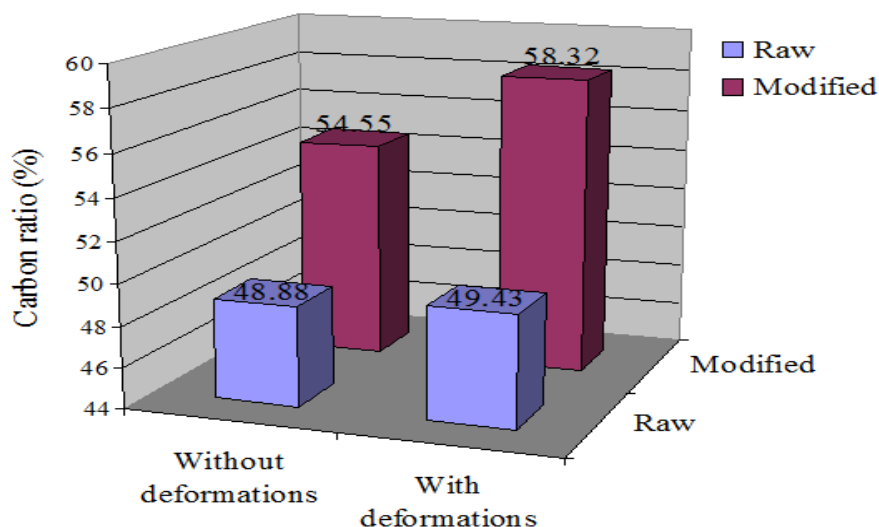
Fig. 5.11 Comparison of carbon ratio between raw and DTAB modified hemp fibres in the regions without and with deformations

As described above, the amount of absorbed DTAB influences the absorption of nanocellulose on hemp fibres; therefore, we used the amount of absorbed DTAB to evaluate the effect of deformation on the absorption of nanocellulose. Due to the difference of carbon ratio between DTAB and hemp fibres, we employed EDX to calculate the carbon ratio of DTAB and hemp fibres. The results of EDX measure are shown in Fig. 5.11, as shown in Fig. 5.11, before DTAB treatment, the carbon ratios in the regions without deformations and with deformation are 48.85 % and 49.43 % respectively; after DTAB treatment, the carbon ratios in both of regions are increased, especially in the regions of deformation, the carbon ratios in the regions without deformations and with deformation are 54.55 % and 58.32 % respectively. The DTAB absorption ratio of the regions without deformation and with deformation can be calculated with Eq. 5.1 and 5.2; and these values are 0.59 and 0.98 respectively. This indicates that in the regions of deformations, much more DTAB are absorbed. The deformation in the fibre not only the weak point but also the region which can be easily "attacked" by chemical acid or alkali [574]. Moreover, as described in *5.3.2.2 Crystallinity index of deformation*, the crystallinity index in deformation is lower than that in the region without deformation; and exist much more non-crystalline regions. Therefore, under the alkaline condition, the accessibility in deformation will much higher than that in the region without deformation. This will gives rise to the increase of DTAB absorption on the fibres.

5.3.3.1.2 Surface morphologies of two-step modified hemp fibres

The natural fibres before and after two-step modification were observed with FEG-SEM. As described in *5.3.2.1 Morphologies of deformation*, overall the surface of deformations of hemp fibres looks more amorphous than that of hemp fibres

without deformations, therefore the characterization of the surface of two-step modified hemp fibres focus on the deformations in hemp fibres. As shown in Fig.5.12(a), impurity and interfibrillar gap can be found on the surface of raw hemp fibres, while Fig. 5.12(b) clearly shows the presence of nanocellulose around the fibres after two-step modification. FEG-SEM micrograph shows that nanocellulose covers the deformation of fibres with two ways, namely, (i) nanocellulose filling in the stria and (ii) bonding the inter-fibril on the gap between two fibrils.

| (a) | (b) |
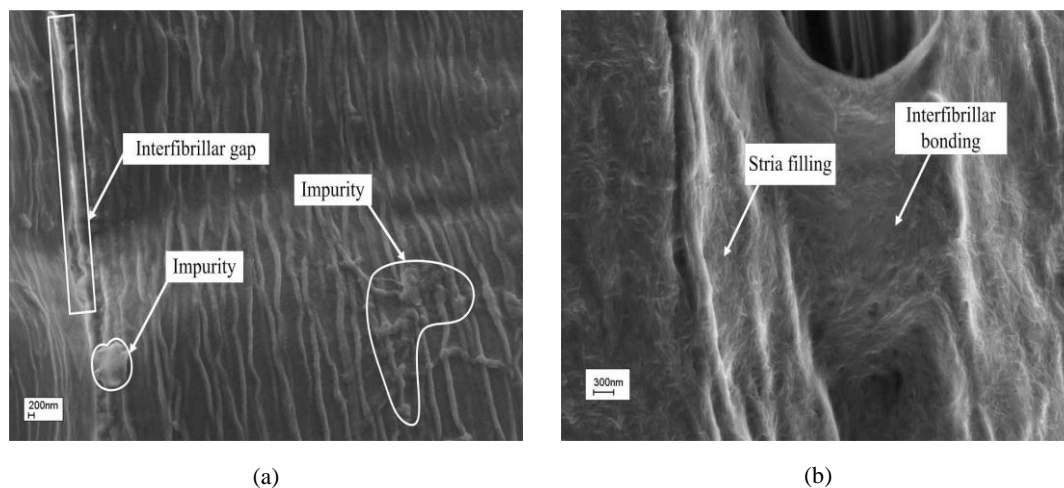
Fig. 5.12 FEG-SEM morphologies of (a) untreated and (×20 K) (b) two-step modified (×48 K) hemp fibres.

The first way may give rise to the improvement of interfacial property of hemp fibres. Because compared with macro-fibres from nature, nanocellulose possesses higher specific surface area (up to 170 $m^2 \cdot g^{-1}$ [69]) [69, 353, 575-577], and the higher specific surface area will provides more contact or bonding points on fibres surface and hence lead to a stronger interface with resins.

The second way may in favour of the improvement of the mechanical properties of hemp fibres. The interfibrillar gap is one of the typical characteristic of deformation [578], due to the high mechanical properties [70-72], the cover of nanocellulose on the interfibrillar gap may induce the increase of mechanical properties of hemp fibres.

5.3.3.1.3 Crystallinity index of the modified hemp fibres

X-ray diffraction was used to investigate the crystallinity of unmodified, DTAB modified and two-step modified hemp fibres. X-ray powder diffraction measurement results from these hemp fibres are given in Fig. 5.13. CI analysis was summarized in Table 5.8. It can be seen from Table 5.8 that the major crystalline peak of the hemp fibres with various treatments occur from 21.77° to 22.63°, which represents the cellulose crystallographic plane (002, Bragg reflection). The minimum intensity (I_{am}) between 002 and 110 peaks is from 18.52° to 19.11°. The CI for un-modification, DTAB pretreatment and two-step modification are 55.17 %, 65.95 % and 76.39 % respectively. This indicates clearly that after modification, crystallinity of hemp fibres is increased significantly. Compared with the un-modification, DTAB pretreatment,

the CI of two-step modification can increase by 38.46 % and 15.83 % respectively. This may be due to the repair of nanocellulose on cell wall or non-crystalline of the hemp fibres. Because:

(i) According to the CI results, the DTAB pretreatment is 65.95, the two-step modification, i.e. DTAB-nanocellulose is 76.39 %, and the CI of nanocellulose is 86.6 %, if the increase of CI is just contributed by the high crystallinity of nanocellulose, the ratio of nanocellulose should up to 50.38 %. But in the pretreatment, the dosage of DTAB is only 0.1 %, namely, the absorbed nanocellulose of the fibres is not possible higher than the fibres. Therefore, the significant increase of CI must be contributed by the interaction between the nanocellulose and fibres.

(ii) The thickness of delamination in the S2 layer of hemp fibres is 100 nm [542], this allows small size of nanocellulose particle penetrate into the delamination. Moreover, under the alkaline condition, due to the swelling of cellulose by the interaction with sodium hydroxide, the accessibility of cellulose will increase [572]. This will increase the probability of reaction between nanocellulose with hemp fibres.

(iii) The high density of hydroxyl groups [69] on the surface of nanocellulose provides the change for the formation of hydroxyl bonds between nanocellulose and hemp fibres.
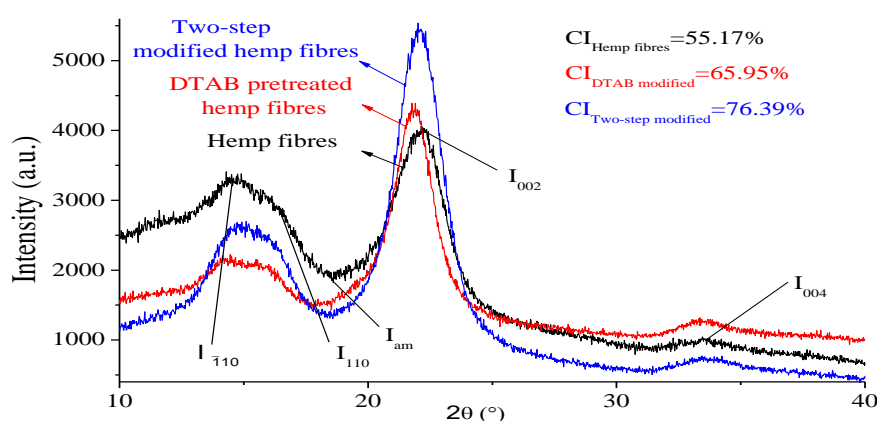
Fig. 5.13 X-ray diffractogram of unmodified, DTAB pretreated, and two-step modified hemp fibres.

Table 5. 8 Results of CI of unmodified, DTAB pretreated and two-step modified hemp fibres determined by XRD

Samples	2θ (°)		Intensity (a.u)		CI (%)
	I_{am}	I_{002}	I_{am}	I_{002}	
Raw fibres	19.11	22.63	1822	4064	55.17
DTAB modified fibres	18.52	21.77	1529	4491	65.95
Two-step modified fibres	18.58	21.94	1307	5538	76.39

5.3.3.2 Interfacial property of two-step modified natural fibres

Interfacial property of fibres is the main factor which determines the final performance of the fibres-based composites. Various methods (e.g. micro-mechanical techniques [579-581], spectroscopic techniques [582-585], surface characterization [40, 586, 587]) have been developed for assessment of fibres interfacial property. Especially, for spectroscopic techniques, researchers always use Soxhlet extraction as pretreatment before FTIR or XPS characterization [465, 588]. In the present work, we develop a novel method without Soxhlet extraction pretreatment for the measurement of polyester adsorption on the surface of fibres and the characterization of fibres surface by FTIR and XPS. The adsorbed unsaturated polyester on the surface of fibres with various treatments is summarized in Table 5.9. As Table 5.9 shown, after two-step treatment, the resin adsorption was increased from 0.05205 g to 0.07235 g; but for DTAB pretreatment, the adsorbed resin was decreased from 0.05205 g to 0.03365 g. This indicates that two-step modification has improved the interfacial properties of fibres.

Table 5. 9 Absorbed resin of raw hemp fibres and modified fibres

Samples	Absorbed resin (g)
Raw fibres	0.05205
DTAB	0.03365
Two-step Modification	0.07235
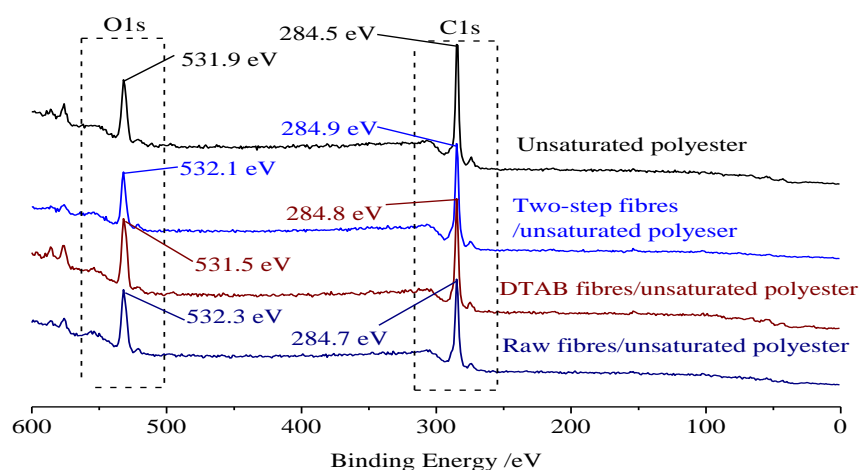
Fig. 5.14 XPS wide scans spectra of unsaturated polyester and fibres for un-modification, DTAB pretreatment and two-step modification immersed with unsaturated polyester.

XPS has been commonly used to investigate the chemical compositions of cellulosic and polymeric materials as well as their chemical interactions. Fig. 5.14 shows XPS wide scans spectra for unsaturated polyester, unsaturated polyester coated fibres which were pretreated with various methods. It can be seen that oxygen and carbon are the main elements on the surface of fibres. High resolution of spectra at O1s and

C1s were shown in Fig. 5.15. Atomic ratio of O/C also be calculated according this figure. It is apparent that two-step modification results in a decrease in the O/C atomic ratio which is 0.272. This value is quite similar with unsaturated polyester which is 0.245, indicating that almost all of the surface of the fibres were covered with the resin. For DTAB pretreated and unmodified fibres, O/C atomic ratio is 0.356 and 0.349 respectively. These results agree quite well with the resin adsorption measurement as illustrated above. The XPS characterization results also indicate that the developed method in this research can be used as novel assessment way for the interfacial property of fibres.
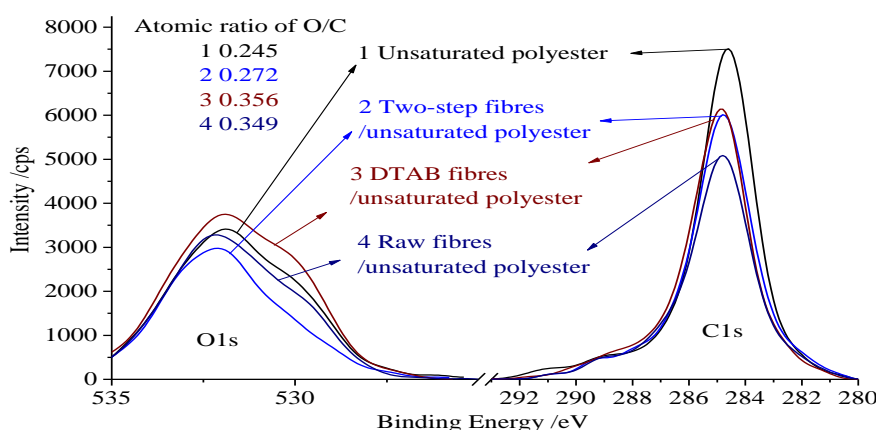
Fig. 5.15 O1s and C1s narrow spectra of unsaturated polyester and fibres for un-modification, DTAB pretreatment and two-step modification immersed with unsaturated polyester.
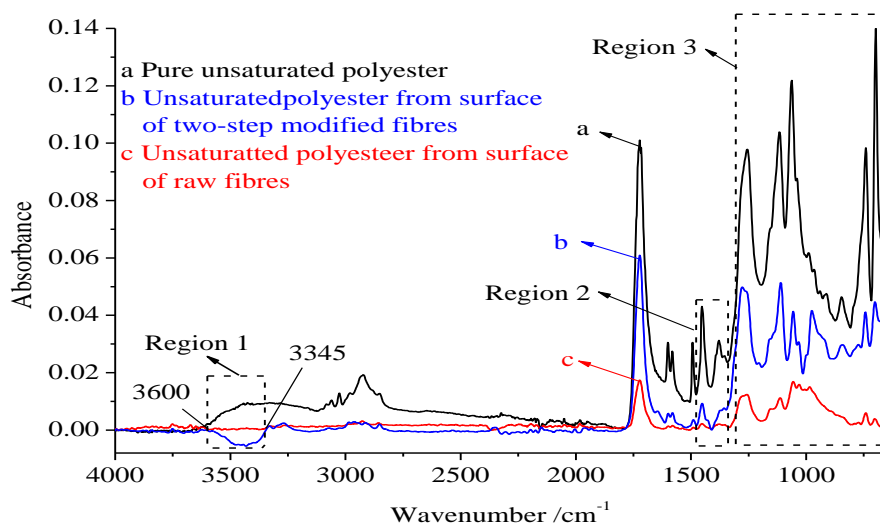
Fig. 5.16 ATR-FTIR spectra of pure unsaturated polyester, subtraction from two-step modified fibres and raw fibres.

ATR-FTIR has been used extensively to investigate the surface of fibres as well as the resin adhesion, and spectra subtraction is useful in variety of analysis, such as the inspection of incoming raw materials, comparison of batches or samples, evaluation of organic reactions, and so on. This study employs spectra subtraction to subtract unsaturated polyester spectrum from the two-step modified and un-modified hemps fibres which are coated with unsaturated polyester, then compare these subtracting

spectra with raw unsaturated polyester. The different spectrum may be attributed to the effect of nanocellulose.

The ATR-FTIR spectra of pure unsaturated polyester (a), spectra of polyester subtraction from two-step modified fibres (b) and raw fibres (c) after resin coating were presented in Fig. 5.16. More details about region 2 and region 3 are shown in Fig. 5.17(a) and 5.17(b). As can be seen, the subtracted spectrum (b) appears negative absorbance in region 1 (from 3600 to 3345). According to previous reports [557, 589], free hydroxyl groups (C2, C6) in cellulose were assigned around 3561-3358 cm^{-1}, also nanocellulose possesses high density of hydroxyl groups [69]. The negative absorbance in spectrum b of Fig. 5.16 may be due to the esterification between hydroxyl groups at C-2 and C-6 of nanocellulose and carboxyl groups of unsaturated polyester. This can be further proved from the peak at 1426 cm^{-1} (Fig. 5.17(a)) which is assigned with the H-C-H bending vibration [518]. Moreover, the appearance of peak around 1380 cm^{-1} can be observed obviously in spectrum a in Fig. 5.17(a) also further support this observation. Generally, the peak at 912 cm^{-1} is assigned with C-H (in CH=CH) out-of-plane blending of styrene, 989 cm^{-1} is assigned with C-H (in CH=CH) out-of-plane blending of unsaturated polyester [590, 591], the disappearance of 912 cm^{-1} in spectrum indicated that less styrene was absorbed on the surface of raw fibres. However, this peak appears in spectrum b in Fig. 5.17(b), this shows that two-step modification can benefit the adhesion of styrene on the surface of modified fibres. The appearance of peak at 975 cm^{-1} in spectrum b and peak at 984 cm^{-1} in spectrum c show that unsaturated polyester is adsorbed by both of the fibres.
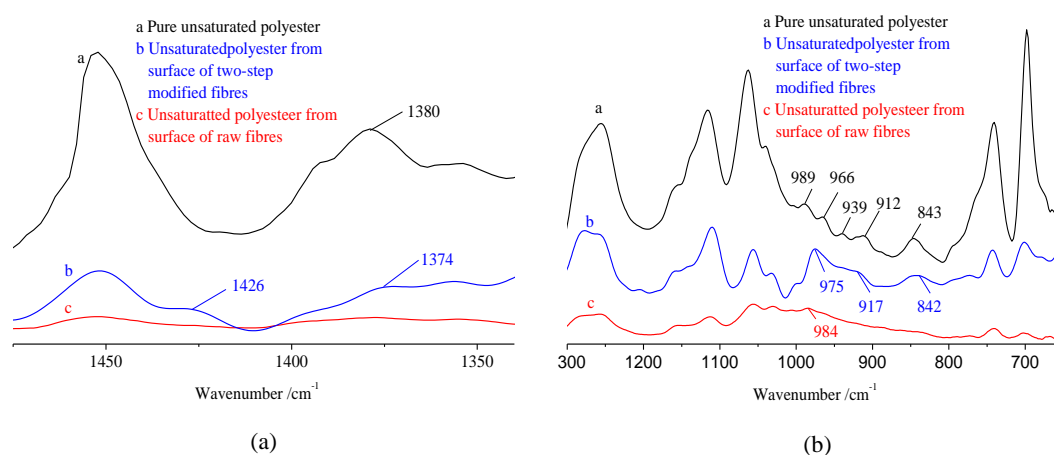
Fig. 5.17 ATR-FTIR spectra of pure unsaturated polyester, subtraction from two-step modified fibres and raw fibres in 1475-1340 cm^{-1} (a) and 1300-650 cm^{-1} (b).

5.4 Interim Conclusions

In this chapter, we firstly characterized hemp fibres by employing microscopy technology. The MFA of hemp fibres were measured by optical microscope and the results showed average MFA in S1 layer was 80.35° and the average MFA in S2 inner layer was 2.65°. Optical microscope was also used to observe the deformation of hemp fibres which could be cataloged into four forms, namely kink bands, deformations, nodes and slip planes. FEG-SEM was employed to observe the crack of hemp fibres under tensile loading, and found that the initial crack of hemp fibres starts from the primary cell wall. The MFA of S2 inner layer at fracture point which was measured by optical and their mean value was 6.16°. Compared with that of 2.65°, this confirmed that deformation is the weak link point of fibres.

Secondly, we further revealed the mechanism of deformation on the mechanical properties of hemp fibres by employing spectroscopy technology. The crystallinity index examined by FTIR was 48.4 % for the hemp without deformations and 41.3 % for those within deformation regions, showing a significant reduction of crystallinity in the deformations.

The deconvolved four bands of the OH stretching region gave rise to a clear indication of changes in the valence vibration of hydrogen-bonded OH groups: i.e. the intramolecular hydrogen bond of O(2)H---O(6) (3451 cm^{-1}), the intramolecular hydrogen bond of O(3)H---O(5) (3350 cm^{-1}), the intermolecular hydrogen bond of O(6)H---O(3`) (3264 cm^{-1}) and the O-H stretching (3167 cm^{-1}), with the absorbance of these bands in the deformation regions being much lower than that in the regions without deformations. The weaker inter- and intra-molecular hydrogen bonding in the deformations could be the main cause that induced the decrease of tensile strength in the hemp fibres, especially the intramolecular hydrogen bond of O(3)H---O(5).

The FTIR spectra from 1370 cm^{-1} to 1330 cm^{-1} illustrated that the band at 1368 cm^{-1} and 1363 cm^{-1} disappeared in deformation regions, indicating the removal of the hemicelluloses in deformations and hence possible loss of lignin. The deconvolved FTIR spectra from 1330 cm^{-1} to 1215 cm^{-1} showed the S ring stretching, CH$_2$ rocking at C6 in cellulose, G ring stretching, C-C plus C-O plus C=O stretch and COH bending at C6 in cellulose, indicating reduction of lignin content in the deformation regions. The ratio of S (Syringyl, 1325cm^{-1})/ G (Guaiacyl, 1259 cm^{-1}) was 1.1 for the hemp without deformations comparing to 0.9 for the deformation regions, indicating higher cellulose content in the deformation regions.

Thirdly, we employed nanotechnology to modify hemp fibres. The nanotechnology modification was carried out in two steps, namely, DTAB pretreatment and nanocellulose modification. By comparing with un-modification, DTAB pretreatment, the two-step (two-step nanocellulose) modification displayed more significant reinforcement on the mechanical properties of hemp fibres. Compared with raw hemp

fibres, the modulus, tensile stress and tensile strain of the two-step nanocellulose modified hemp fibres increase by 36.13 %, 72.80 % and 67.89 % respectively. EDX, FEG-SEM and XRD were employed to reveal the reinforce mechanism of the two-step nanocellulose modification. EDX measurement showed that deformations affected the absorption of DTAB significantly. In the deformation of hemp fibres, the absorption ratio of DTAB was 0.98, while in the region without deformation this value was only 0.59. This indicated that much more nanocellulose could be adsorbed on the deformation of hemp fibres. FEG-SEM results showed that nanocellulose covers the deformation of fibres with two ways, namely, (i) nanocellulose filling in the stria and (ii) bonding the inter-fibril on the gap between two fibrils. XRD results showed that the CI of un-modification, DTAB pretreatment and two-step modification were 55.17 %, 65.95 % and 76.39 % respectively. This indicated that the two-step nanocellulose modification could improve the crystallinity index of hemp fibres. We conjecture that the increase of CI is caused by the formation of hydroxyl bonds between nanocellulose with hemp fibres in the S2 layers and the non-crystalline regions of hemp fibres.

After two-step treatment, the resin (unsaturated polyester) adsorption was increased from 0.05205 g to 0.07235 g. But for DTAB pretreatment, the adsorbed resin was decreased from 0.05205 g to 0.03365 g. This indicates that two-step modification could improve the interfacial property of fibres. The interfacial property improvement was revealed by employing XPS and ATR-FTIR. XPS characterization results showed that the O/C atomic ratio of fibres without modification, DTAB pretreatment and two-step treatment were 0.349, 0.356 and 0.272 respectively. The value of O/C atomic ratio with two-step modification was quite similar with unsaturated polyester which is 0.245. This indicated that much more unsaturated polyester could be absorbed on the fibres with two-step modification. ATR-FTIR characterization showed that (i) the higher resin adsorption may be due to the esterification between hydroxyl groups at C-2 and C-6 of nanocellulose and carboxyl groups of unsaturated polyester, and (ii) the nanocellulose modification can benefit the adhesion of styrene on the surface of the modified fibres.

Chapter 6 Nanocellulose/Epoxy Nanocomposite

6.1 Introduction

Nanocomposites in general are two-phase materials in which one of the phases has at least one dimension in the nanometer range (1–100 nm) [358]. Over the last 16 years, a significant amount of research has been dedicated to the use of nanocellulose as the filler for polymeric matrices to make nanocomposite since Favier et al [254, 255] firstly reported the fabrication of nanocellulose reinforced composites in 1995. It has been found that nanocellulose can improve the mechanical properties (e.g. tensile strength, tensile modulus, strain and so on) of polymeric matrices significantly. For example, Park et al [399] employed nanocellulose as the filler to make nanocellulose /poly(ethylene oxide) (PEO) (hydrophilic polymer) nanocomposite. They found that the existence of nanocellulose was effective in improving the mechanical properties of PEO. After the incorporation of the nanocellulose (0.4 %) into the PEO, the tensile modulus, tensile strength and strain of PEO were increased by 193.9%, 72.3% and 233.3%. Ten et al [442] employed solvent casting method to make nanocellulose/ polyester (hydrophobic polymer) nanocomposite. The results showed nanocellulose was an effective nucleation agent for polyester. Tensile stress, Young's modulus and strain of polyester increased with the increasing concentration of nanocellulose.

As one of the hydrophobic polymeric matrices, epoxy resin systems are increasingly used in a wide range of applications, e.g. shipbuilding or electronic devices, medical devices, optical components, structural composites and so on [592, 593]. However, there are only a few of works [467, 594-596] have been reported about the mixture of epoxy with nanocellulose. Only one method about the dispersion of nanocellulose into the epoxy matrix has been reported [467, 596], namely, organic solvent dispersion methodology. Lu et al [467] successfully incorporated nanocellulose into the epoxy resin system using acetone as the organic solvent, at a 3.7 % addition of nanocellulose, the storage modulus at 30 ℃ increased about 20%. Tang et al [467, 594-596] employed dimethyl formamide as the organic solvent to disperse nanocellulose into the epoxy matrix, at a 20 % addition of nanocellulose, the storage modulus at 30 ℃ increased from 1.6 GPa to 5.7 GPa. But none of them reported the effect of nanocellulose on the tensile stress and modulus of epoxy. A unique feature of nanocomposites is that a dramatic improvement in properties is reached at low filler content [597]. However, among these reports about the fabrication of nanocellulose /epoxy nanocomposite, the addition of nanocellulose was very high.

In this chapter, we investigate the application of nanocellulose as reinforced filler for epoxy. We develop a novel method for the dispersion of nanocellulose into the epoxy by employing the curing agent of epoxy---diethylenetriamine (DETA) to modified nanocellulose. The preparation conditions (curing temperature and dosage of modified nanocellulose) of modified nanocellulose/epoxy nanocomposite will be optimized

firstly. Secondly, the modification will be investigated further by employing FEG-SEM to compare the dispersion of modified nanocellulose in the matrix with that of without modification. Finally, DSC will be employed to calculate the cure kinetics of modified nanocellulose/epoxy by using three different methods, i.e. KAS, Friedman and Málek method.

6.2 Theoretical foundation of cure kinetics

The first attempts to develop authentic models of solid state kinetics date back to the late 1920s [598]. The earliest kinetic studies were performed under isothermal conditions. While non-isothermal methods were used [599] to follow the reaction rates in solids, the results of these studies were not used for kinetic evaluations until the 1930s. The explosive development of non-isothermal kinetics began in the late 1950s when thermal analysis instruments became commercially available [600, 601]. Since that time there has been an ever increasing number of works dealing with methods of determining Arrhenius parameters and the reaction model from non-isothermal experiments. The advantages of the non-isothermal experimental technique are at least partially offset by the computational difficulties associated with the kinetic analysis [602]. In particular, DSC has been widely recognized as useful method to determine cure kinetics of thermosetting resins [603]. Assuming proportionality between the heat flow (Φ) and the rate of cure ($d\alpha/dt$) can be expressed as:

$$\frac{d\alpha}{dt} = \frac{\Phi}{\Delta H_c} \quad \text{(Eq. 6.1)}$$

where ΔH_c corresponds to the total enthalpy change associated with the crystallization process, Φ corresponds to the heat flow (W/g). The fractional conversion (α) can be easily obtained by partial integration of DSC curves with Eq. 5.1 In non-isothermal conditions, α can be calculated as:

$$\alpha = \frac{1}{\Delta H_c \beta} \int_{T_0}^{T} \Phi dT \quad \text{(Eq. 6.2)}$$

where β is the heating rate and T_0 corresponds to the beginning of the baseline approximation. The rate of kinetic process can be expressed as a product of temperature dependent rate constant K(T) and α dependent kinetic model function f(α):

$$\frac{d\alpha}{dt} = K(T)f(\alpha) \quad \text{(Eq. 6.3)}$$

According the assumption, the rate constant in Eq. 6.3 follows Arrhenius equation:

$$K(T) = Ae^{\frac{-E_a}{RT}} \quad \text{(Eq. 6.4)}$$

where A is the pre-exponential factor and E_a is the activation energy, R is the universal gas constant, and T is the absolute temperature (K). The curing kinetic calculation can be obtained by many different methods, e.g. Kissinger–Akahira–Sunose (KAS) method [604, 605], Friedman method [606], and integral methods, e.g. Friedman

method [607, 608]. Recently, many novel methods have been reported to calculate the cure kinetic, e.g. Málek method [609-611], Popescu method [612], Dollimore method [613], Strarink method [614], Vyazovkin method [615], especially, Málek method [603, 616-618] is getting more and more attention.

KAS, which has also been named maximum reaction rate method, is based on Coats-Redfern approximation [619]. E_a can be obtained from the maximum reaction rate where d(dα/dt)/dt is zero under a constant heating rate condition. The basic equation of the method in the integral form is:

$$\ln\left(\frac{\beta_i}{T^2{}_{P,i}}\right) = \ln\left(\frac{AR}{E_a}\right) - \frac{E_a}{RT_{P,i}} \quad \text{(Eq. 6.5)}$$

where β_i is the heating rate, $T_{p,i}$ is the peak temperature at different heating rates, R is the universal gas constant, A is the pre-exponential factor and E_a is the activation energy. In this method, E_a and A can be calculated from the slope and y intersect of the linear plot of -ln(β/$T^2{}_{pi}$) against (1/T_p), respectively. The value of E_a obtained in Eq. 6.5 is an overall value representing all complex reactions that occur during curing.

Friedman method is isoconversional procedure, introduced by Friedman [606], uses as its basis the following relationship:

$$\ln\left(\frac{d\alpha}{dt}\right) = \ln f(\alpha) + \ln A - \frac{E_a}{RT} \quad \text{(Eq. 6.6)}$$

which makes it possible to find the activation energy value from the slope of the line when ln(dα/dt) is plotted against 1/T for isoconversional fractions. In non-isothermal conditions, integral of the kinetic model function can be express as follow:

$$G(\alpha) = \frac{A}{\beta}\int_{T_0}^{T} e^{-\frac{E_a}{RT}} dT \quad \text{(Eq. 6.7)}$$

Using the logarithmic form of the kinetic Eq. 6.7, we obtain:

$$\ln G(\alpha) = \ln\frac{AE_a}{R} - \ln\beta + \ln\left(\frac{e^{-\frac{E_a}{RT}}}{\frac{E_a}{RT}} - \int_{\infty}^{\frac{E_A}{RT}}\frac{e^{-\frac{E_a}{RT}}}{\frac{E_a}{RT}}d(\frac{E_a}{RT})\right) \quad \text{(Eq. 6.8)}$$

Defining

$$x = \frac{E_a}{RT} \quad \text{(Eq. 6.9)}$$

$$P(x) = \frac{e^{-x}}{x} - \int_{\infty}^{x}\frac{e^{-x}}{x}dx \quad \text{(Eq. 6.10)}$$

The Eq. 6.8 can be rewritten as:

$$\ln G(\alpha) = \ln\frac{AE_a}{R} - \ln\beta + \ln P(x) \quad \text{(Eq. 6.11)}$$

where P(x) is the integral of temperature, the pre-exponential factor (A) can be got by the following equation:

$$A = \frac{G(\alpha)\beta R}{p(x)E_a} \quad \text{(Eq. 6.12)}$$

Málek method is another isoconversional procedure. It is an effective method to further determine the most probable mechanism function [620]. This method using the logarithmic form of the kinetic Eq. 6.3:

$$\ln\frac{d\alpha}{dt} = \ln[Af(\alpha)] - \frac{E_a}{RT} \quad \text{(Eq. 6.13)}$$

In non-isothermal conditions, dt=(dβ/dt). Therefore, Eq. 6.13 can be replaced by:

$$\ln\left(\frac{\beta d\alpha}{dt}\right) = \ln(Af(\alpha)) - \frac{E_a}{RT} \quad \text{(Eq. 6.14)}$$

The slope of ln (βdα/dt) versus 1/T for the same value of α at any heating rate gives the value of E_a [611]. The value of E_a can be used to find the appropriate kinetic model which best describes the non-isothermal DSC data. In the Málek method, two special functions (i.e. y(α) and z(α)) are defined as follows:

$$y(\alpha) = (\frac{d\alpha}{dt})e^x \quad \text{(Eq.6.15)}$$

$$z(\alpha) = \pi(x)(\frac{d\alpha}{dt})\frac{T}{\beta} \quad \text{(Eq. 6.16)}$$

where x is reduced activation energy and π(x) is an approximation of the temperature integral. In this method, π(x) function is expressed by the 4th rational expression of Senum et al [621]:

$$\pi(x) = \frac{x^3 + 18x^2 + 88x + 96}{x^4 + 20x^3 + 120x^2 + 240x + 120} \quad \text{(Eq. 6.17)}$$

The maximum of y(α) function (α_M) and z(α) function (α_p^∞) are the important parameters in this method for the determination of the most suitable f(α) function. Their combination can suggest the choice of the kinetic model as shown in Fig. 6.1 [611]. By differentiation of Eq. 6.16, and get z`(α)=0, we obtain that:

$$-f'(\alpha_p^\infty) \times G(\alpha_P^\infty) = 1 \quad \text{(Eq. 6.18)}$$

where f`(α) is the differential of the kinetic model function and G(α) is integral of the kinetic model function, namely:

$$G(\alpha) = \frac{AE_a}{\beta R} \times \frac{e^{-x}}{x} \times \pi(x) \quad \text{(Eq. 6.19)}$$

Combining Eq. 6.17 and Eq. 6.18, pre-exponential factor (A) can be expressed as:

$$A = -\frac{\beta x_p^{\infty}}{T_p^{\infty} f^{'}(\alpha_p^{\infty})} e^{x_p^{\infty}} \quad \text{(Eq. 6.20)}$$
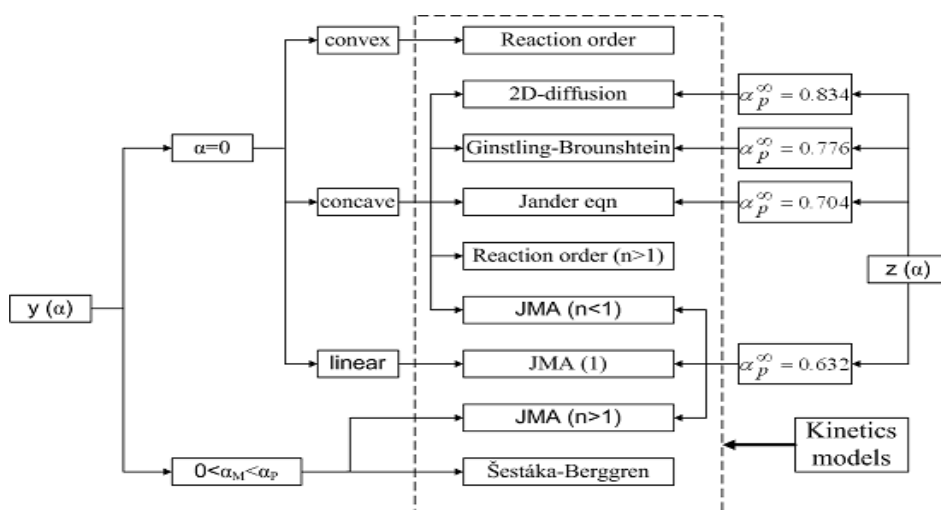
Fig. 6.1 Schematic diagram of the kinetic model determination.

6.3 Materials and Methods

6.3.1 Materials

The materials used in the study are summarized in Table 6.1.

Table 6. 1 Summary of chemical reagents and instruments for analysis

Chemical reagent, raw material, instrument	Provider
SP®Epoxy SP106 (Bisphenol-A-epichlorohydrin epoxy)	Gurit UK Ltd
DETA	Sigma-Aldrich Company Ltd
Heating mantle (500)	Fisher Scientific UK Ltd
3-neck round bottom flask (500 ml)	Fisher Scientific UK Ltd
Freeze dryer	MMM Medcenter
IKA®Overhead stirrer	Fisher Scientific UK Ltd
Fisherbrand®Ultrasonic bath	Fisher Scientific UK Ltd
Spectrum Two™ ATR-FTIR	PerkinElmer UK Ltd
Zeiss Supra 35 VP FEG-SEM	Oxford Instruments GmbH
MMM Vacucell 22 litre Vacuum Oven	MMM Medcenter

6.3.2 Fabrication of nanocellulose/epoxy nanocomposite

Obviously, the curing agent for the matrix must possess high compatibility with the matrix. Therefore, if the curing agent can react with nanocellulose, the curing agent modified nanocellulose will also possess high compatibility with the matrix. It has been found that DETA can react with cellulose and form DETA-cellulose complex [622-626]. The main chemical structure of nanocellulose is similar with cellulose.

Therefore, in this chapter, we employed DETA to modify the nanocellulose which was fabricated as described in chapter 3.

Nanocellulose powder was obtained by freezing dryer as described by Habib et al [446]. Then, 4 % of the nanocellulose powder (on the weight of DETA, in this experiment we found that when the addition of nanocellulose powder was larger than 4%, the suspension would form gel) was added into 3-neck round bottom flask and mixed with 150 ml DETA. The mixture was then treated at 100 °C in conjunction with the ultrasonication. After 1 hour, the mixture was kept in thermostat water-bath at 50 °C. The modified nanocellulose and 10 parts per one hundred (phr) (the amount of DETA for epoxy system is always used around 7-20 phr [627]) DETA were then added into the epoxy. After degasing, the resin was put into the model (110×20×1 mm) and cured for 2h under various curing temperatures (80 ℃, 90 ℃, 100 ℃, 110 ℃, 120 ℃, 130 ℃, 140 ℃) with 0.025 % dosage of nanocellulose. In this chapter the factors what we investigated were curing temperature and the dosage of nanocellulose, but the number of level for each factors were high. Therefore we employed single factor method to investigate the effect of both factors. We then optimized the curing temperature and investigated the effect of the dosage of nanocellulose with various levels 0 %, 0.0175 %, 0.035 %, 0.0525 % and 0.07 % (on the weight of epoxy) under the optimized curing temperature.

6.3.3 Tensile testing

The tensile testing of nanocomposite films was carried out with Instron 5566 according to ASTM D638 at $20\pm2°C$ and $65\pm2\%$ relative humidity with a 25 mm gauge length (crosshead speed of 0.1 mm min^{-1}).

6.3.4 Size of nanocellulose in the matrix

Zeiss Supra 35 VP FEG-SEM was performed to investigate the effect of modification on the dispersion of nanocellulose into the epoxy. Unmodified nanocellulose/epoxy nanocomposite and the DETA modified nanocellulose/epoxy nanocomposite were used for the FEG-SEM observation. The test pieces were plasma etched to clean the surface of test pieces at first. Following etching, in order to obtain high resolution image, surface of nanocomposites observations were performed under the following conditions: an acceleration voltage of 9.65 kV and the secondary electron mode with images collected digitally. UTHSCSA ImageTool software was finally used to measure the size of nanocellulose.

6.3.5 Cure kinetics of nanocellulose/epoxy nanocomposite

DSC which measures the heat flow of the sample as a function of temperature has widely used to study the cure kinetics of thermosetting polymer [603]. The advantages of the non-isothermal experimental technique are at least partially offset

by the computational difficulties associated with the kinetic analysis [602]. Therefore, in this chapter, we employed DSC to investigate the cure kinetics of nanocellulose/ epoxy nanocomposite with non-isothermal method. The cure kinetics of nanocellulose /epoxy nanocomposites were measured by employing a DSC 6000 modulated differential scanning calorimeter from Pekin-Elmer. The procedure of cure kinetics analysis was performed as following:

(i) Preparation of samples

Nanocellulose which was pretreated with DETA was added into 10 g epoxy with 0, 0.0175 %, 0.035 %, 0.0525 % and 0.07 % with the weight of epoxy. The addition of DETA is 10 phr (this is a normal addition for the epoxy curing with DETA). After mixing, the sample was put into vacuum oven and degas for 5 min. Finally, store these samples in the fridge to avoid the curing of epoxy.

(ii) DSC measurement

About 8.0 mg of sample was used for each DSC running (the cure kinetics calculations are most reliable on data from experiments that use low sample weight between 1-10 mg [464]). The sample was heated from 30 to 170 °C (in our trial for the cure kinetics experiment the finishing temperature was between 160 °C and 170 °C) with different heating rates i.e. 5, 10, 15 and 20 °C min^{-1} (for reliable cure kinetics results the portion of the data to be analyzed should fall in a reasonable progression from slow to fast heating rates [464], the rate between 5 °C min^{-1} and 15 °C min^{-1} is slow heating rate [464]) under nitrogen atmosphere (the purity is 99.9999%, and the gas input rate is 30 ml min^{-1}).The curing thermal data were obtained by means of DSC 6000 modulated differential scanning calorimeter from Pekin-Elmer,

(iii) Data analysis

The curing thermal data which were obtained from the second step were analyzed by three main methods (corresponding background knowledge have been demonstrated in *6.2 Theoretical foundation of cure kinetics*), namely, KAS, Friedman and Málek method. The integral of the kinetic model function and temperature were calculated using Maple 13 software, and the other data were calculated using Excel 2003.

In addition, the ATR-FTIR analysis was carried out as described in *4.2.2.5 ATR-FTIR*.

6.4 Results and Discussion

6.4.1 Preparation of nanocellulose/epoxy nanocomposite

6.4.1.1 Effect of curing temperature

Table 6. 2 Effect of the curing temperature on nanocomposite mechanical properties (nanocellulose 0.025%)

Curing temperature (°C)	Modulus (MPa)	C.V.	Tensile stress (MPa)	C.V.	Tensile strain (%)
80	1243.61	6.14	50.14	6.86	5.13
90	1293.24	4.27	52.64	5.16	5.30
100	1174.86	23.86	53.21	6.39	5.66
110	1125.41	6.82	53.86	4.60	6.36
120	1131.24	5.04	55.35	7.08	6.47
130	1150.85	6.81	59.38	7.56	6.80
140	1072.15	12.48	50.11	13.14	5.40

Curing temperature is a main parameter which can affect the curing degree of epoxy [628]. Mechanical properties of nanocomposites with various curing temperatures were summarized in Table 6.2. Although with the increase of temperature the modulus of nanocomposite shows a tendency of decrease, a slight increase of modulus at 90 °C can be observed. As for the tensile stress and strain, it shows similar tendency that: the values increase with the increase of curing temperature at first, when the curing temperature is 130 °C, the tensile stress and strain can get maximum of 59.38 MPa, 6.8 %, respectively. This may be due to the conversion of epoxy which can affect the crystallinity of composite.

6.4.1.2 Effect of dosage of nanocellulose

Table 6. 3 Effect of dosage of nanocellulose on nanocomposite mechanical properties (curing temperature 130 °C)

Dosage of Nanocellulose (%)	Modulus (MPa)	Tensile stress (MPa)	Tensile strain (%)
0	1271.20	54.16	5.52
0.0175	1227.08	51.24	5.02
0.025	1150.85	59.38	6.80
0.0325	1289.32	62.52	7.04
0.0525	1154.29	55.22	5.57
0.07	1100.94	51.56	5.42

Table 6.3 summarized the effect of the dosage of nanocellulose which was modified high content of DETA on the mechanical properties of epoxy nanocomposites. Polymer-particle and particle-particle interactions are commonly the determining factors for the strength of the particle reinforced polymers [629]. In low addition, due to the steric hindrance, the aggregation of nanoparticles is less than that of in high addition. Therefore, the polymer-particle interaction effect plays an important role for the mechanical properties of composite, the better internal interface will in favour of the dispersion of nanocellulose and improve the mechanical properties of composite

[630]. But, as Table 6.3 shows, a slight decrease can be observed when the addition of nanocellulose is 0.0175 %. This can be explained as follows:

(i) Formation of carboxylic acid ammonium salt in the DETA modified nanocellulose. This can be proved by the ATR-FTIR As shown in Fig. 6.2, compared with nanocellulose without modification, three bands can be observed in the spectrum of DETA modified nanocellulose, i.e. the band at 1568 cm^{-1} which is assigned as O=C stretching from amide [631], the band at 1558 cm^{-1} which is assigned as asymmetric stretching of O=C from carboxylic acid salts and the band at 1471 cm^{-1} which is assigned as symmetric stretching of O=C from carboxylic acid salts [632]. As described in Chapter 4, the hydroxyl groups in cellulose were oxidized into carboxyl groups during the nanocellulose fabrication process. The formation of carboxylic acid ammonium salt can be ascribed to the reaction between carboxyl in nanocellulose and primary amine in DETA (see the step 1 in Fig. 6.3).
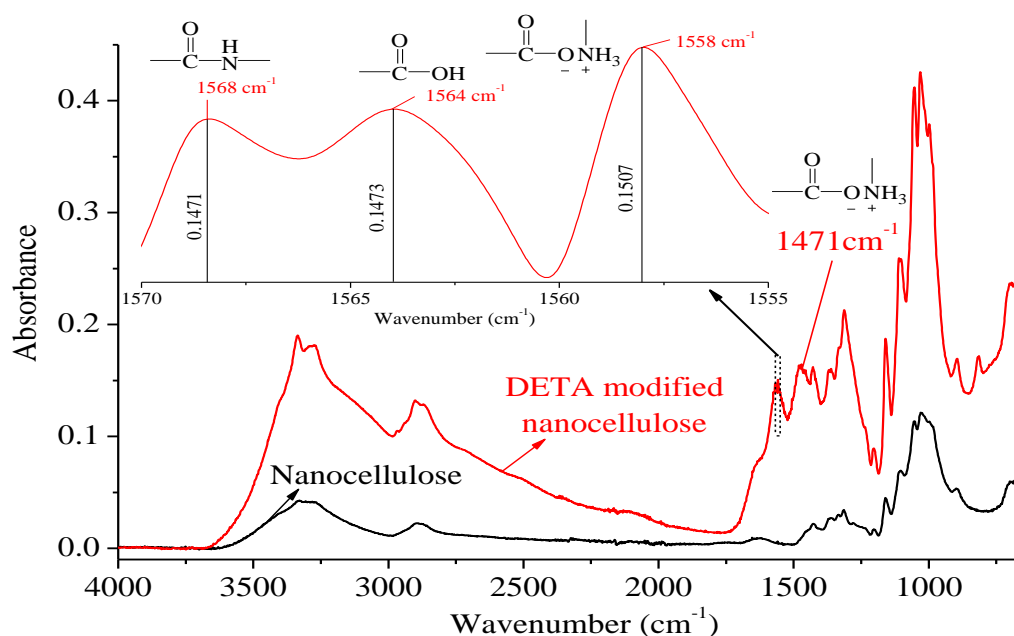
Fig. 6.2 ATR-FTIR spectra of nanocellulose and DETA modified nanocellulose.

(ii) Carboxylic acid ammonium salt in DETA-nanocellulose complex crosslink epoxy (see the step 2 in Fig. 6.3), because carboxylic acid ammonium salt can catalytically crosslink epoxy by ammonium and form quaternary ammonium salt [633].

(iii) Low chemical bond strength. Due to the crosslink of carboxylic acid ammonium with long chain epoxy, the ionic diameter of the quaternary ammonium salt get very large, which in turn gives rise to the decrease of the ionic band strength which far less the covalent bond between primary amine and epoxy [634]. Therefore the reaction between the carboxylic acid ammonium salt and epoxy will reduce the mechanical properties of the epoxy.
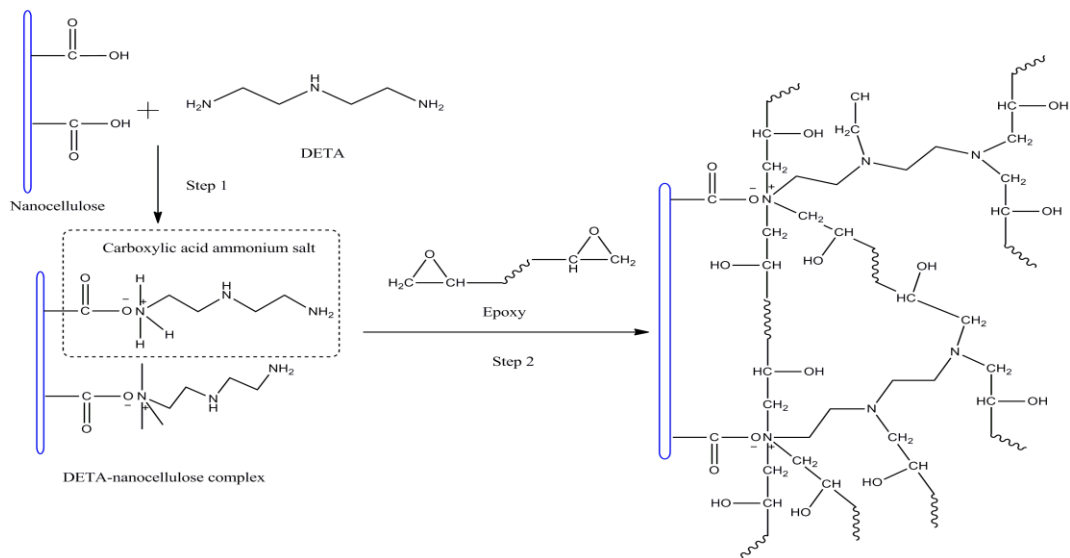
Fig. 6.3 Schematic of formation of DETA-nanocellulose complex and the reaction of DETA-nanocellulose complex with epoxy.

Table 6. 4 Summary of the enthalpy change, mean enthalpy change under various heating rate and dosage of nanocellulose

Dosage of nanocellulose (%)	Heating rate (°C min^{-1})	ΔH (J g^{-1})	Mean ΔH (J g^{-1})
0	5	-208.99	-218.61
	10	-227.25	
	15	-247.82	
	20	-190.38	
0.0175	5	-261.05	-260.35
	10	-256.17	
	15	-274.64	
	20	-249.55	
0.035	5	-356.34	-348.43
	10	-357.35	
	15	-382.56	
	20	-297.48	
0.0525	5	-254.27	-297.93
	10	-287.53	
	15	-345.22	
	20	-304.70	
0.07	5	-230.37	-238.56
	10	-254.27	
	15	-242.53	
	20	-227.07	

However, with the increase of nanocellulose, the tensile stress and tensile strain increase. It can be observed from Table 6.3 that the best reinforcement effect appears when the addition of nanocellulose is 0.035 %. Compared with the pure epoxy, the tensile stress and tensile strain of nanocomposite increase from 54.16 MPa and 5.52 % to 62.52 MPa and 7.04 % respectively. The increase of tensile stress and tensile strain are 15.44 % and 27.47 % respectively. In low addition, the formation of quaternary ammonium salt can result in the decrease of mechanical of nanocomposite. Therefore the increase in high addition the chemical reaction between nanocellulose and epoxy should be different with that of in low addition. We conjecture that the chemical reaction is carboxyl-epoxyl reaction. This assumption is based on two evidences:

(i) The increase of the absolute enthalpy change (ΔH). The enthalpy change of the curing reaction was determined by DSC (as shown in Table 6.4, ΔH can be calculated from the area of the region between the curve and the baseline), the negative ΔH indicates the curing process of epoxy is heat-releasing exothermic processes. As Table 6.4 shows, the mean ΔH of curing reaction is -260.35 J g^{-1} when the nanocellulose addition is 0.0175 %. But when the addition of nanocellulose is 0.035 %, the ΔH decrease significantly (the value is -348.43 J g^{-1}) indicating that a reaction with more heat-release appear when the addition of nanocellulose is 0.035 %. Carboxyl can react with epoxy and form carboxyl-epoxy ester (but need higher activation energy) [633]. Moreover, the carboxyl-epoxyl reaction releases more heat than that of DETA-epoxy curing reaction [635]. Therefore, the increase of the absolute enthalpy change (ΔH) can be ascribed to the reaction of carboxyl in the nanocellulose.

(ii) Higher activation energy (Ea). The activation energy (this term is defined as the energy that must be overcome for a chemical reaction to occur [636]) of curing which will be discussed in *6.4.3 Cure kinetics of nanocellulose/epoxy nanocomposite*. Calculation shows that the higher activation energy appears in 0.035 % or 0.0525 % addition of nanocellulose. When the addition of nanocellulose is 0.0175 % or 0.07 %, the activation energy of curing is lower than that without nanocellulose. Moreover, the carboxyl-epoxy reaction needs higher activation energy [633]. Therefore, the increase of the activation energy can be ascribed to the reaction of carboxyl in the nanocellulose with epoxy.

As for the mechanism of the dosage of nanocellulose on the occurrence of various chemical reactions, we assume this is related with the steric hindrance. As Fig. 6.2 shows, the band at 1564 cm^{-1} which is assigned as O=C stretching from carboxyl [480] and the absorbance of this band is very close to the band at 1558 cm^{-1} which is assigned as asymmetric stretching of O=C from carboxylic acid salts. This indicates inside the DETA-nanocellulose complex there still exists lots of carboxyl groups which has similar number with the carboxylic acid salts. In low addition, the concentration of DETA-nanocellulose complex in the epoxy matrix is low; the steric effect of the DETA will decrease the probability of the collision between carboxyl

groups with epoxy. In high addition, before the occurrence of aggregation, the probability of the collision between carboxyl groups with epoxy can increase.

When the addition of nanocellulose higher than 0.035 %, the tensile stress and tensile strain start to decrease which may be due to the aggregation of nanocellulose particles in the epoxy matrix, because (i) the particle aggregation tends to reduce the strength of the material [637] and (ii) the aggregation can decrease the surface area of the particles [638] resulting in the decrease the interface between particles and the matrix. Nevertheless, for the modulus of the nanocomposites, it seems not to show any correlation ship with the dosage of nanocellulose.

6.4.2 Effect of DETA modification

The mechanical properties of nanocellulose/epoxy nanocomposites without and with modification are summarized in Table 6.5. As Table 6.5 shows, DETA modification can improve the mechanical properties of composites. Compared with unmodified nanocellulose nanocomposite, the modulus, tensile stress and tensile strain of modified nanocellulose nanocomposite were increased by 4.93 %, 29.36 % and 57.49 % respectively. As described above, the DETA modification will introduce the carboxylic acid ammonium salt into the nanocellulose and results in the crosslink of nanocellulose with epoxy groups. The better interaction between nanocellulose and the epoxy will increases the dispersity of nanocellulose into epoxy. This can be confirmed by the measurement of the nanocellulose in the matrix with FEG-SEM. As shown in Table 6.5, after modification, the size of nanocellulose in the matrix decreases from 785 nm to 350 nm.

Table 6. 5 Comparison of mechanical properties unmodified and modified nanocellulose nanocomposites and the size of nanocellulose in the matrix

Samples	Modulus (MPa)	Tensile stress (MPa)	Tensile strain (%)	Size of nanocellulose in the matrix (nm)	C.V. (%)
Unmodification	1228.72	48.33	4.47	785	22.66
DETA modification	1289.32	62.52	7.04	350	23.17

6.4.3 Cure kinetics of nanocellulose/epoxy nanocomposite

6.4.3.1 KAS cure kinetics

KAS, which has also been named maximum reaction rate method, the activation energy (E_a) and pre-exponential factors can be obtained by using this method without assuming any model of kinetic parameters and integrating the exothermic peak. In this method peak temperature under various heating rate is a key parameter. Fig. 6.4 shows the DSC thermograms of the nanocomposites with various amounts of nanocellulose addition were recorded at 5, 10, 15, 20 °C min^{-1}, illustrating the

variation of the fractional conversion as a function of temperature for these nanocomposites. From DSC thermograms of these samples as shown in Fig. 6.4, key information about the curing reaction (1) peak temperature (T_p) and (2) enthalpy change (ΔH) can be obtained. The results of enthalpy change are recorded in Table 6.4 and the other results of peak temperature are recorded in Table 6.6. As shown in Table 6.6, the peak temperature increases at first, but starts to decrease follow the 0.035 % addition of nanocellulose. This may be due to the different of the maximum exothermal peak temperature between the reaction of carboxylic acid ammonium salt with epoxy and DETA with epoxy. The logarithm plots of heating rate versus the reciprocal of the absolute peak temperature of nanocellulose/epoxy nanocomposite under various dosages of nanocellulose are given in Fig. 6.5. As shown in Fig. 6.5, a good linear relationship (the R^2 more than 0.98) between the heating rate and the reversal of the exothermic peak temperature can be observed. Activation energy and pre-exponential factor are listed in Table 6.6. It can be found that with the increase of the nanocellulose addition, activation energy for the systems increases at first, and decreases when the dosage of nanocellulose higher than 0.0525 %.

Table 6. 6 Curing characteristics of epoxy/nanocellulose with various dosages of nanocellulose and kinetic parameters evaluated with KAS analysis

Dosage of nanocellulose (%)	Heating rate (°C min^{-1})	T_p (°C)	E_a (KJ mol^{-1})	lnA
0	5	67.75	52.7070	10.3686
	10	80.65		
	15	87.72		
	20	91.89		
0.0175	5	68.61	51.1669	9.7607
	10	81.16		
	15	88.49		
	20	93.96		
0.035	5	78.02	53.9854	10.2825
	10	88.85		
	15	96.54		
	20	103.63		
0.0525	5	72.34	54.6751	10.8463
	10	83.52		
	15	91.54		
	20	96.38		
0.07	5	66.92	50.5724	9.6396
	10	79.68		
	15	86.21		
	20	92.62		
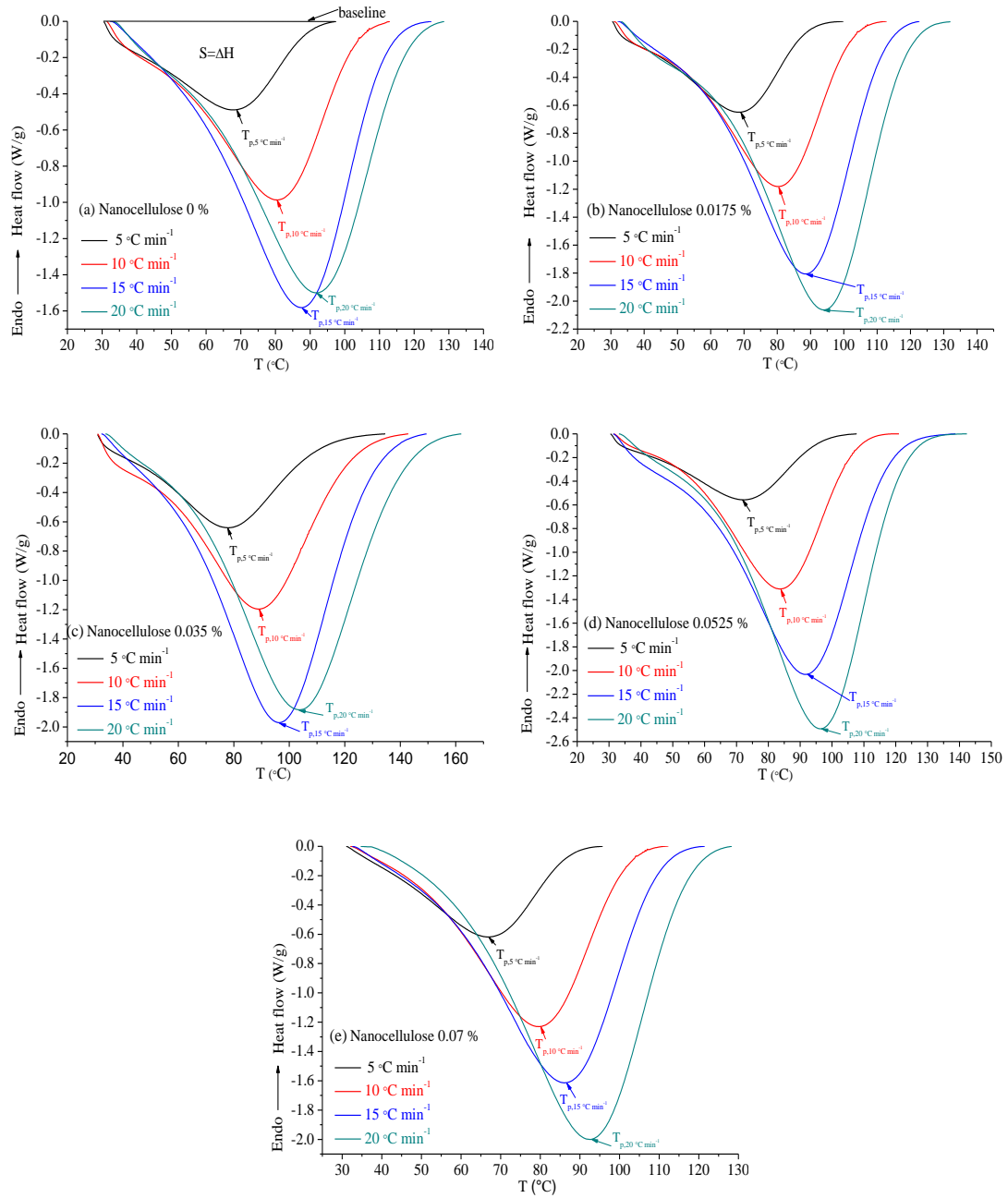
Fig. 6.4 DSC curves recorded for nanocellulose/epoxy nanocomposites at different heating rate with various addition of nanocellulose: (a) 0 %; (b) 0.0175 %; (c) 0.035 %; (d) 0.0525 % and (e) 0.07 %.
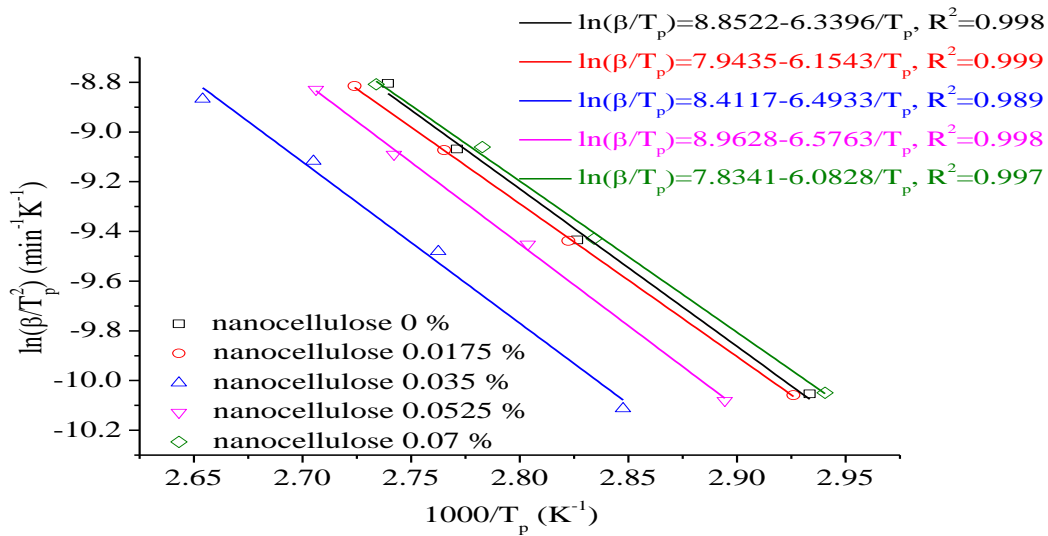
Fig. 6.5 KAS analysis of the cure process of epoxy with various dosages of nanocellulose.

,

6.4.3.2 Friedman cure kinetics

According to the Friedman method, linear relationships $\ln(d\alpha/dt)$ vs $1000/T$ under various dosages of modified nanocellulose for the fractional conversion (α) from 0.1 to 0.9 were established, these plots are shown in Fig. 6.6. Model independent values of the activation energy were determined from the slope of the resulted plots. Obtained values are invariant with respect to fractional conversion (Fig. 6.7). It can be observed from Fig. 6.7 that: (i) when the dosage of nanocellulose is 0.035 % or 0.0525 %, the E_a of the nanocomposite curing is higher than that of neat epoxy, especially when the dosage of nanocellulose is 0.035 %; in contrast, when the dosage of nanocellulose is 0.0175 % or and 0.07 %, the E_a of the nanocomposite curing is lower than that of neat epoxy; these changing tendencies agree quite well with that of mechanical properties of the composite; (ii) for the samples of neat epoxy, dosage of nanocellulose with 0.0175 % and 0.07 %, E_a is practically constant in the conversion interval $0.3<\alpha<0.7$, with a slight tendency to decrease for conversion out of this interval; however, for the nanocellulose addition with 0.035 % and 0.0525 %, the dependence of the E_a as a function of conversion was observed, this may be due to the kinetic compensation effect [639]. Pre-exponential factor and average E_a for different nanocellulose/epoxy system with various heating rates are listed in Table 6.7. As shown in Table 6.7, compared with the E_a which was calculated by KAS method, under the same heating rate, substantially different values can be found from Friedman method. It is possible that this disagreement between Friedman method and KAS and Vyazovkin may be attribute to the systematic errors which arise from the numerical differentiation of the experimental data involved in Friedman method.[640]
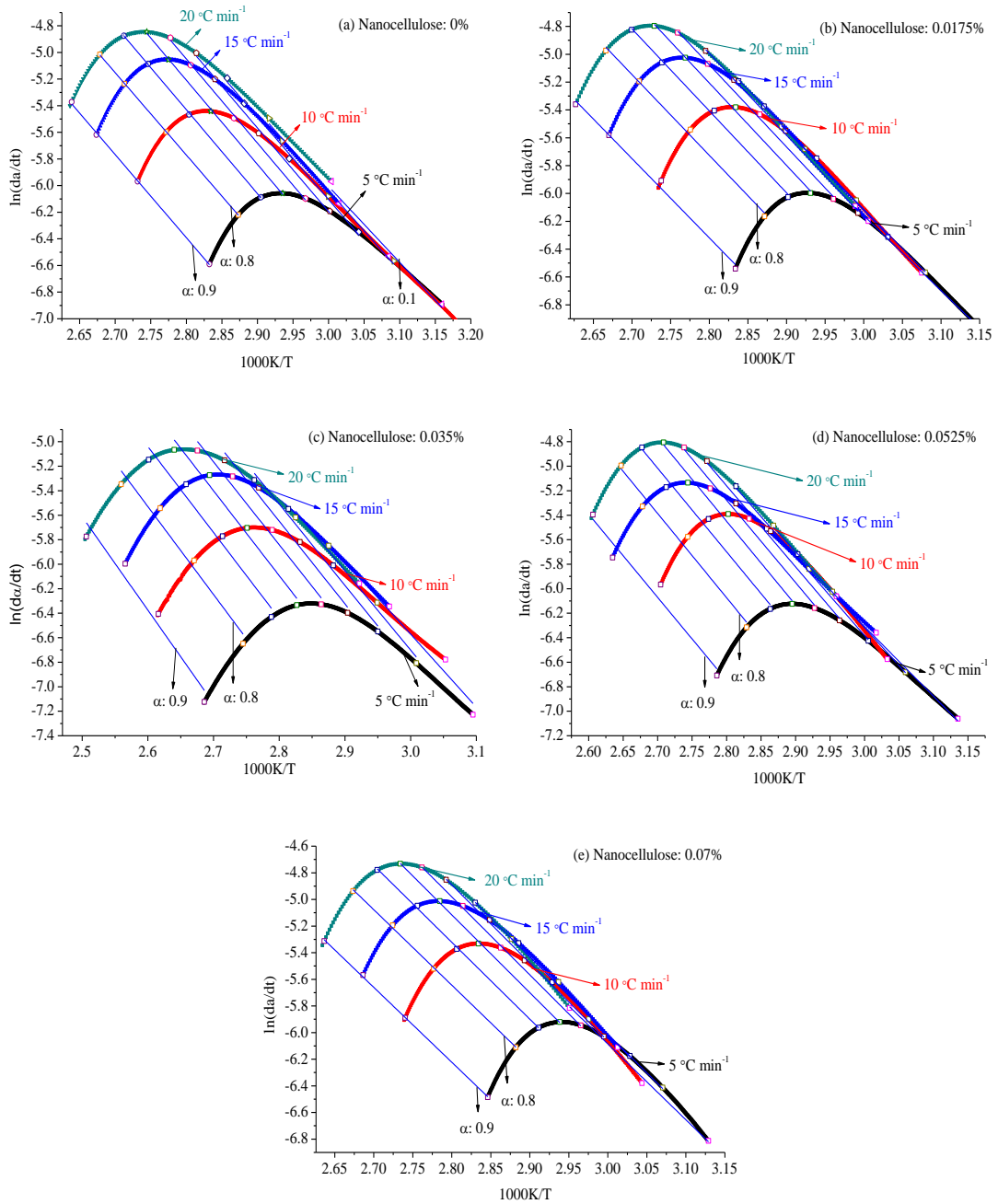
Fig. 6.6 Friedman plots of the epoxy/nanocellulose nanocomposite with various dosages of nanocellulose: (a) 0 %; (b) 0.0175 %; (c) 0.035 %; (d) 0.0525 % and (e) 0.07 %.
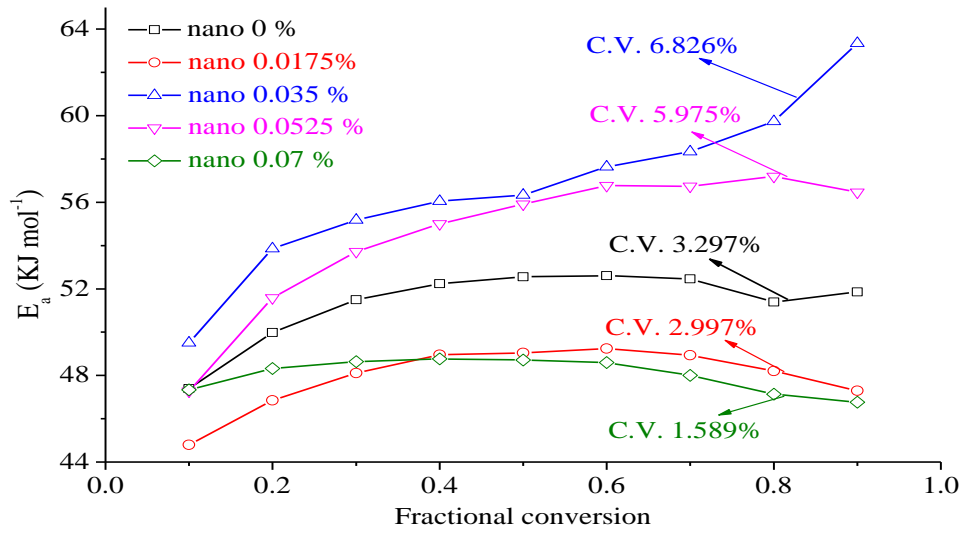
Fig. 6.7 Variation of E_a versus conversion for epoxy cure kinetics with various dosages of nanocellulose.

Table 6. 7 The kinetic parameter evaluated with Friedman method

Dosage of nanocellulose (%)	Heating rate (ºC min⁻¹)	E_a (KJ mol⁻¹)	lnA	lnA
0	5	52.4673	17.45535	17.54677
	10		17.50858	
	15		17.61276	
	20		17.61037	
0.0175	5	49.0413	17.26578	16.65813
	10		16.63354	
	15		16.66624	
	20		16.06696	
0.035	5	57.0912	19.61427	18.90331
	10		19.11522	
	15		18.64162	
	20		18.24214	
0.0525	5	56.1063	19.68315	18.92552
	10		18.96891	
	15		18.68455	
	20		18.36547	
0.07	5	48.5199	17.44949	16.828645
	10		16.95426	
	15		16.59674	
	20		16.31409	

6.4.3.3 Málek cure kinetics
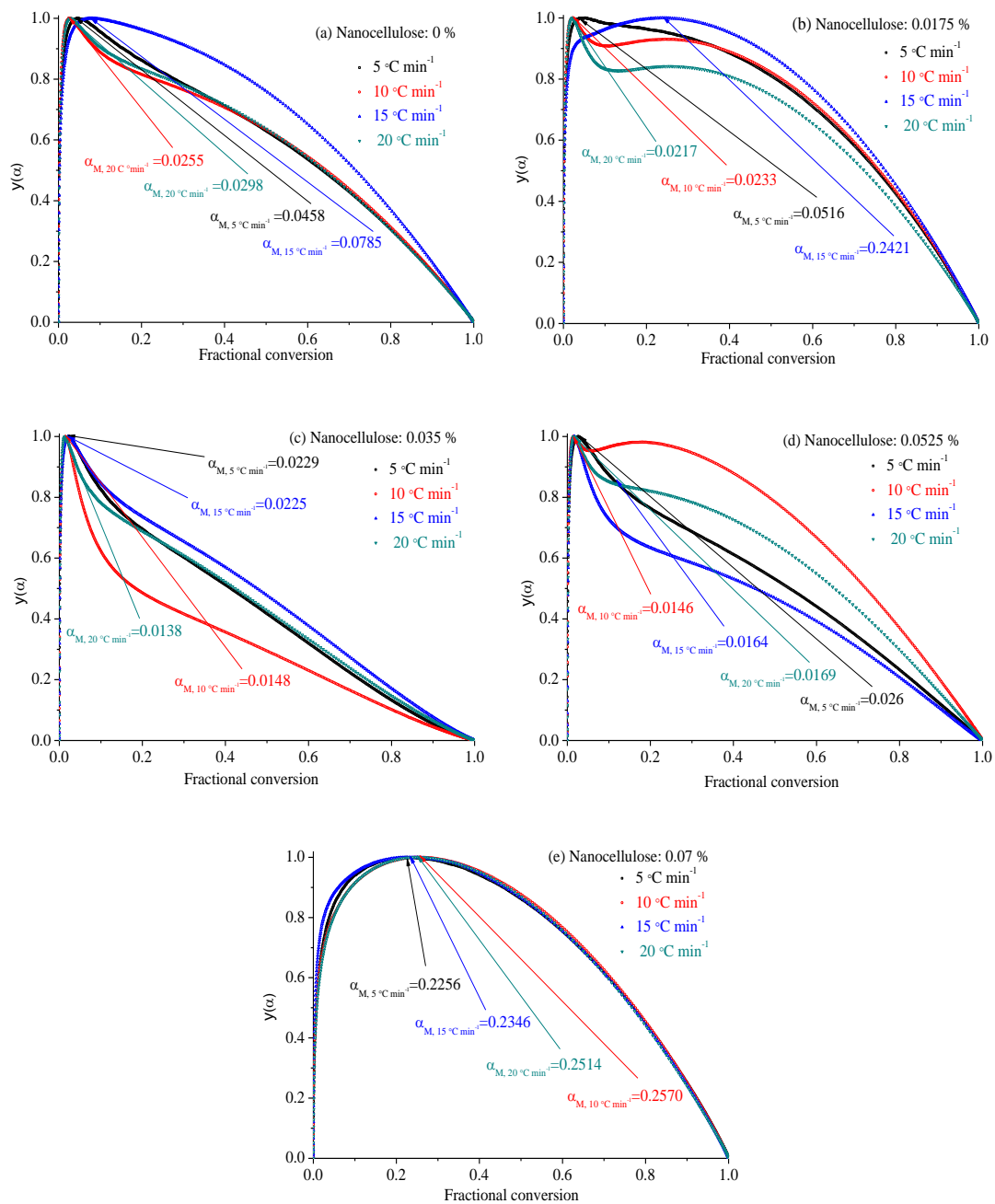
Fig. 6.8 Variation of y(α) function versus conversion for nanocellulose/epoxy nanocomposites at different heating rate with various addition of nanocellulose : (a) 0 %; (b) 0.0175 %; (c) 0.035 %; (d) 0.0525 % and (e) 0.07 %.
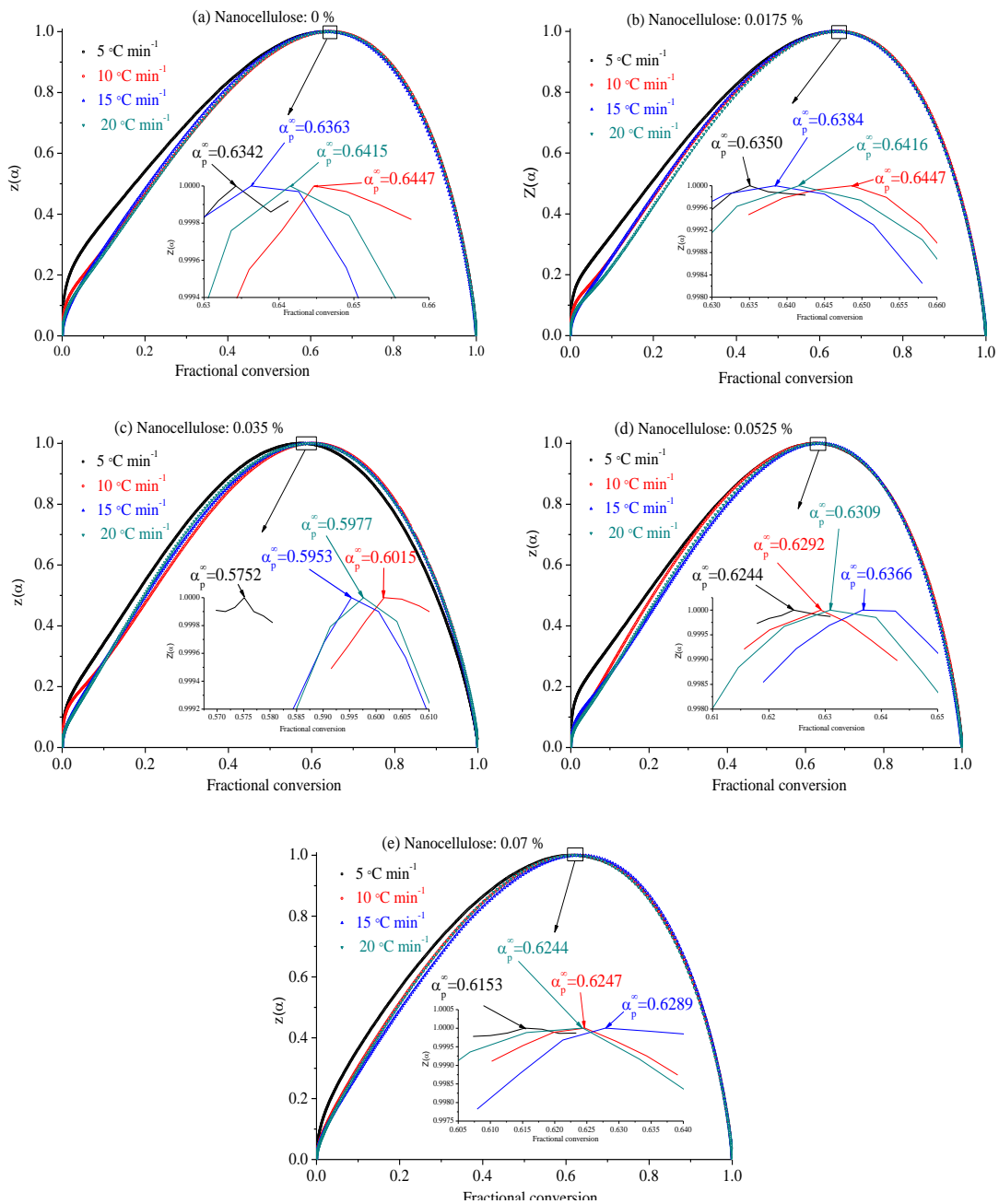
Fig. 6.9 Variation of z(α) function versus conversion for nanocellulose/epoxy nanocomposites at different heating rate with various addition of nanocellulose : (a) 0 %; (b) 0.0175 %; (c) 0.035 %; (d) 0.0525 % and (e) 0.07 %.

The value of E_a determined from DSC data was used to calculate both $y(\alpha)$ and $z(\alpha)$ using Eqs. 6.15 and 6.16, respectively. It should be noted that the procedure for calculated the activation energy by Málek method is same with Friedman method. Therefore, in this section, the E_a which were calculated in the previous section was used as the activation energy in this section. Fig. 6.8 and 6.9 show the variation of $y(\alpha)$ and $z(\alpha)$ values with conversion, respectively. The values of both $y(\alpha)$ and $z(\alpha)$ were normalized within the (0, 1) for various heating rates.

Table 6. 8 The values of α_p, α_M and α_p^{∞} obtained from DSC thermograms analysis

Dosage of nanocellulose (%)	Heating rate (ºC min^{-1})	α_p	α_M	α_p^{∞}
0	5	0.6085	0.0458	0.6342
	10	0.6273	0.0255	0.6447
	15	0.6107	0.0785	0.6363
	20	0.6179	0.0298	0.6415
0.0175	5	0.6176	0.0516	0.635
	10	0.6164	0.0233	0.6487
	15	0.6121	0.2421	0.6384
	20	0.6168	0.0217	0.6416
0.035	5	0.5446	0.0229	0.5752
	10	0.5714	0.0148	0.6015
	15	0.5696	0.0225	0.5953
	20	0.5597	0.0138	0.5977
0.0525	5	0.6047	0.026	0.6244
	10	0.5974	0.0146	0.6292
	15	0.6072	0.0164	0.6366
	20	0.6064	0.0169	0.6309
0.07	5	0.5912	0.2256	0.6153
	10	0.6005	0.257	0.6247
	15	0.6079	0.2346	0.6289
	20	0.5980	0.2514	0.6244

(α_p the fractional conversion at the maximal heat flow, α_M the fractional conversion at the maximum of y(α) function and α_p^{∞} the fractional conversion at the maximum of z(α) function)

Maxima of y(α) and z(α) function are the main parameters to decide the choice of the kinetic model [609]. The values of α_p, α_M and α_p^{∞} obtained from DSC thermograms analysis were shown in Table 6.8. As Table 6.8 shows, these values are independently of the heating rate. The values of α_M are higher than 0, but lower than α_p^{∞}, furthermore the value of α_M are not 0.632. Therefore, according the Málek method (see Fig. 6.1), the better kinetic model for nanocellulose/epoxy nanocomposite is Šesták-Berggren (SB) kinetic model. This indicates that the nanocellulose/epoxy systems still has autocatalytic feature of epoxy. The Šesták-Berggren kinetic model can be expressed as follow [641]:

$$f(\alpha) = \alpha^m (1-\alpha)^n \quad \text{(Eq. 6.21)}$$

where m and n are the kinetic exponents [609]. The kinetic parameter n can be obtained by the slope of the linear dependence ln(dα/dt) e^x) vs ln(α^p(1-α)), and

$$m = pn \quad \text{(Eq. 6.22)}$$

where

$$p = \frac{\alpha_M}{1 - \alpha_M} \quad \text{(Eq. 6.23)}$$

Table 6.9 shows the kinetic parameter evaluated by SB kinetic model, as it is shown in Table 6.8, the variation of the kinetic parameter values with the heating rate is placed in the experimental errors limit (within 10 % of the average value). To check the correctness of the SB kinetic model, plots of dα/dt vs temperature for various dosages of nanocellulose were pictured in Fig. 6.10 by using the data listed in Table 6.9. By comparison, the predicated curves of thee thermograms fit well with the experimental results (dots shown in Fig. 6.10). This indicates that two parameter SB model well describes the curing process of nanocellulose/epoxy resin systems.

Table 6. 9 The kinetic parameters evaluated for the curing of the tested epoxy with various dosages of nanocellulose

Dosage of nano (%)	Heating rate (°C min^{-1})	Ea (KJ mol^{-1})	m	Mean m	n	Mean n	lnA	Mean lnA
0	5	52.4673	0.03841	0.04093	0.80026	0.85331	13.24284	13.26891
	10		0.02273		0.86874		13.24582	
	15		0.0766		0.89919		13.32214	
	20		0.02596		0.84504		13.26483	
0.0175	5	49.0413	0.04704	0.08727	0.86451	0.8512	12.0765	12.08712
	10		0.01987		0.83301		12.09085	
	15		0.26254		0.8219		12.16716	
	20		0.01964		0.88539		12.01396	
0.035	5	57.0912	0.02413	0.01895	1.02945	1.00508	14.00609	14.06559
	10		0.01566		1.04258		14.10455	
	15		0.02234		0.97055		14.1031	
	20		0.01368		0.97775		14.04864	
0.0525	5	56.1063	0.02468	0.01789	0.92449	0.95086	14.28489	14.346
	10		0.01299		0.87696		14.34393	
	15		0.01727		1.03598		14.37146	
	20		0.01661		0.966		14.38372	
0.07	5	48.5199	0.24792	0.27739	0.851	0.86661	14.29123	14.27003
	10		0.3029		0.8757		14.27457	
	15		0.26687		0.87069		14.26706	
	20		0.29185		0.86904		14.24727	
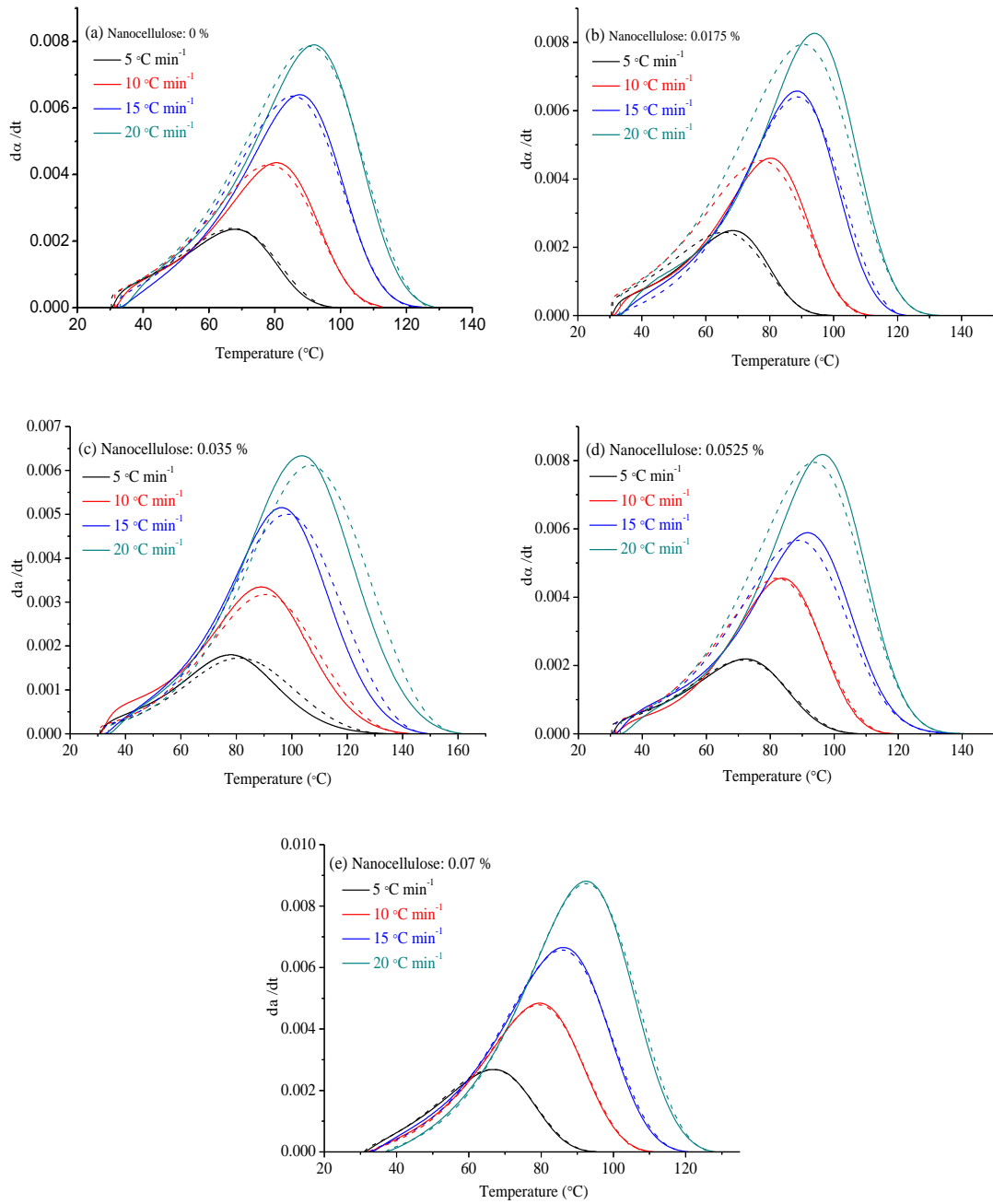
Fig. 6.10 Comparison of experimental (dot) and that predicated from SB model with various dosages of nanocellulose : (a) 0 %; (b) 0.0175 %; (c) 0.035 %; (d) 0.0525 % and (e) 0.07 %. (Solid curves= experimental data; dashed curves=predicted data)

6.5 Interim conclusions

In this chapter we investigated the second application of nanocellulose, i.e. nanocellulose nanocomposite. Epoxy was used as the matrix, and DETA was used as the curing agent of the matrix. Nanocellulose was modified by the curing agent (DETA). ATR-FTIR results showed that carboxylic acid ammonium salt was introduced into the nanocellulose under the DETA modification.

The preparation of modified nanocellulose/epoxy nanocomposite was optimized by the single factor method. The optimized results showed that the best mechanical properties of nanocomposite can be obtained under the conditions: curing temperature 130 ℃, and dosage of nanocellulose 0.035 %. Compared with epoxy, the modulus, tensile stress and tensile strain of the modified nanocellulose/epoxy nanocomposite increased 1.42 %, 15.44 % and 27.47 % respectively. The DETA modification facilitates the dispersion of nanocellulose into epoxy. FEG-SEM showed that the size of nanocellulose particle in the matrix can decrease from 785 nm to 350 nm. Compared with the unmodified nanocellulose/epoxy nanocomposite, the modulus, tensile stress and tensile strain of the modified nanocellulose/epoxy nanocomposite were increased by 4.93 %, 29.36 % and 57.49 % respectively.

DSC was used to investigate the effect of nanocellulose on the cure kinetics of epoxy. Three methods were employed for the analysis of cure kinetics, i.e. KAS, Friedman and Málek method. Substantially different of activation energy values can be found between Friedman method and KAS. The cure kinetics results which were calculated by Málek method showed that the DETA modified nanocellulose/epoxy systems still has autocatalytic feature of epoxy and Šesták-Berggren kinetic model can describe the curing process of DETA modified nanocellulose/epoxy resin systems very well.

Chapter 7 Conclusions

7.1 Major conclusions

This project focused on the (i) efficient production of nanocellulose from hemp fibres, and (ii) the application of nanocellulose, including the modification of hemp fibres with nanocellulose and the reinforcement of epoxy with nanocellulose.

The oxidation/sonication method was developed successfully to fabricate nanocellulose. RSM based on a five-level-four-variable CCD was employed to optimize the preparation conditions of nanocellulose, the yield of nanocellulose up to 54.11 % under the optimal condition, i.e. hydrolysis time 5h, hydrolysis temperature 67 °C, dosage of swelling agent 4.00 % and dosage of oxidant 70 %.

The nanocellulose was then characterized systematically by employing various analytical instruments. Three main characteristics of the nanocellulose, namely, size distribution and morphologies, chemical structure and crystalline, and thermal properties, were characterized. NTA results disclosed that oxidation/sonication method was able to fabricate nano-scale cellulose. This result was evidenced by the morphologies characterization with AFM and FEG-SEM. Morphologies analysis revealed that nanocellulose fabricated by oxidation/sonication had a low aspect ratio value (only 4) far less than that of acid method or mechanical method. XPS analysis revealed that hydroxyl groups in cellulose were oxidized into carboxyl groups during the oxidation/sonication process. ATR-FTIR results further reveal that parts of hydroxyl group in C2, C3 and C6 were during the process. XRD measurement showed that CI for hemp yarn and nanocellulose were 84.66 % and 86.59 % respectively. This indicated that the oxidation/sonication did not damage the crystalline structure of cellulose. DSC results showed that nanocellulose had lower carbonization temperature and thermostability.
.
The first application of nanocellulose in this project was the modification of hemp fibres with nanocellulose. Deformation of hemp fibres was the main research point in this part.

Four forms of deformation were found from hemp fibres, the MFA of S2 inner layer at fracture point which was measured by optical and their mean value was 6.16°. This indicated that deformation is the weak link point of fibres. The mechanism of deformation on the mechanical properties of hemp fibres was further revealed by employing spectroscopy technology. The crystallinity index examined by FTIR was 48.4 % for the hemp without deformations and 41.3 % for those within deformation regions, showing a significant reduction of crystallinity in the deformations. The chemical structure of deformations in hemp fibres was further revealed by FTIR. Weaker inter-and intra-molecular hydrogen bonding in the deformations of hemp

fibres were found by the deconvolution of FTIR spectra in the OH stretching region. This may be the main cause that induced the decrease of tensile strength in the hemp fibres, especially the intramolecular hydrogen bond of O(3)H---O(5). The FTIR spectra from 1370 cm^{-1} to 1330 cm^{-1} illustrated that the band at 1368 cm^{-1} and 1363 cm^{-1} disappeared in deformation regions, indicating the removal of the hemicelluloses in deformations and hence possible loss of lignin. The deconvolved FTIR spectra from 1330 cm^{-1} to 1215 cm^{-1} showed the S ring stretching, CH$_2$ rocking at C6 in cellulose, G ring stretching, C-C plus C-O plus C=O stretch and COH bending at C6 in cellulose, indicating reduction of lignin content in the deformation regions. The ratio of S (Syringyl, 1325cm^{-1})/ G (Guaiacyl, 1259 cm^{-1}) was 1.1 for the hemp without deformations comparing to 0.9 for the deformation regions, indicating higher cellulose content in the deformation regions. The effect of deformation on the modification which was carried out by DTAB-nanocellulose nanotechnology was revealed by EDX which showed that deformations affected the absorption of DTAB significantly. In the deformation of hemp fibres, the absorption ratio of DTAB was 0.98, while in the region without deformation this value was only 0.59. This indicated that much more nanocellulose was adsorbed on the deformation of hemp fibres

The reinforcing mechanism of the two-step nanocellulose modification on hemp fibres was also revealed by employing other two instruments, i.e. FEG-SEM and XRD. FEG-SEM results showed that nanocellulose covers the deformation of fibres with two ways, namely, (i) nanocellulose filling in the stria and (ii) bonding the inter-fibril on the gap between two fibrils. XRD results showed that the CI of un-modification, DTAB pretreatment and two-step modification were 55.17 %, 65.95 % and 76.39 % respectively. This indicated that the two-step nanocellulose modification could improve the crystallinity index of hemp fibres. We conjecture that the increase of CI is caused by the formation of hydroxyl bonds between nanocellulose with hemp fibres in the S2 layers and the non-crystalline regions of hemp fibres.

The interfacial property improvement of two-step modification on hemp fibres was investigated by employing XPS and ATR-FTIR. XPS confirmed that much more unsaturated polyester could be absorbed on the fibres with two-step modification. ATR-FTIR characterization showed that (i) the higher resin adsorption may be due to the esterification between hydroxyl groups at C-2 and C-6 of nanocellulose and carboxyl groups of unsaturated polyester, and (ii) the nanocellulose modification can benefit the adhesion of styrene on the surface of the modified fibres.

The second application of nanocellulose was the fabrication of nanocellulose/epoxy nanocomposite. DETA was used to modify nanocellulose. The preparation of nanocellulose/epoxy nanocomposite was optimized by single factor method. The optimized results showed that the maximal mechanical properties of nanocomposite can be obtained under the conditions: curing temperature 130 ℃, dosage of nanocellulose 0.035 %. Compared with epoxy, the modulus, tensile stress and tensile

strain of the modified nanocellulose/epoxy nanocomposite increased 1.42 %, 15.44 % and 27.47 % respectively. The DETA modification facilitates the dispersion of nanocellulose into epoxy. FEG-SEM showed that the size of nanocellulose particle in the matrix can decrease from 785 nm to 350 nm. Compared with the unmodified nanocellulose/epoxy nanocomposite, the modulus, tensile stress and tensile strain of the modified nanocellulose/epoxy nanocomposite were increased by 4.93 %, 29.36 % and 57.49 % respectively.

DSC was used to investigate the effect of nanocellulose on the cure kinetics of epoxy. Three methods were employed for the analysis of cure kinetics, i.e. KAS, Friedman and Málek method. Substantial difference in activation energy values can be found between Friedman method and KAS. The cure kinetics results which were calculated by Málek method showed that the DETA modified nanocellulose/epoxy system still have autocatalytic feature of epoxy and Šesták-Berggren kinetic model can describe the curing process of DETA modified nanocellulose/epoxy resin systems very well.

7.2 Recommendation for future work

Further investigation on the feature of natural fibres treated with nanocellulose is required in order to thoroughly understand the reaction of nanocellulose with natural fibres.

1. The efficiency of nanocellulose production could be further improved.

2. It is desirable to carry out a large scale of production for nanocellulose from raw hemp fibres.

3. The similar technologies could be applied to other natural fibres, such as, wood, flax, straw or other materials. Therefore, future work on these has great potential.

4. Nanocellulose-epoxy composites should be studied further for better understanding of their functionality of nanocellulose, such as state of the nanocellulose within the composites.

5. Up-scaling production of nanocellulose for specific application has been planned in the research group.

References

[1] Bledzki AK, Gassan J. Effect of coupling agents on the moisture absorption of natural fibre-reinforced plastics. Angewandte Makromolekulare Chemie. 1996;236:129-38.

[2] Bledzki AK, Gassan J. Composites reinforced with cellulose based fibres. Progress in Polymer Science. 1999;24:221-74.

[3] Keller A, Leupin M, Mediavilla V, Wintermantel E. Influence of the growth stage of industrial hemp on chemical and physical properties of the fibres. Industrial Crops and Products. 2001;13:35-48.

[4] Mediavilla V, Leupin M, Keller A. Influence of the growth stage of industrial hemp on the yield formation in relation to certain fibre quality traits. Industrial Crops and Products. 2001;13:49-56.

[5] Lakkad SC, Patel JM. Mechanical properties of bamboo, a natural composite. Fibre Science and Technology. 1981;14:319-22.

[6] Jain S, Kumar R, Jindal UC. Mechanical behaviour of bamboo and bamboo composite. Journal of Materials Science. 1992;27:4598-604.

[7] Ratna Prasad AV, Mohana Rao K. Mechanical properties of natural fibre reinforced polyester composites: Jowar, sisal and bamboo. Materials and Design. 2011;32:4658-63.

[8] Sridhar MK, Basavarajappa G, Kasturi SG, Balasubramanian N. Evaluation of jute as a reinforcement in composites. Indian J Fibre Text Res. 1982;7:87-92.

[9] Mohanty AK, Misra M, Hinrichsen G. Biofibres, biodegradable polymers and biocomposites: An overview. Macromolecular Materials and Engineering. 2000;276-277:1-24.

[10] Charlet K, Jernot J-P, Breard J, Gomina M. Scattering of morphological and mechanical properties of flax fibres. Industrial Crops and Products. 2010;32:220-4.

[11] Wambua P, Ivens J, Verpoest I. Natural fibres: can they replace glass in fibre reinforced plastics? Composites Science and Technology. 2003;63:1259-64.

[12] Korte S. Processing-Property Relationships of Hemp Fibre: University of Canterbury, 2006.

[13] Hughes JM. On the mechanical properties of bast fibre reinforced thermosetting polymer matrix composites University of Wales, 2000.

[14] Liu W, Drzal LT, Mohanty AK, Misra M. Influence of processing methods and fiber length on physical properties of kenaf fiber reinforced soy based biocomposites. Composites Part B: Engineering. 2007;38:352-9.

[15] Ochi S. Mechanical properties of kenaf fibers and kenaf/PLA composites. Mechanics of Materials. 2008;40:446-52.

[16] Du Y. An applied investigation of kenaf-based fiber/polymer composites as potential lightweight materials for automotive components [3412650]. United States -- Mississippi: Mississippi State University, 2010.

[17] Elsaid A, Dawood M, Seracino R, Bobko C. Mechanical properties of kenaf fiber reinforced concrete. Construction and Building Materials. 2011;25:1991-2001.

[18] Mohanty AK, Misra M, Drzal LT. Plant Fibers as Reinforcement for Green Composites. In: Bismarck A, Mishra S, Lampke T, editors. Natural fibers, biopolymers, and biocomposites: CRC; 2005.

[19] Mohanty AK, Misra M, Drzal LT. Natural fibers, biopolymers, and Biocomposites CRC Press Taylor & Francis Group, 2005.

[20] Merlini C, Soldi V, Barra GMO. Influence of fiber surface treatment and length on physico-chemical properties of short random banana fiber-reinforced castor oil polyurethane composites. Polymer Testing. 2011;30:833-40.

[21] Arib RMN, Sapuan SM, Ahmad M, Paridah MT, Zaman H. Mechanical properties of pineapple leaf fibre reinforced polypropylene composites. Materials & Design. 2006;27:391-6.

[22] Satyanarayana KG, Sukumaran K, Mukherjee PS, Pavithran C, Pillai SGK. Natural fibre-polymer composites. Cement and Concrete Composites. 1990;12:117-36.

[23] Hill CAS, Khalil H. The effect of environmental exposure upon the mechanical properties of coir or oil palm fiber reinforced composites. Journal of Applied Polymer Science. 2000;77:1322-30.

[24] Shinoj S, Visvanathan R, Panigrahi S, Kochubabu M. Oil palm fiber (OPF) and its composites: A review. Industrial Crops and Products. 2011;33:7-22.

[25] Neagu R, Gamstedt E, Lindström M. Characterization Methods for Elastic Properties of Wood Fibers from Mats for Composite Materials. Wood and Fiber Science. 2006;38:95-111.

[26] Neagu RC, Gamstedt EK, Berthold F. Stiffness Contribution of Various Wood Fibers to Composite Materials. Journal of Composite Materials. 2006;40:663-99.

[27] Nilsson T, Gustafsson PJ. Influence of dislocations and plasticity on the tensile behaviour of flax and hemp fibres. Composites Part A-Applied Science and Manufacturing. 2007;38:1722-8.

[28] Baley C. Influence of kink bands on the tensile strength of flax fibers. Journal of Materials Science. 2004;39:331-4.

[29] Satyanarayana KG, Sukumaran K, Mukherjee PS, Pillai SGK. Materials science of some lignocellulosic fibers. Metallography. 1986;19:389-400.

[30] Ray AK, Das SK, Mondal S, Ramachandrarao P. Microstructural characterization of bamboo. Journal of Materials Science. 2004;39:1055-60.

[31] Wong KJ, Zahi S, Low KO, Lim CC. Fracture characterisation of short bamboo fibre reinforced polyester composites. Materials & Design. 2010;31:4147-54.

[32] Kulkarni AG, Satyanarayana KG, Rohatgi PK, Vijayan K. Mechanical properties of banana fibres (Musa sepientum). Journal of Materials Science. 1983;18:2290-6.

[33] Kulkarni AG, Satyanarayana KG, Sukumaran K, Rohatgi PK. Mechanical behaviour of coir fibres under tensile load. Journal of Materials Science. 1981;16:905-14.

[34] Rout J, Tripathy SS, Nayak SK, Misra M, Mohanty AK. Scanning electron microscopy study of chemically modified coir fibers. Journal of Applied Polymer Science. 2001;79:1169-77.

[35] McLaughlin EC, Tait RA. Fracture mechanism of plant fibres. Journal of

Materials Science. 1980;15:89-95.

[36] Stamboulis A, Baillie CA, Peijs T. Effects of environmental conditions on mechanical and physical properties of flax fibers. Composites Part A: Applied Science and Manufacturing. 2001;32:1105-15.

[37] Bismarck A, Aranberri-Askargorta I, Springer J, Lampke T, Wielage B, Stamboulis A, et al. Surface characterization of flax, hemp and cellulose fibers; Surface properties and the water uptake behavior. Polymer Composites. 2002;23:872-94.

[38] Arbelaiz A, Cantero G, Fernandez B, Mondragon I, Ganan P, Kenny JM. Flax fiber surface modifications: Effects on fiber physico mechanical and flax/polypropylene interface properties. Polymer Composites. 2005;26:324-32.

[39] Baltazar-y-Jimenez A, Bismarck A. Wetting behaviour, moisture up-take and electrokinetic properties of lignocellulosic fibres. Cellulose. 2007;14:115-27.

[40] Park J-M, Quang ST, Hwang B-S, DeVries KL. Interfacial evaluation of modified Jute and Hemp fibers/polypropylene (PP)-maleic anhydride polypropylene copolymers (PP-MAPP) composites using micromechanical technique and nondestructive acoustic emission. Composites Science and Technology. 2006;66:2686-99.

[41] Cordeiro N, Gouveia C, Moraes AGO, Amico SC. Natural fibers characterization by inverse gas chromatography. Carbohydrate Polymers. 2011;84:110-7.

[42] Bismarck A, Mohanty AK, Aranberri-Askargorta I, Czapla S, Misra M, Hinrichsen G, et al. Surface characterization of natural fibers; surface properties and the water up-take behavior of modified sisal and coir fibers. Green Chemistry. 2001;3:100-7.

[43] Hearle JWS, Stevenson PJ. Nonwoven Fabric Studies Part III: The Anisotropy of Nonwoven Fabrics. Textile Research Journal. 1963;33:877-88.

[44] Rebenfeld L. Morphological foundations of fiber properties. Journal of Polymer Science Part C: Polymer Symposia. 1965;9:91-112.

[45] Cowdrey DR, Preston RD. Elasticity and Microfibrillar Angle in the Wood of Sitka Spruce. Proceedings of the Royal Society of London Series B Biological Sciences. 1966;166:245-72.

[46] Page DH, El-Hosseiny F, Winkler K, Bain R. The mechanical properties of single wood-pulp fibres. Part I: A new approach. Pulp and paper Magazine of Canada. 1972;73:72-7.

[47] Gordon JE, Jeronimidis G. Work of fracture of natural cellulose. Nature. 1974;252:116.

[48] Treloar LRG. Physics of textiles. Physics Today. 1977;30:23-30.

[49] Thygesen A. Properties of hemp fibre polymer composites - An optimisation of fibre properties using novel defibration methods and fibre characterisation 2006.

[50] He J, Tang Y, Wang S. Differences in Morphological Characteristics of Bamboo Fibres and other Natural Cellulose Fibres: Studies on X-Ray Diffraction, Solid State ^{13}C-CP/MAS NMR, and Second Derivative FTIR Spectroscopy Data. Iranian Polymer Journal. 2007;16:807-18.

[51] Bogoeva-Gaceva G, Avella M, Malinconico M, Buzarovska A, Grozdanov A,

Gentile G, et al. Natural fiber eco-composites. Polymer Composites. 2007;28:98-107.

[52] Le Troedec M, Sedan D, Peyratout C, Bonnet JP, Smith A, Guinebretiere R, et al. Influence of various chemical treatments on the composition and structure of hemp fibres. Composites Part A: Applied Science and Manufacturing. 2008;39:514-22.

[53] Ouajai S, Shanks RA. Composition, structure and thermal degradation of hemp cellulose after chemical treatments. Polymer Degradation and Stability. 2005;89:327-35.

[54] Li Y, Pickering KL. Hemp fibre reinforced composites using chelator and enzyme treatments. Composites Science and Technology. 2008;68:3293-8.

[55] Razera IAT, Frollini E. Composites based on jute fibers and phenolic matrices: Properties of fibers and composites. Journal of Applied Polymer Science. 2004;91:1077-85.

[56] Saha P, Manna S, Chowdhury SR, Sen R, Roy D, Adhikari B. Enhancement of tensile strength of lignocellulosic jute fibers by alkali-steam treatment. Bioresource Technology. 2010;101:3182-7.

[57] Öztürk İ, Irmak S, Hesenov A, Erbatur O. Hydrolysis of kenaf (Hibiscus cannabinus L.) stems by catalytical thermal treatment in subcritical water. Biomass and Bioenergy. 2010;34:1578-85.

[58] Kumar R, Choudhary V, Mishra S, Varma I. Banana fiber-reinforced biodegradable soy protein composites. Frontiers of Chemistry in China. 2008;3:243-50.

[59] Venkateshwaran N, Elayaperumal A. Banana Fiber Reinforced Polymer Composites - A Review. Journal of Reinforced Plastics and Composites. 2010;29:2387-96.

[60] Chand N, Tiwary RK, Rohatgi PK. Bibliography Resource structure properties of natural cellulosic fibres — an annotated bibliography. Journal of Materials Science. 1988;23:381-7.

[61] de Paiva JMF, Frollini E. Unmodified and modified surface sisal fibers as reinforcement of phenolic and lignophenolic matrices composites: Thermal analyses of fibers and composites. Macromolecular Materials and Engineering. 2006;291:405-17.

[62] Mukherjee PS, Satyanarayana KG. An empirical evaluation of structure-property relationships in natural fibres and their fracture behaviour. Journal of Materials Science. 1986;21:4162-8.

[63] John MJ, Anandjiwala RD. Recent developments in chemical modification and characterization of natural fiber-reinforced composites. Polymer Composites. 2008;29:187-207.

[64] Karnani R. Kenaf-reinforced polypropylene composites [1381878]. United States -- Michigan: Michigan State University, 1996.

[65] Payen A. Mémoire sur la composition du tissu propre des plantes et du ligneux. CR Hebd Seances Acad Sci. 1838;7:1052-6.

[66] Crawford RL. Lignin biodegradation and transformation. New York: Wiley New York, 1981.

[67] Sjöström E. Wood chemistry: fundamentals and applications. Second ed. London:

Academic Press, 1993.

[68] Ohad I, Danon D. On the dimensions of cellulose microfibrils. The Journal of cell biology. 1964;22:302-5.

[69] Stenstad P, Andresen M, Tanem B, Stenius P. Chemical surface modifications of microfibrillated cellulose. Cellulose. 2008;15:35-45.

[70] Guhados G, Wan W, Hutter JL. Measurement of the Elastic Modulus of Single Bacterial Cellulose Fibers Using Atomic Force Microscopy. Langmuir. 2005;21:6642-6.

[71] Cheng Q, Wang S. A method for testing the elastic modulus of single cellulose fibrils via atomic force microscopy. Composites Part A: Applied Science and Manufacturing. 2008;39:1838-43.

[72] Iwamoto S, Kai W, Isogai A, Iwata T. Elastic Modulus of Single Cellulose Microfibrils from Tunicate Measured by Atomic Force Microscopy. Biomacromolecules. 2009;10:2571-6.

[73] Saha B. Hemicellulose bioconversion. Journal of Industrial Microbiology & Biotechnology. 2003;30:279-91.

[74] Schulz FF. Beitrag zur Kenntniss des Lignins. Chemisches Zentralblatt. 1857:321-5.

[75] Achyuthan KE, Achyuthan AM, Adams PD, Dirk SM, Harper JC, Simmons BA, et al. Supramolecular Self-Assembled Chaos: Polyphenolic Lignin's Barrier to Cost-Effective Lignocellulosic Biofuels. Molecules. 2010;15:8641-88.

[76] Adler E. Lignin chemistry—past, present and future. Wood Science and Technology. 1977;11:169-218.

[77] Chen L, Auh C, Chen F, Cheng X, Aljoe H, Dixon RA, et al. Lignin Deposition and Associated Changes in Anatomy, Enzyme Activity, Gene Expression, and Ruminal Degradability in Stems of Tall Fescue at Different Developmental Stages. Journal of Agricultural and Food Chemistry. 2002;50:5558-65.

[78] Begum AN, Nicolle C, Mila I, Lapierre C, Nagano K, Fukushima K, et al. Dietary Lignins Are Precursors of Mammalian Lignans in Rats. The Journal of Nutrition. 2004;134:120-7.

[79] Chen Y, Gratton JL, Liu J. Power Requirements of Hemp Cutting and Conditioning. Biosystems Engineering. 2004;87:417-24.

[80] Schäfer T, Honermeier B. Effect of sowing date and plant density on the cell morphology of hemp (Cannabis sativa L.). Industrial Crops and Products. 2006;23:88-98.

[81] Härkäsalmi T. Bast fibres by short fibre methods-towards productization of flax and hemp environmentally consciously: University of Art and Design, 2006.

[82] Garcia C, Jaldon, Dupeyre D, Vignon MR. Fibres from semi-retted hemp bundles by steam explosion treatment. Biomass and Bioenergy. 1998;14:251-60.

[83] Haudek HW, Viti E. Textilfasern, Verlag Johann L. Bondi & Sohn, Wien-Perchtoldsdorf, Austria. 1978.

[84] http://www.innvista.com/health/foods/hemp/hempbiol.htm.

[85] Blake A, Marcus S, Copeland J, Blackburn R, Knox J. In situ analysis of cell wall polymers associated with phloem fibre cells in stems of hemp, *Cannabis sativa* L.

Planta. 2008;228:1-13.

[86] Sankari H. Towards bast fibre production in Finland: stem and fibre yields and mechanical fibre properties of selected fibre hemp and linseed genotypes. Viikki: University of Helsinki, 2000.

[87] Ranalli P. Agronomical and physiological advances in hemp crops. In: Ranalli P, editor. Advances in Hemp Research Binghamton, NY, USA: Haworth Press; 1999. p. 61-83.

[88] Hannele S S. Comparison of bast fibre yield and mechanical fibre properties of hemp (Cannabis sativa L.) cultivars. Industrial Crops and Products. 2000;11:73-84.

[89] Hayward HE. The Structure of Economic Plants. Soil Science. 1939;48:358.

[90] Winterborne J. Hydroponics: indoor horticulture: Pukka Press, 2005.

[91] Pleasants S, Batchelor WJ, Parker IH. Measuring the fibril angle of bleached fibres using micro-Raman spectroscopy. Appita Journal. 1998;51:373-6.

[92] Prasad BM, Sain MM. Mechanical properties of thermally treated hemp fibers in inert atmosphere for potential composite reinforcement. Materials Research Innovations. 2003;7:231-8.

[93] Bhatnagar A, Sain M. Processing of cellulose nanofiber-reinforced composites. Journal of Reinforced Plastics and Composites. 2005;24:1259-68.

[94] Peetla P, Schenzel KC, Diepenbrock W. Determination of mechanical strength properties of hemp fibers using near-infrared Fourier transform Raman microspectroscopy. Applied Spectroscopy. 2006;60:682-91.

[95] Purz HJ, Fink HP, Graf H. The structure of natural cellulosic fibres. Part I: The structure of bast fibres and their changes by scouring and mercerization as revealed by optical and electron microscopy. Das Papier 1998;6:315-24.

[96] Beckermann G. Performance of hemp-fibre reinforced polypropylene composite materials: The University of Waikato, 2007.

[97] Nykter M. Mcirobial quality of hemp (*Cannabis sativa L.*) and flax (*Linum usitatissimum L.*) from plants to thermal insulation. Viikki: University of Helsinki, 2006.

[98] Sharma HSS. Studies on chemical and enzyme retting of flax on a semi-industrial scale and analysis of the effluents for their physico-chemical components. International Biodeterioration. 1987;23:329-42.

[99] Di Candilo M, Ranalli P, Bozzi C, Focher B, Mastromei G. Preliminary results of tests facing with the controlled retting of hemp. Industrial Crops and Products. 2000;11:197-203.

[100] Thomsen AB, Thygesen A, Bohn V, Nielsen KV, Pallesen B, Jorgensen MS. Effects of chemical-physical pre-treatment processes on hemp fibres for reinforcement of composites and for textiles. Industrial Crops and Products. 2006;24:113-8.

[101] Vignon MR, Garcia-Jaldon C, Dupeyre D. Steam explosion of woody hemp chènevotte. International Journal of Biological Macromolecules. 1995;17:395-404.

[102] Vignon MR, Dupeyre D, Garcia-Jaldon C. Morphological characterization of steam-exploded hemp fibers and their utilization in polypropylene-based composites. Bioresource Technology. 1996;58:203-15.

[103] Nykter M, Kymäläinen H-R, Thomsen AB, Lilholt H, Koponen H, Sjöberg A-M, et al. Effects of thermal and enzymatic treatments and harvesting time on the microbial quality and chemical composition of fibre hemp (Cannabis sativa L.). Biomass and Bioenergy. 2008;32:392-9.

[104] Ray PK, Chakravarty AC, Bandyopadhaya SB. Fine structure and mechanical properties of jute differently dried after retting. Journal of Applied Polymer Science. 1976;20:1765-7.

[105] Da Cunha C, Deffieux A, Fontanille M. Synthesis and polymerization of lignin-based macromonomers. III. Radical copolymerization of lignin-based macromonomers with methyl methacrylate. Journal of Applied Polymer Science. 1993;48:819-31.

[106] Semsarzadeh MA. Fiber matrix interactions in jute reinforced polyester resin. Polymer Composites. 1986;7:23-5.

[107] Bisanda ETN, Ansell MP. The effect of silane treatment on the mechanical and physical properties of sisal-epoxy composites. Composites Science and Technology. 1991;41:165-78.

[108] Haig Zeronian S, Kawabata H, Alger KW. Factors Affecting the Tensile Properties of Nonmercerized and Mercerized Cotton Fibers. Textile Research Journal. 1990;60:179-83.

[109] Brett CT, Waldron K. Physiology and biochemistry of plant cell walls. London: Chapman & Hall, 1996.

[110] Stamboulis A, Baillie CA, Garkhail SK, van Melick HGH, Peijs T. Environmental Durability of Flax Fibres and their Composites based on Polypropylene Matrix. Applied Composite Materials. 2000;7:273-94.

[111] Belgacem MN, Bataille P, Sapieha S. Effect of corona modification on the mechanical properties of polypropylene/cellulose composites. Journal of Applied Polymer Science. 1994;53:379-85.

[112] Wakida T, Tokino S. Surface modification of fibre and polymeric materials by discharge treatment and its application to textile processing. Indian Journal of Fibre and Textile Research. 1996;21:69-78.

[113] Wong KK, Tao XM, Yuen CWM, Yeung KW. Topographical Study of Low Temperature Plasma Treated Flax Fibers. Textile Research Journal. 2000;70:886-93.

[114] Lee SG, Choi SS, Park WH, Cho DW. Characterization of surface modified flax fibers and their biocomposites with PHB. Macromolecular Symposia. 2003;197:89-99.

[115] Martin AR, Manolache S, Denes FS, Mattoso LHC. Functionalization of sisal fibers and high-density polyethylene by cold plasma treatment. Journal of Applied Polymer Science. 2002;85:2145-54.

[116] Molina R, Jovančić P, Jocić D, Bertran E, Erra P. Surface characterization of keratin fibres treated by water vapour plasma. Surface and Interface Analysis. 2003;35:128-35.

[117] http://en.wikipedia.org/wiki/File:Plasma-lamp_2.jpg.

[118] Ragoubi M, Bienaime D, Molina S, George B, Merlin A. Impact of corona treated hemp fibres onto mechanical properties of polypropylene composites made

thereof. Industrial Crops and Products. 2010;31:344-9.

[119] Radetic M, Jovancic P, Topalovic T, Puac N, Petrovic ZLJ. The influence of low-temperature plasma and enzymatic treatment on hemp fabric dyeability. Fibres & Textiles in Eastern Europe. 2007;15:93-6.

[120] Jovančić P, Jocić D, Radetić M, Topalović T, Petrović ZL. The Influence of Surface Modification on Related Functional Properties of Wool and Hemp Materials Science Forum. 2005;494:283-90.

[121] Titova Y, Stokozenko V, Maximov A. Application of plasma-solution treatment for modification of bast fibers. Surface Engineering and Applied Electrochemistry. 2009;45:16-20.

[122] Baltazar-y-Jimenez A, Bistritz M, Schulz E, Bismarck A. Atmospheric air pressure plasma treatment of lignocellulosic fibres: Impact on mechanical properties and adhesion to cellulose acetate butyrate. Composites Science and Technology. 2008;68:215-27.

[123] http://en.wikipedia.org/wiki/Mercerization.

[124] Klemm D, Heinze T. Comprehensive cellulose chemistry Volume1: Fundamental and Analytical Methods. Weinheim: Wiley-VCH, 1998.

[125] Ganan P, Garbizu S, Llano-Ponte R, Mondragon I. Surface modification of sisal fibers: Effects on the mechanical and thermal properties of their epoxy composites. Polymer Composites. 2005;26:121-7.

[126] Ray D, Sarkar BK, Bose NR. Impact fatigue behaviour of vinylester resin matrix composites reinforced with alkali treated jute fibres. Composites Part A: Applied Science and Manufacturing. 2002;33:233-41.

[127] de Albuquerque AC, Joseph K, Hecker de Carvalho L, d'Almeida JRM. Effect of wettability and ageing conditions on the physical and mechanical properties of uniaxially oriented jute-roving-reinforced polyester composites. Composites Science and Technology. 2000;60:833-44.

[128] Okano T, Sarko A. Mercerization of cellulose. I. X-ray diffraction evidence for intermediate structures. Journal of Applied Polymer Science. 1984;29:4175-82.

[129] Okano T, Sarko A. Mercerization of cellulose. II. Alkali–cellulose intermediates and a possible mercerization mechanism. Journal of Applied Polymer Science. 1985;30:325-32.

[130] Nishimura H, Sarko A. Mercerization of cellulose. III. Changes in crystallite sizes. Journal of Applied Polymer Science. 1987;33:855-66.

[131] Oh SY, Yoo DI, Shin Y, Kim HC, Kim HY, Chung YS, et al. Crystalline structure analysis of cellulose treated with sodium hydroxide and carbon dioxide by means of X-ray diffraction and FTIR spectroscopy. Carbohydrate Research. 2005;340:2376-91.

[132] Rodriguez ES, Stefani PM, Vazquez A. Effects of Fibers' Alkali Treatment on the Resin Transfer Molding Processing and Mechanical Properties of Jute—Vinylester Composites. Journal of Composite Materials. 2007;41:1729-41.

[133] Mansikkamäki P, Lahtinen M, Rissanen K. The conversion from cellulose I to cellulose II in NaOH mercerization performed in alcohol–water systems: An X-ray powder diffraction study. Carbohydrate Polymers. 2007;68:35-43.

[134] Mwaikambo LY, Ansell MP. Hemp fibre reinforced cashew nut shell liquid composites. Composites Science and Technology. 2003;63:1297-305.

[135] Gulati D, Sain M. Surface characteristics of untreated and modified hemp fibers. Polymer Engineering and Science. 2006;46:269-73.

[136] Yackel EC, Kenyon WO. Preparation of oxycellulose. US1941.

[137] Nabar GM, Padmanabhan CV. Studies in oxycellulose. Part III. Oxidation of cellulose with a mixture of nitrogen dioxide and oxygen. Proceedings Mathematical Sciences. 1950;32:212-31.

[138] Colvin JR. Oxidation of cellulose microfibril segments by alkaline silver nitrate and its relation to the fine structure of cellulose. Journal of Applied Polymer Science. 1964;8:2763-74.

[139] Shenai VA, Singh OP. Studies in Accelerated Oxidation of Cellulose. I—Hypochlorite Oxidation of Cellulose in Presence of Manganous Hydroxide. Journal of the Society of Dyers and Colourists. 1971;87:228-31.

[140] Arendt JH, Carrière JP, Bouchez P, Sachetto JP. Oxidation of cellulose by acid-sodium nitrite systems. Journal of Polymer Science: Polymer Symposia. 1973;42:1521-9.

[141] Heinze T, Klemm D, Loth F, Nehls I. Sphärische ionotrope gele carboxygruppenhaltiger cellulosederivate als trägermaterialien für biologische wirkstoffe, IV. Synthese von carboxycellulose und ionotrope gelbildung mit calciumionen. Die Angewandte Makromolekulare Chemie. 1990;178:95-107.

[142] Schnabelrauch M, Heinze T, Klemm D, Nehis I, Kötz J. Investigations on synthesis and characterization of carboxy-groups containing cellulose sulfates. Polymer Bulletin. 1991;27:147-53.

[143] Isogai A, Kato Y. Preparation of Polyuronic Acid from Cellulose by TEMPO-mediated Oxidation. Cellulose. 1998;5:153-64.

[144] Hirota M, Tamura N, Saito T, Isogai A. Surface carboxylation of porous regenerated cellulose beads by 4-acetamide-TEMPO/NaClO/NaClO$_2$ system. Cellulose. 2009;16:841-51.

[145] Toda T. Graft copolymerization to cellulose by sodium periodate. Journal of Polymer Science. 1962;58:411-27.

[146] Sihtola H. Chemical properties of modified celluloses. Die Makromolekulare Chemie. 1960;35:250-65.

[147] Rowland SP, Cousins ER. Periodate oxidative decrystallization of cotton cellulose. Journal of Polymer Science Part A-1: Polymer Chemistry. 1966;4:793-9.

[148] Kangle PJ, Nabar GM. Studies in chemically modified celluloses. I. Oxidative susceptibility of chemically, modified cellulose. Journal of Applied Polymer Science. 1969;13:323-36.

[149] Morooka T, Norimoto M, Yamada T. Periodate oxidation of cellulose by homogeneous reaction. Journal of Applied Polymer Science. 1989;38:849-58.

[150] Shibata I, Yanagisawa M, Saito T, Isogai A. SEC-MALS analysis of cellouronic acid prepared from regenerated cellulose by TEMPO-mediated oxidation. Cellulose. 2006;13:73-80.

[151] Saito T, Isogai A. Introduction of aldehyde groups on surfaces of native

cellulose fibers by TEMPO-mediated oxidation. Colloids and Surfaces A: Physicochemical and Engineering Aspects. 2006;289:219-25.

[152] Saito T, Okita Y, Nge TT, Sugiyama J, Isogai A. TEMPO-mediated oxidation of native cellulose: Microscopic analysis of fibrous fractions in the oxidized products. Carbohydrate Polymers. 2006;65:435-40.

[153] DiFlavio J-L, Pelton R, Leduc M, Champ S, Essig M, Frechen T. The role of mild TEMPO–NaBr–NaClO oxidation on the wet adhesion of regenerated cellulose membranes with polyvinylamine. Cellulose. 2007;14:257-68.

[154] Isogai T, Yanagisawa M, Isogai A. Degrees of polymerization (DP) and DP distribution of cellouronic acids prepared from alkali-treated celluloses and ball-milled native celluloses by TEMPO-mediated oxidation. Cellulose. 2009;16:117-27.

[155] Johnson R, Zink-Sharp A, Renneckar S, Glasser W. A new bio-based nanocomposite: fibrillated TEMPO-oxidized celluloses in hydroxypropylcellulose matrix. Cellulose. 2009;16:227-38.

[156] Fujisawa S, Isogai T, Isogai A. Temperature and pH stability of cellouronic acid. Cellulose. 2010;17:607-15.

[157] Hirota M, Tamura N, Saito T, Isogai A. Oxidation of regenerated cellulose with NaClO2 catalyzed by TEMPO and NaClO under acid-neutral conditions. Carbohydrate Polymers. 2009;78:330-5.

[158] Praskalo J, Kostic M, Potthast A, Popov G, Pejic B, Skundric P. Sorption properties of TEMPO-oxidized natural and man-made cellulose fibers. Carbohydrate Polymers. 2009;77:791-8.

[159] Xhanari K, Syverud K, Chinga-Carrasco G, Paso K, Stenius P. Reduction of water wettability of nanofibrillated cellulose by adsorption of cationic surfactants. Cellulose. 2011;18:257-70.

[160] Fukuzumi H, Saito T, Okita Y, Isogai A. Thermal stabilization of TEMPO-oxidized cellulose. Polymer Degradation and Stability. 2010;95:1502-8.

[161] Potthast A, Kostic M, Schiehser S. Studies on oxidative modifications of cellulose by the TEMPO and periodate oxidation system. Proc Italic. 2007:8-10.

[162] Matsui T, Yamaoka A. Ozone-oxidation of hemp and graft copolymerization of mathyl mechacrylate onto it. Research memoirs of the Kobe Technical College 1997;36:51-5.

[163] Matsui T, Yamaoka A. Graft-copolymerization of Methylmethacrylate onto Hamp Oxidized with Ozone II : Effects of the Graft-copolymerization on Fine Structures, Mechanical Properties and Chemical Resistances. Research memoirs of the Kobe Technical College. 1998;38:21-4.

[164] Jones EW, Rayburn JA. Crosslinking of cotton cellulose with diglycidyl ether. Journal of Applied Polymer Science. 1961;5:714-20.

[165] Clingman AL, Schwenker RF. The alkane dithioether and the polysulfide crosslinking of cellulose. Journal of Polymer Science Part C: Polymer Symposia. 1965;11:107-18.

[166] Lee N, Kwon O-J, Chun B, Cho J, Park J-S. Characterization of castor oil/polycaprolactone polyurethane biocomposites reinforced with hemp fibers. Fibers

and Polymers. 2009;10:154-60.

[167] Gupta KC, Sahoo S, Khandekar K. Graft Copolymerization of Ethyl Acrylate onto Cellulose Using Ceric Ammonium Nitrate as Initiator in Aqueous Medium. Biomacromolecules. 2002;3:1087-94.

[168] Nayak PL, Lenka S, Pati NC. Grafting vinyl monomers onto silk fibers. II. Graft copolymerization of methyl methacrylate onto silk by hexavalent chromium ion. Journal of Applied Polymer Science. 1979;23:1345-54.

[169] Mishra S, Misra M, Tripathy SS, Nayak SK, Mohanty AK. Graft copolymerization of acrylonitrile on chemically modified sisal fibers. Macromolecular Materials and Engineering. 2001;286:107-13.

[170] Pracella M, Chionna D, Anguillesi I, Kulinski Z, Piorkowska E. Functionalization, compatibilization and properties of polypropylene composites with Hemp fibres. Composites Science and Technology. 2006;66:2218-30.

[171] Lu JZ, Wu Q, McNabb HS. Chemical coupling in wood fiber and polymer composites: A review of coupling agents and treatments. Wood and Fiber Science. 2000;32:88-104.

[172] Kushwaha PK, Kumar R. Effect of Silanes on Mechanical Properties of Bamboo Fiber-epoxy Composites. Journal of Reinforced Plastics and Composites. 2010;29:718-24.

[173] Hepworth DG, Hobson RN, Bruce DM, Farrent JW. The use of unretted hemp fibre in composite manufacture. Composites Part a-Applied Science and Manufacturing. 2000;31:1279-83.

[174] Ouajai S, Shanks RA. Morphology and structure of hemp fibre after bioscouring. Macromolecular Bioscience. 2004;5:124-34.

[175] Bhattacharya SD, Shah JN. Enzymatic Treatments of Flax Fabric. Textile Research Journal. 2004;74:622-8.

[176] Research L. Nanotechnology: Where Does the US Stand? In: Research L, editor. Testimony before the Research Subcommittee of the House Committee on Science. New York: Lux Research; 2005.

[177] Sawhney APS, Condon B, Singh KV, Pang SS, Li G, Hui D. Modern Applications of Nanotechnology in Textiles. Textile Research Journal. 2008;78:731-9.

[178] Xue C-H, Jia S-T, Zhang J, Tian L-Q. Superhydrophobic surfaces on cotton textiles by complex coating of silica nanoparticles and hydrophobization. Thin Solid Films. 2009;517:4593-8.

[179] Ngo YH, Li D, Simon GP, Garnier G. Paper surfaces functionalized by nanoparticles. Advances in Colloid and Interface Science. 2011;163:23-38.

[180] Dubas ST, Kumlangdudsana P, Potiyaraj P. Layer-by-layer deposition of antimicrobial silver nanoparticles on textile fibers. Colloids and Surfaces A: Physicochemical and Engineering Aspects. 2006;289:105-9.

[181] Wang Q, Hauser PJ. Developing a novel UV protection process for cotton based on layer-by-layer self-assembly. Carbohydrate Polymers. 2010;81:491-6.

[182] Strydom SJ, Otto DP, Liebenberg W, Lvov YM, de Villiers MM. Preparation and characterization of directly compactible layer-by-layer nanocoated cellulose. International Journal of Pharmaceutics. 2011;404:57-65.

[183] Uğur ŞS, Sarışık M, Aktaş AH. Nano-Al$_2$O$_3$ multilayer film deposition on cotton fabrics by layer-by-layer deposition method. Materials Research Bulletin. 2011;46:1202-6.

[184] Wang CX, Chen SL. Surface treatment of cotton using β-cyclodextrins sol–gel method. Applied Surface Science. 2006;252:6348-52.

[185] Li F-Y, Xing Y-J, Ding X. Immobilization of papain on cotton fabric by sol–gel method. Enzyme and Microbial Technology. 2007;40:1692-7.

[186] Alongi J, Ciobanu M, Malucelli G. Novel flame retardant finishing systems for cotton fabrics based on phosphorus-containing compounds and silica derived from sol–gel processes. Carbohydrate Polymers. 2011;85:599-608.

[187] Brancatelli G, Colleoni C, Massafra MR, Rosace G. Effect of hybrid phosphorus-doped silica thin films produced by sol-gel method on the thermal behavior of cotton fabrics. Polymer Degradation and Stability. 2011;96:483-90.

[188] Chen C-Y, Chiang C-L. Preparation of cotton fibers with antibacterial silver nanoparticles. Materials Letters. 2008;62:3607-9.

[189] Zhang F, Wu X, Chen Y, Lin H. Application of silver nanoparticles to cotton fabric as an antibacterial textile finish. Fibers and Polymers. 2009;10:496-501.

[190] Ravindra S, Murali Mohan Y, Narayana Reddy N, Mohana Raju K. Fabrication of antibacterial cotton fibres loaded with silver nanoparticles via "Green Approach". Colloids and Surfaces A: Physicochemical and Engineering Aspects. 2010;367:31-40.

[191] Onar N, Ebeoglugil MF, Kayatekin I, Celik E. Low-temperature, sol–gel-synthesized, silver-doped titanium oxide coatings to improve ultraviolet-blocking properties for cotton fabrics. Journal of Applied Polymer Science. 2007;106:514-25.

[192] Zheng C, Chen G, Qi Z. Ultraviolet resistant/antiwrinkle finishing of cotton fabrics by sol-gel method. Journal of Applied Polymer Science. 2011;122:2090-8.

[193] Schmidt H, Jonschker G, Goedicke S, Mennig M. The Sol-Gel Process as a Basic Technology for Nanoparticle-Dispersed Inorganic-Organic Composites. Journal of Sol-Gel Science and Technology. 2000;19:39-51.

[194] Yeh J-T, Chen C-L, Huang K-S. Preparation and application of fluorocarbon polymer/SiO2 hybrid materials, part 1: Preparation and properties of hybrid materials. Journal of Applied Polymer Science. 2007;103:1140-5.

[195] Yeh J-T, Chen C-L, Huang K-S. Preparation and application of fluorocarbon polymer/SiO2 hybrid materials, part 2: Water and oil repellent processing for cotton fabrics by sol–gel method. Journal of Applied Polymer Science. 2007;103:3019-24.

[196] Yadav A, Prasad V, Kathe A, Raj S, Yadav D, Sundaramoorthy C, et al. Functional finishing in cotton fabrics using zinc oxide nanoparticles. Bulletin of Materials Science. 2006;29:641-5.

[197] Becheri A, Dürr M, Lo Nostro P, Baglioni P. Synthesis and characterization of zinc oxide nanoparticles: application to textiles as UV-absorbers. Journal of Nanoparticle Research. 2008;10:679-89.

[198] Juntaro J, Pommet M, Mantalaris A, Shaffer M, Bismarck A. Nanocellulose enhanced interfaces in truly green unidirectional fibre reinforced composites. Composite Interfaces. 2007;14:753-62.

[199] Mohanty AK, Misra M, Drzal LT. Natural Fibers, Biopolymers, and Biocomposites: An Introduction. In: Mohanty AK, Misra M, Drzal LT, Selke SE, Harte BR, Hinrichsen G, editors. Natural fibers, biopolymers, and biocomposites: CRC; 2005. p. 1.

[200] Yuan H, Zhou P, Zhou D. What is Low-Carbon Development? A Conceptual Analysis. Energy Procedia. 2011;5:1706-12.

[201] Duppong TA. Industrial Hemp: How the Classification of Industrial Hemp as Marijuana under the Controlled Substances Act Has Caused the Dream of Growing Industrial Hemp in North Dakota to Go Up in Smoke. N Dak L Rev. 2009;85:403-919.

[202] http://faostat.fao.org/.

[203] Johnson R. Hemp as an Agricultural Commodity: CRS, 2010.

[204] Allin S. Building with hemp: Seed Press, 2005.

[205] Evrard A, De Herde A, Minet J. Dynamical interactions between heat and mass flows in Lime-Hemp Concrete. In: Fazio, editor. Third International Building Physics Conferences. Concordia University: Taylor & Francis Group; 2006. p. 27-31.

[206] Evrard A. Sorption behaviour of Lime-Hemp Concrete and its relation to indoor comfort and energy demand. The 23rd Conference on Passive and Low Energy Architecture. Geneva2006.

[207] Cerezo V. Propriétés mécaniques, thermiques et acoustiques d'un matériau: L'Ecole Nationale des Travaux Publics de l'Etat, 2005.

[208] Bütschi PY, Deschenaux C, Miao B, Srivastava NK. Utilisation du chanvre pour la préfabrication d'éléments de construction: Département de génie civil, Faculté d'ingénierie, Université de Moncton, 2004.

[209] Latif E, Wijeyesekera DC, Newport D, Tucker S. Potential for research on hemp insulation in the UK construction sector. University of East London, School of Computing, Information Technology and Engineering; 2010. p. 143-50.

[210] http://www.renewable-house.co.uk/.

[211] Code for Sustainable Homes. UK: Department for Communities and Local Government, 2006.

[212] Busbridge R, Rhydwen R. An investigation of the thermal properties of hemp and clay monolithic walls. Advances in Computing and Technology 5th Annual Conference: University of East London, School of Computing, Information Technology and Engineering; 2010. p. 163-70.

[213] Elfordy S, Lucas F, Tancret F, Scudeller Y, Goudet L. Mechanical and thermal properties of lime and hemp concrete ("hempcrete") manufactured by a projection process. Construction and Building Materials. 2008;22:2116-23.

[214] Le Troedec M, Peyratout CS, Smith A, Chotard T. Influence of various chemical treatments on the interactions between hemp fibres and a lime matrix. Journal of the European Ceramic Society. 2009;29:1861-8.

[215] Le Troëdec M, Rachini A, Peyratout C, Rossignol S, Max E, Kaftan O, et al. Influence of chemical treatments on adhesion properties of hemp fibres. Journal of Colloid and Interface Science. 2011;356:303-10.

[216] Collet F, Bart M, Serres L, Miriel J. Porous structure and water vapour sorption

of hemp-based materials. Construction and Building Materials. 2008;22:1271-80.

[217] Tran Le AD, Maalouf C, Mai TH, Wurtz E, Collet F. Transient hygrothermal behaviour of a hemp concrete building envelope. Energy and Buildings. 2010;42:1797-806.

[218] Mohanty AK, Tummala P, Liu W, Misra M, Mulukutla PV, Drzal LT. Injection Molded Biocomposites from Soy Protein Based Bioplastic and Short Industrial Hemp Fiber. Journal of Polymers and the Environment. 2005;13:279-85.

[219] Ochi S. Development of high strength biodegradable composites using Manila hemp fiber and starch-based biodegradable resin. Composites Part a-Applied Science and Manufacturing. 2006;37:1879-83.

[220] Nättinen K, Hyvärinen S, Joffe R, Wallström L, Madsen B. Naturally compatible: Starch acetate/cellulosic fiber composites. I. Processing and properties. Polymer Composites. 2010;31:524-35.

[221] Osabohien E, Egboh SHO. Utilization of bowstring hemp fiber as a filler in natural rubber compounds. Journal of Applied Polymer Science. 2008;107:210-4.

[222] Kozłowski R, Władyka-Przybylak M. Flammability and fire resistance of composites reinforced by natural fibers. Polymers for Advanced Technologies. 2008;19:446-53.

[223] Wibowo AC, Mohanty AK, Misra M, Drzal LT. Chopped Industrial Hemp Fiber Reinforced Cellulosic Plastic Biocomposites: Thermomechanical and Morphological Properties. Industrial & Engineering Chemistry Research. 2004;43:4883-8.

[224] Van de Velde K, Kiekens P. Thermoplastic pultrusion of natural fibre reinforced composites. Composite Structures. 2001;54:355-60.

[225] Bledzki AK, Fink HP, Specht K. Unidirectional hemp and flax EP- and PP-composites: Influence of defined fiber treatments. Journal of Applied Polymer Science. 2004;93:2150-6.

[226] Thygesen A, Thomsen AB, Daniel G, Lilholt H. Comparison of composites made from fungal defibrated hemp with composites of traditional hemp yarn. Industrial Crops and Products. 2007;25:147-59.

[227] Li Y, Pickering KL, Farrell RL. Analysis of green hemp fibre reinforced composites using bag retting and white rot fungal treatments. Industrial Crops and Products. 2009;29:420-6.

[228] Mutje P, Vallejos ME, Girones J, Vilaseca F, Lopez A, Lopez JP, et al. Effect of maleated polypropylene as coupling agent for polypropylene composites reinforced with hemp strands. Journal of Applied Polymer Science. 2006;102:833-40.

[229] Pickering KL, Beckermann GW, Alam SN, Foreman NJ. Optimising industrial hemp fibre for composites. Composites Part a-Applied Science and Manufacturing. 2007;38:461-8.

[230] Sawpan MA, Pickering KL, Fernyhough A. Improvement of mechanical performance of industrial hemp fibre reinforced polylactide biocomposites. Composites Part A: Applied Science and Manufacturing. 2011;42:310-9.

[231] Islam MS, Pickering KL, Foreman NJ. Influence of alkali treatment on the interfacial and physico-mechanical properties of industrial hemp fibre reinforced polylactic acid composites. Composites Part A: Applied Science and Manufacturing.

2010;41:596-603.

[232] Vilaseca F, López A, Llauró X, PèLach MA, Mutjé P. Hemp Strands as Reinforcement of Polystyrene Composites. Chemical Engineering Research and Design. 2004;82:1425-31.

[233] Hautala M, Pasila A, Pirila J. Use of hemp and flax in composite manufacture: a search for new production methods. Composites Part a-Applied Science and Manufacturing. 2004;35:11-6.

[234] Rouison D, Sain M, Couturier M. Resin transfer molding of hemp fiber composites: optimization of the process and mechanical properties of the materials. Composites Science and Technology. 2006;66:895-906.

[235] Mehta G, Drzal LT, Mohanty AK, Misra M. Effect of fiber surface treatment on the properties of biocomposites from nonwoven industrial hemp fiber mats and unsaturated polyester resin. Journal of Applied Polymer Science. 2006;99:1055-68.

[236] Nickerson RF. Hydrolysis and Catalytic Oxidation of Cellulosic Materials. Industrial & Engineering Chemistry. 1941;33:1022-7.

[237] Conrad CC, Scroggie AG. Chemical Characterization of Rayon Yarns and Cellulosic Raw Materials. Industrial & Engineering Chemistry. 1945;37:592-8.

[238] Battista OA, Coppick S. Hydrolysis of Native Versus Regenerated Cellulose Structures. Textile Research Journal. 1947;17:419-22.

[239] Nickerson RF, Habrle JA. Cellulose Intercrystalline Structure. Industrial & Engineering Chemistry. 1947;39:1507-12.

[240] Hermans PH, Weidinger A. Change in crystallinity upon heterogeneous acid hydrolysis of cellulose fibers. Journal of Polymer Science. 1949;4:317-22.

[241] Battista OA. Hydrolysis and Crystallization of Cellulose. Industrial & Engineering Chemistry. 1950;42:502-7.

[242] Rånby BG. The cellulose micelles. Tappi. 1952;35:53-8.

[243] Rånby BG. Physico-chemical investigations on animal cellulose (Tunicin). Ark Kemi. 1952;4:241-8.

[244] Ranby BG. Physico-chemical investigations on bacterial cellulose. Ark Kemi. 1952;4:249-57.

[245] Mukherjee SM, Woods HJ. X-ray and electron microscope studies of the degradation of cellulose by sulphuric acid. Biochimica et Biophysica Acta. 1953;10:499-511.

[246] Sharples A. The hydrolysis of cellulose Part I. The fine structure of egyptian cotton. Journal of Polymer Science. 1954;13:393-401.

[247] Dilip Kumar Roy C. Accessibility of Various Cellulose Preparations from Jute. Textile Research Journal. 1959;29:394-7.

[248] Marchessault RH, Morehead FF, Walter NM. Liquid Crystal Systems from Fibrillar Polysaccharides. Nature. 1959;184:632-3.

[249] Marchessault RH, Morehead FF, Koch MJ. Some hydrodynamic properties of neutral suspensions of cellulose crystallites as related to size and shape. Journal of Colloid Science. 1961;16:327-44.

[250] Turbak AF, Snyder FW, Sandberg KR. Food products containing microfibrillated cellulose. U.S.: International Telephone and Telegraph Corporation;

1982.

[251] Turbak AF, Snyder FW, Sandberg KR. Microfibrillated cellulose, a new cellulose product: properties, uses, and commercial potential. In: Sarko A, editor. Proceedings of the Ninth Cellulose Conference Applied Polymer Symposia. New York City: Wiley; 1983. p. 815-27.

[252] Turbak AF, Snyder FW, Sandberg KR. Suspensions containing microfibrillated cellulose. International Telephone and Telegraph Corporation; 1983.

[253] Turbak AF, Snyder FW, Sandberg KR. Microfibrillated cellulose. U.S.: International Telephone and Telegraph Corporation; 1983.

[254] Favier V, Canova GR, Cavaillé JY, Chanzy H, Dufresne A, Gauthier C. Nanocomposite materials from latex and cellulose whiskers. Polymers for Advanced Technologies. 1995;6:351-5.

[255] Favier V, Chanzy H, Cavaille JY. Polymer Nanocomposites Reinforced by Cellulose Whiskers. Macromolecules. 1995;28:6365-7.

[256] Brown AJ. XLIII.-On an acetic ferment which forms cellulose. Journal of the Chemical Society, Transactions. 1886;49:432-9.

[257] Ross P, Mayer R, Benziman M. Cellulose biosynthesis and function in bacteria. Microbiological Reviews. 1991;55:35-58.

[258] Nakagaito AN, Yano H. Novel high-strength biocomposites based on microfibrillated cellulose having nano-order-unit web-like network structure. Applied Physics A: Materials Science & Processing. 2005;80:155-9.

[259] Yu H, Liu RG, Shen DW, Wu ZH, Huang Y. Arrangement of cellulose microfibrils in the wheat straw cell wall. Carbohydrate Polymers. 2008;72:122-7.

[260] Li D, Liu Z, Al-Haik M, Tehrani M, Murray F, Tannenbaum R, et al. Magnetic alignment of cellulose nanowhiskers in an all-cellulose composite. Polymer Bulletin. 2010;65:635-42.

[261] Hirota M, Tamura N, Saito T, Isogai A. Water dispersion of cellulose II nanocrystals prepared by TEMPO-mediated oxidation of mercerized cellulose at pH 4.8. Cellulose. 2010;17:279-88.

[262] Stelte W, Sanadi AR. Preparation and Characterization of Cellulose Nanofibers from Two Commercial Hardwood and Softwood Pulps. Industrial & Engineering Chemistry Research. 2009;48:11211-9.

[263] Iwamoto S, Kai W, Isogai T, Saito T, Isogai A, Iwata T. Comparison study of TEMPO-analogous compounds on oxidation efficiency of wood cellulose for preparation of cellulose nanofibrils. Polymer Degradation and Stability. 2010;95:1394-8.

[264] Chen W, Yu H, Liu Y, Hai Y, Zhang M, Chen P. Isolation and characterization of cellulose nanofibers from four plant cellulose fibers using a chemical-ultrasonic process. Cellulose. 2011;18:433-42.

[265] Qua E, Hornsby P, Sharma H, Lyons G. Preparation and characterisation of cellulose nanofibres. Journal of Materials Science. 2011;46:6029-45.

[266] Wang B, Sain M, Oksman K. Study of Structural Morphology of Hemp Fiber from the Micro to the Nanoscale. Applied Composite Materials. 2007;14:89-103.

[267] Wang L, Kumar R, Zhang L. Investigation into hemp fiber- and

whisker-reinforced soy protein composites. Frontiers of Chemistry in China. 2009;4:313-20.

[268] Cao XD, Chen Y, Chang PR, Stumborg M, Huneault MA. Green composites reinforced with hemp nanocrystals in plasticized starch. Journal of Applied Polymer Science. 2008;109:3804-10.

[269] Morán J, Alvarez V, Cyras V, Vázquez A. Extraction of cellulose and preparation of nanocellulose from sisal fibers. Cellulose. 2008;15:149-59.

[270] Abe K, Yano H. Comparison of the characteristics of cellulose microfibril aggregates isolated from fiber and parenchyma cells of Moso bamboo (Phyllostachys pubescens). Cellulose. 2010;17:271-7.

[271] de Morais Teixeira E, Corrêa A, Manzoli A, de Lima Leite F, de Oliveira C, Mattoso L. Cellulose nanofibers from white and naturally colored cotton fibers. Cellulose. 2010;17:595-606.

[272] Wang Y, Cao X, Zhang L. Effects of Cellulose Whiskers on Properties of Soy Protein Thermoplastics. Macromolecular Bioscience. 2006;6:524-31.

[273] Zuluaga R, Putaux J-L, Restrepo A, Mondragon I, Ganan P. Cellulose microfibrils from banana farming residues: isolation and characterization. Cellulose. 2007;14:585-92.

[274] Zuluaga R, Putaux JL, Cruz J, Velez J, Mondragon I, Ganan P. Cellulose microfibrils from banana rachis: Effect of alkaline treatments on structural and morphological features. Carbohydrate Polymers. 2009;76:51-9.

[275] Hassan M, Hassan E, Oksman K. Effect of pretreatment of bagasse fibers on the properties of chitosan/microfibrillated cellulose nanocomposites. Journal of Materials Science. 2011;46:1732-40.

[276] Corrêa A, de Morais Teixeira E, Pessan L, Mattoso L. Cellulose nanofibers from curaua fibers. Cellulose. 2010;17:1183-92.

[277] Alemdar A, Sain M. Isolation and characterization of nanofibers from agricultural residues-wheat straw and soy hulls. Bioresource Technology. 2008;99:1664-71.

[278] Alemdar A, Sain M. Biocomposites from wheat straw nanofibers: Morphology, thermal and mechanical properties. Composites Science and Technology. 2008;68:557-65.

[279] Helbert W, Cavaillé JY, Dufresne A. Thermoplastic nanocomposites filled with wheat straw cellulose whiskers. Part I: Processing and mechanical behavior. Polymer Composites. 1996;17:604-11.

[280] Cheng Q, Wang S, Rials T, Lee S-H. Physical and mechanical properties of polyvinyl alcohol and polypropylene composite materials reinforced with fibril aggregates isolated from regenerated cellulose fibers. Cellulose. 2007;14:593-602.

[281] Tischer PCSF, Sierakowski MR, Westfahl H, Tischer CA. Nanostructural Reorganization of Bacterial Cellulose by Ultrasonic Treatment. Biomacromolecules. 2010;11:1217-24.

[282] Pinjari DV, Pandit AB. Cavitation milling of natural cellulose to nanofibrils. Ultrasonics Sonochemistry. 2010;17:845-52.

[283] Chakraborty A, Sain M, Kortschot M. Cellulose microfibrils: A novel method of

preparation using high shear refining and cryocrushing. Holzforschung. 2005;59:102-7.

[284] Ahmed KS, Vijayarangan S, Kumar A. Low velocity impact damage characterization of woven jute-glass fabric reinforced isothalic polyester hybrid composites. Journal of Reinforced Plastics and Composites. 2007;26:959-76.

[285] Iwamoto S, Nakagaito AN, Yano H. Nano-fibrillation of pulp fibers for the processing of transparent nanocomposites. Applied Physics A: Materials Science & Processing. 2007;89:461-6.

[286] Iwamoto S, Abe K, Yano H. The Effect of Hemicelluloses on Wood Pulp Nanofibrillation and Nanofiber Network Characteristics. Biomacromolecules. 2008;9:1022-6.

[287] Zimmermann T, Bordeanu N, Strub E. Properties of nanofibrillated cellulose from different raw materials and its reinforcement potential. Carbohydrate Polymers. 2010;79:1086-93.

[288] Lee SY, Chun SJ, Kang IA, Park JY. Preparation of cellulose nanofibrils by high-pressure homogenizer and cellulose-based composite films. Journal of Industrial and Engineering Chemistry. 2009;15:50-5.

[289] Henriksson M, Henriksson G, Berglund LA, Lindström T. An environmentally friendly method for enzyme-assisted preparation of microfibrillated cellulose (MFC) nanofibers. European Polymer Journal. 2007;43:3434-41.

[290] Yoo S, Hsieh JS. Enzyme-Assisted Preparation of Fibrillated Cellulose Fibers and Its Effect on Physical and Mechanical Properties of Paper Sheet Composites. Industrial & Engineering Chemistry Research. 2010;49:2161-8.

[291] Pääkkö M, Ankerfors M, Kosonen H, Nykänen A, Ahola S, Österberg M, et al. Enzymatic Hydrolysis Combined with Mechanical Shearing and High-Pressure Homogenization for Nanoscale Cellulose Fibrils and Strong Gels. Biomacromolecules. 2007;8:1934-41.

[292] Kaushik A, Singh M. Isolation and characterization of cellulose nanofibrils from wheat straw using steam explosion coupled with high shear homogenization. Carbohydrate Research. 2011;346:76-85.

[293] Saito T, Isogai A. TEMPO-Mediated Oxidation of Native Cellulose. The Effect of Oxidation Conditions on Chemical and Crystal Structures of the Water-Insoluble Fractions. Biomacromolecules. 2004;5:1983-9.

[294] Fukuzumi H, Saito T, Iwata T, Kumamoto Y, Isogai A. Transparent and High Gas Barrier Films of Cellulose Nanofibers Prepared by TEMPO-Mediated Oxidation. Biomacromolecules. 2008;10:162-5.

[295] Grunert M. Cellulose nanocrystals: Preparation, surface modification, and application in nanocomposites [3047403]. United States -- New York: State University of New York College of Environmental Science and Forestry, 2002.

[296] Satyamurthy P, Jain P, Balasubramanya RH, Vigneshwaran N. Preparation and characterization of cellulose nanowhiskers from cotton fibres by controlled microbial hydrolysis. Carbohydrate Polymers. 2011;83:122-9.

[297] Svagan A. Bio-inspired polysaccharide nanocomposites and foams. Stockholm, Sweden: Kungliga Tekniska högskolan, 2006.

[298] Araki J, Wada M, Kuga S, Okano T. Flow properties of microcrystalline cellulose suspension prepared by acid treatment of native cellulose. Colloids and Surfaces A: Physicochemical and Engineering Aspects. 1998;142:75-82.

[299] Bondeson D, Kvien I, Oksman K. Strategies for Preparation of Cellulose Whiskers from Microcrystalline Cellulose as Reinforcement in Nanocomposites. In: Oksman K, Sain M, editors. Cellulose Nanocomposites Processing, Characterization, and Properties: American Chemical Society; 2006. p. 10-25.

[300] Li R, Fei J, Cai Y, Li Y, Feng J, Yao J. Cellulose whiskers extracted from mulberry: A novel biomass production. Carbohydrate Polymers. 2009;76:94-9.

[301] Abe K, Iwamoto S, Yano H. Obtaining Cellulose Nanofibers with a Uniform Width of 15 nm from Wood. Biomacromolecules. 2007;8:3276-8.

[302] Horikawa Y, Itoh T, Sugiyama J. Preferential Uniplanar Orientation of Cellulose Microfibrils Reinvestigated by the FTIR Technique. Cellulose. 2006;13:309-16.

[303] Duchesne I, Hult E, Molin U, Daniel G, Iversen T, Lennholm H. The influence of hemicellulose on fibril aggregation of kraft pulp fibres as revealed by FE-SEM and CP/MAS 13C-NMR. Cellulose. 2001;8:103-11.

[304] Peura M, Müller M, Vainio U, Sarén M-P, Saranpää P, Serimaa R. X-ray microdiffraction reveals the orientation of cellulose microfibrils and the size of cellulose crystallites in single Norway spruce tracheids. Trees - Structure and Function. 2008;22:49-61.

[305] De Souza Lima MM, Wong JT, Paillet M, Borsali R, Pecora R. Translational and Rotational Dynamics of Rodlike Cellulose Whiskers. Langmuir. 2003;19:24-9.

[306] Terech P, Chazeau L, Cavaille JY. A Small-Angle Scattering Study of Cellulose Whiskers in Aqueous Suspensions. Macromolecules. 1999;32:1872-5.

[307] Bonini C, Heux L, Cavaillé J-Y, Lindner P, Dewhurst C, Terech P. Rodlike Cellulose Whiskers Coated with Surfactant: A Small-Angle Neutron Scattering Characterization. Langmuir. 2002;18:3311-4.

[308] Ebeling T, Paillet M, Borsali R, Diat O, Dufresne A, Cavaillé JY, et al. Shear-Induced Orientation Phenomena in Suspensions of Cellulose Microcrystals, Revealed by Small Angle X-ray Scattering. Langmuir. 1999;15:6123-6.

[309] Elazzouzi-Hafraoui S, Nishiyama Y, Putaux JL, Heux L, Dubreuil F, Rochas C. The shape and size distribution of crystalline nanoparticles prepared by acid hydrolysis of native cellulose. Biomacromolecules. 2008;9:57-65.

[310] Hanley SJ, Giasson J, Revol J-F, Gray DG. Atomic force microscopy of cellulose microfibrils: comparison with transmission electron microscopy. Polymer. 1992;33:4639-42.

[311] Xu P, Donaldson LA, Gergely ZR, Staehelin LA. Dual-axis electron tomography: a new approach for investigating the spatial organization of wood cellulose microfibrils. Wood Science and Technology. 2007;41:101-16.

[312] Chinga-Carrasco G, Syverud K. Computer-assisted quantification of the multi-scale structure of films made of nanofibrillated cellulose. Journal of Nanoparticle Research. 2010;12:841-51.

[313] Cheng Q, Wang S, Harper DP. Effects of process and source on elastic modulus of single cellulose fibrils evaluated by atomic force microscopy. Composites Part A:

Applied Science and Manufacturing. 2009;40:583-8.

[314] Iwamoto S, Kai WH, Isogai A, Iwata T. Elastic Modulus of Single Cellulose Microfibrils from Tunicate Measured by Atomic Force Microscopy. Biomacromolecules. 2009;10:2571-6.

[315] Lahiji RR, Xu X, Reifenberger R, Raman A, Rudie A, Moon RJ. Atomic Force Microscopy Characterization of Cellulose Nanocrystals. Langmuir. 2010;26:4480-8.

[316] Michael TP, András V, John D, Natalia F, Bin M, Ryan W, et al. Development of the metrology and imaging of cellulose nanocrystals. Measurement Science and Technology. 2011;22:024005.

[317] Sakurada I, Nukushina Y, Ito T. Experimental determination of the elastic modulus of crystalline regions in oriented polymers. Journal of Polymer Science. 1962;57:651-60.

[318] Šturcová A, Davies GR, Eichhorn SJ. Elastic Modulus and Stress-Transfer Properties of Tunicate Cellulose Whiskers. Biomacromolecules. 2005;6:1055-61.

[319] Rusli R, Eichhorn SJ. Determination of the stiffness of cellulose nanowhiskers and the fiber-matrix interface in a nanocomposite using Raman spectroscopy. Applied Physics Letters. 2008;93:033111.

[320] Hsieh YC, Yano H, Nogi M, Eichhorn S. An estimation of the Young's modulus of bacterial cellulose filaments. Cellulose. 2008;15:507-13.

[321] Tanaka F, Iwata T. Estimation of the Elastic Modulus of Cellulose Crystal by Molecular Mechanics Simulation. Cellulose. 2006;13:509-17.

[322] Jaswon MA, Gillis PP, Mark RE. The Elastic Constants of Crystalline Native Cellulose. Proceedings of the Royal Society of London Series A Mathematical and Physical Sciences. 1968;306:389-412.

[323] Tashiro K, Kobayashi M. Theoretical evaluation of three-dimensional elastic constants of native and regenerated celluloses: role of hydrogen bonds. Polymer. 1991;32:1516-26.

[324] Reis D, Vian B, Chanzy H, Roland J-C. Liquid crystal-type assembly of native cellulose-glucuronoxylans extracted from plant cell wall. Biology of the Cell. 1991;73:173-8.

[325] Oldenbourg R, Wen X, Meyer RB, Caspar DLD. Orientational Distribution Function in Nematic Tobacco-Mosaic-Virus Liquid Crystals Measured by X-Ray Diffraction. Physical Review Letters. 1988;61:1851-4.

[326] Davis VA, Ericson LM, Parra-Vasquez ANG, Fan H, Wang Y, Prieto V, et al. Phase Behavior and Rheology of SWNTs in Superacids. Macromolecules. 2003;37:154-60.

[327] Siqueira G, Abdillahi H, Bras J, Dufresne A. High reinforcing capability cellulose nanocrystals extracted from *Syngonanthus nitens* (Capim Dourado). Cellulose. 2010;17:289-98.

[328] Dong XM, Kimura T, Revol J-F, Gray DG. Effects of Ionic Strength on the Isotropic−Chiral Nematic Phase Transition of Suspensions of Cellulose Crystallites. Langmuir. 1996;12:2076-82.

[329] Orts WJ, Godbout L, Marchessault RH, Revol JF. Enhanced Ordering of Liquid Crystalline Suspensions of Cellulose Microfibrils: A Small Angle Neutron Scattering

Study. Macromolecules. 1998;31:5717-25.

[330] Wang N, Ding E, Cheng RS. Preparation and 'liquid crystalline properties of spherical cellulose nanocrystals. Langmuir. 2008;24:5-8.

[331] Araki J, Wada M, Kuga S. Steric Stabilization of a Cellulose Microcrystal Suspension by Poly(ethylene glycol) Grafting. Langmuir. 2001;17:21-7.

[332] Beck-Candanedo S, Viet D, Gray DG. Induced phase separation in cellulose nanocrystal suspensions containing ionic dye species. Cellulose. 2006;13:629-35.

[333] Beck-Candanedo S, Viet D, Gray DG. Induced phase separation in low-ionic-strength cellulose nanocrystal suspensions containing high-molecular-weight blue dextrans. Langmuir. 2006;22:8690-5.

[334] Oksman K, Etang JA, Mathew AP, Jonoobi M. Cellulose nanowhiskers separated from a bio-residue from wood bioethanol production. Biomass and Bioenergy. 2011;35:146-52.

[335] Araki J, Wada M, Kuga S, Okano T. Birefringent Glassy Phase of a Cellulose Microcrystal Suspension. Langmuir. 2000;16:2413-5.

[336] Fleming K, Gray DG, Matthews S. Cellulose Crystallites. Chemistry – A European Journal. 2001;7:1831-6.

[337] Sugiyama J, Chanzy H, Maret G. Orientation of cellulose microcrystals by strong magnetic fields. Macromolecules. 1992;25:4232-4.

[338] Kim J, Chen Y, Kang KS, Park YB, Schwartz M. Magnetic field effect for cellulose nanofiber alignment. Journal of Applied Physics. 2008;104.

[339] Kvien I, Oksman K. Orientation of cellulose nanowhiskers in polyvinyl alcohol. Applied Physics A: Materials Science & Processing. 2007;87:641-3.

[340] Furuta T, Yamahara E, Konishi T, Ise N. Ordering in Aqueous Cellulose Hydrolysate Dispersions: An Ultra-Small-Angle X-ray Scattering Study. Macromolecules. 1996;29:8994-5.

[341] Lu X, Hu Z, Gao J. Synthesis and Light Scattering Study of Hydroxypropyl Cellulose Microgels. Macromolecules. 2000;33:8698-702.

[342] de Souza Lima MM, Borsali R. Static and Dynamic Light Scattering from Polyelectrolyte Microcrystal Cellulose. Langmuir. 2002;18:992-6.

[343] Bica CID, Borsali R, Geissler E, Rochas C. Dynamics of Cellulose Whiskers in Agarose Gels. 1. Polarized Dynamic Light Scattering. Macromolecules. 2001;34:5275-9.

[344] Bercea M, Navard P. Shear Dynamics of Aqueous Suspensions of Cellulose Whiskers. Macromolecules. 2000;33:6011-6.

[345] Han CD. Rheology and processing of polymeric materials: Polymer rheology. New York: Oxford University Press, Inc, 2007.

[346] Lowys MP, Desbrières J, Rinaudo M. Rheological characterization of cellulosic microfibril suspensions. Role of polymeric additives. Food Hydrocolloids. 2001;15:25-32.

[347] Agoda-Tandjawa G, Durand S, Gaillard C, Garnier C, Doublier JL. Rheological behaviour and microstructure of microfibrillated cellulose suspensions/low-methoxyl pectin mixed systems. Effect of calcium ions. Carbohydrate Polymers. 2012;87:1045-57.

[348] Lewandowski Z. Application of a linear synthetic polymer to improve the properties of cellulose fibers made by the NMMO process. Journal of Applied Polymer Science. 2002;83:2762-73.

[349] Goussé C, Chanzy H, Cerrada ML, Fleury E. Surface silylation of cellulose microfibrils: preparation and rheological properties. Polymer. 2004;45:1569-75.

[350] Lasseuguette E, Roux D, Nishiyama Y. Rheological properties of microfibrillar suspension of TEMPO-oxidized pulp. Cellulose. 2008;15:425-33.

[351] Karppinen A, Vesterinen A-H, Saarinen T, Pietikäinen P, Seppälä J. Effect of cationic polymethacrylates on the rheology and flocculation of microfibrillated cellulose. Cellulose. 2011;18:1381-90.

[352] Agoda-Tandjawa G, Durand S, Berot S, Blassel C, Gaillard C, Garnier C, et al. Rheological characterization of microfibrillated cellulose suspensions after freezing. Carbohydrate Polymers. 2010;80:677-86.

[353] Azizi Samir MAS, Alloin F, Dufresne A. Review of Recent Research into Cellulosic Whiskers, Their Properties and Their Application in Nanocomposite Field. Biomacromolecules. 2005;6:612-26.

[354] Putaux J-L. Morphology and Structure of Crystalline Polysaccharides: Some Recent Studies. Macromolecular Symposia. 2005;229:66-71.

[355] Nishiyama Y. Structure and properties of the cellulose microfibril. Journal of Wood Science. 2009;55:241-9.

[356] Czaja WK, Young DJ, Kawecki M, Brown RM. The Future Prospects of Microbial Cellulose in Biomedical Applications. Biomacromolecules. 2006;8:1-12.

[357] Kohler R, Nebel K. Cellulose-Nanocomposites: Towards High Performance Composite Materials. Macromolecular Symposia. 2006;244:97-106.

[358] Siró I, Plackett D. Microfibrillated cellulose and new nanocomposite materials: a review. Cellulose. 2010;17:459-94.

[359] Duran N, Paula Lemes A, B. Seabra A. Review of Cellulose Nanocrystals Patents: Preparation, Composites and General Applications Recent Patents on Nanotechnology,. 2012;6:16-28.

[360] Hubbe MA, Rojas OJ, Lucia LA, Sain M. Cellulosic nanocomposites: a review. BioResources. 2008;3:929-80.

[361] Dufresne A, Belgacem MN. Cellulose-reinforced composites: From micro-to nanoscale. Polímeros: Ciência e Tecnologia. 2010;20:1-10.

[362] Eichhorn S, Dufresne A, Aranguren M, Marcovich N, Capadona J, Rowan S, et al. Review: current international research into cellulose nanofibres and nanocomposites. Journal of Materials Science. 2010;45:1-33.

[363] Siqueira G, Bras J, Dufresne A. Cellulosic Bionanocomposites: A Review of Preparation, Properties and Applications. Polymers. 2010;2:728-65.

[364] Moon RJ, Martini A, Nairn J, Simonsen J, Youngblood J. Cellulose nanomaterials review: structure, properties and nanocomposites. Chemical Society Reviews. 2011;40:3941-94.

[365] Susheel K, Alain D, Bibin Mathew C, Luc A, James N, Elias N. Cellulose-Based Bio-and Nanocomposites: A Review. International Journal of Polymer Science. 2011;2011.

[366] Henriksson M, Berglund LA, Isaksson P, Lindström T, Nishino T. Cellulose Nanopaper Structures of High Toughness. Biomacromolecules. 2008;9:1579-85.

[367] Olsson RT, Samir M, Salazar-Alvarez G, Belova L, Strom V, Berglund LA, et al. Making flexible magnetic aerogels and stiff magnetic nanopaper using cellulose nanofibrils as templates. Nature Nanotechnology. 2010;5:584-8.

[368] Sehaqui H, Liu A, Zhou Q, Berglund LA. Fast Preparation Procedure for Large, Flat Cellulose and Cellulose/Inorganic Nanopaper Structures. Biomacromolecules. 2010;11:2195-8.

[369] Chun S-J, Lee S-Y, Doh G-H, Lee S, Kim JH. Preparation of ultrastrength nanopapers using cellulose nanofibrils. Journal of Industrial and Engineering Chemistry. 2011;17:521-6.

[370] Liu A, Walther A, Ikkala O, Belova L, Berglund LA. Clay Nanopaper with Tough Cellulose Nanofiber Matrix for Fire Retardancy and Gas Barrier Functions. Biomacromolecules. 2011;12:633-41.

[371] Sehaqui H, Zhou Q, Ikkala O, Berglund LA. Strong and Tough Cellulose Nanopaper with High Specific Surface Area and Porosity. Biomacromolecules. 2011;12:3638-44.

[372] Ahola S, Österberg M, Laine J. Cellulose nanofibrils—adsorption with poly(amideamine) epichlorohydrin studied by QCM-D and application as a paper strength additive. Cellulose. 2008;15:303-14.

[373] Hult E-L, Iotti M, Lenes M. Efficient approach to high barrier packaging using microfibrillar cellulose and shellac. Cellulose. 2010;17:575-86.

[374] Taipale T, Osterberg M, Nykanen A, Ruokolainen J, Laine J. Effect of microfibrillated cellulose and fines on the drainage of kraft pulp suspension and paper strength. Cellulose. 2010;17:1005-20.

[375] Nogi M, Iwamoto S, Nakagaito AN, Yano H. Optically Transparent Nanofiber Paper. Advanced Materials. 2009;21:1595-8.

[376] Liebner F, Haimer E, Wendland M, Neouze M-A, Schlufter K, Miethe P, et al. Aerogels from Unaltered Bacterial Cellulose: Application of scCO2 Drying for the Preparation of Shaped, Ultra-Lightweight Cellulosic Aerogels. Macromolecular Bioscience. 2010;10:349-52.

[377] Kistler SS. Coherent Expanded Aerogels and Jellies. Nature. 1931;127:741.

[378] Tan C, Fung BM, Newman JK, Vu C. Organic Aerogels with Very High Impact Strength. Advanced Materials. 2001;13:644-6.

[379] Jin H, Nishiyama Y, Wada M, Kuga S. Nanofibrillar cellulose aerogels. Colloids and Surfaces A: Physicochemical and Engineering Aspects. 2004;240:63-7.

[380] Hoepfner S, Ratke L, Milow B. Synthesis and characterisation of nanofibrillar cellulose aerogels. Cellulose. 2008;15:121-9.

[381] Gawryla MD, van den Berg O, Weder C, Schiraldi DA. Clay aerogel/cellulose whisker nanocomposites: a nanoscale wattle and daub. Journal of Materials Chemistry. 2009;19:2118-24.

[382] Kettunen M, Silvennoinen RJ, Houbenov N, Nykänen A, Ruokolainen J, Sainio J, et al. Photoswitchable Superabsorbency Based on Nanocellulose Aerogels. Advanced Functional Materials. 2011;21:510-7.

[383] Frensemeier M, Koplin C, Jaeger R, Kramer F, Klemm D. Mechanical Properties of Bacterially Synthesized Nanocellulose Hydrogels. Macromolecular Symposia. 2010;294:38-44.

[384] Haimer E, Wendland M, Schlufter K, Frankenfeld K, Miethe P, Potthast A, et al. Loading of Bacterial Cellulose Aerogels with Bioactive Compounds by Antisolvent Precipitation with Supercritical Carbon Dioxide. Macromolecular Symposia. 2010;294:64-74.

[385] Sehaqui H, Zhou Q, Berglund LA. High-porosity aerogels of high specific surface area prepared from nanofibrillated cellulose (NFC). Composites Science and Technology. 2011;71:1593-9.

[386] Shin Y, Bae I-T, Arey BW, Exarhos GJ. Simple preparation and stabilization of nickel nanocrystals on cellulose nanocrystal. Materials Letters. 2007;61:3215-7.

[387] Shin Y, Exarhos GJ. Template synthesis of porous titania using cellulose nanocrystals. Materials Letters. 2007;61:2594-7.

[388] Ifuku S, Tsuji M, Morimoto M, Saimoto H, Yano H. Synthesis of Silver Nanoparticles Templated by TEMPO-Mediated Oxidized Bacterial Cellulose Nanofibers. Biomacromolecules. 2009;10:2714-7.

[389] Drogat N, Granet R, Sol V, Memmi A, Saad N, Klein Koerkamp C, et al. Antimicrobial silver nanoparticles generated on cellulose nanocrystals. Journal of Nanoparticle Research. 2010:1-6.

[390] Gruber S, Taylor RNK, Scheel H, Greil P, Zollfrank C. Cellulose-biotemplated silica nanowires coated with a dense gold nanoparticle layer. Materials Chemistry and Physics. 2011;129:19-22.

[391] Shin Y, Blackwood JM, Bae I-T, Arey BW, Exarhos GJ. Synthesis and stabilization of selenium nanoparticles on cellulose nanocrystal. Materials Letters. 2007;61:4297-300.

[392] Zhou Y, Ding EY, Li WD. Synthesis of TiO_2 nanocubes induced by cellulose nanocrystal (CNC) at low temperature. Materials Letters. 2007;61:5050-2.

[393] Padalkar S, Capadona J, Rowan S, Weder C, Moon R, Stanciu L. Self-assembly and alignment of semiconductor nanoparticles on cellulose nanocrystals. Journal of Materials Science. 2011;46:5672-9.

[394] Hage JLT, Reuter MA, Schuiling RD, Ramtahalsing IS. Reduction of copper with cellulose in an autoclave; an alternative to electrolysis? Minerals Engineering. 1999;12:393-404.

[395] Padalkar S, Capadona JR, Rowan SJ, Weder C, Won YH, Stanciu LA, et al. Natural biopolymers: novel templates for the synthesis of nanostructures. Langmuir. 2010;26:8497-502.

[396] López-Rubio A, Lagaron JM, Ankerfors M, Lindström T, Nordqvist D, Mattozzi A, et al. Enhanced film forming and film properties of amylopectin using micro-fibrillated cellulose. Carbohydrate Polymers. 2007;68:718-27.

[397] Siqueira G, Tapin-Lingua S, Bras J, Perez DdS, Dufresne A. Mechanical properties of natural rubber nanocomposites reinforced with cellulosic nanoparticles obtained from combined mechanical shearing, and enzymatic and acid hydrolysis of sisal fibers. Cellulose. 2011;18:57-65.

[398] Qua EH, Hornsby PR, Sharma HSS, Lyons G, McCall RD. Preparation and characterization of poly(vinyl alcohol) nanocomposites made from cellulose nanofibers. Journal of Applied Polymer Science. 2009;113:2238-47.

[399] Park W-I, Kang M, Kim HS, Jin HJ. Electrospinning of Poly(ethylene oxide) with Bacterial Cellulose Whiskers. Macromolecular Symposia. 2007;249-250:289-94.

[400] Oksman K, Mathew AP, Bondeson D, Kvien I. Manufacturing process of cellulose whiskers/polylactic acid nanocomposites. Composites Science and Technology. 2006;66:2776-84.

[401] Sorrentino A, Gorrasi G, Vittoria V. Potential perspectives of bio-nanocomposites for food packaging applications. Trends in Food Science & Technology. 2007;18:84-95.

[402] Frenot A, Henriksson MW, Walkenström P. Electrospinning of cellulose-based nanofibers. Journal of Applied Polymer Science. 2007;103:1473-82.

[403] Lee SY, Mohan DJ, Kang IA, Doh GH, Lee S, Han SO. Nanocellulose reinforced PVA composite films: Effects of acid treatment and filler loading. Fibers and Polymers. 2009;10:77-82.

[404] Bras J, Hassan ML, Bruzesse C, Hassan EA, El-Wakil NA, Dufresne A. Mechanical, barrier, and biodegradability properties of bagasse cellulose whiskers reinforced natural rubber nanocomposites. Industrial Crops and Products. 2010;32:627-33.

[405] Dufresne A, Vignon MR. Improvement of Starch Film Performances Using Cellulose Microfibrils. Macromolecules. 1998;31:2693-6.

[406] Dufresne A, Dupeyre D, Vignon MR. Cellulose microfibrils from potato tuber cells: Processing and characterization of starch–cellulose microfibril composites. Journal of Applied Polymer Science. 2000;76:2080-92.

[407] Anglès MN, Dufresne A. Plasticized Starch/Tunicin Whiskers Nanocomposites. 1. Structural Analysis. Macromolecules. 2000;33:8344-53.

[408] Anglès MN, Dufresne A. Plasticized Starch/Tunicin Whiskers Nanocomposite Materials. 2. Mechanical Behavior. Macromolecules. 2001;34:2921-31.

[409] Roohani M, Habibi Y, Belgacem NM, Ebrahim G, Karimi AN, Dufresne A. Cellulose whiskers reinforced polyvinyl alcohol copolymers nanocomposites. European Polymer Journal. 2008;44:2489-98.

[410] Fernandes SCM, Freire CSR, Silvestre AJD, Pascoal Neto C, Gandini A, Berglund LA, et al. Transparent chitosan films reinforced with a high content of nanofibrillated cellulose. Carbohydrate Polymers. 2010;81:394-401.

[411] Li Q, Zhou JP, Zhang LN. Structure and Properties of the Nanocomposite Films of Chitosan Reinforced with Cellulose Whiskers. Journal of Polymer Science Part B-Polymer Physics. 2009;47:1069-77.

[412] Roy D, Semsarilar M, Guthrie JT, Perrier S. Cellulose modification by polymer grafting: a review. Chemical Society Reviews. 2009;38:2046-64.

[413] Çetin NS, Tingaut P, Özmen N, Henry N, Harper D, Dadmun M, et al. Acetylation of Cellulose Nanowhiskers with Vinyl Acetate under Moderate Conditions. Macromolecular Bioscience. 2009;9:997-1003.

[414] Lin N, Huang J, Chang PR, Feng J, Yu J. Surface acetylation of cellulose

nanocrystal and its reinforcing function in poly(lactic acid). Carbohydrate Polymers. 2011;83:1834-42.

[415] Rodionova G, Lenes M, Eriksen Ø, Gregersen Ø. Surface chemical modification of microfibrillated cellulose: improvement of barrier properties for packaging applications. Cellulose. 2011;18:127-34.

[416] Birgit B, John RD. Single-Step Method for the Isolation and Surface Functionalization of Cellulosic Nanowhiskers. Biomacromolecules. 2009;10:334-41.

[417] de Menezes AJ, Siqueira G, Curvelo AAS, Dufresne A. Extrusion and characterization of functionalized cellulose whiskers reinforced polyethylene nanocomposites. Polymer. 2009;50:4552-63.

[418] Lee KY, Quero F, Blaker J, Hill C, Eichhorn S, Bismarck A. Surface only modification of bacterial cellulose nanofibres with organic acids. Cellulose. 2011;18:595-605.

[419] Pahimanolis N, Hippi U, Johansson L-S, Saarinen T, Houbenov N, Ruokolainen J, et al. Surface functionalization of nanofibrillated cellulose using click-chemistry approach in aqueous media. Cellulose. 2011;18:1201-12.

[420] Goussé C, Chanzy H, Excoffier G, Soubeyrand L, Fleury E. Stable suspensions of partially silylated cellulose whiskers dispersed in organic solvents. Polymer. 2002;43:2645-51.

[421] Pei A, Zhou Q, Berglund LA. Functionalized cellulose nanocrystals as biobased nucleation agents in poly(l-lactide) (PLLA) - Crystallization and mechanical property effects. Composites Science and Technology. 2010;70:815-21.

[422] Zhang J, Jiang N, Dang Z, Elder T, Ragauskas A. Oxidation and sulfonation of cellulosics. Cellulose. 2008;15:489-96.

[423] Okita Y, Fujisawa S, Saito T, Isogai A. TEMPO-Oxidized Cellulose Nanofibrils Dispersed in Organic Solvents. Biomacromolecules. 2010;12:518-22.

[424] Nge T, Nogi M, Yano H, Sugiyama J. Microstructure and mechanical properties of bacterial cellulose/chitosan porous scaffold. Cellulose. 2010;17:349-63.

[425] Habibi Y, Goffin AL, Schiltz N, Duquesne E, Dubois P, Dufresne A. Bionanocomposites based on poly([varepsilon]-caprolactone)-grafted cellulose nanocrystals by ring-opening polymerization. Journal of Materials Chemistry. 2008;18:5002-10.

[426] Lasseuguette E. Grafting onto microfibrils of native cellulose. Cellulose. 2008;15:571-80.

[427] Zoppe JO, Österberg M, Venditti RA, Laine J, Rojas OJ. Surface Interaction Forces of Cellulose Nanocrystals Grafted with Thermoresponsive Polymer Brushes. Biomacromolecules. 2011;12:2788-96.

[428] Ramsden W. Separation of Solids in the Surface-Layers of Solutions and 'Suspensions' (Observations on Surface-Membranes, Bubbles, Emulsions, and Mechanical Coagulation). Proceedings of the Royal Society of London. 1903;72:156-64.

[429] Briggs TR. Emulsions with Finely Divided Solids. Journal of Industrial & Engineering Chemistry. 1921;13:1008-10.

[430] Oza KP, Frank SG. Microcrystalline cellulose stabilized emulsions. Journal of

Dispersion Science and Technology. 1986;7:543-61.

[431] Ougiya H, Watanabe K, Morinaga Y, Yoshinaga F. Emulsion-stabilizing effect of bacterial cellulose. Japan Society for Bioscience, Biotechnology, and Agrochemistry. 1997;61:1541-5.

[432] Andresen M, Johansson L-S, Tanem BS, Stenius P. Properties and characterization of hydrophobized microfibrillated cellulose. Cellulose. 2006;13:665-77.

[433] Andresen M, Stenius P. Water-in-oil Emulsions Stabilized by Hydrophobized Microfibrillated Cellulose. Journal of Dispersion Science and Technology. 2007;28:837-44.

[434] Lif A, Stenstad P, Syverud K, Nydén M, Holmberg K. Fischer-Tropsch diesel emulsions stabilised by microfibrillated cellulose and nonionic surfactants. Journal of Colloid and Interface Science. 2010;352:585-92.

[435] Kalashnikova I, Bizot H, Cathala B, Capron I. New Pickering Emulsions Stabilized by Bacterial Cellulose Nanocrystals. Langmuir. 2011;27:7471-9.

[436] Xhanari K, Syverud K, Chinga-Carrasco G, Paso K, Stenius P. Structure of nanofibrillated cellulose layers at the o/w interface. Journal of Colloid and Interface Science. 2011;356:58-62.

[437] Xhanari K, Syverud K, Stenius P. Emulsions Stabilized by Microfibrillated Cellulose: The Effect of Hydrophobization, Concentration and O/W Ratio. Journal of Dispersion Science and Technology. 2011;32:447-52.

[438] Okubo K, Fujii T, Thostenson ET. Multi-scale hybrid biocomposite: Processing and mechanical characterization of bamboo fiber reinforced PLA with microfibrillated cellulose. Composites Part A: Applied Science and Manufacturing. 2009;40:469-75.

[439] Bondeson D, Oksman K. Polylactic acid/cellulose whisker nanocomposites modified by polyvinyl alcohol. Composites Part A: Applied Science and Manufacturing. 2007;38:2486-92.

[440] Jonoobi M, Harun J, Mathew AP, Oksman K. Mechanical properties of cellulose nanofiber (CNF) reinforced polylactic acid (PLA) prepared by twin screw extrusion. Composites Science and Technology. 2010;70:1742-7.

[441] Pei A, Malho J-M, Ruokolainen J, Zhou Q, Berglund LA. Strong Nanocomposite Reinforcement Effects in Polyurethane Elastomer with Low Volume Fraction of Cellulose Nanocrystals. Macromolecules. 2011;44:4422-7.

[442] Ten E, Turtle J, Bahr D, Jiang L, Wolcott M. Thermal and mechanical properties of poly(3-hydroxybutyrate-co-3-hydroxyvalerate)/cellulose nanowhiskers composites. Polymer. 2010;51:2652-60.

[443] http://en.wikipedia.org/wiki/Nanocellulose.

[444] O'Sullivan A. Cellulose: the structure slowly unravels. Cellulose. 1997;4:173-207.

[445] Zhong LX, Fu SY, Zhou XS, Zhan HY. Effect of surface microfibrillation of sisal fibre on the mechanical properties of sisal/aramid fibre hybrid composites. Composites Part A: Applied Science and Manufacturing. 2011;42:244-52.

[446] Habibi Y, Mahrouz M, Vignon MR. Microfibrillated cellulose from the peel of prickly pear fruits. Food Chemistry. 2009;115:423-9.

[447] Bhattacharyya A, Dutta S, De P, Ray P, Basu S. Removal of mercury (II) from aqueous solution using papain immobilized on alginate bead: Optimization of immobilization condition and modeling of removal study. Bioresour Technol. 2010;101:9421-8.

[448] Box GEP, Wilson KB. On the experimental attainment of optimum conditions. Journal of the royal statistical society series b (methodological). 1951;13:1-45.

[449] Cui FJ, Li Y, Xu ZH, Xu HY, Sun K, Tao WY. Optimization of the medium composition for production of mycelial biomass and exo-polymer by Grifola frondosa GF9801 using response surface methodology. Bioresour Technol. 2006;97:1209-16.

[450] Istadi I, Saidina Amin NA. Catalytic-Dielectric Barrier Discharge Plasma Reactor For Methane And Carbon Dioxide Conversion. Bulletin of Chemical Reaction Engineering & Catalysis. 2007;2:37-44.

[451] Xu C, Shamey R, Hinks D. Activated peroxide bleaching of regenerated bamboo fiber using a butyrolactam-based cationic bleach activator. Cellulose. 2010;17:339-47.

[452] Noordin MY, Venkatesh VC, Sharif S, Elting S, Abdullah A. Application of response surface methodology in describing the performance of coated carbide tools when turning AISI 1045 steel. Journal of Materials Processing Technology. 2004;145:46-58.

[453] Aguilar MAS, Rodríguez GJM, Cabrera-Ríos M. Statistical characterization and optimization of artificial neural networks in time series forecasting: the one-period forecast case. Computación y Sistemas. 2006;10:69-81.

[454] Lachiver ED, Abatzoglou N, Cartilier L, Simard J-S. Agglomeration tendency in dry pharmaceutical granular systems. European Journal of Pharmaceutics and Biopharmaceutics. 2006;64:193-9.

[455] Lee K-M, Gilmore DF. Formulation and process modeling of biopolymer (polyhydroxyalkanoates: PHAs) production from industrial wastes by novel crossed experimental design. Process Biochemistry. 2005;40:229-46.

[456] Dufour J, Lopez L, Negro C, Latorre R, Formoso A, Lopez-Mateos F. Mathematical model of magnetite synthesis by oxidation of sulfuric pickling liquors from steelmaking. Chemical Engineering Communications. 2002;189:285-97.

[457] Karacan F, Ozden U, Karacan S. Optimization of manufacturing conditions for activated carbon from Turkish lignite by chemical activation using response surface methodology. Applied Thermal Engineering. 2007;27:1212-8.

[458] Shukla P, Garai D, Zafar M, Gupta K, Shrivastava S. Process parameters optimization for lipase production by Rhizopus oryzae kg-10 under submerged fermentation using response surface methodology. Journal of Applied Sciences in Environmental Sanitation. 2007;2:93-103.

[459] Multifactor RSM Tutorial-Part 1.   Design-Expert 8 User`s Guide Minneapolis: Stat-Ease Inc; 2010.

[460] Ahn JH, Kim YP, Lee YM, Seo EM, Lee KW, Kim HS. Optimization of microencapsulation of seed oil by response surface methodology. Food Chemistry. 2008;107:98-105.

[461] van der Wel NN, Putman CAJ, van Noort SJT, de Groot BG, Emons AMC.

Atomic force microscopy of pollen grains, cellulose microfibrils, and protoplasts. Protoplasma. 1996;194:29-39.

[462] Dufresne A, Cavaille JY, Vignon MR. Mechanical behavior of sheets prepared from sugar beet cellulose microfibrils. Journal of Applied Polymer Science. 1997;64:1185-94.

[463] Segal L, Creely JJ, Martin AE, Conrad CM. An Empirical Method for Estimating the Degree of Crystallinity of Native Cellulose Using the X-Ray Diffractometer. Textile Research Journal. 1959;29:786-94.

[464] Pyris Kinetics Software Guide. USA: PerkinElmer Instruments LLC., 2002.

[465] Matuana LM, Balatinecz JJ, Sodhi RNS, Park CB. Surface characterization of esterified cellulosic fibers by XPS and FTIR Spectroscopy. Wood Science and Technology. 2001;35:191-201.

[466] Johansson L-S. Monitoring Fibre Surfaces with XPS in Papermaking Processes. Microchimica Acta. 2002;138:217-23.

[467] Lu J, Askeland P, Drzal LT. Surface modification of microfibrillated cellulose for epoxy composite applications. Polymer. 2008;49:1285-96.

[468] Kalaskar D, Ulijn R, Gough J, Alexander M, Scurr D, Sampson W, et al. Characterisation of amino acid modified cellulose surfaces using ToF-SIMS and XPS. Cellulose. 2010;17:747-56.

[469] Zimmermann KA, LeBlanc JM, Sheets KT, Fox RW, Gatenholm P. Biomimetic design of a bacterial cellulose/hydroxyapatite nanocomposite for bone healing applications. Materials Science and Engineering: C. 2011;31:43-9.

[470] Bastidas JC, Venditti R, Pawlak J, Gilbert R, Zauscher S, Kadla JF. Chemical force microscopy of cellulosic fibers. Carbohydrate Polymers. 2005;62:369-78.

[471] Paleos CM, Tsiourvas D. Thermotropic Liquid Crystals Formed by Intermolecular Hydrogen Bonding Interactions. Angewandte Chemie International Edition in English. 1995;34:1696-711.

[472] Nelson ML, O'Connor RT. Relation of certain infrared bands to cellulose crystallinity and crystal latticed type. Part I. Spectra of lattice types I, II, III and of amorphous cellulose. Journal of Applied Polymer Science. 1964;8:1311-24.

[473] Kondo T, Sawatari C. A Fourier transform infra-red spectroscopic analysis of the character of hydrogen bonds in amorphous cellulose. Polymer. 1996;37:393-9.

[474] Schwanninger M, Rodrigues JC, Pereira H, Hinterstoisser B. Effects of short-time vibratory ball milling on the shape of FT-IR spectra of wood and cellulose. Vibrational Spectroscopy. 2004;36:23-40.

[475] Merk S, Blume A, Riederer M. Phase behaviour and crystallinity of plant cuticular waxes studied by Fourier transform infrared spectroscopy. Planta. 1997;204:44-53.

[476] Dubis EN, Dubis AT, Morzycki JW. Comparative analysis of plant cuticular waxes using HATR FT-IR reflection technique. Journal of Molecular Structure. 1999;511-512:173-9.

[477] Singthong J, Cui SW, Ningsanond S, Douglas Goff H. Structural characterization, degree of esterification and some gelling properties of Krueo Ma Noy (Cissampelos pareira) pectin. Carbohydrate Polymers. 2004;58:391-400.

[478] Singthong J, Ningsanond S, Cui SW, Douglas Goff H. Extraction and physicochemical characterization of Krueo Ma Noy pectin. Food Hydrocolloids. 2005;19:793-801.

[479] Xu L, Lio A, Hu J, Ogletree DF, Salmeron M. Wetting and Capillary Phenomena of Water on Mica. The Journal of Physical Chemistry B. 1998;102:540-8.

[480] Calvini P, Gorassini A, Luciano G, Franceschi E. FTIR and WAXS analysis of periodate oxycellulose: Evidence for a cluster mechanism of oxidation. Vibrational Spectroscopy. 2006;40:177-83.

[481] Fengel D. Möglichkeiten und Grenzen der FTIR-Spektroskopie bei der Charakterisierung von Cellulose. Das Papier. 1991;46:7-11.

[482] Faix O. Classification of Lignins from Different Botanical Origins by FT-IR Spectroscopy. Holzforschung. 1991;45:21-8.

[483] Kubo S, Kadla JF. Hydrogen Bonding in Lignin: A Fourier Transform Infrared Model Compound Study. Biomacromolecules. 2005;6:2815-21.

[484] Rana AK, Basak RK, Mitra BC, Lawther M, Banerjee AN. Studies of acetylation of jute using simplified procedure and its characterization. Journal of Applied Polymer Science. 1997;64:1517-23.

[485] Cael JJ, Gardner KH, Koenig JL, Blackwell J. Infrared and Raman spectroscopy of carbohydrates. Paper V. Normal coordinate analysis of cellulose I. The Journal of Chemical Physics. 1975;62:1145-53.

[486] Colom X, Carrillo F. Crystallinity changes in lyocell and viscose-type fibres by caustic treatment. European Polymer Journal. 2002;38:2225-30.

[487] Carrillo F, Colom X, Suñol JJ, Saurina J. Structural FTIR analysis and thermal characterisation of lyocell and viscose-type fibres. European Polymer Journal. 2004;40:2229-34.

[488] Ruan D, Zhang L, Mao Y, Zeng M, Li X. Microporous membranes prepared from cellulose in NaOH/thiourea aqueous solution. Journal of Membrane Science. 2004;241:265-74.

[489] Collier W, Kalasinsky VF, Schultz TP. Infrared study of lignin: Assignment of methoxyl C-H bending and stretching bands. Holzforschung. 1997;51:167-8.

[490] Cao Y, Tan H. Structural characterization of cellulose with enzymatic treatment. Journal of Molecular Structure. 2004;705:189-93.

[491] Liang CY, Marchessault RH. Infrared spectra of crystalline polysaccharides. II. Native celluloses in the region from 640 to 1700 cm^{-1}. Journal of Polymer Science. 1959;39:269-78.

[492] Maréchal Y, Chanzy H. The hydrogen bond network in I_β cellulose as observed by infrared spectrometry. Journal of Molecular Structure. 2000;523:183-96.

[493] http://en.wikipedia.org/wiki/Hydrogen_bond.

[494] Ivanova NV, Korolenko EA, Korolik EV, Zhbankov RG. IR spectrum of cellulose. Journal of Applied Spectroscopy. 1989;51:847-51.

[495] Liang CY, Marchessault RH. Infrared spectra of crystalline polysaccharides. I. Hydrogen bonds in native celluloses. Journal of Polymer Science. 1959;37:385-95.

[496] Kalutskaya EP, Gusev SS. An infrared spectroscopic investigation of the hydration of cellulose. Polymer Science USSR. 1980;22:550-6.

[497] Ivanova N, Korolenko E, Korolik E, Zbankov R. Mathematical processing of IR-spectra of cellulose. Zurnal Prikladnoj Spektroskopii. 1989;51:301-6.

[498] Lu P, Hsieh Y-L. Preparation and properties of cellulose nanocrystals: Rods, spheres, and network. Carbohydrate Polymers. 2010;82:329-36.

[499] Quievy N, Jacquet N, Sclavons M, Deroanne C, Paquot M, Devaux J. Influence of homogenization and drying on the thermal stability of microfibrillated cellulose. Polymer Degradation and Stability. 2010;95:306-14.

[500] Roman M, Winter WT. Effect of Sulfate Groups from Sulfuric Acid Hydrolysis on the Thermal Degradation Behavior of Bacterial Cellulose. Biomacromolecules. 2004;5:1671-7.

[501] Wang N, Ding E. Thermal behavior of nanocrystalline cellulose treated by acid or alkali. Acta polymerica sinica. 2004:925-8.

[502] Karus M, Kaup M. Natural Fibres in the European Automotive Industry. Journal of Industrial Hemp. 2002;7:119-31.

[503] Mohanty AK, Misra M, Drzal LT. Sustainable Bio-Composites from Renewable Resources: Opportunities and Challenges in the Green Materials World. Journal of Polymers and the Environment. 2002;10:19-26.

[504] Karus M, Vogt D. European hemp industry: Cultivation, processing and product lines. Euphytica. 2004;140:7-12.

[505] Van de Velde K, Kiekens P. Thermoplastic pultrusion of natural fibre reinforced composites. Composite Structures.54:355-60.

[506] Jain S, Jindal UC, Kumar R. Development and fracture mechanism of the bamboo/polyester resin composite. Journal of Materials Science Letters. 1993;12:558-60.

[507] Pothan LA, Thomas S, Neelakantan NR. Short Banana Fiber Reinforced Polyester Composites: Mechanical, Failure and Aging Characteristics. Journal of Reinforced Plastics and Composites. 1997;16:744-65.

[508] Rout J, Misra M, Tripathy SS, Nayak SK, Mohanty AK. Novel eco-friendly biodegradable coir-polyester amide biocomposites: Fabrication and properties evaluation. Polymer Composites. 2001;22:770-8.

[509] Williams GI, Wool RP. Composites from Natural Fibers and Soy Oil Resins. Applied Composite Materials. 2000;7:421-32.

[510] Hepworth DG, Hobson RN, Bruce DM, Farrent JW. The use of unretted hemp fibre in composite manufacture. Composites Part A: Applied Science and Manufacturing. 2000;31:1279-83.

[511] Plackett D, Løgstrup Andersen T, Batsberg Pedersen W, Nielsen L. Biodegradable composites based on -polylactide and jute fibres. Composites Science and Technology. 2003;63:1287-96.

[512] Nishino T, Hirao K, Kotera M, Nakamae K, Inagaki H. Kenaf reinforced biodegradable composite. Composites Science and Technology. 2003;63:1281-6.

[513] Lei W, Lei W, Ren C. Effect of volume fraction of ramie cloth on physical and mechanical properties of ramie cloth/UP resin composite. Transactions of Nonferrous Metals Society of China. 2006;16, Supplement 2:s474-s7.

[514] Malunka ME, Luyt AS, Krump H. Preparation and characterization of

EVA–sisal fiber composites. Journal of Applied Polymer Science. 2006;100:1607-17.

[515] Boey FYC. Microbuckling compression failure of a radiation-induced wood/polymer composite. Composites Science and Technology. 1990;38:159-73.

[516] Belgacem MN, Gandini A. The surface modification of cellulose fibres for use as reinforcing elements in composite materials. Composite Interfaces. 2005;12:41-75.

[517] Lee HJ, Yeo SY, Jeong SH. Antibacterial effect of nanosized silver colloidal solution on textile fabrics. Journal of Materials Science. 2003;38:2199-204.

[518] Tarimala S, Kothari N, Abidi N, Hequet E, Fralick J, Dai LL. New approach to antibacterial treatment of cotton fabric with silver nanoparticle–doped silica using sol–gel process. Journal of Applied Polymer Science. 2006;101:2938-43.

[519] Ilić V, Šaponjić Z, Vodnik V, Potkonjak B, Jovančić P, Nedeljković J, et al. The influence of silver content on antimicrobial activity and color of cotton fabrics functionalized with Ag nanoparticles. Carbohydrate Polymers. 2009;78:564-9.

[520] Qi K, Chen X, Liu Y, Xin JH, Mak CL, Daoud WA. Facile preparation of anatase/SiO2 spherical nanocomposites and their application in self-cleaning textiles. Journal of Materials Chemistry. 2007;17:3504-8.

[521] Uddin MJ, Cesano F, Scarano D, Bonino F, Agostini G, Spoto G, et al. Cotton textile fibres coated by Au/TiO2 films: Synthesis, characterization and self cleaning properties. Journal of Photochemistry and Photobiology A: Chemistry. 2008;199:64-72.

[522] Veronovski N, Rudolf A, Smole M, Kreže T, Geršak J. Self-cleaning and handle properties of TiO_2-modified textiles. Fibers and Polymers. 2009;10:551-6.

[523] Yu M, Gu G, Meng WD, Qing FL. Superhydrophobic cotton fabric coating based on a complex layer of silica nanoparticles and perfluorooctylated quaternary ammonium silane coupling agent. Applied Surface Science. 2007;253:3669-73.

[524] Tomšič B, Simončič B, Orel B, Černe L, Tavčer P, Zorko M, et al. Sol–gel coating of cellulose fibres with antimicrobial and repellent properties. Journal of Sol-Gel Science and Technology. 2008;47:44-57.

[525] Bae GY, Min BG, Jeong YG, Lee SC, Jang JH, Koo GH. Superhydrophobicity of cotton fabrics treated with silica nanoparticles and water-repellent agent. Journal of Colloid and Interface Science. 2009;337:170-5.

[526] Wang RH, Xin JH, Tao XM. UV-Blocking Property of Dumbbell-Shaped ZnO Crystallites on Cotton Fabrics. Inorganic Chemistry. 2005;44:3926-30.

[527] Mondal S, Hu JL. A novel approach to excellent UV protecting cotton fabric with functionalized MWNT containing water vapor permeable PU coating. Journal of Applied Polymer Science. 2007;103:3370-6.

[528] Gulati D, Sain M. Fungal-modification of Natural Fibers: A Novel Method of Treating Natural Fibers for Composite Reinforcement. Journal of Polymers and the Environment. 2006;14:347-52.

[529] Juntaro J, Pommet M, Mantalaris A, Shaffer M, Bismarck A. Nanocellulose enhanced interfaces in truly green unidirectional fibre reinforced composites. Composite Interfaces. 2007;14:753-62.

[530] Pommet M, Juntaro J, Heng JYY, Mantalaris A, Lee AF, Wilson K, et al. Surface Modification of Natural Fibers Using Bacteria: Depositing Bacterial

Cellulose onto Natural Fibers To Create Hierarchical Fiber Reinforced Nanocomposites. Biomacromolecules. 2008;9:1643-51.

[531] Uchiyama H, Tokuoka Y, Abe M, Ogino K. Solubilization of oil—soluble azo dye by anionic—nonionic mixed surfactants in aqueous solutions, II. Journal of Colloid and Interface Science. 1989;132:88-93.

[532] Tavčer PF, Špan J. Dye-Surfactant Interactions Studied Using Job's Method. Textile Research Journal. 1999;69:278-84.

[533] Biswas SC, Chattoraj DK. Polysaccharide−Surfactant Interaction. 1. Adsorption of Cationic Surfactants at the Cellulose−Water Interface. Langmuir. 1997;13:4505-11.

[534] Akbaş H, Kartal Ç. Conductometric studies of the interaction of C.I. Reactive Orange 16 with cationic alkyltrimethylammonium bromide surfactants. Dyes and Pigments. 2007;72:383-6.

[535] Blomstedt M, Vuorinen T. Modification of softwood kraft pulp with carboxymethyl cellulose and cationic surfactants. Journal of Wood Science. 2007;53:223-8.

[536] Biswas SC, Chattoraj DK. Polysaccharide−Surfactant Interaction. 2. Binding of Cationic Surfactants to Carboxymethyl Cellulose and Dextrin. Langmuir. 1997;13:4512-9.

[537] Vargantwar PH. Preparation of ionic cellulose for wrinkle resistant fabrics: North Carolina State University, 2008.

[538] http://en.wikipedia.org/wiki/Energy-dispersive_X-ray_spectroscopy.

[539] http://www.sigmaaldrich.com/catalog/product/sigma/d5047?lang=en&region=GB.

[540] http://www.webelements.com/.

[541] Wang HH, Drummond JG, Reath SM, Hunt K, Watson PA. An improved fibril angle measurement method for wood fibres. Wood Science and Technology. 2001;34:493-503.

[542] Thygesen A, Daniel G, Lilholt H, Thomsen AB. Hemp Fiber Microstructure and Use of Fungal Defibration to Obtain Fibers for Composite Materials. Journal of Natural Fibers. 2006;2:19-37.

[543] Fink HP, Walenta E, Kunze J. The structure of natural cellulosic fibres-Part 2. The supermolecular structure of bast fibres and their changes by mercerization as revealed by X-ray diffraction and ^{13}C-NMR-spectroscopy. Papier. 1999;53:534-42.

[544] Ander P, Nyholm K. Deformations in wood and spruce pulp fibres: their importance for wood and pulp properties. In: Stanzl-Tschegg SE, Reiterer A, editors. Proceeding of the International Symposium on Wood Machining: Properties of Wood and Wood Composites related to wood machining2000. p. 3-19.

[545] Nyholm K, Ander P, Bardage S, Daniel G. Dislocations in pulp fibres-their origin, characteristics and importance-a review. Nordic Pulp and Paper Research Journal. 2001;16:376-84.

[546] Hughes M. Defects in natural fibres: their origin, characteristics and implications for natural fibre-reinforced composites. Journal of Materials Science. 2012;47:599-609.

[547] Hughes M, Sebe G, Hague J, Hill C, Spear M, Mott L. An investigation into the

effects of micro-compressive defects on interphase behaviour in hemp-epoxy composites using half-fringe photoelasticity. Composite Interfaces. 2000;7:13-29.

[548] Terziev N, Daniel G, Marklund A. Dislocations in Norway spruce fibres and their effect on properties of pulp and paper. Holzforschung2005. p. 163.

[549] Bos HL, Van den Oever MJA, Peters O. Tensile and compressive properties of flax fibres for natural fibre reinforced composites. Journal of Materials Science. 2002;37:1683-92.

[550] Persson K. Modelling of wood properties by a micromechanical approach: Lund Univ., Lund Inst. of Technology, Div. Structural Mechanics, 1997.

[551] Kataoka Y, Kondo T. FT-IR Microscopic Analysis of Changing Cellulose Crystalline Structure during Wood Cell Wall Formation. Macromolecules. 1998;31:760-4.

[552] O'Connor RT, DuPré EF, Mitcham D. Applications of Infrared Absorption Spectroscopy to Investigations of Cotton and Modified Cottons. Textile Research Journal. 1958;28:382-92.

[553] Ferruz R, Pages P. Water Retention Value and Degree of Crystallinity by Infrared Absorption Spectroscopy in Caustic Soda Treated Cotton. Cellulose Chemistry and Technology. 1977;11:633-7.

[554] Hearle JWS. A fringed fibril theory of structure in crystalline polymers. Journal of Polymer Science. 1958;28:432-5.

[555] Fengel D. Influence of Water on the OH Valency Range in Deconvoluted FTIR Spectra of Cellulose. Holzforschung. 1993;47:103-8.

[556] Kondo T. Hydrogen bonds in regioselectively substituted cellulose derivatives. Journal of Polymer Science Part B: Polymer Physics. 1994;32:1229-36.

[557] Kondo T. The assignment of IR absorption bands due to free hydroxyl groups in cellulose. Cellulose. 1997;4:281-92.

[558] Kondo T. The relationship between intramolecular hydrogen bonds and certain physical properties of regioselectively substituted cellulose derivatives. Journal of Polymer Science Part B: Polymer Physics. 1997;35:717-23.

[559] Itagaki H, Tokai M, Kondo T. Physical gelation process for cellulose whose hydroxyl groups are regioselectively substituted by fluorescent groups. Polymer. 1997;38:4201-5.

[560] Kondo T, Sawatari C, Manley RSJ, Gray DG. Characterization of hydrogen bonding in cellulose-synthetic polymer blend systems with regioselectively substituted methylcellulose. Macromolecules. 1994;27:210-5.

[561] Kondo T, Sawatari C. Intermolecular hydrogen bonding in cellulose/poly(ethylene oxide) blends: thermodynamic examination using 2,3-di-O- and 6-O-methylcelluloses as cellulose model compounds. Polymer. 1994;35:4423-8.

[562] del Río JC, Gutiérrez A, Rodríguez IM, Ibarra D, Martínez ÁT. Composition of non-woody plant lignins and cinnamic acids by Py-GC/MS, Py/TMAH and FT-IR. Journal of Analytical and Applied Pyrolysis. 2007;79:39-46.

[563] Marchessault RH, Liang CY. Infrared spectra of crystalline polysaccharides. III. Mercerized cellulose. Journal of Polymer Science. 1960;43:71-84.

[564] Edeerozey AMM, Akil HM, Azhar AB, Ariffin MIZ. Chemical modification of

kenaf fibers. Materials Letters. 2007;61:2023-5.

[565] Ouajai S, Hodzic A, Shanks RA. Morphological and grafting modification of natural cellulose fibers. Journal of Applied Polymer Science. 2004;94:2456-65.

[566] Eder M, Terziev N, Daniel G, Burgert I. The effect of (induced) dislocations on the tensile properties of individual Norway spruce fibres. Holzforschung. 2007;62:77-81.

[567] Dai D, Fan M. Investigation of the dislocation of natural fibres by Fourier-transform infrared spectroscopy. Vibrational Spectroscopy. 2011;55:300-6.

[568] Emerson MF, Holtzer A. Hydrophobic bond in micellar systems. Effects of various additives on the stability of micelles of sodium dodecyl sulfate and of n-dodecyltrimethylammonium bromide. The Journal of Physical Chemistry. 1967;71:3320-30.

[569] Cosgrove T. Colloid science: principles, methods and applications. USA: Wiley-Blackwell, 2010.

[570] Paria S, Manohar C, Khilar KC. Adsorption of anionic and non-ionic surfactants on a cellulosic surface. Colloids and Surfaces A: Physicochemical and Engineering Aspects. 2005;252:221-9.

[571] Yatcilla MT, Herrington KL, Brasher LL, Kaler EW, Chiruvolu S, Zasadzinski JA. Phase Behavior of Aqueous Mixtures of Cetyltrimethylammonium Bromide (CTAB) and Sodium Octyl Sulfate (SOS). The Journal of Physical Chemistry. 1996;100:5874-9.

[572] Sfiligoj Smole M, Peršin Z, Kreže T, Stana Kleinschek K, Ribitsch V, Neumayer S. X-ray study of pre-treated regenerated cellulose fibres. Materials Research Innovations. 2003;7:275-82.

[573] Inglesby M, Zeronian S. The accessibility of cellulose as determined by dye adsorption. Cellulose. 1996;3:165-81.

[574] Thygesen LG. Quantification of dislocations in hemp fibers using acid hydrolysis and fiber segment length distributions. Journal of Materials Science. 2008;43:1311-7.

[575] Wagberg L, Decher G, Norgren M, Lindstrom T, Ankerfors M, Axnas K. The Build-Up of Polyelectrolyte Multilayers of Microfibrillated Cellulose and Cationic Polyelectrolytes. Langmuir. 2008;24:784-95.

[576] Habibi Y, Lucia LA, Rojas OJ. Cellulose Nanocrystals: Chemistry, Self-Assembly, and Applications. Chemical Reviews. 2010;110:3479-500.

[577] Azizi Samir MAS, Alloin F, Gorecki W, Sanchez J-Y, Dufresne A. Nanocomposite Polymer Electrolytes Based on Poly(oxyethylene) and Cellulose Nanocrystals. The Journal of Physical Chemistry B. 2004;108:10845-52.

[578] Kennedy C, Cameron G, Šturcová A, Apperley D, Altaner C, Wess T, et al. Microfibril diameter in celery collenchyma cellulose: X-ray scattering and NMR evidence. Cellulose. 2007;14:235-46.

[579] Mandell JF, Chen JH, McGarry FJ. A microdebonding test for in situ assessment of fibre/matrix bond strength in composite materials. International Journal of Adhesion and Adhesives. 1980;1:40-4.

[580] Gaur U, Miller B. Microbond method for determination of the shear strength of

a fiber/resin interface: Evaluation of experimental parameters. Composites Science and Technology. 1989;34:35-51.

[581] Yue CY, Looi HC, Quek MY. Assessment of fibre-matrix adhesion and interfacial properties using the pull-out test. International Journal of Adhesion and Adhesives. 1995;15:73-80.

[582] Zadorecki P, Rönnhult T. An ESCA study of chemical reactions on the surfaces of cellulose fibers. Journal of Polymer Science Part A: Polymer Chemistry. 1986;24:737-45.

[583] Hua L, Flodin P, Rönnhult T. Cellulose fiber-polyester composites with reduced water sensitivity (2)—surface analysis. Polymer Composites. 1987;8:203-7.

[584] Takase S, Shiraishi N. Studies on composites from wood and polypropylenes. II. Journal of Applied Polymer Science. 1989;37:645-59.

[585] Felix JM, Gatenholm P. The nature of adhesion in composites of modified cellulose fibers and polypropylene. Journal of Applied Polymer Science. 1991;42:609-20.

[586] Gassan J, Gutowski VS, Bledzki AK. About the surface characteristics of natural fibres. Macromolecular Materials and Engineering. 2000;283:132-9.

[587] Montes-Morán MA, Martínez-Alonso A, Tascón JMD, Paiva MC, Bernardo CA. Effects of plasma oxidation on the surface and interfacial properties of carbon fibres/polycarbonate composites. Carbon. 2001;39:1057-68.

[588] Park SJ, Kim MH. Effect of acidic anode treatment on carbon fibers for increasing fiber-matrix adhesion and its relationship to interlaminar shear strength of composites. Journal of Materials Science. 2000;35:1901-5.

[589] Singh B, Gupta M, Verma A, Tyagi OS. FT-IR microscopic studies on coupling agents: treated natural fibres. Polymer International. 2000;49:1444-51.

[590] Rahmat AR, Day RJ. Curing Characteristics Of Unsaturated Polyester/Aramid Reinforced Composite: Microwave Vs. Thermal Energy. Jurnal Teknologi Siri Khas A. 2003:83-96.

[591] Worzakowska M. Chemical modification of unsaturated polyesters influence of polyester's structure on thermal and viscoelastic properties of low styrene content copolymers. Journal of Applied Polymer Science. 2009;114:720-31.

[592] Wetzel B, Rosso P, Haupert F, Friedrich K. Epoxy nanocomposites – fracture and toughening mechanisms. Engineering Fracture Mechanics. 2006;73:2375-98.

[593] Chen C, Justice RS, Schaefer DW, Baur JW. Highly dispersed nanosilica–epoxy resins with enhanced mechanical properties. Polymer. 2008;49:3805-15.

[594] Shimazaki Y, Miyazaki Y, Takezawa Y, Nogi M, Abe K, Ifuku S, et al. Excellent thermal conductivity of transparent cellulose nanofiber/epoxy resin nanocomposites. Biomacromolecules. 2007;8:2976-8.

[595] Omrani A, Simon LC, Rostami AA. Influences of cellulose nanofiber on the epoxy network formation. Materials Science and Engineering a-Structural Materials Properties Microstructure and Processing. 2008;490:131-7.

[596] Tang LM, Weder C. Cellulose Whisker/Epoxy Resin Nanocomposites. ACS Applied Materials & Interfaces. 2010;2:1073-80.

[597] Kotsilkova R, Pissis P. Thermoset nanocomposites for engineering applications:

Rapra Technology, 2007.

[598] Tammann G, Hesse W. Die Abhängigkeit der Viscosität von der Temperatur bie unterkühlten Flüssigkeiten. Zeitschrift fur Anorganische und Allgemeine Chemie. 1926;156:245-57.

[599] Honda K. On a Thermobalance. Sci Rep Tohuku Univ. 1915;4:97-103.

[600] Joseph H F. Thermal analysis kinetics-past, present and future. Thermochimica Acta. 1992;203:519-26.

[601] Vyazovkin S, Wight CA. Isothermal and non-isothermal kinetics of thermally stimulated reactions of solids. International Reviews in Physical Chemistry. 1998;17:407-33.

[602] Vyazovkin S, Wight CA. Kinetics in solids. Annual Review of Physical Chemistry. 1997;48:125-49.

[603] Roşu D, Caşcaval CN, Mustaţă F, Ciobanu C. Cure kinetics of epoxy resins studied by non-isothermal DSC data. Thermochimica Acta. 2002;383:119-27.

[604] Kissinger HE. Reaction Kinetics in Differential Thermal Analysis. Analytical Chemistry. 1957;29:1702-6.

[605] Akahira T, Sunose T. Joint convention of four electrical institutes. Research Report Chiba Institute Technology. 1971;16:22-31.

[606] Friedman HL. Kinetics of thermal degradation of char-forming plastics from thermogravimetry. Application to a phenolic plastic. Journal of Polymer Science Part C: Polymer Symposia. 1964;6:183-95.

[607] Ozawa T. A new method of analyzing thermogravimetric data. Bulletin of the Chemical Society of Japan. 1965;38:1881-6.

[608] Flynn JH, Wall LA. A quick, direct method for the determination of activation energy from thermogravimetric data. Journal of Polymer Science Part B: Polymer Letters. 1966;4:323-8.

[609] Jiří M. The kinetic analysis of non-isothermal data. Thermochimica Acta. 1992;200:257-69.

[610] Jiří M. The shape of thermoanalytical curves as a function of the reaction kinetics. Thermochimica Acta. 1993;222:105-13.

[611] Montserrat S, Málek J. A kinetic analysis of the curing reaction of an epoxy resin. Thermochimica Acta. 1993;228:47-60.

[612] Popescu C, Segal E, Iditoiu C. A kinetic model for the thermal decomposition of wool. Thermochimica Acta. 1995;256:419-27.

[613] Dollimore D, Tong P, Alexander KS. The kinetic interpretation of the decomposition of calcium carbonate by use of relationships other than the Arrhenius equation. Thermochimica Acta. 1996;282-283:13-27.

[614] M.J S. A new method for the derivation of activation energies from experiments performed at constant heating rate. Thermochimica Acta. 1996;288:97-104.

[615] Vyazovkin S. Evaluation of activation energy of thermally stimulated solid-state reactions under arbitrary variation of temperature. Journal of Computational Chemistry. 1997;18:393-402.

[616] Montserrat S, Flaqué C, Calafell M, Andreu G, Málek J. Influence of the accelerator concentration on the curing reaction of an epoxy-anhydride system.

Thermochimica Acta. 1995;269-270:213-29.

[617] Sbirrazzuoli N, Girault Y, Elégant L. The Málek method in the kinetic study of polymerization by differential scanning calorimetry. Thermochimica Acta. 1995;249:179-87.

[618] Li H, Shao T, Li D, Chen D. Nonisothermal reaction kinetics of diasporic bauxite. Thermochimica Acta. 2005;427:9-12.

[619] Coats AW, Redfern JP. Kinetic Parameters from Thermogravimetric Data. Nature. 1964;201:68-9.

[620] Liu Xw, Feng Yl, Li Hr. Preparation of basic magnesium carbonate and its thermal decomposition kinetics in air. Journal of Central South University of Technology. 2011;18:1865-70.

[621] Senum GI, Yang RT. Rational approximations of the integral of the Arrhenius function. Journal of Thermal Analysis and Calorimetry. 1977;11:445-7.

[622] Segal L, Loeb L. The diethylenetriamine-cellulose complex. Journal of Polymer Science. 1960;42:351-6.

[623] Segal L, Eggerton FV. Infrared Spectra of Diethylenetriamine and 2-(2-Aminoethylamino)ethanol. Applied Spectroscopy. 1961;15:148-50.

[624] Segal L. Concerning the diethylenetriamine-cellulose complex. Journal of Polymer Science Part B: Polymer Letters. 1963;1:241-4.

[625] Creely JJ, Wade RH. Complexes of cellulose with sterically hindered amines. Journal of Polymer Science: Polymer Letters Edition 1978;16:477-80.

[626] Creely JJ, Wade RH, French AD. X-Ray Diffraction, Thermal, and Physical Studies of Complexes of Cellulose with Secondary Diamines. Textile Research Journal. 1978;48:37-43.

[627] Lam DCC, Chong ACM. Effect of cross-link density on strain gradient plasticity in epoxy. Materials Science and Engineering: A. 2000;281:156-61.

[628] Loos AC, Springer GS. Curing of Epoxy Matrix Composites. Journal of Composite Materials. 1983;17:135-69.

[629] Kotsilkova R. Chapter 1 Introduction. In: Kotsilkova R, Pissis P, editors. Thermoset nanocomposites for engineering applications: Rapra Technology; 2007. p. 1-18.

[630] Bal S, Samal S. Carbon nanotube reinforced polymer composites—A state of the art. Bulletin of Materials Science. 2007;30:379-86.

[631] Moore DJ, Rerek ME, Mendelsohn R. FTIR Spectroscopy Studies of the Conformational Order and Phase Behavior of Ceramides. The Journal of Physical Chemistry B. 1997;101:8933-40.

[632] Yusufoglu Y, Hu Y, Kanapathipillai M, Kramer M, Kalay YE, Thiyagarajan P, et al. Bioinspired synthesis of self-assembled calcium phosphate nanocomposites using block copolymer-peptide conjugates. Journal of Materials Research. 2008;23:3196-212.

[633] Blank WJ, He ZA, Picci M. Catalysis of the Epoxy-Carboxyl Reaction. International Waterborne, High-Solids and Powder Coatings Symposium. New Orleans, LA USA2001.

[634] Manning P. Chemical bonds. USA: Infobase Publishing, 2008.

[635] Han SO, Drzal LT. Curing characteristics of carboxyl functionalized glucose resin and epoxy resin. European Polymer Journal. 2003;39:1377-84.

[636] Yang X, Zeng Y, Ma F, Zhang X, Yu H. Effect of biopretreatment on thermogravimetric and chemical characteristics of corn stover by different white-rot fungi. Bioresource Technology. 2010;101:5475-9.

[637] Dufresne A, Paillet M, Putaux JL, Canet R, Carmona F, Delhaes P, et al. Processing and characterization of carbon nanotube/poly(styrene-co-butyl acrylate) nanocomposites. Journal of Materials Science. 2002;37:3915-23.

[638] Dourandish M, Simchi A, Hokamoto K, Tanaka S. Interface formation and bond strength in 3Y-TZP/Cr composite bilayers produced by sinter–joining. Materials Science and Engineering: A. 2010;527:449-53.

[639] Zvetkov VL. Comparative DSC kinetics of the reaction of DGEBA with aromatic diamines.: I. Non-isothermal kinetic study of the reaction of DGEBA with m-phenylene diamine. Polymer. 2001;42:6687-97.

[640] Sbirrazzuoli N. Is the Friedman Method Applicable to Transformations with Temperature Dependent Reaction Heat? Macromolecular Chemistry and Physics. 2007;208:1592-7.

[641] Šesták J, Berggren G. Study of the kinetics of the mechanism of solid-state reactions at increasing temperatures. Thermochimica Acta. 1971;3:1-12.

Appendix

Paper 1

Dasong Dai and Mizi Fan. Characteristic and Performance of Elementary Hemp Fibre. Materials Sciences and Applications.2010, 1(6):336-342.

Scientific
Research

Characteristic and performance of elementary hemp fibre

Dasong Dai and Mizi Fan

Civil Engineering Department, School of Engineering and Design, Brunel University, London, UK.
E-mail: mizi.fan@brunel.ac.uk

ABSTRACT

This paper presents systematic and improved methodologies to characterize the surface and fracture of elementary hemp fibres by field emission scanning microscope (FE-SEM), determine the microfibril angles (MFA) by an advanced microscopy technology and examine the crystallinity by X-ray diffraction (XRD) and Fourier transform infrared (FTIR). The results showed that 1) there existed various deformations/defects in elementary hemp fibres, showing four types of deformations, namely kink bands, dislocations, nodes and slip planes. The crack on the surface of elementary fibres was the initial breaking point under stress; 2) under tension the primary wall and secondary wall of hemp fibres showed different deformation and breaking behaviour. The crack initiated in a weak point of primary wall and subsequently propagated along radial direction from S1 to S2 layers; 3) the average MFA for the broken regions of S2 layer was 6.16° compared to 2.65° for the normal hemp fibres and the breaking of hemp fibres occurred at the points where had the biggest MFA; 4) the average MFA was 2.65° for S2 layer and 80.35° for S1 layer; 5) the crystallinity index (CI) determined by XRD and FTIR was very similar, showing the lattice parameters of the hemp fibres tested a=6.97Å, b=6.26 Å, c=11.88 Å and γ=97.21°, and the ratio of 1423 to 896cm-1 was found more suitable for CI evaluation for hemp fibres.
Keywords: Natural fibres, Fracture, Crack, X-ray diffraction (XRD), Fourier transform infrared spectroscopy (FTIR)

1. Introduction

Hemp fibre has widely been used in many civilizations. It has been reported that the earliest use of hemp was over 6000 years ago [1-3]. The increasing environmental awareness, growing global waste problems and continuously rising high crude oil prices have motivated governments all over the world to increase the legislative pressure. This in turn promotes researchers, industries and farmers to develop the concepts of environmental sustainability and reconsider renewable resources. Renewable resources from agricultural or forestry products form a basis for new industrial products or alternative energy sources, such as hemp fibre [4]. Hemp fibres have long been valued for their high strength and long fibre length, and used extensively in the fabrication of ropes and sails, as well as for paper and textiles. Hemp fibres consist of different hierarchical microstructures, whereby microfibrils serve as basic units. The microfibrils are embedded in a matrix of hemicelluloses and form the different cell wall layers of an elementary fibre, which generally has a large average diameter ranging from 10 to 50 μm [5]. The elementary fibres are bonded together with pectin's

and small amounts of lignin framing the next level of microstructure, i.e. technical fibres, with a diameters ranging from 50 to 100 μm [6]. These filaments are fixed together with a pectin-lignin matrix to form fibre bundles in the cortex of plant stems. Thus, bast fibres are bundles of individual strands of fibres held together by a pectin-lignin interface [7].

The fibres of never dried hemp contain numerous deformations. All these deformations appear where there is a change in microfibril direction and a distorsion of the fibrils. The deformations can be seen under polarized light [8-14], but the largest of them also could be discerned without polarisers [15] (e.g. SEM [16-18], Raman spectroscopy [19-22]). The deformation of fibres can affect the strain distribution in elementary fibre, leading to localized strain concentrations [23], and hence reduce both compressive strength and tensile strength [24], which was also proved by a finite element (FE) modeling of the tensile behaviour of single flax and hemp fibre [25]. The fibres in the matrix may break at the point with deformations [26], and the concentration of stresses around the deformation could act as the site of initiation of fibre-matrix debonding as

well as for the formation of micro-cracks in the matrix which contribute to global fracture of composite [27]. Limited work conducted on the breaking behaviour of wood pulp [28], cotton [29], and flax [30] also indicated that the break behaviour of the primary and secondary cell wall of the flax fibres was different from that of wood and cotton [17]. The primary cell wall generally breaks in a brittle manner, whereas the secondary cell wall, bridged by fibrils, splits relatively easily along the length direction.

The experience has highlighted that it is not possible to use or appropriate to compare data available from different investigations reported in the literatures. Measuring natural fibres proves to be a great challenge. Microstructural defects, fibre abstraction (e.g. single fibre) and processing are all yet to be studied. This paper is an attempt to characterize the surface and reveal the failure mechanism of elementary hemp fibres. Systematic and improved methodologies and advanced technologies have been developed to investigate the microfibril angles of elementary hemp fibres and the crystallinity of hemp fibres. The surface of hemp fibres after tensile loading and fracture of fibres after breaking were also observed carefully to characterize the surface and reveal the failure mechanism of elementary hemp fibres. This paper is the first of a series of papers from an intensive research programme aiming at a better understanding of natural fibre resources and the development of their high strength composites for applications in various industrial sectors.

2 Materials and Methods

2.1 Materials
Hemp fibres were supplied by a Hemp Farm & Fibre Company Ltd, UK. The fibres arrived in a form of fibre bundles. Salt products, namely, copper (II) nitrate (30 wt %) and cobalt (II) chloride (≥98.0%) were obtained from Sigma-Aldrich Company Ltd, UK.

2.2. Microfibril angle (MFA) measurement

Hemp fibres (0.1g) were placed into a beaker contained 100 ml salt solution (5%, wt/vol), whether copper nitrate or cobalt chloride, and heated at 80°C for 2 hours. The beaker container was placed into ultrasonic bath and treated at 80°C for 2 hours. The treated hemp fibres were finally washed with distill water. Photomicrographs were taken using BX51 Reflected Light Microscope equipped with a CAM-XC50 – 5MP cooled CCD camera, then using UTHSCSA ImageTool to measure the microfibril angle of S1 and S2 layers. 50 test pieces were used.

2.3. Deformation of hemp fibres

Optical microscopy was employed to examine the deformation of hemp fibres. The BX51 Reflected Light Microscope equips with 5×, 20×, 50×, 100× objectives, a CAM-XC50 – 5MP cooled CCD camera and 100W Halogen for transmitted or reflected light. The fibres were positioned on a slide using cyanacrylate glue and covered with a cover slip. Images were analysed and captured as 2576×1932 RGB jpeg files. The experiments were performed at room temperature and 1000 test pieces were examined.

2.4. Fracture characterization

Surface and fracture characterization of hemp fibres were conducted within a Zeiss Supra 35 VP field emission scanning electron microscope (FE-SEM). Individual fibres were randomly and gently isolated from fibre bundles. The isolated fibres were conditioned at 20±2°C and 65±2% relative humidity before temporarily fixed on the mounting card (Figure 1) with adhesive tape. A droplet of glue was applied on the centre of both sides of the hole along the length of card. The testing was then carried out as fellows:

1) Subject the prepared samples to SEM and characterize the surface of the test pieces;
2) Subject the samples to tensile strength test by using Instron 5566 at a crosshead speed of 0.1 mm/min and with 10 mm gauge length. The test results of mechanical performance of the elementary fibres are presented in a separate paper (Dai, et al. 2010).
3) Re-sample the test pieces for fracture characterization from the broken test pieces after tensile tests and subject them to oven-drying at 105°C. The test pieces were then coated with a thin layer of platinum in an Edwards S150B sputter coater (BOC Edwards, Wilmington, MA) to provide electrical conductivity. The fracture surface of the coated test pieces were observed by using the secondary electron mode images (digitally). 50 test pieces were used.
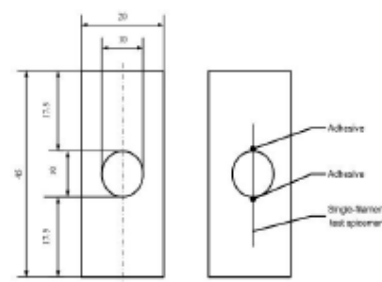

Fig.1 Set-up of single fibre testing: a=specimen mount, b=test specimen mounted on the mount

2.5. Crystallinity of hemp fibres

The crystallinity of hemp fibres was determined by using a powder X-ray diffraction method (PXRD). A D8 advanced Bruker AXS diffractometer, Cu point focus source, graphite monochromator and 2D-area detector GADDS system were used. The diffracted intensity of CuKα radiation (wavelength of 0.1542 nm) was recorded between 5° and 60° (2θ angle range) at 40 kV and 40 mA. Samples were analyzed in transmission mode. The unit cell of hemp fibre was calculated by DIFFRAC ^{plus} software, and the crystallinity index(CI) was evaluated by using Segal empirical method [30] as follows:

$$CI\% = \frac{(I_{002} - I_{am})}{I_{002}} \times 100 \quad (1)$$

where I_{002} is the maximum intensity of diffraction of the (002) lattice peak at a 2θ angle of between 22° and 23°, which represents both crystalline and amorphous materials. And I_{am} is the intensity of diffraction of the amorphous material, which is taken at a 2θ angle between 18° and 19° where the intensity is at a minimum [31]. It should be noted that the crystallinity index is useful only on a comparison basis as it is used to indicate the order of crystallinity rather than the crystallinity of crystalline regions. 100 replicates were used.

2.6. Composition of hemp fibres

Composition of hemp fibres was examined by using Fourier transform infrared spectroscopy (FTIR) measurement which uses a Perking-Elmer spectrometer and the standard KBr pellet technique. A total of 16 scans was taken for the sample between 650 cm^{-1} and 4000 cm^{-1}, with a resolution of 2 cm^{-1}. Hemp fibres were ground and mixed with KBr and then pressed into a pellet for FTIR measurement.

3. Results and discussion

3.1. Microfibril angle (MFA) of hemp fibres

The orientations of hemp fibres treated with both copper (II) nitrate and cobalt (II) chloride solutions can be detected under light microscope. However, it was found that the orientations of MFA in the samples treated with the former solution were much more distinctive than those with the latter solution treatment. This may result in more accurate measurements of MFA. An example of microfibril orientations in S1 and S2 layers observed under light microscope at 1000× is given in Figures 2a and 2b. It was found that, microfibrils in S2 layer have a Z-helical orientation, while in S1 layer have S-helical orientation. The average MFA in S2 inner layer is 2.65° (arrange from 1° to 3.27°), which is smaller than 4° measured previously by Fink [32]. This may be due partly to the different hemp fibres from different geographical sources. The average MFA in the outer part of S2 layer ranges from 23 to 30°. The average MFA in S1
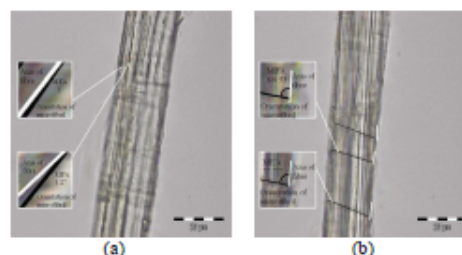
Fig.2 Microfibril angle of hemp fibre: MFA in S2 layer (a); MFA in S1 layer (b)

layer is 80.35° (arrange from 77.7° to 86.2°), which is in agreement with the results of previous worker [33] who found the average angle in S1 layer was 70-90°.

3.2. Crystal structure of hemp fibres

X-ray crystallography was used to investigate the crystallinity of hemp fibres. An example of X-ray powder diffraction photograph from hemp fibres is given in Figure 3. It can be seen from Figure 3 that the major crystalline peak of the hemp fibres occurred at 2θ = 22.1°, which represents the cellulose crystallographic plane (002, Bragg reflection). The minimum intensity between 002 and 110 peaks (I_{am}) is at 2θ = 18.6°. The crystallinity index of hemp fibre is 56%. Other well-defined peaks present on the X-ray diffractogram are at 2θ = 14.3°, 2θ = 16.8° and 2θ = 32.3°, and these reflections correspond with the ($\bar{1}$10), (110) and (004) crystallographic planes, respectively. The lattice parameters of hemp fibres which were calculated by DIFFRAC ^{plus} are: a: 6.97Å; b: 6.26 Å; c: 11.88 Å; γ: 97.21°.

Fig.3 X-ray diffractogram of hemp fibres

Fig.4 FTIR spectra of hemp fibres

Table 1 Main infrared transition for hemp fibre

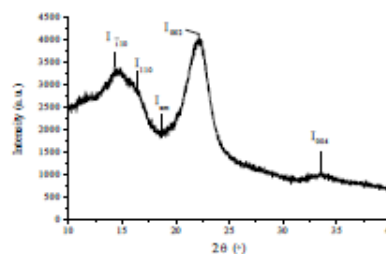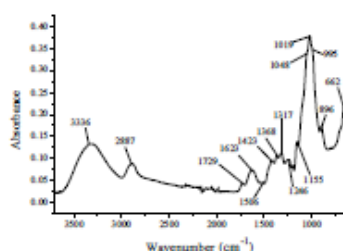| Wavenumber (cm-1)	Vibration	Sources
3336	OH stretching	Cellulose, Hemicellulose
2887	C–H symmetrical stretching	Cellulose, Hemicellulose
1729	C=O stretching vibration	Pectin, Waxes
1623	OH bending of absorbed water	Water
1506	C=C aromatic symmetrical stretching	Lignin
1423	HCH and OCH in-plane bending vibration	Cellulose
1368, 1362	In-the-plane CH bending	Cellulose, Hemicellulose
1317	CH2 rocking vibration	Cellulose
1246	C=O and G ring stretching	Lignin
1202	C-O-C symmetric stretching	Cellulose, Hemicellulose
1155	C-O-C asymmetrical stretching	Cellulose, Hemicellulose
1048, 1019, 995	C-C, C-OH, C-H ring and side group vibrations	Cellulose, Hemicellulose
896	COC,CCO and CCH deformation and stretching	Cellulose
662	C-OH out-of-plane bending	Cellulose

3.3. FTIR analysis

Infrared spectrum of hemp fibres is displayed in Figure 4. The typical functional groups and the IR signal with the possible sources are listed in Table 1 for a reference. It could be observed from table 1 that five components exist in the hemp fibres after retting pretreatment. Figure 4 shows a weak absorbance around 1729 cm^{-1} in the FTIR spectrum of hemp fibre, which might be attributed to the presence of the carboxylic ester (C=O) in pectin and waxes. Intensities of some bands in IR spectra have been found to be sensitive to variations of cellulose crystallinity and have been used to evaluate crystallinity index (CI) of cellulose. The ratios of peaks at 1423cm^{-1} and 896 cm^{-1}, 1368 cm^{-1} and 2887 cm^{-1} and 1368 cm^{-1} and 662 cm^{-1} are normally used to measure CI [e.g. 34-37]. In this study, the ratio of 1368 cm^{-1} and 2887
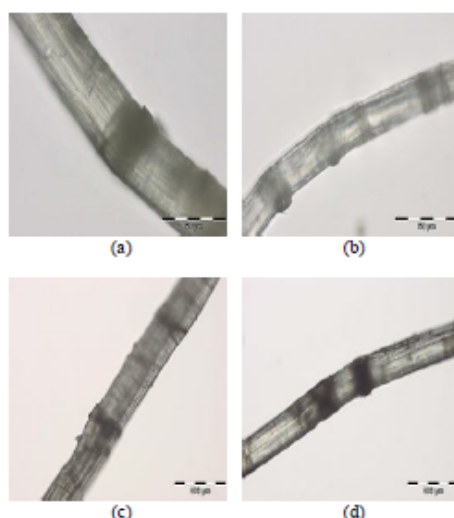
Fig.5 Deformation of hemp fibre: a=kink band (x 500 magnification), b=node (x 500 magnification), c=dislocation (x 200 magnification), d=slip plane (x200 magnification)

cm^{-1} is above 1 which seems to be unsuitable for evaluation, while the ratios of 1423 to 896 cm^{-1} and 1368 to 662 cm^{-1} are 55.7% and 49.3% respectively. The value calculated by using Segal empirical method is 56%, indicating that the ratio of 1423 to 896 cm^{-1} is more suitable for CI evaluation.

3.4. Deformation of hemp fibres

Optical microscope observation showed that much deformation has occurred in hemp fibres and some types of deformation are difficult to distinguish. In this study, any defect of fibres which may affect the mechanical properties of the fibres, especially the tensile strength, was recorded and called deformation. The results of numerous examinations (1000 test pieces) of hemp fibres can be cataloged into four types of deformation of hemp fibres (Figure 5). The characteristic of each type deformation are as follows: a) kind bands, formed in the fibres as a result of axial curing stresses; b) nodes, formed in the regions of localized delamination and compressive strain; c) dislocations, appeared in untreated natural fibre; and d) slip planes, crinkled in the cell wall resulting from a slight linear displacement of the wall lamellae. It is apparent that these deformations appear when there is a change in microfibril direction and a distorsion of fibrils.

Nevertheless, whilst it is clear that some of deformations occur during plant growth, a significant amount of deformation is resulted from decortication and other down-line processing. Deformations could be the weak points which broken at beating, mechanical treatment and in acidic environments. It is believed that stress concentrations around deformations can act as sites for the initiation of fibre matrix debonding as well as for the formation of micro cracks in the matrix.

3.5. Breaking process

Figures 6a, 6b and 6c illustrate the initial and final fracture of an elementary hemp fibre. It was found that the initial crack of hemp fibres starts from primary wall (Figure 6a). This may be due partly to the fact that the primary cell wall could contain a large fraction of amorphous pectin, hemicelluloses, cross-linked lignin and randomly oriented cellulose as reported previously [38-40]. The crack then proceeds into the secondary cell wall (S2) which forms the major part of hemp fibre. While the S2 layer has been reported containing several layers [41], this study showed that it at least contains the outer and inner parts of S2 layers and the MFA of which gradually decreases. The S2 layer consists of highly crystalline (CI 60%) cellulose microfibrils (Figure 4) bounded together by lignin and hemicellulose. The microfibrils are oriented spirally around the fibre axis. In this study, the microfibrils in the inner part of S2 layer have an MFA of about 2.65° with respect to the fibre axis, which explains the stiffness and strength of the fibre in the axial direction. The MFA in the outer part of S2 layer ranges from 23 to 30°. The microfibril angle can strongly influence mechanical properties of fibres, such as tensile strength and modulus [42], which decrease with MFA increases. This means that the strength of inner part of S2 layer shall be higher than that of the
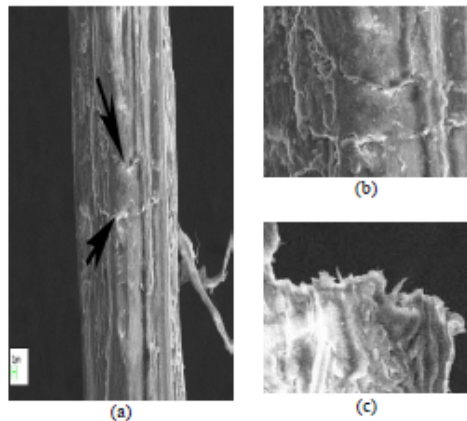
outer part of S2 layers. Therefore, the breaking process in secondary wall of hemp fibres is from S1 layer to outer part of S2 layer to inner part of S2 layer (Figures 6b and 6c).
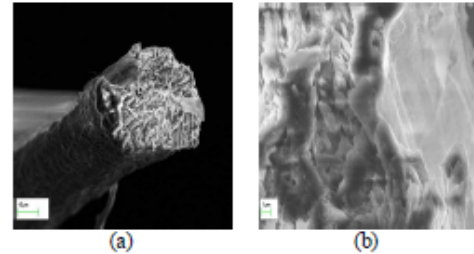

Fig.7 Fractography of hemp fibre: a=overall view, b=detail of single fiber fracture

3.6. Fracture of hemp fibres

Figure 7 shows the fractography of hemp fibres. The macrofibril can be observed clearly in the fracture surface of hemp fibres. The MFA in the S2 layer at fracture point was measured and their mean value is 6.16° with respect to the fibre axis. As discussed in the previous sections, the average MFA in the S2 layer of non-defect hemp fibre is 2.65°, indicating that the microfibril direction changes in the fracture regions of fibre. According to Mohlin et al. [43], the deformations, which change the direction of the fibre axis, have a negative influence on mechanical properties of fibre. Baley [44] reported that cracks in the flax fibre firstly happened in the area of kind band. However, the different strength between the different types of deformation as defined in this study have not been observed, although it was evident that the deformation is the main cause for the break of hemp fibres, that is, deformation is the weak link in hemp fibres.

4. Conclusions

A systematic and comprehensive study on the characteristic and behaviour of elementary hemp fibres presented in the paper concluded that:

1) An improved, accurate method of measure microfibril angle (MFA) of elementary hemp fibres could be developed (in this study): The average MFA was 2.65° for S2 layer and 80.35° for S1 layer. It was observed that the type of solutions had an influence on the effectiveness of pre-treatment which may had an implication of accuracy of measurement. The solution of $Cu(NO_3)_2$ was found more effective than $CoCl_2$.

2) The lattice parameters of hemp fibre studied were a=6.97Å, b=6.26 Å, c=11.88 Å and γ=97.21°. The crystallinity index (CI) determined by XRD and FTIR was very similar, and the ratio of 1423 to 896cm^{-1} was found more suitable for CI evaluation for hemp fibres.

Fig.6 Breaking process under tension: initial crack (a, b), fracture (c) of hemp fibre

3) The characterization on the surface of hemp fibres after tensile testing and the fracture of the broken fibres showed that there existed various deformations in elementary hemp fibres. However, the deformation of hemp fibres could be cataloged into four types, namely kink bands, dislocations, nodes and slip planes.

4) Under tensile stress, the initial crack was mainly from the primary wall and the crack proceeded into the secondary wall of hemp fibre, giving a breaking order of S1 layer to out part of S2 layer to inner layer of S2 layer. The average MFA (6.16°) at the fracture points of the S2 layer was much higher than that of normal fibres (2.65°).

5. Acknowledgements

6. References

[1] J. W. Roulac, "Hemp Horizons: The Comeback of the World's Most Promising Plant," Chelsea Green Publishing Co., White River Junction, 1997.

[2] G. Beckermann, "Performance of Hemp-Fibre Reinforced Polypropylene Composite Materials," Waikato University, Australia, 2007.

[3] P. G. Stafford and J. Bigwood, "Psychedelics Encyclopedia. Berkeley, California," Ronin Publishing, Inc, 1992.

[4] B. B. Jungbauernschaft, "Biomasse–Nachwachsende Rohstoffe," in Fakten & Trends 2002 Zur Situation der Landwitschaft, Eggenfelden, 2002, pp. 191–207.

[5] M. D. Candilo, P. Ranalli, C. Bozzi and B.Focher, "Preliminary results of tests facing with the controlled retting of hemp," Industrial Crops and Products. Vol.11, No. 2, 2001, pp. 197-203.

[6] B. M. Prasad and M. M. Sain, "Mechanical properties of thermally treated hemp fibres in inert atmosphere for potential composite reinforcement," Materials Research Innovation. Vol. 7, No. 4, 2003, pp. 231–238.

[7] H. J. Purz, H. P. Fink and H. Graf, "The structure of natural cellulosic fibres. Part I: The structure of bast fibres and their changes by scouring and mercerization as revealed by optical and electron microscopy," Das Papier. Vol. 6, No. 52, 1998, pp. 315-324.

[8] R. P. Kibblewhite, "Fractures and dislocations in the walls of kraft and bisulphite pulp fibres," Cellulose Chemistry Technology. Vol. 10, No. 4, 1976, pp. 297–503.

[9] P. Hoffmeyer, "Non-linear creep caused by slip plane formation," Wood Science Technology. Vol. 27, No. 5, 1993, pp. 321–335.

[10] U. B. Mohlin and J. Dahlbom, J. Hornatowska, "Fibre deformation and sheet strength," Journal of Tappi. Vol. 79, No. 6, 1996, pp. 105–111.

[11] M. J. Ellis, G. G. Duffy, R. W. Allison and R. P. Kibble-

white, "Fibre deformation during medium consistency mixing: role of residence time and impeller geometry," Appita journal. Vol. 51, No. 1, 1998, pp. 643–649.

[12] R.W. Allison, M. J. Ellis and R.P. Kibblewhite, "Effect of mechanical processes on the strength of oxygen delignified kraft pulp," In: Proceedings of the 1998 International Pulp Bleaching Conference, Book 1, Helsinki, Finland, 1998, pp. 159–166.

[13] C. H. Ljungqvist, R. Lyng and F. Thuvander, "Influence of observable damage on spruce latewood pulp fibre properties," In: H. Lilholt, B. Madsen, H. L. Toftegaard, E. Cendre, M. Megnis, L. P. Mikkelsen, B. S.Sørensen (Eds.), Sustainable Natural and Polymeric Composites-Science and Technolgy, Proceedings from the 23rd Risø International Symposium on Materials Science,2002, pp. 231–238.

[14] C. Baley, "Influence of kink bands on the tensile strength of flax fibres," Journal of Materials Science. Vol.39, No. 1, 2004, pp. 331– 334.

[15] J.Andersons, E.Sparnins and E.PoriKe, "Strength distribution of elementary flax fibres for composite reinforcement," 11 th Int. Inorgantic-Bonded Fibre Composites Conference. Madrid Spain, 2008.

[16] H. L. Bos, Van den Oever MJA and O. C.J. J. Peters, "The influence of fibre structure and deformation on the fracture behaviour of flax fibre reinforced composites," In Proceedings of the 4th International Conference on Deformation and Fracture of Composites, Manchester, UK, 1997, pp. 499–504.

[17] H. L. BOS and A.M.Donald, "In situ ESEM study of the deformation of elementary flax fibres," Journal of materials sciences. Vol. 34, No.13, 1999, pp. 3029-3034.

[18] L. G. Thygesen, J. B. Bilde-Sørensen and P. Hoffmeyer, "Visualisation of dislocations in hemp fibres A comparison between scanning electron microscopy (SEM) and polarized light microscopy (PLM)," Industrial Crops and Products. Vol. 24, No. 2 ,2006, pp. 181–185.

[19] W. Y. Hamad and S. J. Eichhorn, "Deformation micromechanics of cellulose fibres," Journal of Engineering Materials and Technology. Vol. 119, No.3, 1997, pp. 309–313.

[20] S.J Eichhorn, RJ Young and WY. Yeh, "Deformation processes in regenerated cellulose fibres," Textile Research Journal. Vol. 71, No. 2, 2001, pp. 121–129.

[21] S.J Eichhorn, "Strain induced Raman shifts in the spectra of natural cellulose fibres," Journal of materials science letters. Vol. 19, No. 3, 2000. pp. 721– 723.

[22] S. K. Kovur, K. Schenzel and W. Diepenbrock, "Orientation Dependent FT Raman Microspectroscopy on Hemp Fibres," Macromolecular Symposia. Vol. 265, No.1, 2008, pp. 205–210.

[23] L. Mott, S. M. Shaler and L. H. Groom, "A technique to measure strain distributions in single wood pulp fibres," Wood and Fibre Science. Vol. 28, No. 4, 1996, pp. 439-437.

[24] J. H. Greenwood and P. G. Rose, "Compressive behaviour of Kevlar 49 fibres and composites," Journal of materials science. Vol. 9, No. 11, 1974, pp. 1809-1814.

[25] T. Nilsson and P. J. Gustafsson, "Influence of dislocations and plasticity on the tensile behaviour of flax and hemp fibres," Composites Part A: Applied Science and Manufacturing. Vol.38, No. 7, 2007, pp. 1722-1728.

[26] B. Focher, "Physical properties of flax fibre," In H. S. Sharma, C.F. Sumere. van (Eds.): The Biology and Processing of Flax. M Publications, Belfast, 1992, pp. 333.

[27] M. Hughes, G. Sebe and J. Hague, "Investigation into the effects of micro-compressive defects on interphase behaviour in hemp-epoxy composites using half-fringe photoelasticity," Composite Interfaces. Vol.7, No.1, 2000, pp. 13-29.

[28] W.Y.Hamad, "Some microrheological aspects of wood-pulp fibres subjected to fatigue loading," Cellulose. Vol. 4, No. 1, pp. 51–56.

[29] H. E. Gram, "Durability of Natural Fibres in Concrete," Swedish Cement and Concrete Research Institute, 1983, pp. 225.

[30] L. Segal, J. J. Creely, A.E. Martin and C. M. Conrad., "An empirical method for estimating the degree of crystallinity of native cellulose using the X-ray diffractometer," Textile Research Journal. Vol. 29, No. 10, 1959, pp. 786-794.

[31] M. B. Roncero, A. L. Torres, J. F. Colom and T.Vidal, "The effect of xylanase on lignocellulosic components during the bleaching of wood pulps," Bioresource Technology. Vol. 96, No. 1, 2005, pp. 21-30.

[32] H. P. Fink, E. Walenta and J. Kunze, "The structure of natural cellulosic fibres-Part 2. The supermolecular structure of bast fibres and their changes by mercerization as revealed by X-ray diffraction and ^{13}C-NMR-spectroscopy," Papier. Vol. 53, No.9, 1999, pp. 534-542.

[33] A. Thygesen, G. Daniel and H. Lilholt, "Hemp fibre microstructure and use of fungal defibration to obtain fibres for composite materials," Journal of Natural fibres. Vol.2, No. 4, 2006, pp.19-37.

[34] Y. Kataoka and T. Kondo, "FT-IR Microscopic Analysis of Changing Cellulose Crystalline Structure during Wood Cell Wall Formation," Macromolecules. Vol. 31, No. 3, 1998, pp. 760-764.

[35] R. T. O'Connor, E. F. DuPre and D. Mitchman, "Applications of infrared absorption spectroscopy to investigations of cotton and modified cottons," Textile Research Journal. Vol. 28, No.5, 1958, pp.82–392.

[36] L. Ferru and P. Page, "Water retention value and degree of crystallinity by infrared absorption spectroscopy in caustic soda treated cotton," Cellulose Chemistry and Technology. Vol. 11, No. 3, 1977, pp. 633–637.

[37] M.L. Troedec , D. Sedan , C. Peyratout, J. P. Bonneta, A. Smitha, R. Guinebretiereb, V. Gloaguenc and P. Krauszc, "Influence of various chemical treatments on the composition and structure of hemp fibres," Composites Part A: Applied Science and Manufacturing, Vol. 39, No.3, 2008, pp. 514–522.

[38] H.L. Bos, M. J.A. Van den Oever and O.C.J.J. Peters, "Tensile and compressive properties of flax fibres for natural fibre reinforced composites," Journal of materials science. Vol. 37, No.8, 2002, pp1683-1692.

[39] K. Persson, "Modelling of wood properties by a micromechanical approach," Lund University, Scania, 1997.

[40] A.K. Bledzki and J. Gassan, "Composites reinforced with cellulose based fibres," Progress in polymer science. Vol.24, No. 2, 1999, pp 221-274.

[41] A.Thygesen, "Properties of hemp fibre polymer composites—An optimization of fibre properties using novel defibration methods and fibre characterization," Royal Agricultural and Veterinary University of Denmark, 2006, pp. 19.

[42] E. C. McLaughlin and R. A. Tait, "Fracture mechanism of plant fibres," Journal of materials science Vol. 15, No.1, 1980, pp. 89-95.

[43] U.B. Mohlin and C. Alfredsson, "Fibre deformation and its implications in pulp characterization," Nordic Pulp and Paper Research Journal. Vol.5, No.4, 1990, pp. 172-179.

[44] C.Baley, "Influence of kink bands on the tensile strength of flax fibres," Journal of materials science. Vol.39, No.1, 2004, pp. 331-334.

Paper 2

Dasong Dai and Mizi Fan. Investigation of the dislocation of natural

fibres by Fourier-transform infrared. Vibrational Spectroscopy. 2011;

55(2):300-306.

Investigation of the dislocation of natural fibres by Fourier transform infrared spectroscopy

Dasong Dai and Mizi Fan*

Civil Engineering Department, School of Engineering and Design, Brunel University, Kingston Lane, Uxbridge, Middlesex, UB8 3PH, UK

* Corresponding author:

 e-mail address: mizi.fan@brunel.ac.uk；Tel.: +44 0189526466; Fax: +44 01895258728

Abstract:

Dislocations were thought the weakest link in natural fibres which had negative effects on the tensile strength of the fibres. This paper presents a systematic approach to examine the dislocations in hemp fibres firstly by optical microscopy (OM) and field emission scanning electron microscopy (FE-SEM) for the morphologies of the dislocations and then by X-ray diffraction (XRD) and Fourier transform infrared spectroscopy (FTIR) for the crystallinity index and hydrogen bonds and main chemical compositions of the dislocation regions in hemp fibres. The results showed that i) dislocations resulted in fibril distortion and intensified amorphous features of hemp fibres; ii) crystallinity index reduced from 48.4 % examined by FTIR and 56.0 % by XRD determination for hemps without dislocations to 41.3 % for the dislocation regions; iii) the FTIR spectra showed much higher absorbance of hemp fibres without dislocations which was two times that of dislocation regions across the whole range of wavenumbers; iv) deconvolving spectra in O-H stretching region showed a lower number of hydrogen bonds, weaker inter- and intra- molecular hydrogen bonding in the dislocation regions, indicating a possible decrease in the tensile strength of hemp fibres; v) the FTIR spectra indicated the removal of the hemicelluloses in dislocation regions and hence possible loss of lignin because of disappearing the bands at 1368 cm^{-1} , 1363 cm^{-1} and 1506 cm^{-1}; vi) the spectra in fingerprint region gave rise to the ratio of syringyl (S) / guaiacyl (G) of 0.9 in dislocation regions which was lower than that (1.1) of hemp without dislocation, this means a significant reduction of lignin content and a higher cellulose content in the dislocation regions.

Keywords: Natural fibre; FTIR spectra; Hydrogen bonds

1 Introduction

According to the "weakest-link" theory [1], materials are made up of smaller elements linked together. The failure of the material as a whole occurs when any one of these elements or `links' fails. The weakest point in natural fibre could be where there is a dislocation (flaw) or where fibre diameter (diameter variations) is small or a combination of both [2]. Dislocations in natural fibres are also called nodes, slip planes, micro-compressions, misaligned zones, etc. [3]. Correlation between fibre performance and the occurrence of dislocations can be established by using kink index [4] and the other indices [5, 6]. A novel HCl method has also developed for the quantification of dislocations of pulp fibres and other weak points in different types of fibres [7-11]. Dislocations have negative effect on the mechanical properties of paper made from fibres [12-14]. Dislocations not only result in a decrease in the tensile strength and behavior of single fibre [15], but also affect the strength of composites. Investigations done by Focher et al. [16] and Hughes et al. [17] showed that stress concentrations around dislocations of flax, hemp can act as sites for the initiation of fibre-matrix debonding as well as the formation of micro-cracks in the matrix.

Several approaches have been tried to visualize the dislocation of natural fibres. The first of these is the quantification of dislocations in natural fibres by using a polarized light microscopy (PLM) or natural light optical microscopy (OM). This has been used to characterize the surface of dislocations in fibres and quantify the "dislocation number" [18-24]. The second of these methodologies is the image analysis [25] with PLM. This is to measure the proportional area of the bright regions of the fibres from the images by using a PLM. Compared to the first approach discussed above, this approach has the advantage of implicitly quantifying the width and length of the dislocations from the two-dimensional image. This method has been enhanced further by Thygesen and Hoffmeyer [26], who studied the effects of light intensity and the fibre angle (relative to the polarizer) and develop a procedure for semi-automatic determination of the proportion of dislocations for single hemp fibres. The third of these methods is the confocal scanning laser microscopy (CSLM) proposed by Bos et al.[27], who applied this method to observe the deformed areas of flax fibres. They later also used the emission scanning electron

microscopy (ESEM) to investigate the dislocation behavior of single elementary flax fibres and found that the primary and the secondary cell wall of flax fibre showed different dislocation behavior. The primary cell wall broke in a brittle manner, whereas in the secondary cell, due to its fibrillar nature, a coarse crack grew, bridged by fibrils. The secondary cell wall was also been found to split relatively easily along the length direction [28]. However, dislocations were found more numerous and more visible in the images from PLM than from SEM [29].

Fourier transform infrared spectroscopy (FTIR) has been considered one of the best tools to study the change of native cellulose supermolecular structure. This paper employs this technology (FTIR) to study the dislocations in natural (hemp) fibres aiming at a better understanding of the fracture behavior, structure and bonding systems within dislocation regions of the natural fibres.

2 Materials and Methods

2.1 Materials

Hemp fibres were supplied by a Hemp Farm & Fibre Company Ltd, UK. The fibres were treated by retting previously. The hemp fibres arrived in a form of fibre bundles. Individual fibres were randomly and gently isolated from fibre bundles to eliminate any further damage during the processing. The isolated fibres were conditioned at 20±2°C and 65±2% relative humidity before uses.

2.2 Sampling and testing

Test procedures are outlined in Figure 1 and the details of main tests are given as follows:

2.2.1 Optical microscopy examination (OM)

The isolated single fibres were firstly subjected to the OM observation process to determine the diameter (breadth) and the dislocations of the fibres. The fibres with diameter/breadth less than 50 μm and with dislocations across the length of the fibres were selected and divided into two groups. One group was subjected to tensile loading and the other group for field emission scanning electron microscopy (FE-SEM) examination to investigate the morphologies of dislocations

(Figure 1).

2.2.2 FE-SEM characterization

Dislocation of hemp fibres were firstly examined with a Zeiss Supra 35 VP field emission scanning electron microscopy (FE-SEM). The test pieces were coated with thin layer platinum on the surface in an Edwards S150B sputter coater to provide electrical conductivity. Following coating, samples were observed and operated at 10 kV using the secondary electron mode with images collected digitally.

2.2.3 Tensile test

The conditioned individual fibre was temporarily fixed on the mounting card (Figure 2) with adhesive tape. A droplet of glue was applied on the centre of both sides of the hole along the length of card. Subject the test pieces to tensile strength test by using Instron 5566 at a crosshead speed of 0.1 mm/min and with 25 mm gauge length. It must be noted the optical microscopy was used to determine the fibre diameter and only the samples with diameter less than 50 μm were used. About 1000 samples were tested.

2.2.4 FTIR analysis

The test pieces with failure within dislocation cluster (region) were collected after tensile tests. About 0.5 mm length of fibre around fracture points in each test pieces was cut with scissors and such generated two groups of materials: one with fracture (M1) and the other without fracture; the latter group of materials (i.e. those without fracture) was further divided into two parts (M2 and M3). It must be noted that the size of a single dislocation ranges from a few micron to 100 μm, but for hemp fibres multi-dislocations normally exist as a cluster, and the cluster of multi-dislocations and less defect region spread one after another (Figure 3a). Under tension test, the failure always locates within this dislocation cluster if the test pieces contain both dislocation cluster and less defect region. M1 and M2 materials (without drying) were then further processed and examined by using FTIR measurement which uses a Perkin-Elmer spectrometer and the standard KBr pellet technique. A single-beam background spectrum of 16 scans between 650 cm^{-1} and 4000 cm^{-1}, with a resolution of 2 cm^{-1} was recorded with a blank KBr pellet sample, and this spectrum was stored

in the background file. Sample spectra were recorded in absorbance mode and were automatically ratioed to the single-beam background most recently entered in the background file. Hemp fibres were ground in mortar with pestle. Then 1 mg of fibres the size between 40 and 60 mesh were ground and mixed with 100 mg KBr and then pressed into a pellet for FTIR measurement. Three samples were used. The average spectra for both without and with dislocation of fibres were used for the evaluation.

The spectra were linear baseline-corrected using the Omnic V.8 software to correct spectral drifts. After correction, the data of spectra were exported as CSV files for the evaluation of crystallinity index. The recorded FTIR (3660-3000 cm^{-1}) and (1330-1215 cm^{-1}) were deconvolved using Peak Fit V.4.12 software. Deconvolution was performed using Gaussian peak shape and a full width at half maxima (fwhm; cm^{-1}) of 20-40 cm^{-1} and 10-20 cm^{-1} respectively. All data were analyzed and compared on the basis of peak areas. Selection of peaks and calculations of peak areas as a measure of spectral intensity were performed by maximum likelihood peak fitting and all data were fitted with r^2 values above 0.99.

2.2.5 XRD analysis

M3 materials were subjected to a powder X-ray diffraction method analysis (PXRD). For this analysis, a D8 advanced Bruker AXS diffractometer, Cu point focus source, graphite monochromator and 2D-area detector GADDS system were used. The diffracted intensity of CuKα radiation (wavelength of 0.1542 nm) was recorded between 5° and 40° (2θ angle range) at 40 kV and 40 mA. Samples were analyzed in transmission mode. The unit cell of hemp fibre was calculated by DIFFRAC ^{plus} software, and the crystallinity index (CI) was evaluated by using Segal et al. empirical method [30] as follows:

$$CI\% = \frac{(I_{002} - I_{am})}{I_{002}} \times 100 \quad (1)$$

where I_{002} is the maximum intensity of diffraction of the (002) lattice peak at a 2θ angle of between 22° and 23°, which represents both crystalline and amorphous materials. And I_{am} is the intensity of diffraction of the amorphous material, which is taken at a 2θ angle between 18° and 19° where the intensity is at a minimum [31]. It should be noted that the crystallinity index is

useful only on a comparison basis as it is used to indicate the order of crystallinity rather than the crystallinity of crystalline regions. 100 replicates were used.

3 Results and Discussion

3.1 Morphologies of dislocation

The morphologies of dislocations observed by OM and FE-SEM are given in Figure 3a and 3b. The fracture within dislocation regions and that without dislocations are also showed in Figure 3c and 3d respectively. It is evident that OM could not provide the detailed features of the dislocation except the black color around the surface of the fibres (Figure 3a). However, the method is able to identify the dislocation easily and quickly.

The results from FE-SEM shows that overall the surface of dislocations of hemp fibres looks more amorphous than that of hemp fibres without dislocations (Figure 3b). This may be due to the loss of hemicelluloses or lignin, which could combine fibrils together, after beating, mechanical treatment or other effects (e.g. acidic exposures). It is also evident that the fibrils distort in the dislocation regions, which could affect the stiffness and stress of fibres with the stiffness and stress decreasing with the increase of dislocation angle. Figures 3c and 3d compare different fractures within dislocation regions and that without dislocation, showing different fracture behavior with a form of fibrillar break in dislocation regions and a form of granular break in the other regions.

3.2 Crystallinity index of dislocation

The crystallinity index of dislocation regions of hemp fibres were determined by FTIR spectroscopy (CI (IR)). X-ray crystallography examination was also included for a comparison. The results of CI determined for hemp fibres both with and without dislocations are given in Table 1 and an example of X-ray powder diffraction photograph for hemp fibres without dislocation are given in Figure 4. It must be noted that for IR evaluation, the ratios of absorbance at 1423 cm^{-1} and 895 cm^{-1}, 1368 cm^{-1} and 2883 cm^{-1} or 1368 cm^{-1} and 662 cm^{-1} are normally used to measure CI [e.g. 32-35]. In this study, the ratio of absorption band A_{1368}/A_{2883} is above 1 which seems to be unsuitable for evaluation, while the ratios of absorption band A_{1423}/A_{895} and A_{1368}/A_{662} are 72.6 %

and 48.4 % respectively. The value calculated by using Segal empirical method is 56.0 %, indicating that the ratio of absorption band A_{1368}/A_{662} is more suitable for CI evaluation. Table 1 shows that the CI (IR) in dislocation regions is only 41.3 %, which is lower than that of without dislocation region of hemp fibres. According to two-phase model theory [36], there exist two regions in cellulose chain, namely amorphous and crystalline regions. The higher CI in the hemp fibres without dislocation indicates that there exist a higher content of crystalline regions in the hemp without dislocation than in dislocation regions.

3.3 Hydrogen bonds of cellulose in dislocations

Figure 5 shows the FTIR spectra of hemp fibres without dislocation and dislocation regions. The peak positions of the major IR bands are summarized and compared in Table 2. It can be seen that the absorbance of hemp fibres without dislocations in the X-H (O-H and C-H) stretching region is much higher than that with dislocations (Figure 5).

The IR absorption bands for OH stretching region (Region 1 in Figure 5) in without dislocation and dislocation regions were deconvolved into four bands for a curve fitting as shown in Figures 6a and 6b. The peak positions of the four bands for hemp fibres with and without dislocations are summarized in Table 3. The bands are 3450 cm^{-1} (1), 3346 cm^{-1} (2), 3262 cm^{-1} (3) and 3161 cm^{-1} (4) for the hemp without dislocations, and 3451 cm^{-1} (1), 3350 cm^{-1} (2), 3264 cm^{-1} (3) and 3167 cm^{-1} (4) for the dislocation regions. These bands are related to the valence vibration of hydrogen bonded OH groups [62]: i.e. band 1 to the intramolecular hydrogen bond of O(2)H---O(6), band 2 to the intramolecular hydrogen bond of O(3)H---O(5), band 3 to the intermolecular hydrogen bond of O(6)H---O(3`) and band 4 to the O-H stretching respectively. It can be seen that the wave-numbers of peak position of dislocations are higher than those of hemp fibre without dislocation. This indicates that the degree of hydrogen bonding in dislocation regions is lesser than that in without dislocation regions. Furthermore, it can be seen from figure 6a and 6b that the absorbance of these bands in the dislocation regions is much lower than that in the regions without dislocations. The absorbance of the dislocation regions is only about 79.3 % for band 1, 64.4 % for band 2, 64.9 % for band 3 and 75.7 % for band 4 respectively against that of hemp without dislocations. These mean that the number of hydrogen bonds in dislocations is lower than in parts

without dislocations according to Beer-Lambert law. For example, the much more decrease of absorbance in band 2 which is assigned to the intramolecular hydrogen bond of O(3)H---O(5) indicates that in dislocation regions the cellulose molecular chains are more flexible than that in the hemp without dislocation. The formation of inter- and intramolecular hydrogen bonds in cellulose not only has a strong influence on the physical properties of cellulose (including solubility [63, 64], hydroxyl reactivity [65, 66], and crystallinity [67, 68]), but also plays an important role in the mechanical properties of cellulose [69]. The strain energy, calculated by Tashiro and Kobayashi [70], was found mainly being distributed to the deformation of the glucose rings (about 30.0 %), the bending of the ether linkages connecting the adjacent rings (about 20.0 %) and the O(3)H---O(5) hydrogen bond (about 20.0 %). This comes to a conclusion that the weaker inter- and intramolecular hydrogen bonding in the dislocations may be the main cause that induces the decrease of tensile strength in the hemp fibres, especially the intramolecular hydrogen bond of O(3)H---O(5).

3.4 Hemicellulose and lignin in dislocations

A scrutiny of the IR spectra from 1370 cm^{-1} to 1330 cm^{-1} shows that the band at 1368 cm^{-1} and 1363 cm^{-1} almost disappear in dislocation regions (Figure 7a). The bands at 1368 cm^{-1} and 1363 cm^{-1} assigned as the in-plane CH bending may be from hemicellulose or cellulose. The near disappearance of bands of 1368 cm^{-1} and 1363 cm^{-1} may be probably due to the removal of the hemicelluloses in dislocation regions. Hemicelluloses can form a linkage between cellulose and lignin, permitting the effective transfer of shear stress between cellulose microfibrils and the lignin [71]. Hemicellulose also can form lignin-carbohydrate complex with lignin by ether bonds [72]. The removal of hemicelluloses in dislocation regions may cause the decrease of transfer of shear stress under tensile loading and loss of lignin as well.

Figure 7b shows the FTIR spectra of hemp fibres with and without dislocations from 1330 cm^{-1} to 1215 cm^{-1}. It must be noted that the S ring stretching, CH$_2$ rocking at C6 in cellulose, G ring stretching, C-C plus C-O plus C=O stretch and COH bending at C6 in cellulose could normally be seen in bands at 1325, 1314, 1259, 1245 and 1232 cm^{-1} respectively for the hemp fibres without dislocation. Due to overlapping of the bands, only two peaks can be seen in Figure 7b. The

deconvolved FTIR spectra in Figure 7b are shown in Figures 8a (without dislocation) and 8b (dislocation regions). Lignins are composed of three basic units, namely *p*-hydroxyphenyl (H), guaiacyl (G) and syringyl (S) [50]. Guaiacyl (G) and syringyl (S) are the main units of lignin, but the ratio of S/G varies from one to another plant. It was reported recently by del Río et al. [52] that S/G values calculated upon FTIR were in agreement with those calculated upon Py-GC/MS at the bands of 1271 cm^{-1} and 1327 cm^{-1} respectively. However, in this study, the bands at 1271 cm^{-1} and 1327 cm^{-1} assigned as G ring stretching and S ring stretching respectively were found shifted to lower wavenumbers. For the hemp fibres without dislocations (Figure 8a), the G ring and S ring stretching appear at the bands of 1259 cm^{-1} and 1325 cm^{-1}, for the dislocation regions, they appear in the wavenumbers of 1261 cm^{-1} and 1325 cm^{-1} (Figure 8b). The ratio of S/G in hemp plant was reported as about 0.8 (molar contents of G-lignin is 51.0 %, molar contents of S-lignin is 40.0 %) [52], but in this study, the ratio of S/G is 1.1 for the hemp fibre without dislocations and 0.9 for the dislocation regions. According to the investigation carried out by Love et al. [73], syringyl-rich areas of the lignin network were more rigid than guaiacyl-rich areas. It could therefore be concluded that the lignin network in the parts without dislocations would be more rigid than that in dislocation regions. The lower absorbance in dislocations means that the lignin was removed from dislocation regions. It can such be concluded from this study that the cellulose content in dislocations would be higher than that in hemp fibres without dislocations.

4 Conclusions

In this paper a systematic approach has been developed to examine the dislocations in hemp fibres firstly by optical microscopy (OM) and field emission scanning electron microscopy (FE-SEM) for the morphologies of the dislocations and then by X-ray diffraction (XRD) and Fourier transform infrared spectroscopy (FTIR) for the crystallinity and hydrogen bonds and chemical compositions of the dislocation regions of hemp fibres. The developed morphologies of the dislocations showed that the surface of hemp fibres within the dislocation regions was more amorphous than those without dislocations. The fibrils within the dislocations regions were distorted.

Both XRD and FTIR were able to examine the crystallinity index of the dislocations. The CI examined by FTIR was 48.4 % for the hemp without dislocations and 41.3 % for those within dislocation regions, showing a significant reduction in the crystallinity due to the dislocations. The CI obtained by XRD was 56.0 %.

The deconvolved four bands of the OH stretching region gave rise to a clear indication of changes in the valence vibration of hydrogen-bonded OH groups: i.e. the intramolecular hydrogen bond of O(2)H---O(6) (3451 cm^{-1}), the intramolecular hydrogen bond of O(3)H---O(5) (3350 cm^{-1}), the intermolecular hydrogen bond of O(6)H---O(3`) (3264 cm^{-1}) and the O-H stretching (3167 cm^{-1}), with the absorbance of these bands in the dislocation regions being much lower than that in the regions without dislocations. The weaker inter- and intra-molecular hydrogen bonding in the dislocations could be the main cause that induced the decrease of tensile strength in the hemp fibres, especially the intramolecular hydrogen bond of O(3)H---O(5).

The FTIR spectra from 1370 cm^{-1} to 1330 cm^{-1} illustrated that the band at 1368 cm^{-1} and 1363 cm^{-1} disappeared in dislocation regions, indicating the removal of the hemicelluloses in dislocations and hence possible loss of lignin. The deconvolved FTIR spectra from 1330 cm^{-1} to 1215 cm^{-1} showed the S ring stretching, CH$_2$ rocking at C6 in cellulose, G ring stretching, C-C plus C-O plus C=O stretch and COH bending at C6 in cellulose, indicating reduction of lignin content in the dislocation regions. The ratio of S (Syringyl, 1325cm^{-1})/ G (Guaiacyl, 1259 cm^{-1}) was 1.1 for the hemp without dislocations comparing to 0.9 for the dislocation regions, indicating higher cellulose content in the dislocation regions.

References

[1] W. Weibull, Roy. Swedish Inst. Engng. Res. Proc. 11 (1939) 1-45.

[2] Y.P. Zhang, X.A. Wang, J Mater. Sci. 37 (2002)1401-1406.

[3] P. Ander, K. Nyholm, in Proceeding of the International Symposium on Wood Machining, 2000, pp. 3-19.

[4] P.R. Kibblewhite, Tappi J. 57 (1974) 120-121.

[5] D.H. Page, R.S. Seth, B.D. Jordan, M.C. Barbe, in Transactions of the Eighth Fundamental Research Symposium,1985, pp. 183–227.

[6] M. Pihlava, PSC Communications 113, Helsinki University of Technology, 1998.

[7] P. Ander, G. Daniel, in Proceedings of the 2nd International Symposium on Wood Machining, 2004. pp. 247.

[8] P. Ander, G. Daniel, in Proceedings of the 8th European Workshop on Lignocellulosis and Pulp, 2004. pp. 49.

[9] U. Schmitt, P. Ander, J.R. Barnett, A.M.C. Emons, G. Jeronimidis, P. Saranpaa, P. Tschegg, Wood fibre cell walls: methods to study their formation, structure and properties, Swedish University of Agricultural Sciences, 2004.

[10] P. Ander, G. Daniel , C.G. Lindgren, A.C. Marklund, Nord. Pulp Pap. Res. J. 20 (2005) 115-121.

[11] L.G. Thygesen, J Mater. Sci. 43 (2008) 1311-1317.

[12] N. Terziev, G. Daniel, A. Marklund, Holzforschung 59 (2005) 163–169.

[13] M. Eder, N. Terziev, G. Daniel, I. Burgert, Holzforschung 62 (2008) 77-81.

[14] N. Terziev, G. Daniel, A. Marklund, Holzforschung 62 (2008) 149-153.

[15] T. Nilsson, P.J. Gustafsson, Composites Part A.38 (2007)1722-1728.

[16] B. Focher, A. Marzetti, H.S.S. Sharma, in the Biology and Processing of Flax, 1992. pp. 329–342.

[17] M. Hughes, G. Sebe, J. Hague, C. Hill, M. Spear, L. Mott, Compos. Interfaces 7 (2000) 13-29.

[18] R.P. Kibblewhite, Cellul. Chem. Technol. 10 (1976) 497–503.

[19] P. Hoffmeyer, Wood Sci. Tech. 27 (1993) 321–335.

[20] U.B. Mohlin, J. Dahlbom, J. Hornatowska, Tappi J. 79 (1996) 105–111.

[21] M.J. Ellis, G.G. Duffy, R.W. Allison, R.P. Kibblewhite, in 51st Appita Annual General Conf., 1997.pp. 643–649.

[22] R.W. Allison, M.J. Ellis, R.P. Kibblewhite, G.G. Duffy, in Proceedings of the 1998 International Pulp Bleaching Conference, 1998, pp. 159–166.

[23] C.H. Ljungqvist, R. Lyng, F. Thuvander, in 23rd Risø International Symposium on Materials Science, 2002.

pp. 231–238.

[24] C. Baley, J Mater. Sci. 39 (2004) 331– 334.

[25] G.C. Davies, D.M. Bruce, Textile Res. J.68 (1998) 623–629.

[26] L.G. Thygesen, P. Hoffmeyer, Ind. Crops Prod. 21 (2005) 173–184.

[27] H.L. Bos, M.J.A. Van den Oever, O.C.A.A. Peters, in 4th International Conference on Deformation and Fracture of Composites, 1997, pp. 499–504.

[28] H.L. Bos, A.M. Donald, J. Mater. Sci. 34 (1999) 3029 – 3034.

[29] L.G. Thygesen, B. Jørgen, B. Sørensen, P. Hoffmeyer, Ind. Crops.Prod. 24 (2006) 181–185.

[30] L. Segal, J.J. Creely, A.E. Martin, C. M. Conrad, Tex. Res. J.29 (1959) 786-794.

[31] M.B. Roncero, A.L. Torres, J..F. Colom, T. Vidal, Bioresour. Technol.96 (2005) 21-30.

[32] Y. Kataoka, T. Kondo, Macromolecules 31 (1998) 760-764.

[33] R.T. O'Connor , E.F. DuPre, D. Mitchman, Tex. Res. J.28 (1958) 382–392.

[34] L. Ferrús, P. Pagés, Cell. Chem. Technol. 11 (1977) 633.

[35] M.L. Troedec, D. Sedan, C. Peyratout, Composites Part A 39 (2008) 514–522.

[36] J.W.S. Hearle, J. Polym. Sci.28 (1958) 432-435.

[37] M.L. Nelson, R.T. O'Connor, J.Appl.Polym. Sci. 8 (1964) 1311-1324.

[38] T. Kondo, C. Sawatari, Polymer 37 (1996) 393-399.

[39] M. Schwanningera, J.C. Rodriguesc, H. Pereira, B. Hinterstoisser, Vib. Spectrosc. 36 (2004) 23-40.

[40] S. Merk, A. Blume, M. Riedereer, Planta 104 (1998) 44-53.

[41] E.N. Dubis, A.T. Dubis, J. W. Morzycki, J. Mol. Struct. 511-512 (1999) 173–179.

[42] J. Singthong, S.W. Cui, S. Ningsanond, Carbohydr. Polym.58 (2004) 391-400.

[43] J. Singthong, S. Ningsanond, S.W. Cui, Food Hydrocolloids 19 (2005) 793–801.

[44] D. Fengel, M. Ludwig, Das Papier 45 (1991) 45–51.

[45] O. Faix, Holzforschung 45 (1991) 21-27.

[46] S. Kubo, J.F. Kadla, Biomacromolecules 6 (2005) 2815-2821.

[47] J.J. Cael, K.H. Gardner, J.L. Koenig, J. Chem. Phys.62 (1975) 1145-1153.

[48] X. Colom, F. Carrillo, Eur. Polym. J. 38 (2002) 2225–2230.

[49] F. Carrillo, X. Colom, J.J. Suñol, J. Saurina, Eur. Polym. J. 40 (2004) 2229-2234.

[50] D. Ruan, L. Zhang, Y. Mao, J. Membr. Sci.241 (2004) 265-274.

[51] W. Collier, V.F. Kalasinsky, T.P. Schultz, Holzforschung 51 (1997) 167-168.

[52] J.C. del Río, A. Gutiérreza, I.M. Rodrígueza, D. Ibarra, Á.T. Martínez, J.Anal. Appl. Pyrolysis 79 (2007) 39-46.

[53] S.Y. Oh, D. Yoo, Y. Shin, Carbohydr. Res. 340 (2005) 2376-2391.

[54] L. Xu, A. Lio, J. Hu, D.F. Ogletree, M. Salmeron, J. Phys. Chem. B. 102 (1998) 540-548.

[55] C.Y. Liang, R.H. Marchessault, J.Polym.Sci. 39 (1959) 269-278.

[56] Y. Cao, H. Tan, J. Mol. Struct. 705 (2004) 189-193.

[57] Y. Maréchal, H. Chanzy, J. Mol.Struct. 523 (2000) 183-196.

[58] N.V. Ivanova, E.A. Korolenko, E.V. Korolik, R.G. Zbankov, J. Appl. Spectrosc. 51 (1991) 301–306.

[59] C.Y. Liang, R.H. Marchessault, J. Polym. Sci. 37 (1959) 385–395.

[60] E.P. Kalutskaya, S.S. Gusev, Sci. U.S.S.R.22 (1981) 550–556.

[61] R.H. Marchessault, C.Y. Liang, J. Polym. Sci. 43 (1960) 71–84.

[62] D. Fengel, Holzforschung 47 (1993) 103–108.

[63] T. Kondo, J. Polym. Sci.: B., Polym. Phys. 32 (1994) 1229-1236.

[64] T. Kondo, Cellulose 4 (1997) 281-292.

[65] T. Kondo, J. Polym. Sci.: B, Polym. Phys. 35 (1997) 717-723.

[66] H. Itagaki, M. Tokai, T. Kondo, Polymer 38 (1997) 4201-4205.

[67] T. Kondo, C. Sawatari, R. Manley, D.G. Gray, Macromolecules 27 (1994) 210-215.

[68] T. Kondo, C. Sawatari, Polymer 35 (1994) 4423-4428.

[69] A.C. O'Sullivan, Cellulose 4 (1997) 173–207.

[70] K. Tashiro, M. Kobayashi, Polymer 32 (1991) 1516–1526.

[71] J.C.F. Walker, Primary Wood Processing: Principles and Practice, Chapman & Hall, London, 1993.

[72] E. Sjöström, Wood Chemistry: Fundamentals and Applications, Academic Press, San Diego, 1981.

[73] G.D. Love, C.E. Snape, M.C. Jarvis, Phytochemistry 49 (1998) 1191-1194.

Figure Captions:

Fig.1 Schematic of testing procedures

Fig.2 Set-up of single fibre test: a=specimen mount, b=test specimen mounted on the mount (dimensions in mm)

Fig 3 Dislocation of hemp fibres (a) by Optical Microscopy (x 50 magnification), (b) by FE-SEM (x 1500 magnification), (c) the fracture within dislocation regions (x 500 magnification) and (d) without dislocation (x 500 magnification)

Fig.4 X-ray diffractogram of hemp fibres without dislocation

Fig.5 FTIR spectra of hemp fibres without dislocation and dislocation regions

Fig.6 Deconvolved FTIR spectra of the υ_{OH} region of hemp without dislocation (a) and dislocation regions (b)

Fig.7 FTIR spectra of hemp fibres from 1370 cm^{-1} to 1330 cm^{-1}(a); from 1330 cm^{-1} to 1215 cm^{-1} (b): with and without dislocation

Fig.8 Deconvolved FTIR spectra from 1330 to 1215 cm^{-1} of without dislocation (a) and dislocation regions (b)
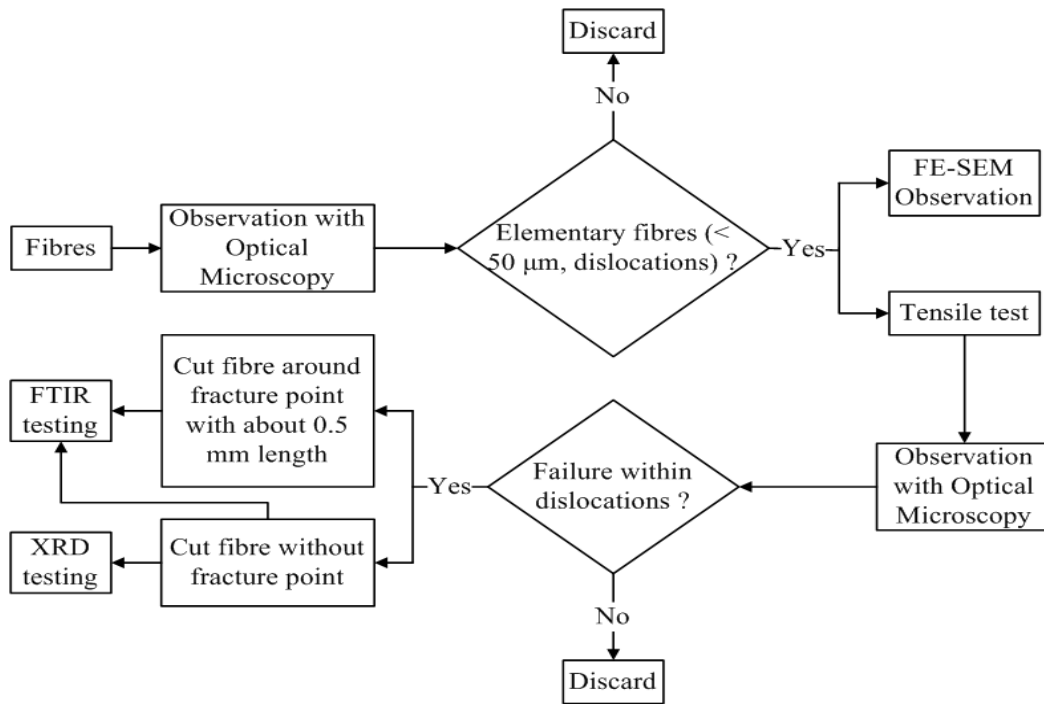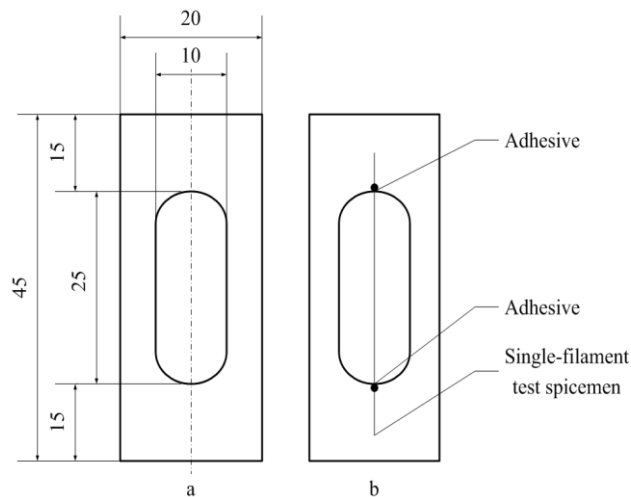
Fig.1 Schematic of testing procedures

Fig.2 Set-up of single fibre test: a=specimen mount, b=test specimen mounted on the mount
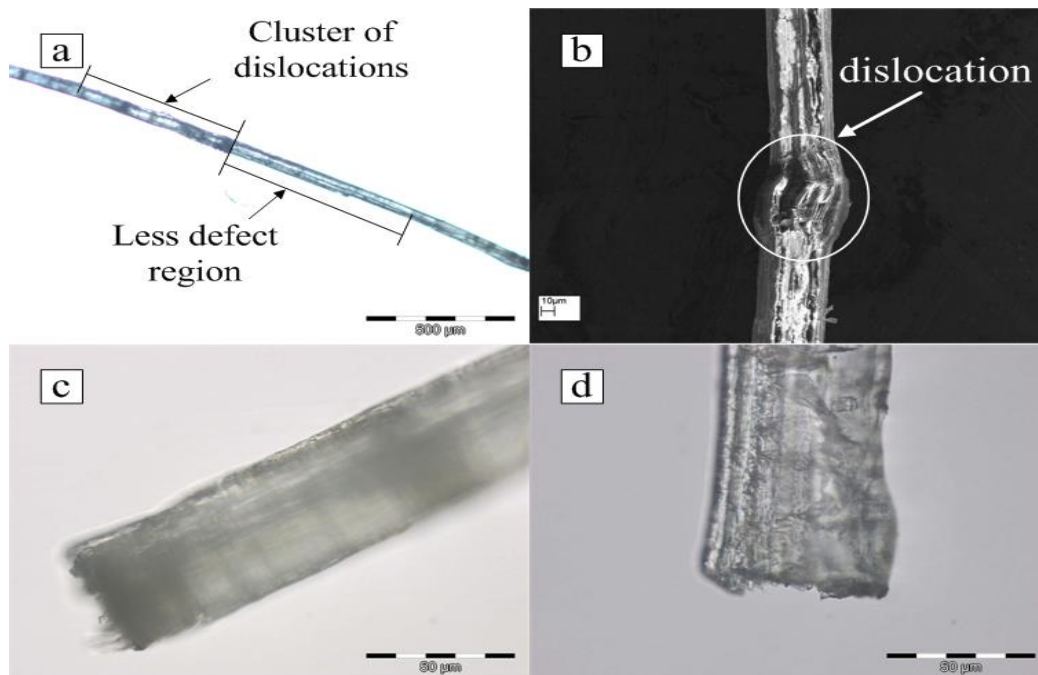
(dimensions in mm)

Fig 3 Dislocation of hemp fibres (a) by Optical Microscopy (x 50 magnification), (b) by FE-SEM (x 1500 magnification), (c) the fracture within dislocation regions (x 500 magnification) and (d) without dislocation (x 500 magnification)
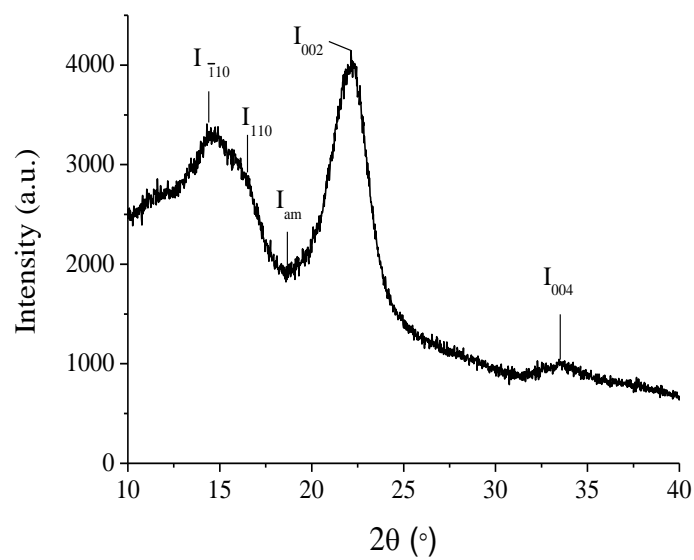

Fig.4 X-ray diffractogram of hemp fibres without dislocation

Fig.5 FTIR spectra of hemp fibres without dislocation and dislocation regions

1 3450 cm^{-1}
2 3346 cm^{-1}
3 3262 cm^{-1}
4 3161 cm^{-1}

1 3451 cm^{-1}
2 3350 cm^{-1}
3 3264 cm^{-1}
4 3167 cm^{-1}

a

b

Fig.6 Deconvolved FTIR spectra of the υ_{OH} region of hemp without dislocation (a) and dislocation regions (b).

(Solid curves=calculated data; dotted curves=experimental data).

Fig.7 FTIR spectra of hemp fibres from 1370 cm^{-1} to 1330 cm^{-1}(a); from 1330 cm^{-1} to 1215 cm^{-1} (b) with and without dislocation

Fig.8 Deconvolved FTIR spectra from 1330 to 1215 cm^{-1} of without dislocation (a) and dislocation regions (b). (Solid curves=calculated data; dotted curves=experimental data).

Table Captions

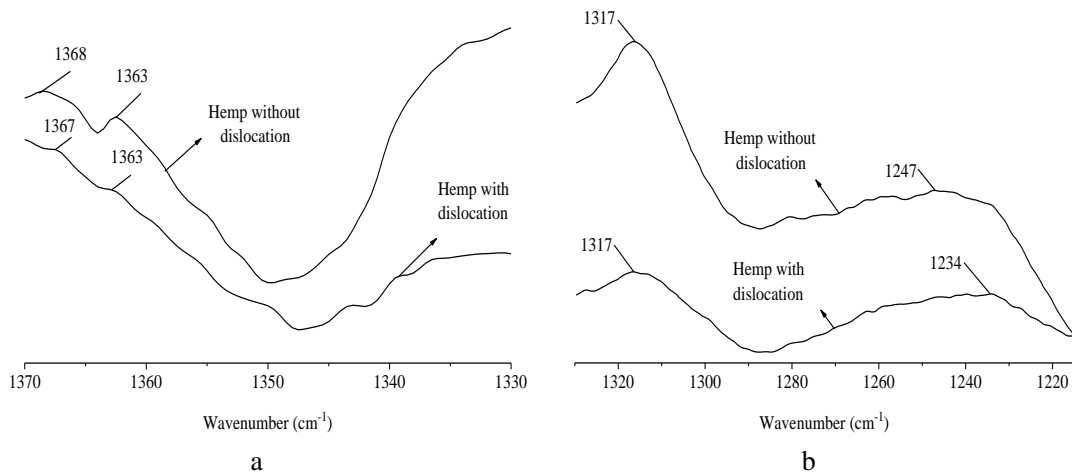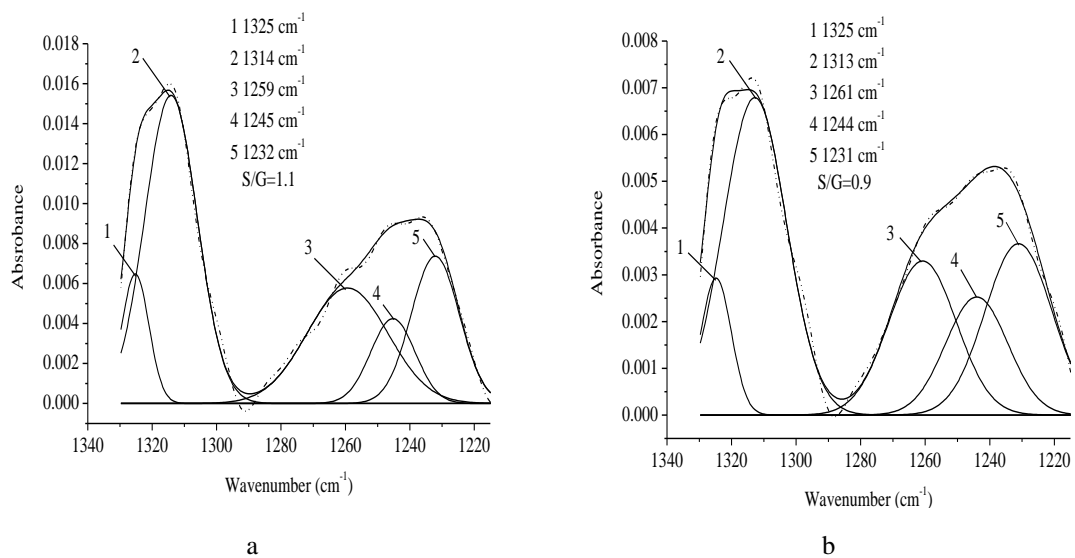Table 1 Results of CI of hemp fibres determined by XRD and FTIR

2θ (°)	Without dislocation (XRD testing)	Without dislocation (FTIR testing)		Dislocation regions (FTIR testing)	
	Intensity (a.u)	Wavenumber (cm^{-1})	Absorbance	Wavenumber (cm^{-1})	Absorbance
19.11 (I_{am})	1822	662	0.1286	663	0.1131
22.63 (I_{002})	4144	1368	0.0621	1367	0.0467
CI (%)	56.0	48.4 (c.v. 2.6%)		41.3 (c.v. 9.1%)	

Table 2 Band characteristics of FTIR spectra related to regions without and with dislocation regions

Wavenumber (cm^{-1}) range of peak		$\Delta\upsilon(cm^{-1})$	Assignment	Sources
Without dislocation	Dislocation regions			
3327	3332	5	OH stretching	Cellulose, Hemicellulose [37, 38]
2883	2882	-1	C–H symmetrical stretching	Cellulose, Hemicellulose [38, 39]
1724	1724	0	C=O stretching vibration	Pectin, Waxes, Hemicellulose [40-43]
1623	1624	1	OH bending of absorbed water	Water [44]
1506	disappear	-	C=C aromatic symmetrical stretching	Lignin [45, 46]
1423	1423	0	HCH and OCH in-plane bending vibration	Cellulose [37, 38, 47-50]
1368, 1363	1367,1363	-1/0	In-the-plane CH bending	Cellulose, Hemicellulose [38, 46, 51]
1325	1325	0	S ring stretching	Lignin [46, 52]
1314	1313	-1	CH_2 rocking vibration at C6	Cellulose [44, 48, 53]
1259	1261	1	G ring stretching	Lignin [46, 52]
1245	1244	-1	C-C plus C-O plus C=O stretch; G condensed > G etherfied	Lignin-carbohydrate Complex [54]
1232	1231	-1	COH bending at C6	Cellulose [45, 48]

1204	1199	-5	C-O-C symmetric stretching, OH plane deformation	Cellulose, Hemicellulose [44, 55]
1152	1156	4	C-O-C asymmetrical stretching	Cellulose, Hemicellulose [37, 44, 56]
1046	1043	-3	C-C, C-OH, C-H ring and side group vibrations	Cellulose, Hemicellulose [44, 45, 57]
1020	1018	-2	C-C, C-OH, C-H ring and side group vibrations	Cellulose, Hemicellulose [44, 53, 56, 57]
994	996	2	C-C, C-OH, C-H ring and side group vibrations	Cellulose, Hemicellulose [44, 53]
895	894	-1	COC,CCO and CCH deformation and stretching	Cellulose [37, 44, 48, 50, 56]
662	663	1	C-OH out-of-plane bending	Cellulose [38, 55]

Table 3 Hydrogen bonds characteristics of FTIR spectra related to without and with dislocation

Wavenumber (cm^{-1}) range of peak		$\Delta\upsilon(\text{cm}^{-1})$	Assignment
Without dislocation	Dislocation regions		
3450	3451	1	O(2)H---O(6) intramolecular in cellulose [58]
3346	3350	4	O(3)H---O(5) intramolecular in cellulose [58, 59]
3262	3264	2	O(6)H---O(3`) intermolecular in cellulose [58-60]
3161	3167	6	O-H stretching [61]

Paper 3

M. Fan, D.Dai, and A. Yang. High Strength Natural Fibre Composite:

Defibrillation and its Mechanisme os Nano Cellulose Hemp Fibres.

International Journal of Polymeric Materials. 2011; 60:1-15.

High Strength Natural Fiber Composite: Defibrillation and its Mechanisms of Nano Cellulose Hemp Fibers

M. Fan, D. Dai, and A. Yang

Nano Cellulose Composites and Research Centre, Brunel University

Mechanisms of micro- and nano-defibrillation of hemp fibers are studied and discussed. The results, generated from subjecting hemp fibers to mechanical shearing (MS), combined MS-heating (MSH), and combined MSH-chemical processes, confirmed that the micro/nano-architecture of cell wall of hemp fibers facilitated the defibrillation during nano process and the different fibril construction and chemical constituents between cell wall layers (i.e., lamella, primary and secondary layers) determined the nature of process and processing parameters to be applied while enabling processes to be tailored for various end products. A low fibril concentration within lamella and primary layers made the regions vulnerable to decompose when wet and heated, and led to the breakdown of cell walls to the secondary layers and consequently microfibril of S_2-layer. Inherent and processing macro- and micro-defects of hemp fibers could be the first accessible points for processing agents and initiating mechanical decomposition when the nano process took place. Nano processing parameters, e.g., heat and chemical agents, were significant contributors to the defibrillation of cellular micro/nano particles and hence the efficacy and productivity of nano process due to the different sensibility of chemical compounds within various layers of cell walls.

Keywords cell wall polymer, defibrillation mechanism, micro- and nano-cellulose fiber, nano processing

INTRODUCTION

Research in nanotechnology (at least one of the dimensions of particles ≤100 nm) is critically important to the emergence of a new generation of composite processes and products. New or enhanced (i.e., its capability to improve or alter existing materials) composites with unique properties can be developed using nanotechnology [1]. The technology potentially offers the twin benefits of reductions in energy consumption and greater ability to compete on price against conventional materials such as steel [2].

Cellulose can be processed to the form of nano-crystals with cross sectional dimension in a range of 2–20 nm. Almost any cellulosic material could be considered as a potential source for the isolation of nano-sized cellulosic structures: 1) cellulosic structures can be excluded from the cell walls of bacteria (e.g., gluconacetobacter xylinus) with cross-sectional dimensions of typically 6 nm by 2 nm [3–5]; 2) rystalline celluloses have also been found in the cell walls of algae (e.g., chlorophyceae) with the nanocrystals having a lateral size of about 10 nm [6–8]; 3) cellulosic structures can be obtained from animals (e.g., tunicates and sea squirts); these nanocrystals are normally parallelepiped rods of lateral size of 10–20 nm [9]; 4) cellulosic structures are generated from plant celluloses (e.g., wood). Wood and other natural resources have been considered as an attractive starting material for making nano-materials because of their great abundance. Brunel University, UK, is engaged in an extensive program of research aimed at a better understanding of the manufacturing and characterization of nano celluloses from natural resources (wood and other plants), and establishing the methods of viable commercial processes for nano cellulose crystallines and their composite production for structural uses in construction. This is one of a series of papers that present the results of the ongoing research project carried out at Brunel. This paper only presents the defibrillation mechanisms of cellulose nano-crystals from hemp fibers through performing various processes.

Hemp bast fiber is a low-density, cellular, polymeric composite. Its ultra-structure can be ascribed as the role of "fiber" to the cellulosic microfibrils, while the lignin and hemicelluloses are considered as separate components of the "matrix." Cellulose occurs in the form of long slender filaments or chains built up within the cell wall from the glucose monomer ($C_6H_{12}O_6$). The number of units per cellulose molecule (the degree of polymerization) can vary considerably, even within one cell wall. However, it is thought that for the cell walls of plants, such as wood, the degree of polymerization is in a range of 8000–10000 for the secondary cell wall whereas the primary cell wall has a degree of polymerization of only 2000–4000 [10,11]. Cellulose chains may crystallize in many ways and the cellulose crystal is characterized by a repeat distance of about 1 nm. The degree of crystallinity of the cellulose is on average about 60%. Research into cellulose nano particles and their nanocomposites are so new

that there are few articles available, although microfibrillated cellulose was developed in the 1980s from plant celluloses (typically from wood pulp) through a high-energy homogenization process and originally intended for use in food and cosmetics [12]. The extraction of cellulose nanofibers is basically by a purely mechanical process or chemo-mechanical process (including bacterial cellulose, modified cellulose). However, a purely mechanical method has a limitation of fineness and uniformity of nano fibers. The bacterial process is very expensive and can cause contamination. Commercial success encounters the greatest obstacles of costs and sustainability (e.g., great amount of energy and water used). A better understanding of process and defibrillation mechanisms is highly required for producing the high quality of cellulose particles, productivity and processing efficacy, and for which this paper is present.

MATERIALS AND METHODS

Materials

Raw materials used in this research are hemp plant fibers (*Cannabis sativa L*). Hemp is the variety grown for industrial uses in many countries around the world. The primary hemp fibers have been used for textiles, cordage, paper, and other composite products. The commercial production of the hemp fibers is normally from the retted hemp, mechanically produced from phloem by separating the fibers from the xylem material (woody core). The bast fibers in most cases occur in bundles that are glued together by pectin and calcium ions. The hemps used are supplied by Springdale Ltd., UK. The materials were dried and stored before use. Main chemical compositions of the hemp fibers used are determined, on average consisting of 72% celluloses, 19% hemicelluloses, 5% lignin, and others. The mean length of hemp fibers or fiber bundles is 36 mm and width 26 μm. The average tensile strength of hemp fibers used is 886 MPa and modulus 66 GPa.

Both alkaline and acidic compounds of the processing media were made in the laboratory by using commercial alkali and acid materials, which were obtained from Sigma-Aldrich Company Ltd, UK. All chemical reagents were used without any further pre-purification.

Defibrillation Process

The main procedures performed in the study are given in Figure 1 twenty grams of dried hemp fibers were prepared [(a)]. The material was mixed with water in the three-neck flask and the mixture was mechanically sheared for 20 minutes (900 rpm) [(b1)]. The process was then continued with a combination of mechanical shearing and heating (60°C) (the process without heating was
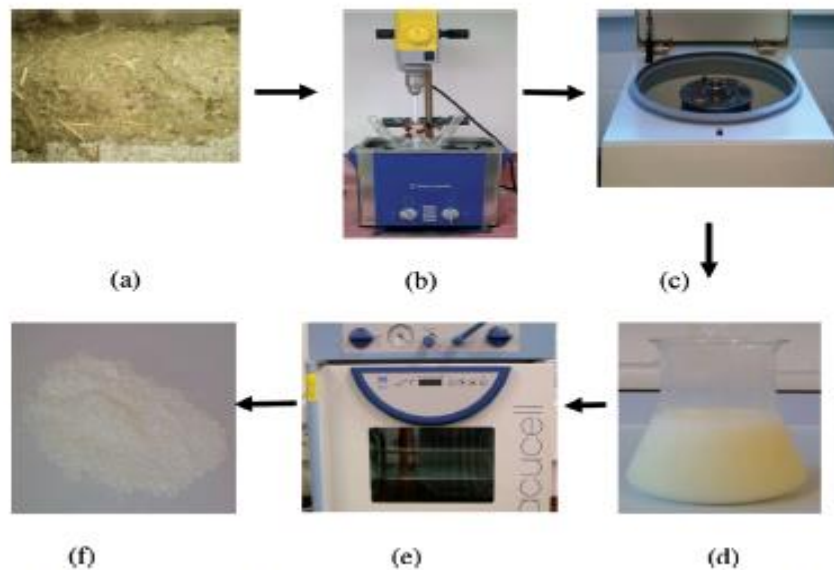
Figure 1: Diagram of defibrillation process of nano hemp fibers. (*Figure is provided in color online.*)

also carried out in parallel) [(b2)]. The process was also continued for another two groups of materials but with a combination of water, alkaline (group one), and acidic (group two) compounds (at 3 wt%) and mechanical shearing [(b3)]. Continuous ultrasonication was also applied to the processes (b2) and (b3). The developed suspension was centrifuged (8300 rpm) for 20 min and washed with distilled water [(c)]. The solidified samples [(d)] were freeze-dried for 48 hours [(e)], and then the nanocellulose powder was obtained [(f)]. The solution from various processes was sampled and tested to determine the effect of various processing parameters.

Characterization of Nanofibers

Sample Preparation

One gram of nano powder was re-dispersed into water and stirred to form a colloidal suspension. Theoretically the samples can be obtained from the solidified nano gel before centrifugation. The use of the developed nano powder is to ensure that the final products are commercially viable. The suspension is maintained at a concentration of 0.1 wt% in 1 wt% uranyl acetate in distilled water. A drop of the resulting mixture was cast onto a 200-mesh holey copper grid, dried and covered with a carbon film. Six samples were prepared for each examination.

Measurements

Measurements were conducted within a Zeiss Supra 35 VP field emission scanning electron microscope (FE-SEM) equipped with an Oxford Instruments Inca energy dispersive X-ray analyzer (EDX). The quantified values of elemental concentration depend on the calibration, which is complex for argon (Ar). However, the relative values can be corrected to a greater level of certainty: the electron accelerating voltage was decreased to bring the silicon EDX signal to zero to ensure that the penetration depth and depth of analysis were less than or equal to the film thickness. Thus the measurement of argon incorporation is only examining the film, not the substrate, which may contain the incorporated argon due to the cleaning process.

RESULTS AND DISCUSSION

Effect of Fiber Defects at the Macroscopic Level

Macro defects may be the first accesses (weak points) for chemical attack and mechanical forces when the defibrillation takes place. The trunk of a hemp performs three functions: i.e., i) it supports the crown, which is responsible for the production of food and seed; ii) it conducts the mineral solutions absorbed by the roots upwards to the crown; and iii) it stores manufactured food. The first function means that the trunk has to withdraw various environmental attacks, such as wind blow, snow load, or other mechanical stresses/forces, resulting in splits or cracks both longitudinally and transversely, which provide weak points to chemical penetration or for initiating mechanical failure. The growing nodes may also provide paths for the transport of the refining agent and be vulnerable to break-down to small sections because of the transverse arrangement of fibrous materials (Figure 2); the mechanisms of flow will be discussed in more detail in the next section.

Harvesting and other processing operations inevitably results in additional cracks and other damages to the hemp fibers (Figure 3), which may further create weak points for chemical attack and initiating points for further mechanical fibrillation of fibers. The microscopy analysis shows that the main damage of the hemp fibers can be grouped into three main categories: namely cell wall crack, pressing (crushing), and scrapping (Figure 4).

Effect of Inherent Micro Defects

The inherent micro defects may facilitate the defibrillation during nano processing. Under the microscope, the hemp fibers exhibit frequent joints, cross striation, and fissures (Figure 5). It has been observed that the addition of a liquid medium firstly penetrated into these weak regions. The penetration
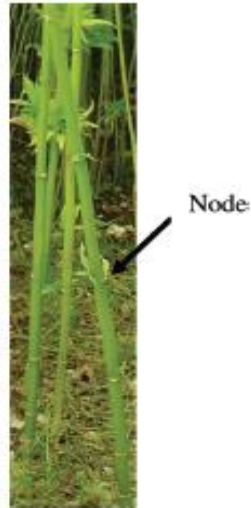
Figure 2: Inherent grown defect (node) of hemp plant. (*Figure is provided in color online.*)

of liquid consequently results in an increase of the moisture content in the region because of the hydrophilic nature of the fibers. This inevitably results in a reduction of the strength of local regions because the strength of natural fiber materials decreases with an increase in the moisture content of hydrophilic materials. For example, an increase of moisture content from 0 to 30% may result in a linear loss (50 to 70%) in the stiffness of Sitka spruce [13]. This process may also create a moisture gradient between the wet areas and their

**Figure 3:** Retted and rolled hemp materials. (*Figure is provided in color online.*)

165

201
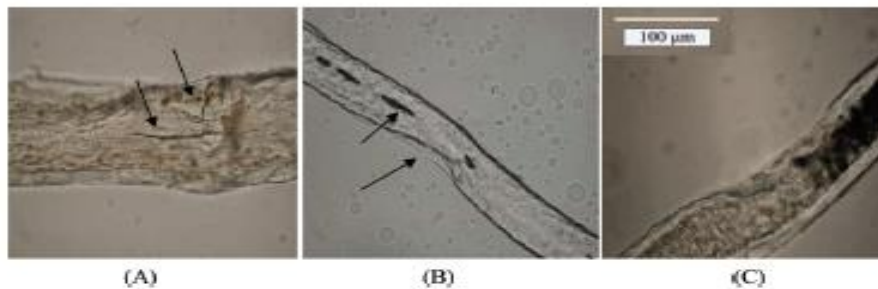
Figure 4: Structural damage of hemp fibers (A = cell wall crack, B = pressing damage, C = scrapping damage) (scale 100 μm for Fig. A, B, and C). (*Figure is provided in color online.*)

surrounding regions and consequently cause stress concentration in the region, which promotes the breakdown of hemp fibers. The application of heat during the nano processing has a similar effect as that of moisture penetration and this will be discussed in more detail in the next section.

Effect of Micro Architecture of Cell Walls of Hemp Fiber

It is apparent that the micro-architecture of cell walls of plant fibers facilitates the nano processes. Figure 6 shows that the first stage of mechanical stirring of fibrous materials in water fibrillates hemp fibers into micro particles due to the repeated mechanical shearing of the fibrous materials. The cell wall of hemp bast fibers consists of middle lamella, primary wall, secondary walls (S_1, S_2 and S_3), and cell lumen (Figure 7), although some investigators have
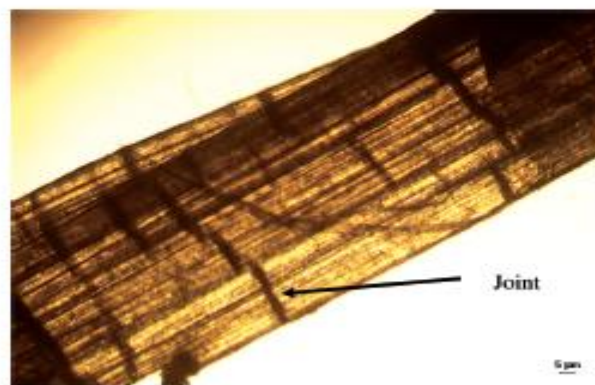

Figure 5: Repeat joints along hemp cell wall. (*Figure is provided in color online.*)
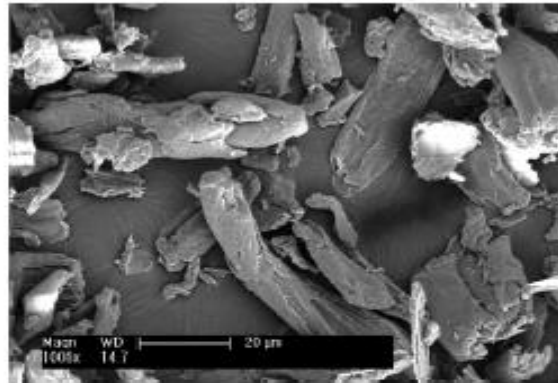
Figure 6: Micro hemp fibers after mechanical shearing process.

recorded the presence of two very thin transition layers, an S_{12} layer between the S_1 and S_2 layers and an S_{23} between the S_2 and S_3 layers with much-improved electron microscopy for wood plant fibers. The diameter/width of a

180
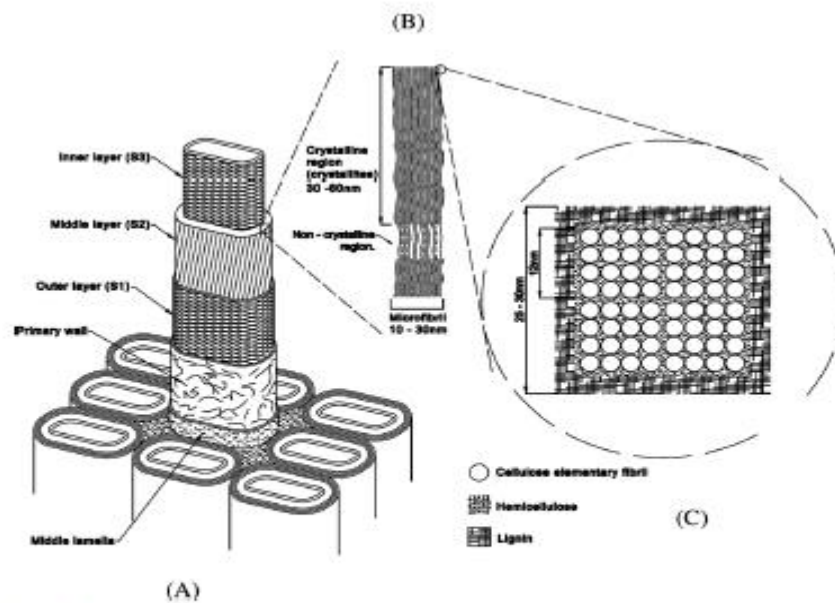
Figure 7: Structure of cell walls of hemp fibers (A = simplified structure showing mean orientation of microfibrils in each of the major cell wall layers, B = microfibril containing crystalline and non-crystalline regions, C = cross-section of a microfibril containing elementary/nano fibrils and hemicellulose and lignin).

single cell of hemp fiber (including cell lumen and S1-S3 layers) ranges from 10 to 30 μm [14]. The thickness of the cell wall layers are tested and in an average of 2% for primary, 6% for S_1 layer, 89% for S_2 layer and 3% for S_3 layer. Therefore, a comparison of sizes of fibrous materials in Figure 6 and the micro fibrils in Figure 7 indicates that this process has possibly fibrillated fibers down from the S_2 layer to single cell wall (S1-S3 layers). However, because of the high proportion of lignin content and loose texture in S1 and S3 layers, both S1 and S3 layers are relatively easily broken down under mechanical sheering and heating, which are conditions given in this study.

The composition and construction vary considerably between the layers: the cell lumen is either filled with water or empty; the middle lamella is devoid of cellulosic microfibril construction; the primary wall has the loosely packed microfibrils, which interweave at random; in the secondary walls the microfibrils are closely packed and parallel to each other. The non-microfibril and loose packed microfibril regions, i.e., middle lamella and primary wall, are more vulnerable to chemical attack and mechanical breakdown than the firmly packed microfibril regions (i.e., second wall layers), and they may be first destroyed when the nano processing takes place. Therefore, the first stage of mechanical sheering process produces particles with a lateral size of 10–15 μm for most of the particles (Figure 6). It is worthy to note that these differences, determining the level of difficulties of either chemical or mechanical or combined processing separation of fibrils, may enable production to be tailored for different results/products.

The examination of hemp fibers under a microscope shows that the length of fibers is in a range of 2–5 mm. More details of fiber characterization will be published in a separate paper [15]. The hemp fiber ends are thick-walled, blunt, and in most cases forked (closed). The cross-sections show polygonal cells with rounded edge (Figures 6 and 8). Like other plant fibers (e.g., wood), interconnection by means of pits occurs between cells to permit the passage of mineral solutions and food in both longitudinal and horizontal planes (Figure 8), and this is believed to be the predominant parameter for the first movement of liquid and gas (i.e., liquid medium used in nano processing), which then mainly passes through the cell lumen and decomposes the cell walls. It is these different pathways that result in anisotropy in the effect of liquid penetration in the three principal axes. For most plant fibers (e.g., wood), permeability values quoted in the literature illustrate that longitudinal permeability is about 10^4 times the transverse permeability [16].

Effect of Chemical Constituents of Cell Walls

As mentioned, the cell wall of hemps is a low-density, cellular, polymeric composite of a multi-layer structure (Figure 7). The chemical compositions within different layers are very different and significantly affect the efficacy of nano processing and the applied parameters, including the type of medium,
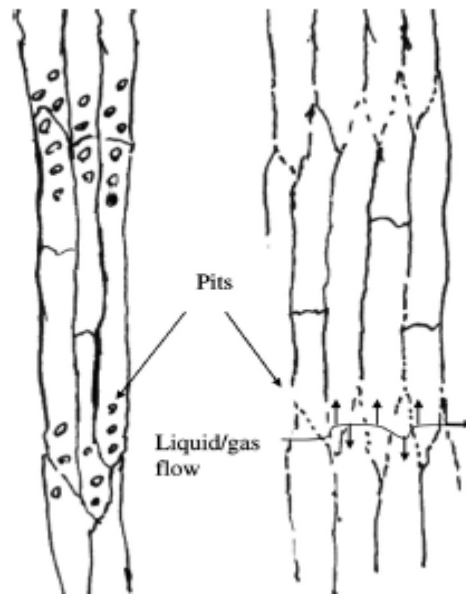
Figure 8: A representation of cellular structure of hemp fibers illustrating the significance of the border pits (A = longitudinal-radial plane, B = longitudinal-tangential plane).

time of addition of the liquid medium and concentration, mechanical forces and motion, and processing temperature. The middle lamella is a lignin-pectin complex, the other S-layers have variable deposition of lignin, which has the prime function of protecting the hydrophilic non-crystalline cellulose and the hemicelluloses, which are mechanically weak when wet, and for cementing together fibrils and in imparting shear resistance in the transference of stress during nano processing. It is evident that the developed processes combined of chemical, mechanical, and ultrasonic components is able to break the S-layer fibers down to microfibril/nano scale (Figure 7). The test of the nano particles shows that the width of particle sizes is in the range of 150–460 nm in length and 15–60 nm in width (Figure 9). The dimension in length, i.e., >60 nm, indicates that majority of the nano particles may contain both crystalline and non-crystalline fibrous regions and the range of lateral size of 15–60 nm indicates that the produced particles exist as a mixture of micro/nano fibers and fiber bundles in comparison of the size of microfibrils, 10–30 nm (Figure 7B). It should be noted that the fibers in the mixtures have a higher level of crystallinity compared to the fiber bundles, because the microfibrils have the gradient transition of crystallinity from elementary fiber to matrix, i.e., passing from the core of the micrfibril the highly crystalline cellulose gives way first

Figure 9: Nano hemp particles after a combined process. (*Figure is provided in color online.*)

to the partly crystalline layer, containing mainly hemicellulose and non-crystalline cellulose, and then to the amorphous lignin (Figure 7C).

Effect of Heat Applied during Nano Processing

Heat may play an important role in the defibrillation of natural fibrous materials. The nano processes with and without heating result in substantially different fibrous products. It is apparent that the process with heating may either reduce the time or result in the finer nano particles (Figure 10). The mechanisms of the heat effect may include that: i) it increases the flow of liquid used as a medium during the process; as aforementioned, the applied heat may create local temperature gradient and hence the internal stresses, which may facilitate mechanical failure; ii) it results in an increase of elasticity of fibers, which facilitates mechanical process, and softens the chemical components, e.g., lignin or hemicelluloses, because of their different melting points; iii) it facilitates chemical reactions within the components of cell walls

(A)   (B)
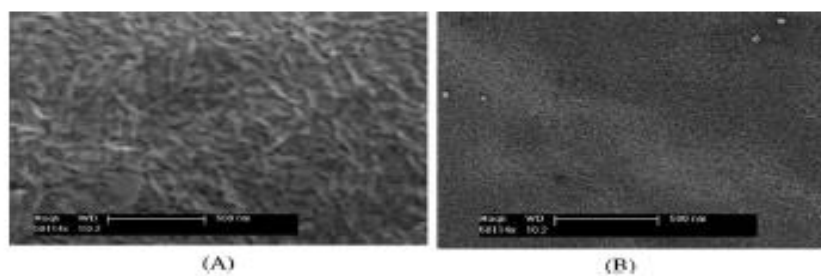
Figure 10: A comparison of nano fibers produced without heating (A) and with heating (B).

and between cell wall components and processing agents or water. Like other plant fibers, the cell walls of hemp plant are also made of the presence of extractives, a series of highly complex organic compounds (e.g., fats, sugars) and inorganic minerals (e.g., calcium, sodium) in relatively small amounts. The microscopy examination of particles after four hour defibrillation process   260 [(b2)] shows that the average lateral size of particles is 68 nm without heating and 52 nm with heating.

Effect of Processing Parameters

The plant material (e.g., wood) is generally neutral and acidic in nature. The acidity in plants is due primarily to the generation of acetic acid by   265 hydrolysis of the acetyl groups of the hemicelluloses in the presence of moisture. The acidic and alkaline processing conditions in the developed processes could result in different effects on the efficacy of the process and the final products. A comparison of the acidic and alkaline processes used in this study shows that the acidic environment has resulted in more significant effect on   270 the final results of the processes (Figure 11), although the measurement of six SEM slides nano particle films shows that majority of fibers have a lateral size of between 20–60 nm and both processes generate a normal size distribution diagram (Figure 12). The particles from acidic process are shorter than that of alkaline process. The nano cellulose fibers isolated under acidic medium   275 have an average of lateral size of 47.3 nm, while under alkaline medium have lateral width of 54.2 nm. It is evident that the fibrillae processed under acidic environment are also less distorted compared to that of alkaline condition, which may be due to the shorter length.

It is also evident that the longer cellulose crystals tend to tangling and   280 agglomeration (Figure 13). Nano-scale hemp celluloses have high thermodynamic potential due to highly developed specific surface, tending to form larger

(A)   (B)
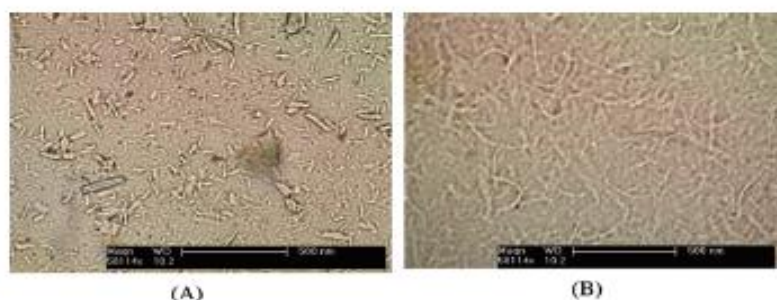
Figure 11: A comparison of nano fibers developed with two processes (A = under acidic medium, B = under alkaline medium). (*Figure is provided in color online.*)
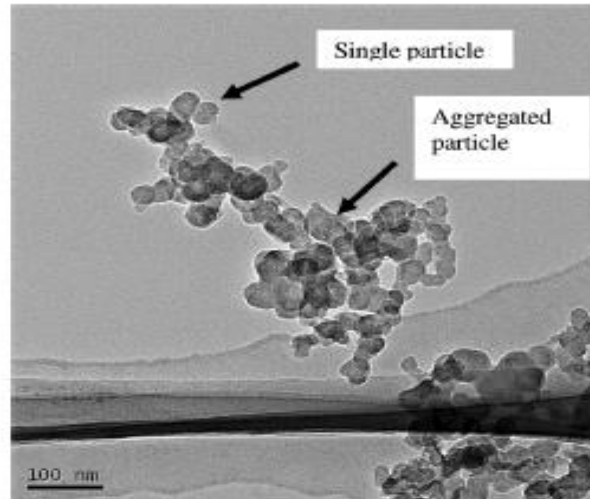
Figure 12: Aggregation of nano particles.

structures via aggregation and agglomeration. Figure 13 shows some of the materials taken before freeze-drying process. The agglomeration may also be related to the particle sizes and aspect ratio, with larger L/D (length/ lateral size) particles having higher specific surface. The L/D of the particles developed is about 33 under acidic medium and 41 under alkaline environ-ment. This difference may give rise to more tangling structures for the latter than the former (Figure 11). The difference in the agglomeration of different processes may also be verified by testing the degree of aggregation of hemp cellulose crystals (Figure 14).
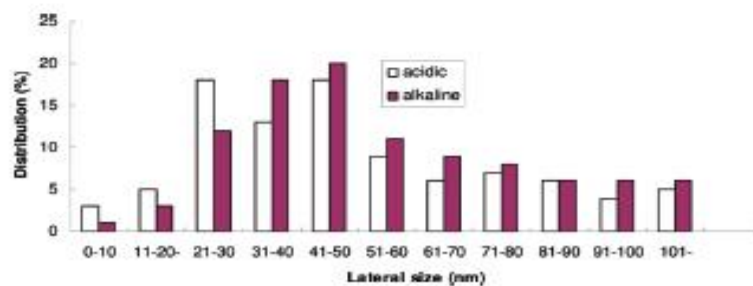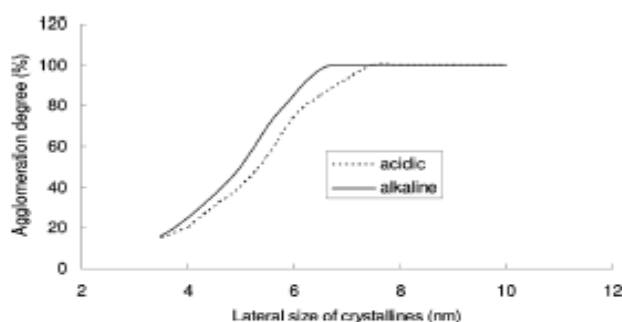

Figure 13: Size of nano hemp particles developed. (*Figure is provided in color online.*)

Figure 14: Agglomeration of hemp crystalline with two different processes.

CONCLUSIOS

Micro- and nano-defibrillation of hemp fibers is attributable to the inherent and operation-induced macro- and micro-defects of hemp fibers, the architecture and chemical composition of cell walls, processing parameters, and the applied agents. Some of these parameters gave rise to the development of incompatible stresses that accelerated the mechanical decomposition of fibers.

Mechanical shearing with the water medium was able to fractionalize hemp fibers to S-layers due to the water reaction with hemp fibers and stress initiation via macro and micro weak points (inherent and processing macro and micro defects), which was thought the first accessible points for processing agents and initiating mechanical decomposition when nano process took place.

Application of heat, in conjunction with water and mechanical shearing, accelerated defibrillation process. The different fibril construction and chemical constituents between cell wall layers (i.e., lamella, primary and secondary layers) contributed to the defibrillation to a large extent: high lignin and hemicellulose (low fibril) concentration within lamella and primary layers made the regions more vulnerable to break/decompose and led to the breakdown of cell walls to micro- and nano-fibrils.

Introduction of chemical agents to nano process further promoted the defibrillation of cellular micro/nano particles and hence the efficacy and productivity of nano process due to the different sensibility of chemical compounds within various layers. However, acidic and alkaline environments resulted in subtle influence on the nano-products, with the acidic medium being more severe than the alkaline medium. The final products were finer and there was less agglomeration for the former than the latter.

REFERENCES

Q4

[1] Fan, M. Nano Technology for Wood Based Composites. In *Performance in Use and New Products of Wood Based Composites*; Fan, M., Ed.; Brunel University Press: 2009; pp. 266–268.

Q4

[2] Fan, M. Composites in Construction. In *Management, Recycling and Reuse of Waste Composites*; Goodship, V., Ed.; Woodhead Publishing: 2009; pp. 289–369.

[3] Gindl, W.; Keckes, J. *Comp. Sci. Technol.* **2004**, *64*, 2407–2413.

Q5

[4] Pink, H.P.; Purz, H.; Bohn, A.; Kunze, J. *Macromol. Symp. 120*, 207–217.

[5] Olabarrieta, I.; Jansson, A.; Gedde, U.W.; Hedenqvist, M.S. *Int. J of Polymeric Mat.* **2002**, *51*, 275–289.

[6] Hayashi, N.; Kondo, T.; Ishihara, M. *Cabohydr. Polym.* **2005**, *61*, 191–197.

Q4

[7] Sugiyama, J.; Vuong, R.; Chanzy, H. *Macromolecules 24*, 4168–4175.

[8] Makiko, K.; Junji, S.; Kakao, I. *Cellulose* **1997**, *4*(2), 147–160.

[9] Favier, V.; Chanzy, H.; Cavaille, J.Y. *Macromolecules* **1995**, *28*, 6365–6367.

[10] Goring, D.A.I.; Timmell, T.E. *TAPPI* **1962**, *45*, 454–459.

Q4

[11] Carrington, H. *Aeronautical Journal 26*, 462–471.

[12] Simson, B.W.; Timmell, T.E. *Cellul. Chem. Technol.* **1978**, *12*, 51–62.

[13] Turbak, A.F.; Sydner, F.W.; Sandberg, K.R. Microfibrillated cellulose. US Patent 4374702 (1983).

[14] Fan, M. *Bioresources* **2010**, *5*(4), 2307–2322.

[15] Dai, D.; Fan, M. *Vibrational Spectroscopy* (in press).

Q4

[16] Illston, J.M., et al. *Construction Materials*; E & FN Spon: London.

320

325

330

335

340

Paper 4

Fourier Transform Infrared Spectroscopy for Natural Fibres

Book: Fourier Transform, ISBN 979-953-307-869-3 (In press)

Chapter number

Fourier Transform Infrared Spectroscopy for Natural Fibres

Professor Mizi Fan[1, 2], Dr Dasong Dai[1, 2] and Professor Biao Huang[2]

Department of Civil Engineering, Brunel University, London, UB8 3PH, UK
School of Material and Engineering, Fujian Agricultural and Forestry University, P.R. China

1. Introduction

Infrared spectroscopy is nowadays one of the most important analytical techniques available to scientists. One of the greatest advantages of the infrared spectroscopy is that virtually any sample in any state may be analyzed. For example, liquids, solutions, pastes, powders, films, fibres, gases and surfaces can all be examined with a judicious choice of sampling technique. The review by Annette, Sudhakar, Ursula and Andrea [1-2] also demonstrates the applicability of dispersion infrared spectroscopy for natural fibres studies.

Fourier transform infrared spectroscopy (FTIR) has facilitated many different IR sampling techniques, including attenuated total reflection and diffuses reflectance infrared Fourier transform (DRIFT) spectroscopy. It has dramatically improved the quality of infrared spectra and minimized the time required to obtain data. The increased speed and higher ratio of signal-to-noise of FTIR relative to dispersion infrared has lead to a substantially greater number of applications of infrared in natural fibres research. In addition, the constant advancing of computer and computing science has made infrared spectroscopy techniques striding further: The availability of a dedicated computer, which is required for the FTIR instrumentation, has allowed the digitized spectra to be treated by sophisticated data processing techniques and increased the utility of the infrared spectra for qualitative and quantitative purposes. With interferometric techniques, the infrared spectroscopy is being launched into a new era and interest in this technique is at an all time high.

Cellulose, which acts as the reinforcing material in the cell wall, is the main constitute in natural fibres. The cellulose molecules are laid down in microfibrils in which there is extensive hydrogen bonding between cellulose chains, producing a strong crystalline structure. Much work has been published on the characterization of the hydrogen bonds in cellulose by using various techniques, among which FTIR has proved to be one of the most useful methods [3-6]. Furthermore, FTIR can provide researchers with further information on the super-molecular structure. FTIR can also be used to determine the chemical compositions of native natural fibres and the modified natural fibres.

This chapter of the book describes the application of FTIR in the hydrogen bonds analysis, determination of structures and chemical compositions, and the morphology characterization for natural fibres.

2. Hydrogen bonds analysis of natural celluloses by using FTIR

A hydrogen bond is the attractive interaction of a hydrogen atom with an electronegative atom, such

as nitrogen, oxygen or fluorine, that comes from another molecule or chemical group. Cellulose is a liner polymer of 1-4 linked β-D-glucose (Figure 1). Hydroxyl groups in C2, C3 and C6 contribute to the formation of various kinds of inter- and intra-molecular hydrogen bonds. The formation of inter- and intra- molecular hydrogen bonds in the cellulose not only has a strong influence on the physical properties of cellulose, including solubility [7, 8], hydroxyl reactivity [9, 10] and crystallinity [11-12], but also plays an important role in the mechanical properties of the cellulose [13]. Calculated by Tashiro and Kobayashi [14] showed that hydrogen bonds contribute about 20% the strain energy to the cellulose. It is apparent that the investigation of hydrogen bonds on cellulosic fibres and other materials gives rise to great benefits for the research on all other aspects of natural fibres and related materials.
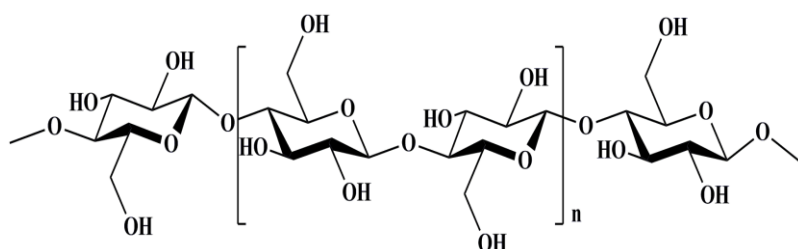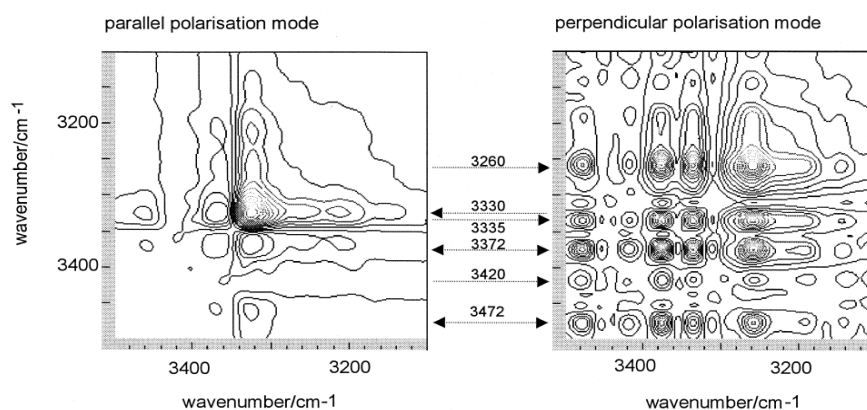

Fig. 1. Chemical structure of cellulose

Fig. 2. Synchronous 2D plot-cross-correlation of in- and out-of-phase spectra [3]

X-ray diffraction has been a powerful tool [15-19] to investigate hydrogen bonds visualization, lengths and angles. FTIR is even a more advanced tool to study hydrogen bonds in cellulose. IR was firstly used to investigate hydrogen bonds in cellulose in the 1950s [e.g. 20-22] and then the whole area of OH stretching wave-number in IR spectra for cellulose I and cellulose II [23-24]. The OH stretching region always covers 3-4 sub-peaks and these sub-peaks cannot be determined in the original data set. Some mathematical methods (e.g. deconvolution [25-27] and second-derivative [28-30]) were used to identify the exact peak for hydrogen bonds. Hinterstoisser and Salmén [3, 31] recently used DMA-FTIR to investigate OH stretching vibration regions between 3700 and 3000 cm^{-1} in the cellulose. In their experiments, cellulose sheets were stretched sinusoidally at low strains while being irradiated with polarized infrared light. For the obtained dynamic IR signals (the in-phase and the out-of-phase responses of the sample), the dynamic IR cross-correlation can be defined. The responses of the OH-groups to an external perturbation can be recorded as in-phase and out-of phase spectra. The cross correlation of these spectra gave the 2D synchronous (Figure 2) and asynchronous (Figure 3) plots,

clearly showing the separated bands in the OH-vibration range and the relation of the OH-groups among them. It is apparent that most of the researchers have focused on the establishment of cellulose structure by investigating hydrogen bonds with FTIR. These (the structure of nature fibres) will be discussed in the next section. Few reports have described the correlation of hydrogen bonds with other characteristics of cellulose by using FTIR technologies.
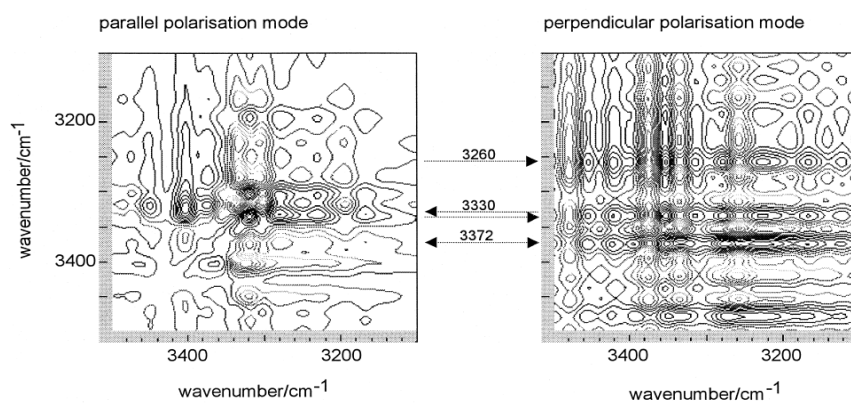

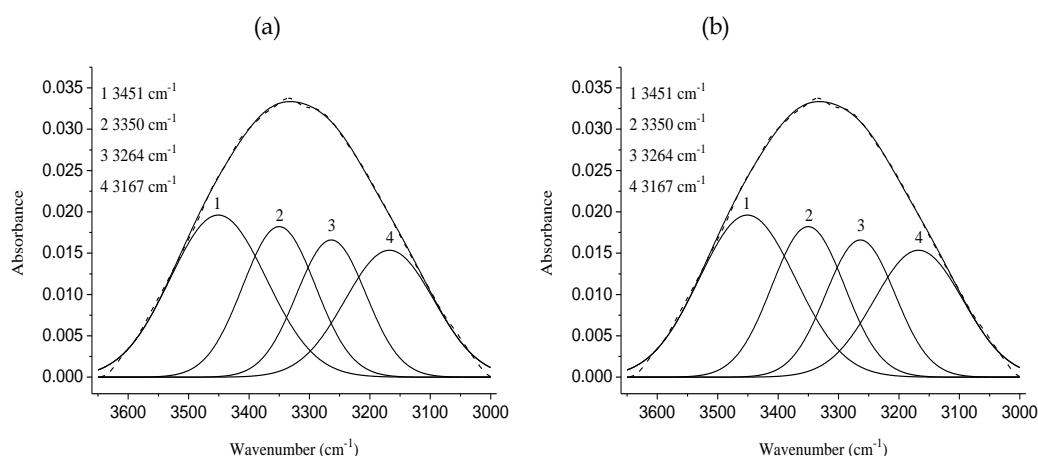Fig. 3. Asynchronous 2D plot-cross-correlation of in- and out-of-phase spectra [3]

Fig. 4. Deconvolved FTIR spectra of the υ_{OH} region of hemp without dislocation (a) and dislocation regions (b). (Solid curves=calculated data; dotted curves=experimental data) [32]

FTIR is very useful for examine the variation of hydrogen-bonds due to various defects [32]. The Nano-cellulose and Bio-composite Research Centre at Brunel University has investigated dislocations in natural fibres (hemp fibres) by using hydrogen-bonding characteristics under FTIR procedure. The test pieces were made from dislocation cluster (region) with the size of a single dislocation from a few microns to 100μm. The test pieces were then processed and examined by using FTIR measurement by using a Perkin-Elmer spectrometer and the standard KBr pellet technique. The recorded FTIR spectra (e.g. 3660–3000cm^{-1}) were deconvolved using Peak Fit V.4.12 software (Figure 4) and the peak positions of the major IR bands can be summarized and compared (Table 1). It can be found that the absorbance of hemp fibres without dislocations in the X–H (O–H and C–H) stretching region is much higher than that with dislocations. The peak positions of the four bands for hemp fibres with and without dislocations are 3450cm^{-1} (1), 3346cm^{-1}, 3262cm^{-1} and 3161cm^{-1} for the hemp without dislocations, and 3451cm^{-1}, 3350cm^{-1}, 3264cm^{-1} and 3167cm^{-1} for the dislocation regions. These bands are related to the

valence vibration of hydrogen bonded OH groups [26]: i.e. band 1 to the intra-molecular hydrogen bond of O(2)H---O, band 2 to the intra-molecular hydrogen bond of O(3)H---O, band 3 to the intermolecular hydrogen bond of O(6)H---O and band 4 to the O---H stretching respectively.

Peak wavenumber (without dislocation) (cm⁻¹)	Peak wavenumber (with dislocation) (cm⁻¹)	Δv (cm⁻¹)	Bonds
3327	3332	5	OH stretching
2883	2882	-1	C–H symmetrical stretching
1724	1724	0	C=O stretching vibration
1623	1624	1	OH bending of absorbed water
1506	disappear	-	C=C aromatic symmetrical stretching
1423	1423	0	HCH and OCH in-plane bending vibration
1368, 1363	1367,1363	-1/0	In-the-plane CH bending
1325	1325	0	S ring stretching
1314	1313	-1	CH_2 rocking vibration at C6
1259	1261	1	G ring stretching
1245	1244	-1	C-C plus C-O plus C=O stretch; G condensed > G etherfied
1232	1231	-1	COH bending at C6
1204	1199	-5	C-O-C symmetric stretching, OH plane deformation
1152	1156	4	C-O-C asymmetrical stretching
1046	1043	-3	C-C, C-OH, C-H ring and side group vibrations
1020	1018	-2	C-C, C-OH, C-H ring and side group vibrations
994	996	2	C-C, C-OH, C-H ring and side group vibrations
895	894	-1	COC,CCO and CCH deformation and stretching
662	663	1	C-OH out-of-plane bending

Table 1. Bonds wavenumber related to regions without and with dislocations

It can be seen that the wave-numbers of peak position of dislocations are higher than those of hemp fibre without dislocation. This indicates that the degree of hydrogen bonding in dislocation regions is lesser than that in without dislocation regions. Furthermore, the absorbance of these bands in the dislocation regions is much lower than that in the regions without dislocations: for dislocation regions being about 79.3% for band 1, 64.4% for band 2, 64.9% for band 3 and 75.7% for band 4 those without dislocations respectively. These mean that the number of hydrogen bonds in dislocations is lower than without dislocation regions according to Beer–Lambert law.

3. Structure of natural fibres determined by using FTIR

The structure of cellulose has a remarkable and complex influence on the course of chemical reactions of the polymer (cellulosic materials). Generally, the structure of cellulose consists of three structural levels: namely (i) the molecular level of the single macromolecule; (ii) the supramolecular level of packing and mutual ordering of the macromolecules; (iii) the morphological level concerning the architecture of

already rather complex structural entities, as well as the corresponding pore system [33]. This section only focuses on the molecular level and supramolecular level, and the morphological level will be discussed in the final section of this chapter.

Molecular orientation is one of the most important parameters, affecting the physical properties of macromolecular systems. It is often introduced in natural macromolecules by the mechanical deformation incurred during their processing. By using FTIR equipped with a microscopic accessory, Kataoka and Kondo [34] determined the molecular orientation of cellulose during the formation of wood cell wall by virtue of the C-O-C stretching mode parallel to molecular chains [23] (Figure 5). It was found that the molecular orientation of cellulose in the primary cell wall coincided with the direction of enlarging cellular growth. It is therefore that the cellulose in the (nascent) primary cell wall might be oriented during crystallization and subsequent formation of microfibrils due to the drawing stress/effect exerted during cellular enlargement. This force, distributed along molecular chains, can cause β-glucose chains in the nascent cellulose to crystallize in the I_α phase with a higher crystallinity, making the molecules orientated in the enlarging direction.
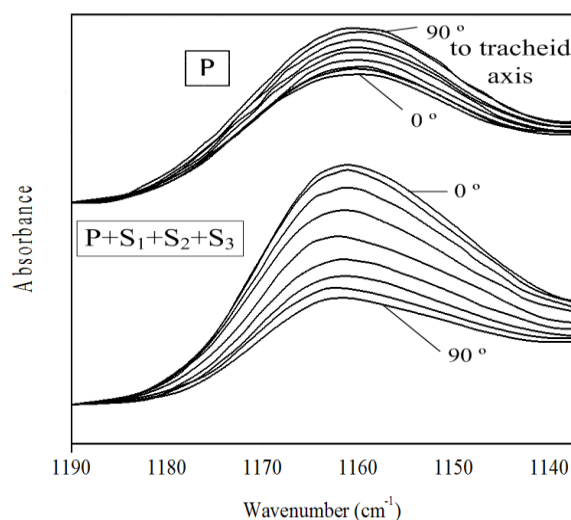

Fig. 5. Changes in FTIR spectra with a rotation of IR polarizer to the tracheid cell axis due to the C-O-C stretching mode: the primary (P) and the mature (P + S1 + S2 + S3) [34]

In order to better understand wood and wood fibres for their potential utilization in advanced materials, some researchers have employed FTIR in conjunction with mechanical loading to study the molecular responses to the stress/load, such as for spruce wood and cellulose paper materials [35] (Figure 6), illustrating the shift of the absorption peak at 1,160 cm-1, C–O–C vibration when the materials successively loaded from 0 up to 24 MPa at 0% RH. The decrease of the shift of absorption peak as the stress increased can be observed (6 wavenumbers in Figure 6). This decrease in wavenumber signifies an increase in the length of the covalent bonds involved in the vibration absorption, i.e. a decrease in the force constant of the bond. This demonstrates that FTIR-spectroscopy may be used to monitor molecular straining of cellulosic material under load and the molecular deformation is linearly related to the macroscopic load of the material. Using FTIR technologies, it was found that spectral deformations occurred in cellulose related groups, but no molecular deformation detected for the lignin or hemicelluloses of wood constituents. The molecular straining of the cellulose molecule resulted in

greater macroscopic force under moist conditions compared to dry conditions, but an equal macroscopic strain under both conditions. This may be interpreted that moisture accessible regions are arranged tending in parallel with the cellulose load bearing entities, suggesting that the cellulose disordered regions may not exist as large regions across the cellulose aggregate structure, rather that are spread out. In addition, the moisture absorbing area of the cellulose structure is probably related to the surface areas of the cellulose.
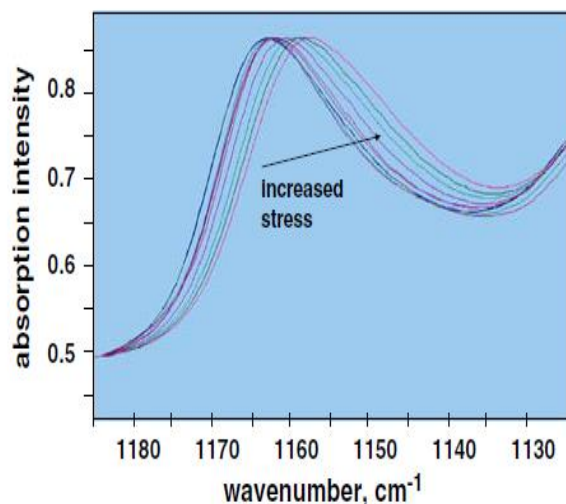

Fig. 6. Absorption spectra of the C–O–C vibration peak with increasing stress levels [35]
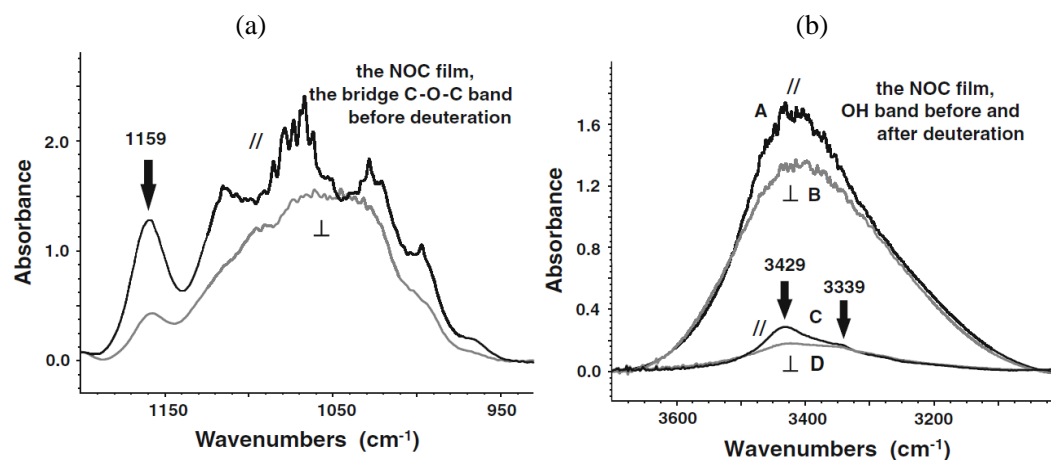

Fig. 7. The bridge C–O–C (a) and OH (b) stretching band for the NOC film before deuteration [for (b) (A, B)=before, (C, D)=after, (//)=electric vector parallel to and (⊥)=perpendicular to the stretching direction]

Polarized FTIR accompanied with a vapor-phase deuteration has been used to characterize orientation of the main chains and hence to study the molecular orientation of Nematic Ordered Cellulose (NOC) [36]. A ratio (R) of the absorbance of the band due to the particular molecular moiety for radiation polarized perpendicular to parallel to the stretching direction was introduced to evaluate the orientation behaviour of the main chains and OH groups. Computation of the FTIR spectra (e.g. Figure 7) shows that R values for the main chain are 0.32, and OH group 0.81 for Intramolecular and 0.91 for intermolecular H.B.

It is apparent that: (1) the R value for the β-glucan main chains of cellulose molecules is not necessarily in agreement with that for the side chains of OH groups; (2) the uniaxial drawing process to prepare the NOC film gave rise to the oriented main chains toward the stretching direction; (3) the nonoriented OH groups in the noncrystalline regions which occupy more than 80% of the drawn film samples could be the key for discouragement of the crystallization.

Supramolecular level investigated with FTIR is mainly focus on the crystal structure, which includes: 1) hydrogen bonding, 2) crystallinity measurement and 3) cellulose I_α and I_β determination. Kondo, Togawa and Brown [37] proposed a concept to describe how various states of molecular association can be categorized in cellulose. Figure 8 demonstrates the schematic representation of their concept.
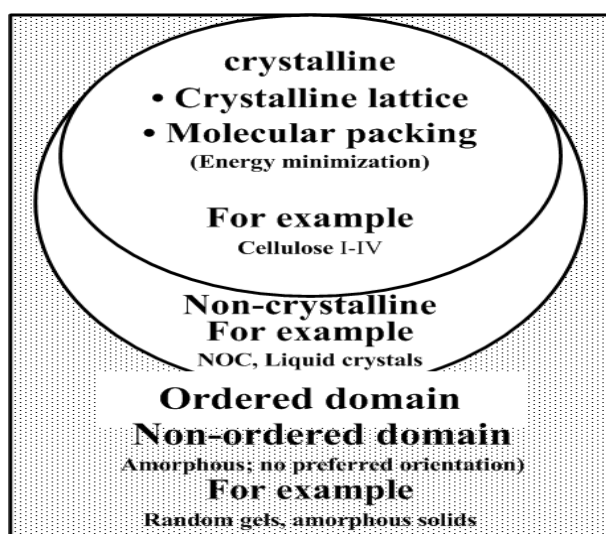

Fig. 8. Concept of glucan chain association for cellulose

According to two-phase model theory [38], there exist two regions in cellulose chain, namely amorphous and crystalline regions. Crystalline region in cellulose is an idealistic assembly of cellulose molecules in the biological system. There exist four different crystalline forms in cellulose. Researchers have developed various techniques to characterize the crystalline structure of cellulose, e.g. XRD, FTIR, Raman spectroscopy, and ^{13}C CP/MAS NMR. Among them FTIR is a more advanced tool for investigating the structure of cellulose. As mentioned above, since 1950s, some important work had been carried out by researchers and there are a number of literatures reporting on the IR/FTIR data of natural fibres [39].

The hydrogen bonds in cellulose mainly distribute in crystal domains and amorphous domains. It is possible to establish relation between the OH-bands and the cellulose structure. In 1913, Nishikawa and Ono [40] firstly revealed the crystalline nature of cellulose with X-ray diffraction. Cellulose has four polymorphic crystalline structures from cellulose I to cellulose IV. However, cellulose I and cellulose II have been most extensively studied. The other crystalline structures are still in question and yet to be studied further. According to Gardner-Blackwell model [41], hydrogen bonds for cellulose I include two intramolecular bonding, namely, O(2)H---O(6) bonding and O(3)H---O(5) bonding and one intermolecular bonding, O(6)H---O(3) (Figure 9a). Based on the Kolpak-Blackwell model [42], hydrogen bonds in cellulose II contains three intramolecular bonds: O(2)H---O(6) bonding, O(3)H---O(5) bonding

and O(2)H---O(2) bonding, and two intermolecular bonding: O(6)H---O(2) and O(6)H---O(3) (Figure 9b). The IR assignments for OH regions in cellulose I and II are summarized in Table 2.
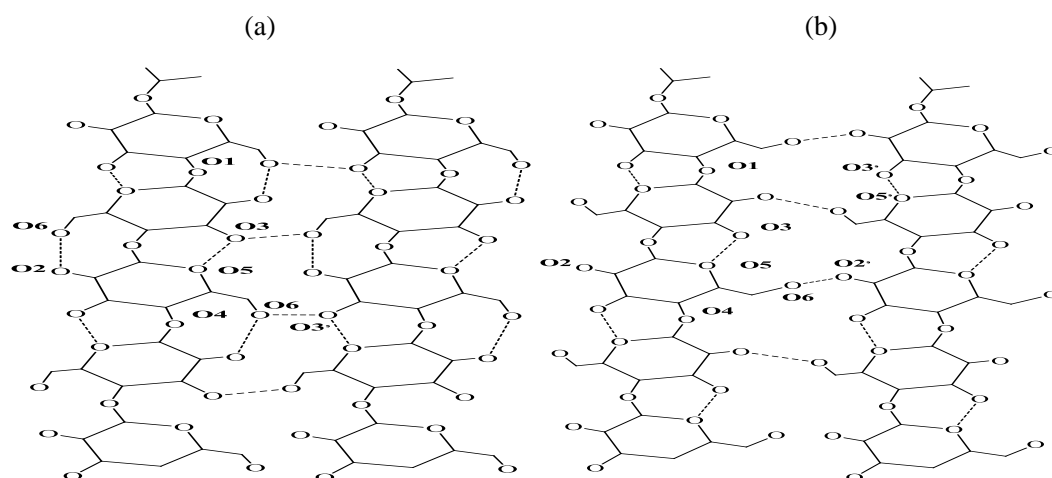
(a)   (b)

Fig. 9. Hydrogen-bonding network: (a) parallel to the *bc* plane   (cellulose I); (b) in the centre chains (Cellulose II)

Peak wavenumber (cellulose I) (cm⁻¹)	Peak wavenumber (cellulose II) (cm⁻¹)	Bonds
	3175	OH stretching
3230-3310		O(6)H---O(3)
	3308	OH Inter H-bond
	3309	OH Inter H-bond
	3315	OH Intra H-bond
3340-3375		O(3)H---O(5)
	3374	OH Intra H-bond
3405-3460		O(2)H---O(6)
	3486	OH Intra H-bond

Table 2. Correlation of bonds and celluloses (structure) [43], [44]

Hatakeyama and his coworkers firstly studied the hydrogen bond in the amorphous regions of cellulose. These studies focus on investigating the effect of temperature on the formation of interchain hydrogen bonds [45], and the effect of hydrogen bonds on the temperature dependence of the dynamic modulus and the mechanical loss tangent [46]. In 1996, Kondo and Sawatari systematic examined in detail the formation of hydrogen bonds in amorphous cellulose. The substituted amorphous cellulose derivatives, 6-O-, 2,3-di-O-, and tri-O-substituted methylcellulose, were used to model the components of amorphous cellulose. An artificial spectrum for amorphous cellulose was then quantitatively constructed mathematically by using compound i.r. spectra in order to investigate hydrogen bond formation in cellulose. The typical absorption wavenumber for the real and artificial spectra were summarized in Table 3.

Peak wavenumber (real) (cm^{-1})	Peak wavenumber (artificial) (cm^{-1})	Absorbance	Bond stretching
669	671	W	OH out-of-phase bending
899	892	M	Nonsymmetric out-phase ring
1040	1040	S	C-O
1070	1075	S	Skeletal vibrations C-O
1108	1108	S	Nonsymmetric in-phase ring
1159	1154	S	Nonsymmtric bridge C-O-C
1374	1375	M	CH bending
1420	1425	W	CH$_2$ symmetric bending
2892	2903	M	CH
3420	3457	S	OH

Table 3. Absorption wavenumber between the real and synthesized IR spectra of amorphous cellulose [43, 47]

The traditional two-phase cellulose model describes cellulose chains as containing both crystalline (ordered) and amorphous (less ordered) regions. A parameter termed the crystallinity index (CI) has been used to describe the relative amount of crystalline material in cellulose. The CI of celluloses have been measured using several different techniques including XRD, solid-state ^{13}C NMR, infrared (IR) spectroscopy and Raman spectroscopy. The determination of CI using FTIR spectroscopy is the simplest method. It should be noted that this method gives only relative values, because the spectrum always contains contributions from both crystalline and amorphous regions. In 1958, O'Connor [49] proposed Lateral Order Index (LOI, A_{1420}/A_{893}) to calculate the CI for cellulose. Later, Nelson and O'Connor [49, 50] introduced Total Crystallinity Index (TCI, A_{1375}/A_{2900}) to evaluate the CI of cellulose. The absorbance ratio A_{1420}/A_{893} was defined as an empirical CI. The absorbance at 1420 and 894 cm^{-1} are sensitive to the amount of crystalline versus amorphous structure in the cellulose, that is, broadening of these bands reflects more disordered structure. As for TCI, various reports seem do not show a coherent result [51, 52].

4. Chemical composition of natural fibres by using FTIR

Compositional variation and physical organization at the microscopic level determine the ability to perform a desired function for most materials. Lignocellulosic fibres from different lignocellulosic materials appear quite different, but the chemical composition is fairly similar although with different magnitudes of constituents. The major compositions of lignocellulosic fibres are cellulose, hemicellulose and lignin (see Figure 10), while the minor constituents include minerals, pectin, waxes and water-soluble components. The application of infrared spectroscopy in lignocellulosic fibres has a long history: The infrared spectroscopy was used to investigate the hydroxyl groups of cellulose in the 1930's [53] and significant efforts were made in the 1950's to assign the different absorption maxima in the IR spectrum of cellulose [54-59]; The absorption maxima in the IR spectra of lignin were investigated from 1940's [60, 61] through 1950's [62-64]; The characteristic absorption maxima of hemicellulose were studied during the 50's [65, 66].
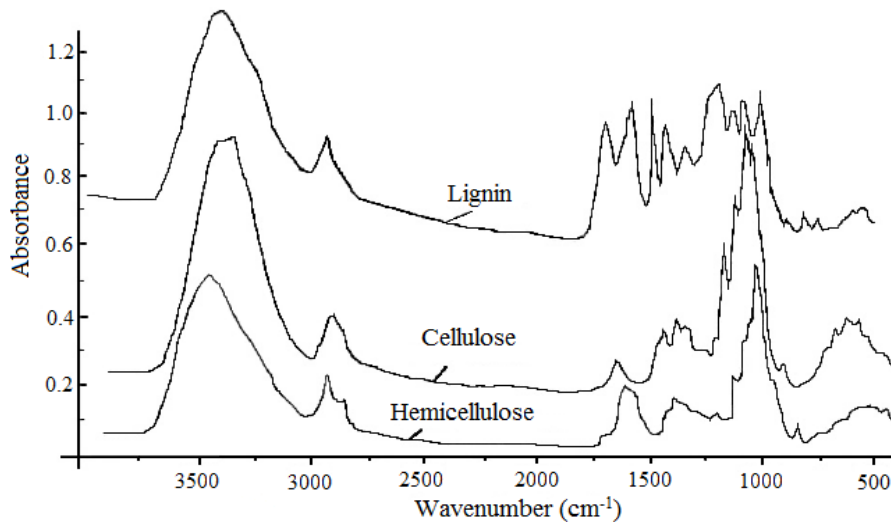
Fig. 10. IR spectra of cellulose, hemicellulose and lignin of natural fibres [60]

FTIR has been commonly used to characterize natural fibres with various treatments, e.g. grafting [67, 68], coupling [69-71], mercerization [72-74]. With the aid of FTIR, researchers are able to obtain much more in-depth information of natural fibres after various modifications. FTIR is also an efficacy technique for the surface and interface characterizations of lignocellulosic fibres [75]. This allows further interpretation of the nature of adhesion between lignocellulosic with other substances. For example, Felix and Gatenholm [76] modified the lignocellulosic fibres with polypropylene–maleic anhydride copolymer. The spectrum of untreated fibres from the spectrum of treated fibres showed two peaks: one located at 1739 cm^{-1} and one at 1746 cm^{-1}, and the FTIR analysis indicated that the reaction between fibres and copolymer can be divided into two main steps: the copolymer is firstly converted into the more reactive anhydride form and then esterification takes place on the surface of cellulose fibres.
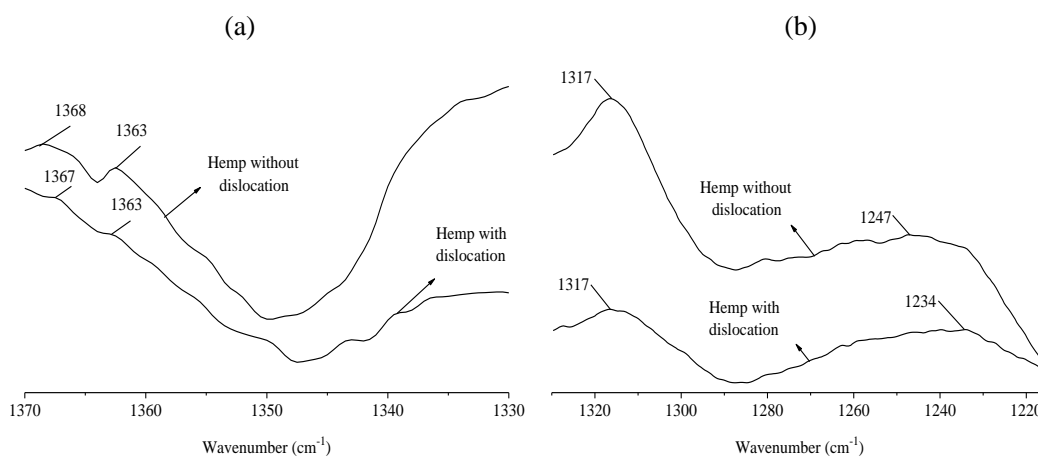

Fig. 11. FTIR spectra of hemp fibres from 1370 cm^{-1} to 1330 cm^{-1}(a) and from 1330 cm^{-1} to 1215 cm^{-1} (b) with and without dislocation [32].

FTIR has recently been found most promising to examine the change of the chemical compositions of natural fibres (hemp fibres) due to inherent defects. An example of the results is given in Figure 11. A scrutiny of the IR spectra from 1370cm^{-1} to 1330cm^{-1} shows that the band at 1368cm^{-1} and 1363cm^{-1} almost disappears in dislocation regions (Figure 11a). These two bands, assigned as the in-plane CH

bending, may be from hemicelluloses or cellulose, the near disappearance of these may be due to the removal of the hemicelluloses in dislocation regions. Hemicelluloses can form a linkage between cellulose and lignin, and lignin-carbohydrate complex with lignin by ether bonds [77]. The removal of hemicelluloses in dislocation regions may cause the decrease of transfer of shear stress under tensile loading and loss of lignin as well.

The S ring (CH2 rocking at C6 in cellulose) and G ring stretching (C–C plus C–O plus C O stretch and COH bending at C6 in cellulose) could normally be observed in bands at 1325, 1314, 1259, 1245 and 1232cm^{-1} respectively for the hemp fibres without dislocation. Due to the overlapping of bands, only two peaks can be seen in Figure 11b. Lignin is composed of three basic units, namely p-hydroxyphenyl (H), guaiacyl (G) and syringyl (S) [78]. Guaiacyl (G) and syringyl (S) are the main units of lignin, but the ratio of S/G varies from one to another plant. It was reported recently by del Río et al. [79] that S/G values calculated upon FTIR were in agreement with those calculated upon Py-GC/MS at the bands of 1271cm^{-1} and 1327cm^{-1} respectively. However, the study on hemp fibre showed that the bands at 1271cm^{-1} and 1327cm^{-1}, assigned as G-ring stretching and S ring stretching respectively, were shifted to lower wavenumbers: for the hemp fibres without dislocations (Figure 12a), the G ring and S ring stretching appear at the bands of 1259cm^{-1} and 1325cm^{-1} and for the dislocation regions at 1261cm^{-1} and 1325cm^{-1} (Figure 12b).
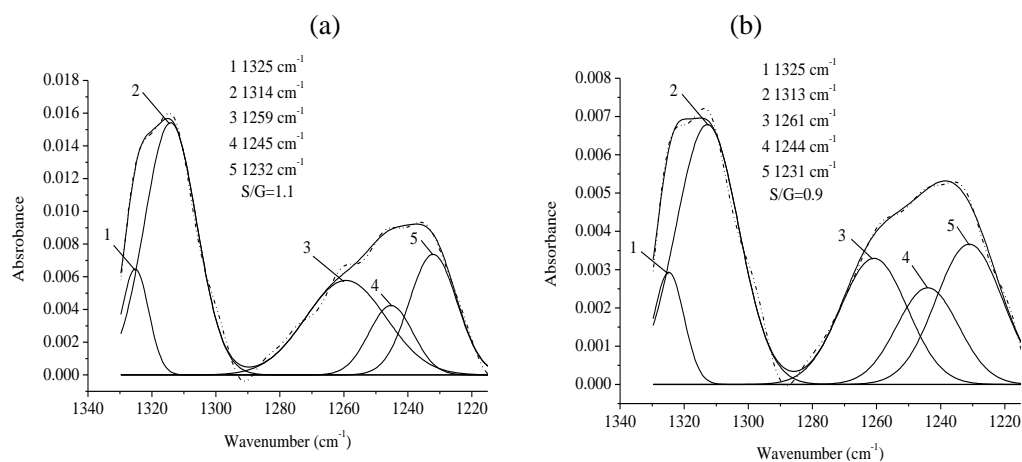

Fig. 12. Deconvolved FTIR spectra without dislocation (a) and dislocation regions (b). (Solid curves=calculated data; dotted curves=experimental data) [32].

The different molar contents of G-lignin and S-lignin of the hemp with and without dislocations gave rise to the ratio of S/G 0.9 for the former and 1.1 for the latter fibres. The lignin network in the parts without dislocations would be more rigid than that in dislocation regions. The lower absorbance in dislocations means that the lignin was removed from dislocation regions, and such the cellulose content in dislocations would be higher than that without dislocations.

FTIR can further be used to investigate the interfacial properties of natural fibre composites [80]. For example, Figures 13a and b exhibits the spectra for different types of composites containing 40% aspen fibres. The highest absorbance value corresponds to the untreated composites and the lowest value to that of composites modified with maleated polypropylene. The FTIR examination on the interface of wood fibre-reinforced polypropylene composites has also confirmed the efficacy of the technique [81].

The spectra are able to illustrate that the coupling agent was located around the wood fibres rather than randomly distributed in the polypropylene matrix, and the compatabilizer was attached to the wood fibres either by ester or hydrogen bonds.
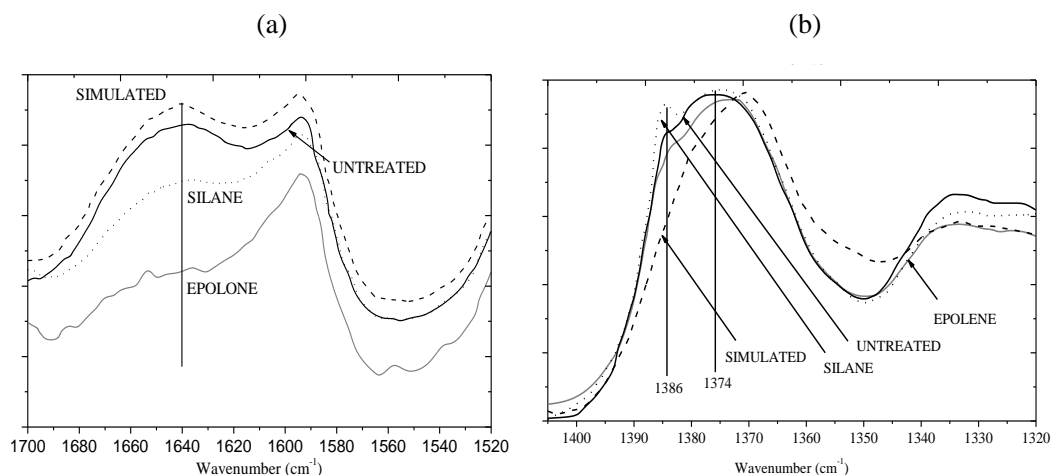
(a)   (b)

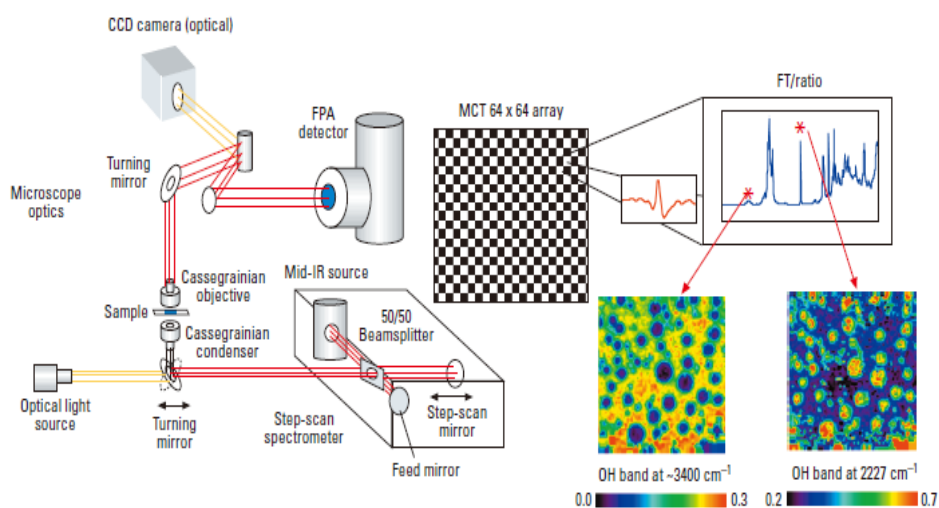Fig. 13. FTIR spectra of various types of composites

Fig. 14. Schematic of a typical FTIR imaging spectrometer [82]

5. Morphologies of natural fibres by using FTIR

FTIR spectroscopic imaging is the complete synthesis of FTIR spectroscopy with sample visualization and greatly extends the capabilities of conventional FTIR spectroscopy. Figure 14 illustrates a general configuration of an FTIR imaging micro- spectrometer. Spectral data can be represented as a picture, showing chemical information simultaneously from thousands of pixels. The main advantages of FTIR imaging are noninvasiveness, fast data collection and the ability to create visually appealing display. FTIR imaging not only provides new scientific capabilities, but it is also a compact and informative way to present results. It can collect more than 10,000 spectra in a few minutes. FTIR imaging has been shown to be a remarkable tool for biological and materials analysis. It can be used extensively to investigate the chemical composition of stem [83-85] and cell wall structure [86] of natural fibres, and

natural fibre composites [87].

FTIR imaging in conjunction with pyrolysis molecular beam mass spectrometry (py- MBMS) can work as a rapid analysis tool to evaluate difference in the chemical composition, for example, from the bark to the pith of wood stern (Figure 15) [85], and the data can statistically be processed to establish the correlation of the change in chemical features and the distance across the xylem (Figure 16).
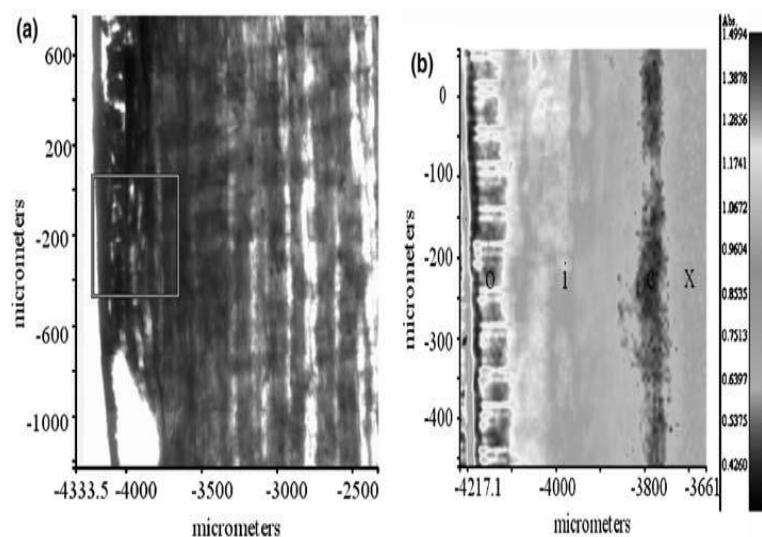

Fig. 15. (a) Visible image of the bark, cambium, and xylem of the control aspen stem. The area in the box was selected for FT-IR spectral analysis. (b) Spectral image of a portion of the outer bark [o], inner bark [I], cambium [c], xylem [x] showing the relative concentration of phenolic in these anatomical features [85].
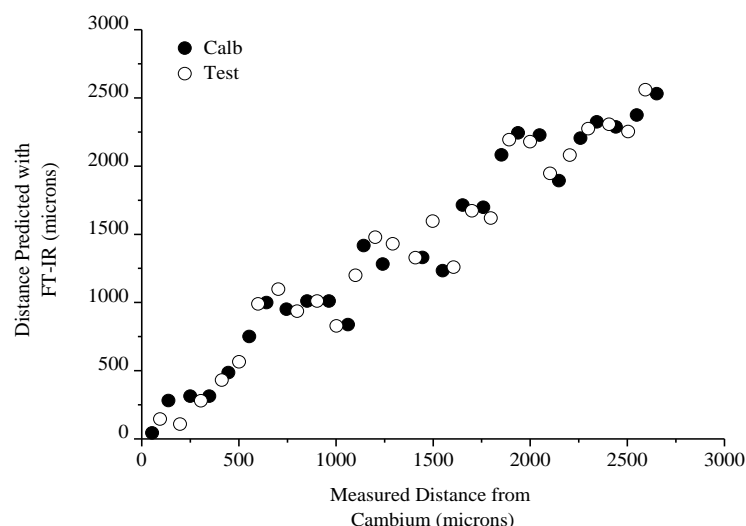
Fig. 16. PLS model predicting the distance from the bark to pith based on changes in the chemical composition. (Filled circles=calibration and open circles =test set) [85].

FTIR spectroscopy imaging has also been used to examine the orientation of the main wood compositions in transverse and longitudinal directions of wood fibres. For example, the examination by using FTIR on spruce fibres (Figures 17 and 18) [86] is able to illustrate that 1) glucomannan and xylan

show a predominant orientation in the S_2 layer of cell wall, 2) hemicelluloses are arranged in parallel with the cellulose microfibrils and accordingly more or less in parallel with the longitudinal axis (the S_2 layer of the cell wall) of fibres, 3) only a little degree of orientation can be observed for lignin and 4) the variation in the molecular orientation along the fibres seems to be uniform in the pore-free regions. These results gave rise to a conclusion that all of three main components within fibres may have a clear anisotropic behaviour under mechanical stress, that is, their properties will be different in the longitudinal direction (along the fibre axis) and the transverse direction.

FTIR can be used to examine the structure of natural fibre based composites, such as, examining the surface distribution of polyacrylamide (PAM) or the in-plane distribution of cellulose within a paper sheet [87].

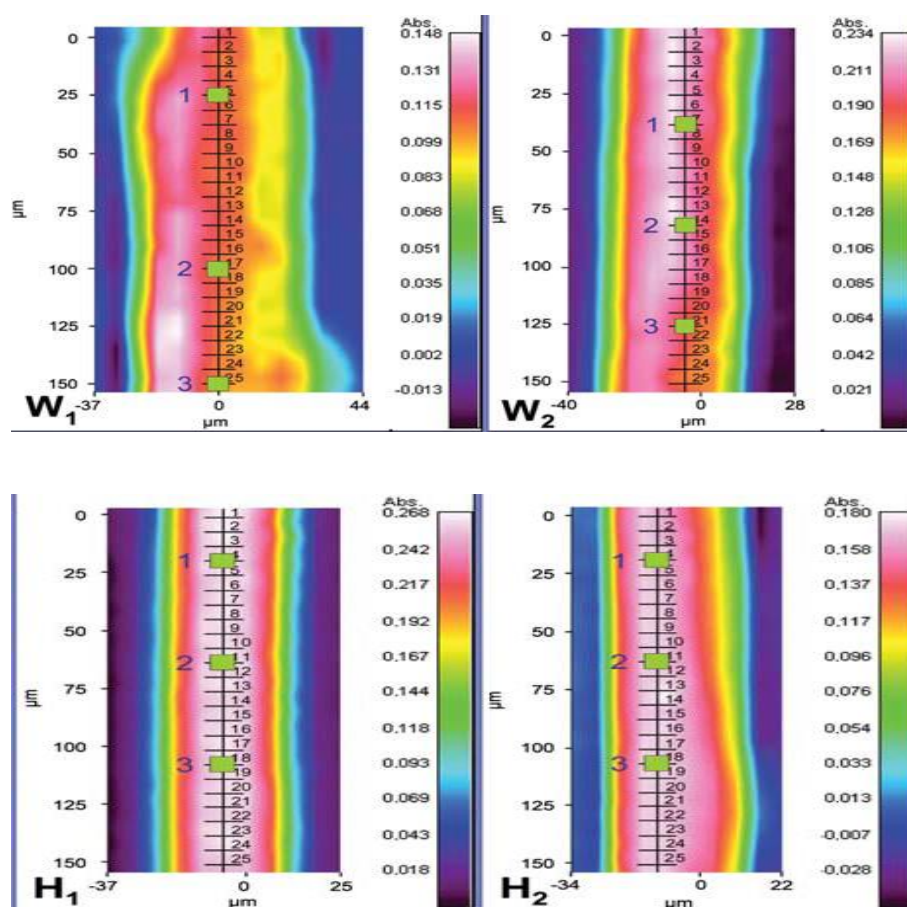Fig. 17. Total IR absorbance full-spectral images of the two *W fibres* (*W*1 and *W*2) and the two *H fibres* (*H*1 and *H*2), showing the 25 pixel positions for each fibre used for evaluating the average orientation spectra as well as the three pixel positions for each fibre selected for evaluating the orientation of the different wood polymers in the fibres [86].
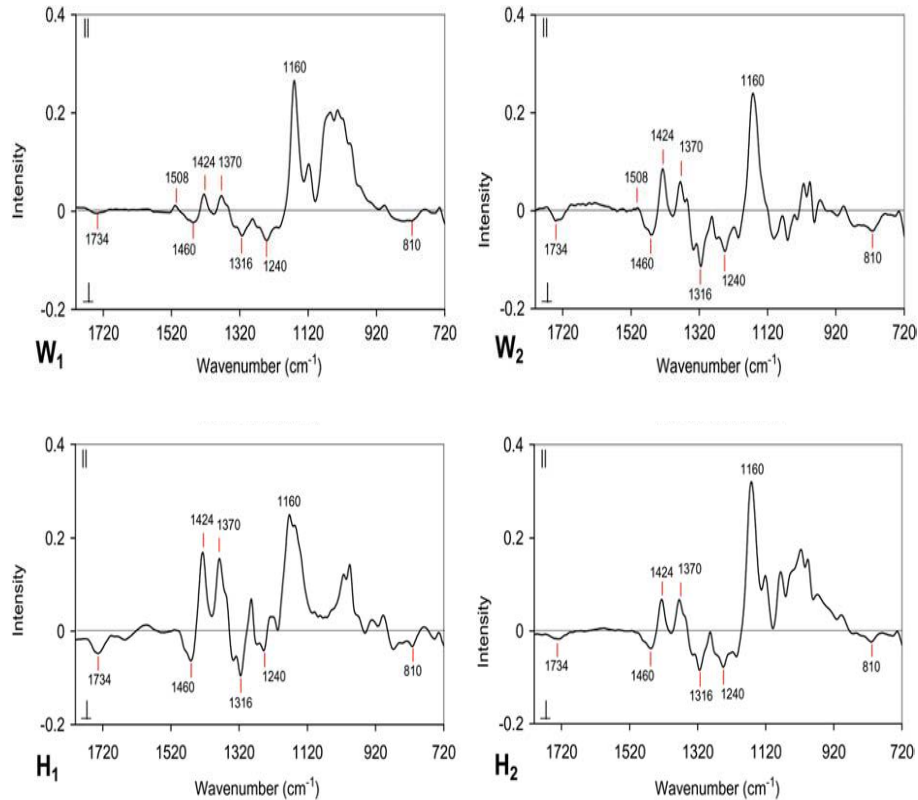
Fig. 18. Average orientation spectra of the two W fibres (W1 and W2) and the two H fibres (H1 and H2): cellulose 1160 cm⁻¹, 1316 cm⁻¹, 1370 cm⁻¹ and 1424 cm⁻¹, glucomannan 810 cm⁻¹, xylan 1734 cm⁻¹, 1460 cm⁻¹ and 1240 cm⁻¹ and lignin 1508 cm⁻¹ [86].

6. Conclusions

FTIR offers scientists an excellent range of solutions for understanding natural fibres and their related modification technologies and products, such as chemical compositions, microstructures, fibre architectures, characterisation of interface, and properties of both natural fibres and related composites.

FTIR is a powerful technique to examine the formation of inter- and intra- molecular hydrogen bonds in cellulose. The detailed database allows the establishment of strong correlation between the nature of hydrogen bonds and physical (e.g. solubility, hydroxyl reactivity, crystallinity) and mechanical properties of cellulose. The capability of accurate examination of hydrogen bonds has lead to an ever increasing uses of FTIR for investigating the defects (e.g. dislocation of hemp fibre) or deterioration (e.g. perturbation) of natural fibres and change of materials after modification.

The structure of cellulose has a profound influence on the course of chemical reactions of cellulose materials and the resulted properties. The molecular orientation and crystallization and formation of microfibrils not only vary from one plant to another, but could also change due to various environmental or other physical effects. FTIR is able to examine the nature of molecular chains, crystallinity and their correlations with various bonds.

In commons with other materials, the chemical composition at microscopic level determines the ability

to perform various functions for the usefulness of natural fibres. FTIR has been mostly successful in accurate analysis of both major (cellulose, hemicellulose and lignin) and minor (mineral, pectin, waxes) constituents of natural fibres. Change in chemical compositions, interface and hence properties of natural fibres and composites could also be effectively identified by using FTIR. FTIR is the most interesting and versatile of all analytical techniques and are well placed to become the technology of the century.

7. References

[1] Urban, M.W. (1993). Fourier Transform Infrared and Fourier Transform Raman Spectroscopy of Polymers, In:,Urban, M.W. & Craver, C.D. (Ed.),3-40, ISBN 0841225257, the University of Virginia, American Chemical Society.

[2] Annette, N.; Sudhakar, P.; Ursula, K. & Andrea, P. Fourier Transform Infrared Microscopy in Wood Analysis. In: Ursula Kües(Ed.) Wood production, wood technology, and biotechnological impacts. Universitätsverlag Göttingen,2007. 179-   ISBN 978-3-940344-11-3.

[3] Hinterstoisser, B.&Salmén, L. (2000). Application of dynamic 2D FTIR to cellulose. Vibrational Spectroscopy, Vol.22, No.1-2, pp. 111-118, ISSN 0924-2031.

[4] Kokot, S.; Czarnik-Matusewicz, B. & Ozaki, Y. (2002). Two-dimensional correlation spectroscopy and principal component analysis studies of temperature-dependent IR spectra of cotton–cellulose. Journal, Vol.67, No.6, pp. 456-469, ISSN 1097-0282.

[5] Guo, Y. & Wu, P. (2008). Investigation of the hydrogen-bond structure of cellulose diacetate by two-dimensional infrared correlation spectroscopy. Biopolymers, Vol.74, No.3, pp. 509-513, ISSN 0144-8617.

[6] http://en.wikipedia.org/wiki/Hydrogen_bond

[7] Kondo, T. (1994). Hydrogen bonds in regioselectively substituted cellulose derivatives. Journal of Polymer Science Part B: Polymer Physics, Vol.32, No.7, pp. 1229-1236, ISSN 1099-0488.

[8] Kondo, T. (1997). The assignment of IR absorption bands due to free hydroxyl groups in cellulose. Cellulose, Vol.4, No.4, pp. 281-292, ISSN 0969-0239.

[9] Kondo, T. (1997). The relationship between intramolecular hydrogen bonds and certain physical properties of regioselectively substituted cellulose derivatives. Journal of Polymer Science Part B: Polymer Physics, Vol.35, No.4, pp. 717-723, ISSN 1099-0488.

[10] Itagaki, H.;Tokai, M.&Kondo, T. (1997). Physical gelation process for cellulose whose hydroxyl groups are regioselectively substituted by fluorescent groups. Polymer, Vol.38, No.16, pp. 4201-4205, ISSN 0032-3861.

[11] Kondo, T.; Sawatari, C.; Manley, R. S. J. & Gray, D. G. (1994). Characterization of hydrogen bonding in cellulose-synthetic polymer blend systems with regioselectively substituted methylcellulose. Macromolecules, Vol.27, No.1, pp. 210-215, ISSN 0024-9297.

[12] Kondo, T. & Sawatari, C. (1994). Intermolecular hydrogen bonding in cellulose/poly(ethylene oxide) blends: thermodynamic examination using 2,3-di-O- and 6-O-methylcelluloses as cellulose model compounds. Polymer, Vol.35, No.20, pp. 4423-4428, ISSN 0032-3861.

[13] O'Sullivan, A. (1997). Cellulose: the structure slowly unravels. Cellulose, Vol.4, No.3, pp. 173-207, ISSN 0969-0239.

[14] Tashiro, K. & Kobayashi, M. (1991). Theoretical evaluation of three-dimensional elastic constants of native and regenerated celluloses: role of hydrogen bonds. Polymer, Vol.32, No.8, pp. 1516-1526, ISSN 0032-3861.

[15] Gardner, K. H. & Blackwell, J. (1974). The hydrogen bonding in native cellulose. Biochimica et Biophysica

Acta (BBA) - General Subjects, Vol.343, No.1, pp. 232-237, ISSN 0304-4165.

[16] Stipanovic, A. J. & Sarko, A. (1976). Packing Analysis of Carbohydrates and Polysaccharides. 6. Molecular and Crystal Structure of Regenerated Cellulose II. Macromolecules, Vol.9, No.5, pp. 851-857, ISSN 0024-9297.

[17] Woodcock, C. & Sarko, A. (1980). Packing Analysis of Carbohydrates and Polysaccharides. 11. Molecular and Crystal Structure of Native Ramie Cellulose. Macromolecules, Vol.13, No.5, pp. 1183-1187, ISSN 0024-9297.

[18] Langan, P.; Nishiyama, Y.&Chanzy, H. (1999). A Revised Structure and Hydrogen-Bonding System in Cellulose II from a Neutron Fibre Diffraction Analysis. Journal of the American Chemical Society, Vol.121, No.43, pp. 9940-9946, ISSN 0002-7863.

[19] Nishiyama, Y.; Sugiyama, J.; Chanzy, H.&Langan, P. (2003). Crystal Structure and Hydrogen Bonding System in Cellulose Iα from Synchrotron X-ray and Neutron Fibre Diffraction. Journal of the American Chemical Society, Vol.125, No.47, pp. 14300-14306, ISSN 0002-7863.

[20] Marrinan, H. J. & Mann, J. (1954). A study by infra-red spectroscopy of hydrogen bonding in cellulose. Journal of Applied Chemistry, Vol.4, No.4, pp. 204-211, ISSN 1934-998X.

[21] Marrinan, H. J. & Mann, J. (1956). Infrared spectra of the crystalline modifications of cellulose. Journal of Polymer Science, Vol.21, No.98, pp. 301-311, ISSN 1542-6238.

[22] Mann, J. & Marrinan, H. J. (1958). Crystalline modifications of cellulose. Part II. A study with plane-polarized infrared radiation. Journal of Polymer Science, Vol.32, No.125, pp. 357-370, ISSN 1542-6238.

[23] Liang, C. Y. & Marchessault, R. H. (1959). Infrared spectra of crystalline polysaccharides. I. Hydrogen bonds in native celluloses. Journal of Polymer Science, Vol.37, No.132, pp. 385-395, ISSN 1542-6238.

[24] Marchessault, R. H. & Liang, C. Y. (1960). Infrared spectra of crystalline polysaccharides. III. Mercerized cellulose. Journal of Polymer Science, Vol.43, No.141, pp. 71-84, ISSN 1542-6238.

[25] Fengel, D. (1992). Characterization of Cellulose by Deconvoluting the OH Valency Range in FTIR Spectra. Holzforschung, Vol.46, No.4, pp. 283-288, ISSN 0018-3830.

[26] Fengel, D. (1993). Influence of Water on the OH Valency Range in Deconvoluted FTIR Spectra of Cellulose. Holzforschung, Vol.47, No.2, pp. 103-108, ISSN 0018-3830.

[27] Fengel, D.; Jakob, H. & Strobel, C. (1995). Influence of the Alkali Concentration on the Formation of Cellulose II. Study by X-Ray Diffraction and FTIR Spectroscopy. Holzforschung, Vol.49, No.6, pp. 505-511, ISSN 0018-3830.

[28] Anthony J, M. (1988). Second derivative F.t.-i.r. spectra of celluloses I and II and related mono- and oligo-saccharides. Carbohydrate Research, Vol.173, No.2, pp. 185-195, ISSN 0008-6215.

[29] Anthony J, M. (1990). Second-derivative F.t.-i.r. spectra of native celluloses. Carbohydrate Research, Vol.197, No.0, pp. 53-60, ISSN 0008-6215.

[30] Anthony J, M. (1993). Second-derivative FTIR spectra of native celluloses from Valonia and tunicin. Carbohydrate Research, Vol.241, No.0, pp. 47-54, ISSN 0008-6215.

[31] Hinterstoisser, B. & Salmén, L. (1999). Two‐dimensional step‐scan FTIR: a tool to unravel the OH-valency-range of the spectrum of Cellulose I. Cellulose, Vol.6, No.3, pp. 251-263, ISSN 0969-0239.

[32] Dai, D. & Fan, M. (2011). Investigation of the dislocation of natural fibres by Fourier-transform infrared spectroscopy. Spectroscopy, Vol.55, No.2, pp. 300-306, ISSN 0924-2031.

[33] Klemm, D.; Philipp, B.; Heinze, T.; & Heinze, U. (1998). Comprehensive cellulose chemistry Volume 1: Fundamentals and analytical methods. ISBN 3-527-29413-9, Weinheim, Germany.

[34] Kataoka, Y. & Kondo, T. (1998). FT-IR Microscopic Analysis of Changing Cellulose Crystalline Structure

during Wood Cell Wall Formation. Journal, Vol.31, No.3, pp. 760-764, ISSN 0024-9297.

[35] Salmén, L. & Bergström, E. (2009). Cellulose structural arrangement in relation to spectral changes in tensile loading FTIR. Cellulose, Vol.16, No.6, pp. 975-982, ISSN 0969-0239.

[36] Hishikawa, Y.; Togawa, E. & Kondo, T. (2010). Molecular orientation in the Nematic Ordered Cellulose film using polarized FTIR accompanied with a vapor-phase deuteration method. Cellulose, Vol.17, No.3, pp. 539-545, ISSN 0969-0239.

[37] Kondo, T.; Togawa, E. & Brown, R. M. (2001). "Nematic Ordered Cellulose": A Concept of Glucan Chain Association. Biomacromolecules, Vol.2, No.4, pp. 1324-1330, ISSN 1525-7797.

[38] Hearle, J. W. S. (1958). A fringed fibril theory of structure in crystalline polymers. Journal of Polymer Science, Vol.28, No.117, pp. 432-435, ISSN 1542-6238.

[39] Salmén, L.; Åkerholm, M. (2005). Two-Dimensional Fourier Transform Infrared Spectroscopy Applied to Cellulose and Paper, In: Dumitriu S (Ed.), ISBN 3-540-37102-8, New York, USA

[40] Nishikawa, S. & Ono, S. (1913). Transmission of X-rays through fibrous, lamellar and granular substances. Proceedings of the Tokyo Mathematico-Physical, Vol.7, pp. 131

[41] Sugiyama, J.; Vuong, R. & Chanzy, H. (1991). Electron diffraction study on the two crystalline phases occurring in native cellulose from an algal cell wall. Macromolecules, Vol.24, No.14, pp. 4168-4175, ISSN 0024-9297.

[42] Kolpak, F. J.&Blackwell, J. (1976). Determination of the Structure of Cellulose II. Macromolecules, Vol.9, No.2, pp. 273-278, ISSN 0024-9297.

[43] Kondo, T.(2005). Hydrogen Bonds in Cellulose and Cellulose Derivatives. In: Dumitriu S (Ed.), ISBN 3-540-37102-8, New York, USA

[44] Popescu, C.-M.;Popescu, M.-C.;Singurel, G.;Vasile, C.;Argyropoulos, D. S.&Willfor, S. (2007). Spectral Characterization of Eucalyptus Wood. Applied Spectroscopy, Vol.61, No.11, pp. 1168-1177, ISSN

[45] Hatakeyama, H.; Hatakeyama, T. & Nakano, J. (1976). The effect of hydrogen-bond formation on the structure of amorphous cellulose. Applied Polymer Symposium, Vol. 28, pp.743-750, ISSN 0271-9460.

[46] Yano, S.; Hatakeyama, H. & Hatakeyama, T. (1976). Effect of hydrogen bond formation on dynamic mechanical properties of amorphous cellulose. Journal of Applied Polymer Science, Vol.20, No.12, pp. 3221-3231, ISSN 1097-4628.

[47] Kondo, T. & Sawatari, C. (1996). A Fourier transform infra-red spectroscopic analysis of the character of hydrogen bonds in amorphous cellulose. Polymer, Vol.37, No.3, pp. 393-399, ISSN 0032-3861.

[48] O'Connor, R. T.;DuPré, E. F.&Mitcham, D. (1958). Applications of Infrared Absorption Spectroscopy to Investigations of Cotton and Modified Cottons. Textile Research Journal, Vol.28, No.5, pp. 382-392, ISSN 0040-5175

[49] Nelson, M. L. & O'Connor, R. T. (1964). Relation of certain infrared bands to cellulose crystallinity and crystal latticed type. Part I. Spectra of lattice types I, II, III and of amorphous cellulose. Journal of Applied Polymer Science, Vol.8, No.3, pp. 1311-1324, ISSN 1097-4628.

[50] Nelson, M.L & O'Connor, R.T. Relation of certain infrared bands to cellulose crystallinity and crystal lattice type. Part II. A new infrared ratio for estimation of crystallinity in cellulose I and II. Journal of Applied Polymer Science, Vol.8, No.3, pp. 1325-1341, ISSN 1097-4628.

[51] Colom, X.; Carrillo, F.; Nogués, F. & Garriga, P. (2003). Structural analysis of photodegraded wood by means of FTIR spectroscopy. Journal, Vol.80, No.3, pp. 543-549, ISSN 0141-3910.

[52] Oh, S. Y.; Yoo, D. I.; Shin, Y. & Seo, G. (2005). FTIR analysis of cellulose treated with sodium hydroxide and carbon dioxide. Carbohydrate Research, Vol.340, No.3, pp. 417-428, ISSN 0008-6215.

[53] Ellis, J.W & Bath, J. (1938). The Near Infra‐Red Absorption Spectrum of Sucrose Crystals in Polarized

Light. Journal of Chemical Physics. Vol. 6, pp. 221-222,ISSN 0021-9606.

[54] Forziati, F.H.; Stone, W.K.; Rowen, J.W. & Appel, W.D. (1950). Cotton powder for infrared transmission measurements. Journal of Research of the National Bureau of Standards, Vol.45, No.(2, pp. 109-113.

[55] Rowen, J. W.; Forziati, F. H. & Reeves, R. E. (1951). Spectrophotometric Evidence for the Absence of Free Aldehyde Groups in Periodate-oxidized Cellulose1. Journal of the American Chemical Society, Vol.73, No.9, pp. 4484-4487, ISSN 0002-7863.

[56] Shirk, H. G. & Greathouse, G. A. (1952). Infrared Spectra of Bacterial Cellulose. Analytical Chemistry, Vol.24, No.11, pp. 1774-1775, ISSN 0003-2700.

[57] Ermolenko, I. N.; Zhbankov, R. G.; Ivanov, V. I.; Lenshina, N. I.&Ivanova, V. S. (1958). Investigation of some oxidation reactions of cellulose by infrared spectroscopy. Russian Chemical Bulletin, Vol.7, No.2, pp. 241-243, ISSN 1066-5285.

[58] Klein, E.&Snowden, J. (1958). Replacing Hydroxyl Groups in Cotton Cellulose. Industrial & Engineering Chemistry, Vol.50, No.1, pp. 80-82, ISSN 0019-7866.

[59] Liang, C. Y. & Marchessault, R. H. (1959). Infrared spectra of crystalline polysaccharides. II. Native celluloses in the region from 640 to 1700 cm^{-1}. Journal of Polymer Science, Vol.39, No.135, pp. 269-278, ISSN 1542-6238.

[60] Jones, E. J. (1948). The infrared spectrum of spruce native lignin. Journal of the American Chemical Society, Vol.70, No.5, pp. 1984-1985, ISSN 0002-7863.

[61] Buchanan, M. A.; Brauns, F. E. & Leaf, R. L. (1949). Native Lignin. II. Native Aspen Lignin. Journal of the American Chemical Society, Vol.71, No.4, pp. 1297-1299, ISSN 0002-7863.

[62] Stevens, G. d.&Nord, F. F. (1951). Investigations on Lignin and Lignification. VIII.1 Isolation and Characterization of Bagasse Native Lignin. Journal of the American Chemical Society, Vol.73, No.10, pp. 4622-4625, ISSN 0002-7863.

[63] Kudzin, S. F. & Nord, F. F. (1951). Investigations on Lignin and Lignification. IV. Studies on Hardwood Lignin. Journal of the American Chemical Society, Vol.73, No.2, pp. 690-693, ISSN 0002-7863.

[64] Hergert, H. L. & Kurth, E. F. (1953). The Infrared Spectra of Lignin and Related Compounds. I. Characteristic Carbonyl and Hydroxyl Frequencies of Some Flavanones, Flavones, Chalcones and Acetophenones1. Journal of the American Chemical Society, Vol.75, No.7, pp. 1622-1625, ISSN 0002-7863.

[65] Srivastava, H. C. & Adams, G. A. (1959). Uronic Acid Components of Jute Fibre Hemicellulose1,2. Journal of the American Chemical Society, Vol.81, No.10, pp. 2409-2412, ISSN 0002-7863.

[66] Timell, T. E. (1959). The constitution of a hemicellulose ffrom sugar maple (acer saccharum). Canadian Journal of Chemistry, Vol.37, No.5, pp. 893-898, ISSN 0008-4042

[67] Castelvetro, V.; Fatarella, E.; Corsi, L.; Giaiacopi, S. & Ciardelli, G. (2006). Graft Polymerisation of Functional Acrylic Monomers onto Cotton Fibres Activated by Continuous Ar Plasma. Plasma Processes and Polymers, Vol.3, No.1, pp. 48-57, ISSN 1612-8869

[68] Krouit, M.; Bras, J. & Belgacem, M. N. (2008). Cellulose surface grafting with polycaprolactone by heterogeneous click-chemistry. European Polymer Journal, Vol.44, No.12, pp. 4074-4081, ISSN 0014-3057

[69] Singh, B.; Gupta, M.; Verma, A. & Tyagi, O. S. (2000). FT-IR microscopic studies on coupling agents: treated natural fibres. Polymer International, Vol.49, No.11, pp. 1444-1451, ISSN 1097-0126

[70] Abdelmouleh, M.; Boufi, S.; Belgacem, M. N.; Duarte, A. P.; Ben Salah, A. & Gandini, A. (2004). Modification of cellulosic fibres with functionalised silanes: development of surface properties. International Journal of Adhesion and Adhesives, Vol.24, No.1, pp. 43-54, ISSN 0143-7496

[71] Sgriccia, N.; Hawley, M. C. & Misra, M. (2008). Characterization of natural fibre surfaces and natural fibre composites. Composites Part A: Applied Science and Manufacturing, Vol.39, No.10, pp. 1632-1637, ISSN

1359-835X

[72] Mwaikambo, L. Y. & Ansell, M. P. (1999). The effect of chemical treatment on the properties of hemp, sisal, jute and kapok for composite reinforcement. Die Angewandte Makromolekulare Chemie, Vol.272, No.1, pp. 108-116, ISSN 1522-9505

[73] Mwaikambo, L. Y. & Ansell, M. P. (2002). Chemical modification of hemp, sisal, jute, and kapok fibres by alkalization. Journal of Applied Polymer Science, Vol.84, No.12, pp. 2222-2234, ISSN 1097-4628

[74] Gwon, J. G.; Lee, S. Y.; Doh, G. H. & Kim, J. H. (2010). Characterization of chemically modified wood fibres using FTIR spectroscopy for biocomposites. Journal of Applied Polymer Science, Vol.116, No.6, pp. 3212-3219, 1097-4628

[75] Jacob, M.; Joseph, S.; Pothan, L. A. & Thomas, S. (2005). A study of advances in characterization of interfaces and fibre surfaces in lignocellulosic fibre-reinforced composites. Composite Interfaces, Vol.12, No.1/2, pp. 95-124, ISSN 0927-6440

[76] Felix, J. M. & Gatenholm, P. (1991). The nature of adhesion in composites of modified cellulose fibres and polypropylene. Journal of Applied Polymer Science, Vol.42, No.3, pp. 609-620, ISSN 1097-4628

[77] Sjöström, E. (1981). Wood Chemistry: Fundamentals and Applications. ISBN 0-12-647481-18, San Diego, USA.

[78] Ruan, D.; Zhang, L.; Mao, Y.; Zeng, M. & Li, X. (2004). Microporous membranes prepared from cellulose in NaOH/thiourea aqueous solution. Journal of Membrane Science, Vol.241, No.2, pp. 265-274, ISBN 0376-7388

[79] del Río, J. C.; Gutiérrez, A.; Rodríguez, I. M.; Ibarra, D. & Martínez, Á. T. (2007). Composition of non-woody plant lignins and cinnamic acids by Py-GC/MS, Py/TMAH and FT-IR. Journal of Analytical and Applied Pyrolysis, Vol.79, No.1-2, pp. 39-46, ISSN 0165-2370

[80] Colom, X.; Carrasco, F.; Pagès, P. & Cañavate, J. (2003). Effects of different treatments on the interface of HDPE/lignocellulosic fibre composites. Composites Science and Technology, Vol.63, No.2, pp. 161-169, ISSN 0266-3538

[81] Hristov, V. & Vasileva, S. (2003). Dynamic Mechanical and Thermal Properties of Modified Poly(propylene) Wood Fibre Composites. Macromolecular Materials and Engineering, Vol.288, No.10, pp. 798-806, ISSN 1439-2054

[82] Koenig, J. L. (2001). FTIR images: a new technique produces images worth a thousand spectra. Analytical chemistry (Washington), Vol.73, No.13, pp. 360A, ISSN 0003-2700

[83] Himmelsbach, D. S.; Khalili, S. & Akin, D. E. (2002). The use of FT-IR microspectroscopic mapping to study the effects of enzymatic retting of flax (Linum usitatissimum L) stems. Journal of the Science of Food and Agriculture, Vol.82, No.7, pp. 685-696, ISSN 1097-0010

[84] Himmelsbach, D.S.; Khalili, S. & Akin, D.E. (1998) FT-IR microspectroscopic imaging of flax (Linum usitatissimum L.) stems. Molecular and Cellular Biology, Vol. 44, No.1, pp.99-108, ISSN 0270-7306

[85] Labbé, N.; Rials, T. G.; Kelley, S. S.; Cheng, Z.-M.; Kim, J.-Y. & Li, Y. (2005). FT-IR imaging and pyrolysis-molecular beam mass spectrometry: new tools to investigate wood tissues. Wood Science and Technology, Vol.39, No.1, pp. 61-76, ISSN 0043-7719

[86] Stevanic, J. S. & Salmén, L. (2009). Orientation of the wood polymers in the cell wall of spruce wood fibres. Holzforschung, Vol.63, No.5, pp. 497-503, ISSN 0018-3830

[87] Sakaemura, T.; Mihara, I. & Yamauchi, T. (2009). Microscopic Attenuated Total Reflection/Fourier Transform Infrared Imaging of Paper Containing a Polyacrylamide Dry Strength Resin. Sen'i Gakkaishi, Vol.65, No.9, pp. 252-255, ISSN OO37-9875